EXTRACTING SONAR RELATIVE BEAM PATTERNS FOR MULTI-SECTOR MULTIBEAM SONAR

ANAND DEVAPPA HIROJI

June 2016

EXTRACTING SONAR RELATIVE BEAM PATTERNS FOR MULTI-SECTOR MULTIBEAM SONAR

Anand Devappa Hiroji

Department of Geodesy and Geomatics Engineering
University of New Brunswick
P.O. Box 4400
Fredericton, N.B.
Canada
E3B 5A3

June 2016

PREFACE

This technical report is a reproduction of a dissertation submitted in partial fulfillment of the requirements for the degree of Doctor of Philosophy in the Department of Geodesy and Geomatics Engineering, June 2016. The research was supervised by Dr. John Hughes Clarke, and funding was provided by the Natural Sciences and Engineering Research Council of Canada (NSERC) and ArcticNet.

As with any copyrighted material, permission to reprint or quote extensively from this report must be received from the author. The citation to this work should appear as follows:

Hiroji, Anand Devappa (2016). *Extracting Sonar Relative Beam Patterns for Multi-Sector Multibeam Sonar*. Ph.D. dissertation, Department of Geodesy and Geomatics Engineering, Technical Report No. 304, University of New Brunswick, Fredericton, New Brunswick, Canada, 260 pp.

ABSTRACT

The use of multibeam acoustic backscatter data for bottom characterization is currently being attempted by many researchers to aid geological, biological, and engineering projects. Ideally the absolute bottom backscatter strength would be measured, but in reality the reported data are overprinted by system-related geometric and radiometric effects. In real time, manufacturer-applied gain only partly reduces these effects. Existing post-processing algorithms undertake improved but still imperfect corrections to better account for these residual artifacts. The geometric effects include changing range, grazing angle and insonified area across the swath, whereas the radiometric effects include the angular variation in the transmitted energy and the receiver sensitivity. Recent developments in motion stabilization that involves multiple sectors, which are used to achieve higher and more equal sounding density, have added significantly more radiometric complications to the backscatter imagery. Before the backscatter data can be used for classification, either in the form of a mosaic or in the form of backscatter strength angular response curves, these remaining artifacts in the data have to be properly minimized.

The residual artifacts reflect the fact that existing empirical beam pattern corrections imperfectly account for geometry and radiometry, and do not adequately distinguish between grazing and sonar relative angle. This research develops a new method of reducing the backscatter data by explicitly differentiating between seafloor angular response and radiometric artifacts. The new method further differentiates between along-track and across-track radiometric beam patterns. The developed method does not require

any prior knowledge of seafloor characteristics. It is capable of propagating standard deviation from the backscatter data to the extracted radiometric beam pattern. This enables the user to access the reliability of extracted radiometric beam patterns.

ACKNOWLEDGEMENTS

Firstly, I would like to express my sincere gratitude to my supervisor Prof. John E. Hughes Clarke, for his immense enthusiasm, continuous support and mentoring, and patience with me. His knowledge and curiosity to explore new things always fascinates me. I am delighted to have a supervisor who cares not only for his students but also for their families. I would like to thank him for his confidence in me and the opportunities he gave me to survey places that I would otherwise not have been seen. I consider myself very lucky to have spent these most intensely educational years of my life having him as my Guru. I would like to express my respect for him and for all the teachers that I have had from my childhood by quoting a Sanskrit shloka:

गुरुर्ब्रह्मा गुरुर्विष्णुः गुरुर्देवो महेश्वरः ।
गुरुरेव परंब्रह्म तस्मै श्रीगुरवे नमः ॥

A Guru is like Lord Brahma as he generates knowledge within us, like Lord Vishnu as he drives ideas and knowledge into our mind onto the right path, and like Mahesh (Shiva) as he destroys the ill-conceived ideas that come from our knowledge, while enlightening us and helping us stay on the right path. Thus the Guru is like our ultimate God and I pray to and respect them.

This research and dissertation would not have been possible without Prof. Hughes Clarke's expertise and time from his very busy schedule.

I am thankfull to the sponsors of the Ocean Mapping Group and Natural Science and Engineering Research Councile (NSERC) for their financial support.

TABLE OF CONTENTS

LIST OF TABLES

LIST OF FIGURES

xiv

LIST OF ABBREVIATIONS

ARC   Angular Response Curve

BS   Backscatter Strength

BSn   Backscatter Strength at nadir

BSo   Backscatter Strength at oblique angle

BTS   Bottom Target Strength

CPA   Center Pointing Angle

DTM   Digital Terrain Model

GRA   Grazing Angle

GUI   Graphical User Interface

MRLI   Modified Relative Linear Intensities

OMG   Ocean Mapping Group

RBP   Radiometric Beam Pattern

RLI   Relative Linear Intensity

RP   Reference Point

RS   Receiver Sensitivity

RSD   Relative Standard Deviation

Rx   Receiver

SD   Standard Deviation

SL   Source Level

SRA   Sonar Relative Angle

SRA-R   Sonar Relative Angle at Receiver at the time of reception

SRA-T	Sonar Relative Angle at Transmitter at the time of transmission
stbd	Starboard (side)
TL	Transmission Loss
TS	Target Strength
TTS	Total Target Strength
TVG	Time Varying Gain
TVG-BS	Time Varying Gain for Backscatter Strength
Tx	Transmitter
UNB	University of New Brunswick
VRA	Vertically Referenced Angle

1   INTRODUCTION

The sediment-water interface is of interest for many applications including understanding seabed structural loading, acoustic signal propagation for anti-submarine warfare, marine geological processes, and marine biological habitats. The least ambiguous approach to precisely determine the type of sediment is to photograph or physically sample the seafloor. Though these methods can be very accurate, they are extremely expensive and give only localized results. For larger areas, it is more practical to use remote sensing technology based on sonar. The potential use of multibeam sonar backscatter for sediment classification was identified in the late 1980s [de Moustier, 1986]. Since then many researchers (as referenced in this thesis) have worked on improving issues associated with multibeam backscatter to achieve a more reliable sediment classification.

A unique radiometric and geometric effect on backscatter data is present in each survey due to changing hardware, software, and environment. For most multibeam sonars, the received backscattered data are at least approximately corrected for radiometric and geometric effects. As a result, for a single survey, even though the absolute backscatter calibration remains in doubt, relative changes in reduced backscattered intensities have long been used as a tool for discrimination of different seabed types. In the case of multiple repetitive surveys of the same area, a more valuable

capability would be to confidently identify discernable changes in seabed backscatter strength even though instrumentation may change between surveys. For single surveys used to identify major sediment types, or for repetitive surveys designed to identify significant sediment changes, the magnitude of differences in backscatter data are much greater than small imperfections due to radiometric and geometric effects. In such a case radiometric and geometric effects are often irrelevant. However for repeat surveys of the same area, where the sediment changes are expected to be subtle, the unique radiometric and geometric effects can thus obscure the real seabed backscatter change.

This research reviews the current state of the art in radiometric and geometric data reduction. A particular focus is on trying to arrive at a precise estimate of the seabed backscatter strength. This reduction requires knowledge of source level, beam pattern, pulse lengths, seabed slopes, and transmitter (Tx) and receiver (Rx) orientations at the respective times. Normally, simplified approximations are undertaken for backscatter data reductions. A greater research focus is on radiometric effects which are a particular weakness, especially in multi-sector systems where the radiation patterns vary much more rapidly with elevation angle than in single sector systems. For example, EM 122 multibeam sonar with eight sectors in single swath has very narrow transmit sectors of about 15° with corresponding rapid angular variations in intensity in across-track direction. As shown in section 3.3 recent developments in complete motion stabilization require multiple sectors, which complicate the radiometric effects on the backscatter data.

1.1   Need of Separating Geometric and Radiometric Effect

When sound energy insonifies a unit area on the seafloor at a particular angle, the energy is reradiated by the seafloor in all directions. The reradiated energy that returns in the direction of the source is referred to as the backscatter. The ratio of the incident and backscattered energy at a reference distance from the seafloor is an inherent property of the material (and its configuration) at the seabed. This ratio, when expressed in logarithmic scale is termed the Backscatter Strength (BS) of the material. The BS is a function of insonification geometry (grazing angle) and physical properties of two materials, the water and the sediment. The BS across an entire insonified swath, when plotted with respect to the grazing angle (GRA) at the seafloor, is commonly referred to as the angular response curve (ARC) or angular variation. This ARC is unique for each sediment type and has been used for classification by many researchers [de Moustier, 1986; Hughes Clarke, 1994; Hughes Clarke et al., 1997; Fonseca & Mayer, 2007; Huang et al., 2013]. Figures 1.1 and 1.2 show some of the earliest compilations of ARCs. This research aims to reduce the backscatter data with maximum possible accuracy and make the ARCs available for researchers for seafloor classification.
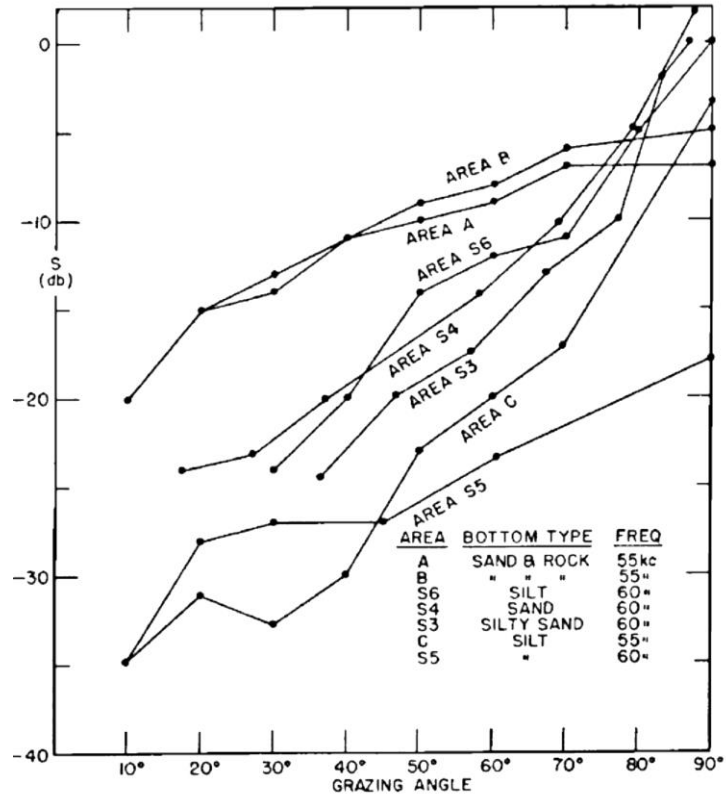
Figure 1.1: Scattering strength as a function of GRA at 55 and 60 kHz by Urick [1954]
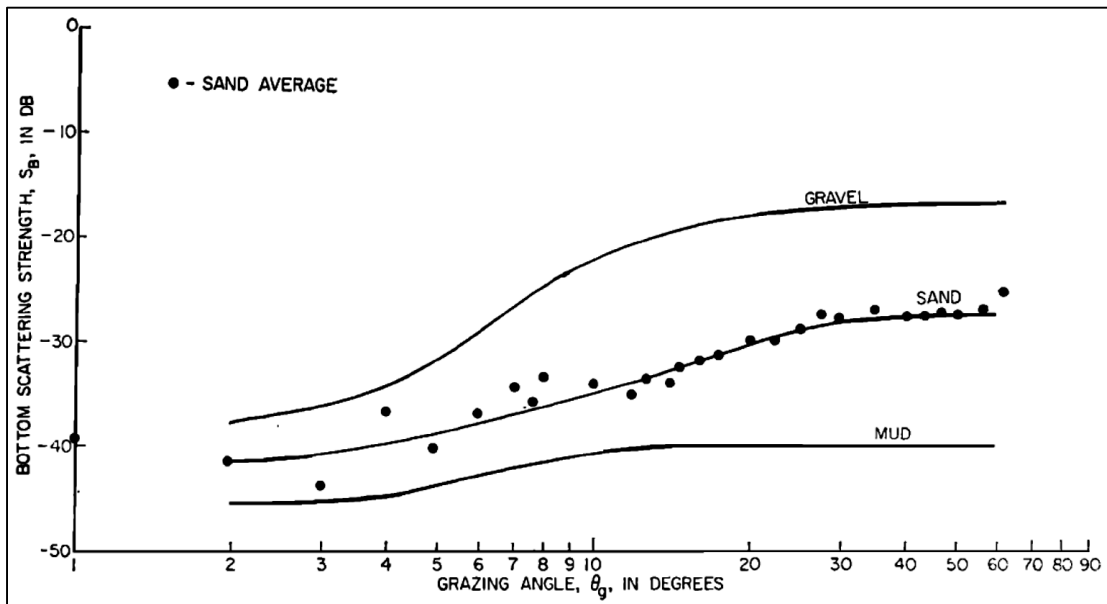
Figure 1.2: Average curves for bottom-backscattering strength S_b as a function of grazing angle θ_g by McKinney [1964]

4

In reality, just an estimate of the BS is available through correcting the received echo for a number of factors. These corrections are explained in detail in Section 2.4 and can be grouped into two categories: radiometric beam pattern (RBP) corrections and geometric corrections. The RBP corrections include corrections associated with sonar properties such as Tx intensities, Rx sensitivity, and applied gains. The geometric corrections are associated with the insonified area, ranges, and topography of the seafloor (local slopes). Most of the end users of the multibeam backscatter data expect a geographically registered map of intensity commonly referred to as the mosaic of the survey area. The mosaic is expected to contain intensities after RBP and geometric corrections are applied. As an additional standard processing step for a mosaic, the intensities have to be normalized such that any grazing angle effect (across-track angular variation) is minimized. Angular variation needs to be normalized to have a uniform representation of backscatter across the swath. To do so Kongsberg (a manufacturer) have real-time angular variation compensator functions based on simplified assumptions. This real-time function is usually known as a time-varying gain (TVG-BS) function as it depends on time or range (and hence geometry) of the sonar beam.

The RBP and geometric corrections are related to different angles associated with the multibeam geometry. The sonar relative angle (SRA) is fixed within the sonar reference frame (shown in green in Figure 1.3) and hence associated with the ship's orientation at the time of either transmit or receive. SRA is defined by its along- and across-track components; Figure 1.3 shows the across-track component. The vertically referenced angle (VRA) is fixed with respect to the local horizontal plane (shown in black in Figure

1.3) and does not roll with the sonar (ship); it is defined by depression (shown in Figure 1.3) and azimuthal angles. The GRA is considered 90° at orthogonal incidence on a perfectly flat seafloor. However in the case of real seafloor, GRA is a function of the beam vector and the along- and across-track slope. The computations of GRAs and SRAs are described in Section 4.1.3. Clearly the RBP is related to SRA while the geometric effects are related to the GRA. During backscatter data reduction, in order to accurately correct for RBP and geometric effects, one has to account for them separately. This approach is used in the method developed in this thesis to obtain ARCs with maximum possible accuracy.
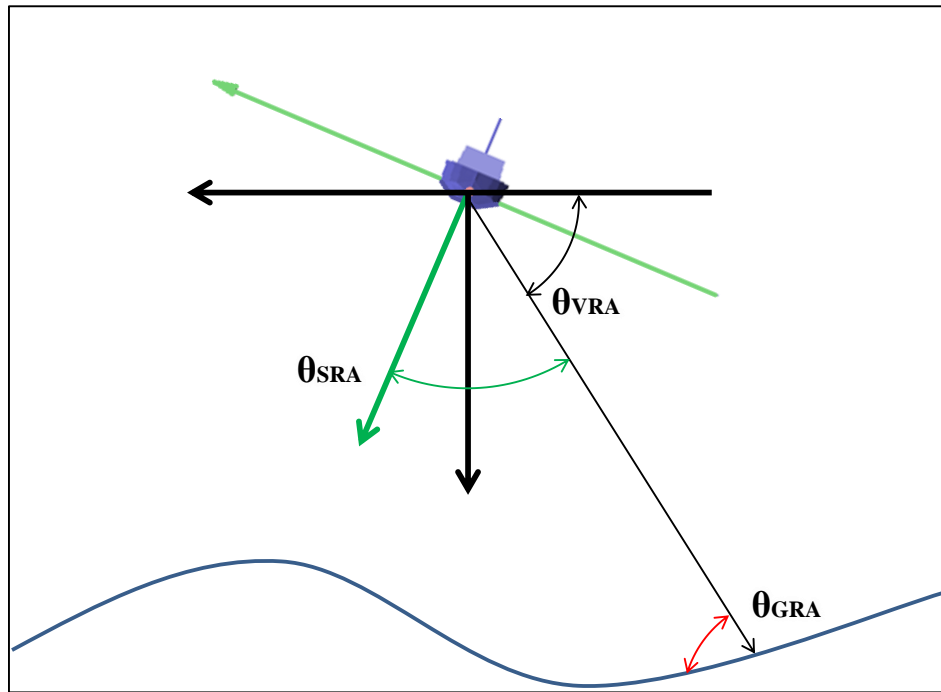
Figure 1.3: Different angles associated with multibeam geometry

1.2   Case Study

This research has used datasets collected at two locations during 2014 and 2015. Detailed maps indicating location and bathymetry are included in Appendix 9.4. The datasets were acquired with specific conditions for the development and verification of this new method. In both the case studies, the multibeam data were collected using a Kongsberg Maritime's EM 710 multibeam sonar which is a multi-sector, multi-swath system. Table 1.1 summarizes the details of datasets while more details can be found in Chapter 5. The data were collected on a uniform seafloor with minimum relief to simplify the geometry. The area was surveyed with multiple modes while first deliberately rolling and then yawing the vessel to try to detect any radiometric issues by increasing the range of SRA used during the survey. These datasets allowed the development and testing of new algorithms in this research.

Table 1.1: Case study datasets

	Dataset 1	**Dataset 2**
Location	Bute Inlet , British Columbia, Canada	Howe Sound, Squamish, British Columbia, Canada
Period	12th and 13th June 2014	19th and 20th April 2015
Instrumentation	EM 710	EM 710
Depths	100m, 200m	50m
Modes	Very Shallow, Shallow	Very Shallow, Shallow
Manufacturer corrections for BS	TVG-BS only	TVG-BS and Bscorr

Though this research is based on the datasets from an EM 710, the intent is to develop algorithms for the full range of multisector, multi-swath systems (including EM 2040, EM 302, EM 122).

1.3   Contribution to the Backscatter Data Processing

The major aim of this research is to develop a method of correcting RBP from backscatter data. The developed method unambiguously extracts RBPs from strategically collected backscatter data on a test site. The extracted RBPs are then removed from the backscatter data for entire survey area, considering different angles involved during the data collection.

The developed method is analogous to the conventional multibeam patch test that is conducted after a new installation of multibeam sonar to ensure the integrity of system offsets, alignments, and timing for optimal bathymetric accuracy. The developed backscatter patch test allows unambiguous separation of RBP from geometric effects allowing users to confidently remove both effects simultaneously from the backscatter data that were collected with any motion history that results in a change in ship orientation or over rapidly varying seafloor slopes. Furthermore, the developed algorithms identify and separate the Rx and Tx RBPs to properly correct for them during data reduction. The developed algorithms compose functions representing the RBPs of the specific sonar hardware and software combination. The functions are unique and

valid until any software or hardware update is performed. This new approach of removing RBPs with respect to SRA and at the same time removing the geometric effect with respect to GRA results in 1) increased confidence in extracted ARCs 2) ability to obtain ARCs with same confidence irrespective of sea state (ship motion) and seafloor geometry as shown in Chapter 6.

The extracted RBP ensures more accurate backscatter data reduction compared to real-time manufacturer applied corrections or empirical beam pattern removal methods. This new approach extracts more reliable ARCs which will help research into seafloor classification.

1.4 Document Organization

This thesis is divided into seven chapters. Multibeam sonar backscatter data (Chapter 2) introduces BS theory, BS and physical properties of the seafloor, and use of BS for seafloor classification. It then reviews corrections applied before reporting multibeam sonar backscatter data and how corrections are dealt with in post processing. Chapter 3 includes detailed discussions on motion stabilization and the resulting radiometric beam pattern and geometric effect; it concludes with a detailed discussion of current methods of removing beam patterns from ARC and outlines the problem statement of this research. Chapter 4 explains in detail the methodology followed and how RBPs are extracted and the challenges encountered. Chapter 5 describes the sensitivity analysis

performed on the developed RBP extraction method. Chapter 6 tests the validity of the developed method using three different approaches. The conclusion of this research is given in Chapter 7.

2 MULTIBEAM SONAR BACKSCATTER

This chapter includes four sections and begins with an introduction to backscatter strength theory in Section 2.1; this section defines basic terms that are used in multibeam sonar backscatter theory. The relationship between physical properties of seafloor and backscatter strength is discussed in Section 2.2; this section briefly defines three widely accepted models used for relating measured sonar backscatter to seafloor properties. The use of multibeam backscatter data for the seafloor classification is briefly reviewed in Section 2.3; this includes comparison between seafloor classification using ARC and mosaic. Section 2.4 explains the multibeam sonar reported backscatter data including some processing steps and assumptions.

2.1 Backscatter Strength Theory

Simply put, the backscatter strength is a comparison of the incident and backscattered energy. The review of publications reveals that there are a few terms that are representative of the way backscatter is usually described depending on the units and the area considered. In this section, all related and required terms are defined.

2.1.1 Backscattering Coefficient

The backscattering coefficient is a dimensionless quantity [Mitchell & Somers, 1989] and defines the ratio of incident to backscattered energy as shown in Equation 1. This parameter is governed by seafloor properties only and not by sonar properties.

$$S_b(\theta) = \frac{P_b}{I_i A} \quad or \quad \sigma = \frac{I_b}{I_i} \tag{1}$$

In Equation 1 the P_b is the power backscattered from the seafloor per unit solid angle ($W/steradian$), I_i is the acoustic incident energy on the surface (W/m^2), A is effective insonified surface area (m^2), and I_b is the acoustic energy backscattered towards the source. This backscatter coefficient is also denoted as σ by other researchers [Lurton, 2002]. In this case, rather than using power per unit solid angle, intensities at a unit distance are substituted. The magnitude of intensity decays with the distance due to spherical spreading and absorption, thus it is necessary to measure the backscattering coefficient at a unit distance. The measured intensity (corrected for attenuation) is corrected by the range to unit distance denoted by r or R and is referred to as the backscattering cross-section defined by Equation 2.

$$\sigma_{bs}(\theta_i) = \frac{I_s(\theta_i)R_{1m}^2}{I_i(\theta_i)} \qquad (in\ m^2) \tag{2}$$

σ_{bs} is a backscattering cross-section at a seabed relative grazing angle of θ_i and I_i is the incident intensity measured at range R from the seabed.

12

2.1.2 Target Strength or Backscattering Strength

The target strength (TS) or BS is the logarithmic form of the backscatter coefficient expressed in dB as $10 \, log_{10} \, S_b(\theta)$ or $10 \, log_{10} \, \sigma(\theta_i)$ [Urick, 1954; Urick, 1983; Mitchell & Somers, 1989; Lurton, 2002]. The target strength is defined with reference to a unit insonified area of $1 \, m^2$ denoted by A_1, and is given in Equation 3 [Lurton, 2002].

$$TS = 10 \, log_{10} \left[\frac{\sigma_{bs}(\theta_i)}{A_1} \right] \qquad (in \, dB \, referenced \, to \, 1 \, m^2 \, per \, m^2) \qquad (3)$$

When the target is a continuous rough surface (seafloor) rather than discrete object, the target strength is more often referred to as the backscatter strength (BS_s) [Lurton, 2002]. The correct use is to express the BS_s or TS in "dB referenced to $1 \, m^2$ per m^2" but it is commonly expressed as only "dB" [Lurton, 2002].

2.1.3 Total Target Strength and Bottom Target Strength

The actual or total target strength (TTS) is the target strength of the total insonified area [Lurton, 2002]. The TTS is referred to as bottom target strength (BTS) by Kongsberg (instrument manufacturer) in their technical notes [Hammerstad, 2000] and defined as shown in Equation 4.

$$BTS = TTS = BS_s + 10log_{10}(A/A_1) \qquad (in\ dB\ referenced\ to\ 1\ m^2) \quad (4)$$

Where BS_s is backscattering strength in dB referenced to 1 m^2 per m^2, A is actual insonified area, and A_1 is unit insonified area (1 m^2). For the rest of this thesis, "BS" is used to indicate the backscattered to incident wave intensity ratio in dB referenced to 1 m^2 per m^2 and BTS is used to represent total backscattered contribution for insonified area in dB referenced to 1 m^2. This is adopted to be consistent with Kongsberg's technical note to avoid confusion.

2.1.4 Actual Insonified Area

For the case of a unsteered transmitted spherical wave where the pulse length is small, a flat horizontal seafloor is insonified at first directly below the ship and then progressively outboard in the across-track direction [Augustin et al., 1996]. Figure 2.1 shows the geometries involved in the insonification. The insonified area depends on along- and across-track seafloor slopes, the along-track Tx (θ_t) and across-track Rx (θ_r) beam width, transmit pulse length (τ), and incident angle θ of the beam. The insonified area is always enclosed within the intersection of Tx and Rx beam footprints as represented in Figure 2.1 using an approximate equivalent beam width of 3dB. In principle the actual equivalent beam width is an integrative measure of beam directivity accounting for shape of the main lobe as well as the side lobes. However, for most of the sonar systems the difference in insonified area is often small [Weber, 2015].
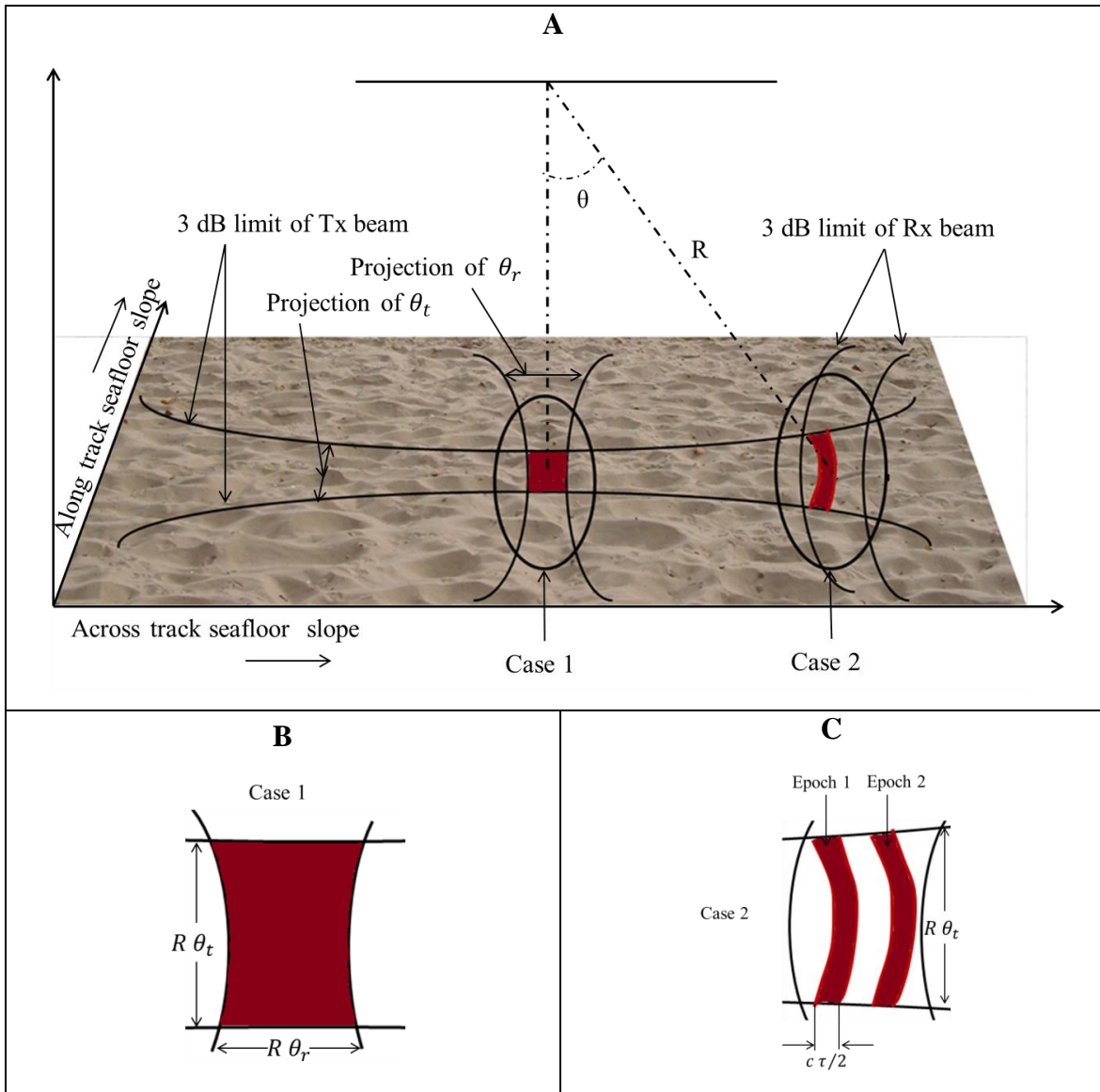
Figure 2.1: Geometries involved in the insonification and instantaneously insonified area for two different cases

When considering the transmitting and receiving beam widths, the beam angles, and the pulse length, two distinct cases are distinguished [Urick, 1954; Augustin et al., 1996]. In case 1, around vertical incidence, the pulse length is sufficient to completely insonify the beam footprint as shown in Figure 2.1B. In that case, the insonified area is approximated by a rectangle and calculated using Equation 5.

15

$$A = \frac{\theta_t R \; \theta_r R}{\cos \theta} \tag{5}$$

As the area in Equation 5 is controlled by transmit and receive beam width, this case near nadir is referred to as the beam width limited case.

In case 2, at oblique beam angles, the pulse length is too short to insonify the whole beam footprint. The projection of pulse length on the surface controls the across-track insonification as shown in Figure 2.1C. The projected pulses have a shape of curved annulus bounded by increasing Tx beam width. As a result, the insonified areas at epoch 1 and epoch 2 are not exactly identical. The area in this pulse length limited case is approximated by a rectangle and calculated by Equation 6, where c represents sound speed.

$$A = \frac{\theta_t R \; c \; \tau}{2 \sin \theta} \tag{6}$$

Figure 2.2 graphically illustrates Equations 5 and 6. The transition from beam width limited case to pulse length limited case happens when the projection of pulse length on the seafloor ($c \, \tau/2$ in Figure 2.1C) is equal to or less than the projection of Rx beam width ($R \, \theta_r$ in Figure 2.1B). The transition depends on pulse length, depth and Rx beam width. For the ideal case of a flat seafloor, increase in depth moves the transition close to nadir (0° incident) and vice-versa, while longer pulse lengths and small Rx beam widths move the transition away from nadir and vice-versa.

16
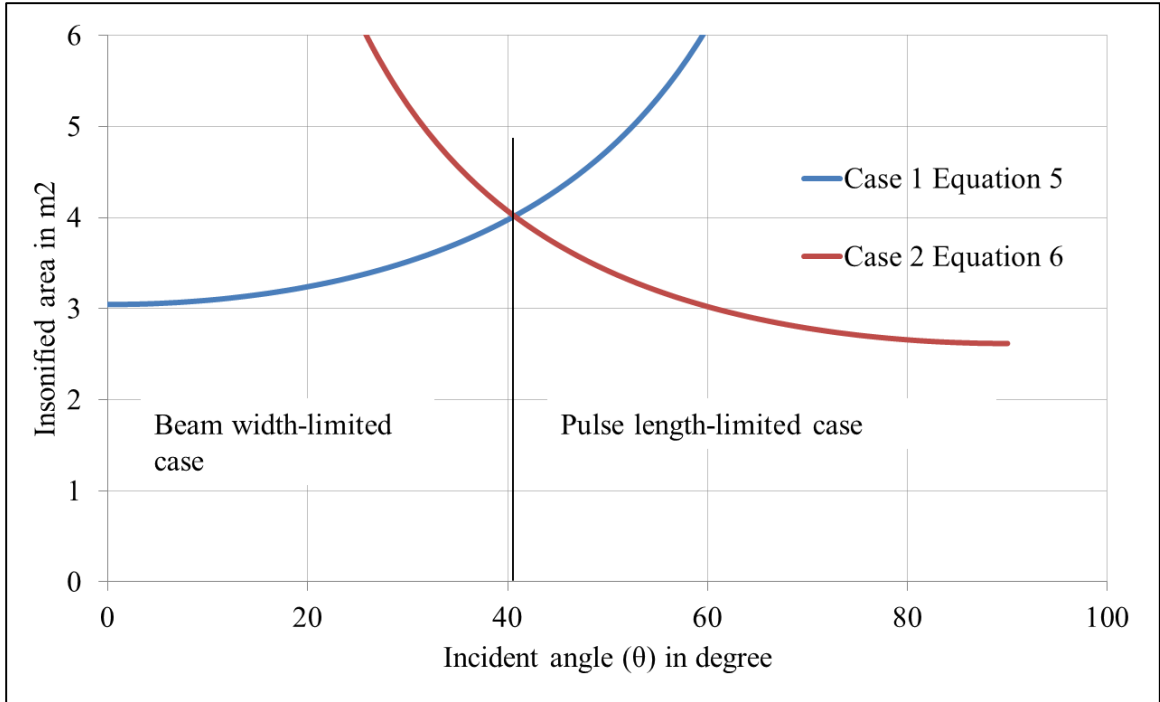
Figure 2.2: Derivation of insonified area using beam width limited and pulse length limited case. (R=50m, $\theta_t=2°$, $\theta_r=2°$, $c=1500$m/s, $\tau=1$ms)

The insonified area in both cases is affected by the seafloor slope in along- and across-track directions. To account for these seafloor geometries, the actual three-dimensional GRA is computed and used for the calculations instead of a beam angle. However, Equations 5 and 6 give sufficient approximate insonified areas for initial calculations.

2.2 Physical Properties of Seafloor and its Effect on Backscatter Strength

In the case of the multibeam sonar, the seafloor is insonified by the Tx in a very narrow along-track and wide across-track beam. The seafloor is illuminated at a range of incident angles and the returned energy is the function of this angle as explained in the following sections. Only a small percentage of the energy comes back, typically between $1/10^{th}$ to $1/10000^{th}$ (-10 to -40 dB). As shown in the introduction (Figures 1.1 and 1.2), the shape and level of these curves depends on the type of sediment. The plot (curve) of BS as a function of incident angle is known as an angular dependency [de Moustier & Alexandrou, 1991], angular response [Hughes Clarke, 1994], or backscatter angular response [Fonseca et al., 2009]. Within this research, it is referred to as an angular response curve (ARC).

Figure 2.3A represents a simple case of the plane sound wave front hitting the flat interface between two perfectly homogenous materials. The incident wave is reflected in the first medium at the similar incident angle θ_1. The ratio of reflected to the incident energy is called the reflection coefficient. The incident wave is refracted into the second medium depending on the difference in the sound speeds at an angle given by the Snell-Descartes law (Equation 7).

$$\frac{\cos \theta_1}{c_1} = \frac{\cos \theta_2}{c_2} \tag{7}$$

18

The amount of reflection and refraction depends on the product of density (ρ) and sound speed (c) of both the materials. This product is termed impedance. Higher differences (contrast) in the impedance of two materials will reflect more energy, and lower impedance contrast will refract most of the incoming energy.

In Figure 2.3B, the incident angle is smaller than a critical angle; if the incident angle is smaller than the critical angle there is no refraction of the sound wave and all the energy is reflected. The value of the critical angle can be calculated using Equation 8.

$$\theta_c = \mathrm{acos}\left(\frac{c_1}{c_2}\right) \tag{8}$$
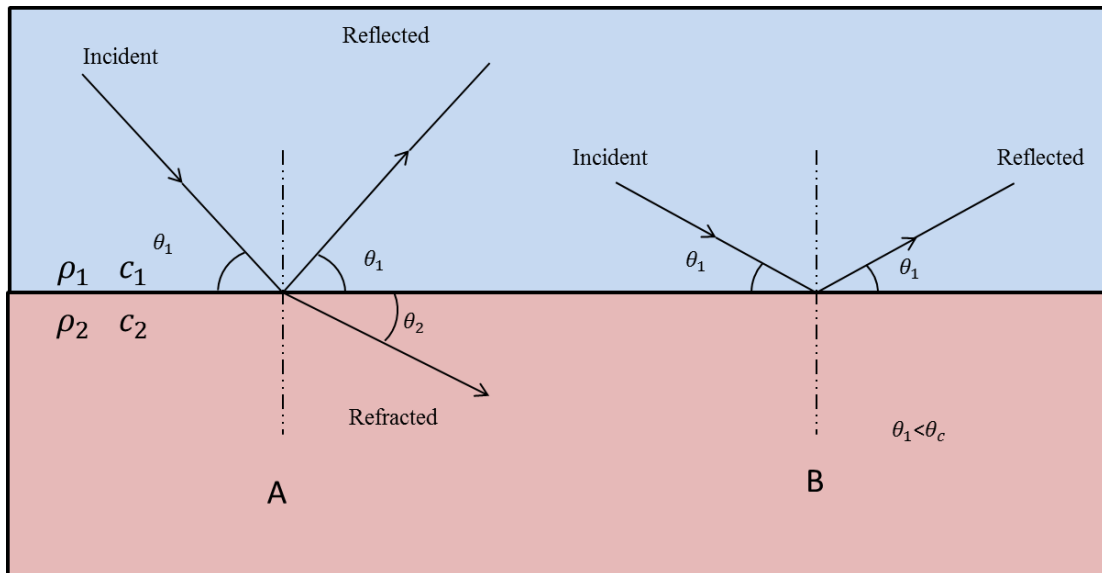
Figure 2.3: Sound wave interface between two homogenous materials

Figure 2.3 represents the particular case of a perfectly smooth seafloor. In the case of a real seafloor-water interface, however, one has to consider the seafloor roughness, impedance contrast, volume heterogeneity, and changing incident angle due to seafloor

slopes [Jackson et al., 1986]. As Figure 2.4 illustrates, a part of the incident acoustic energy is scattered by the water seafloor boundary because of local roughness and impedance. The scattered energy will be radiated over the entire upward hemisphere. However, for the monostatic case of a multibeam (where Tx and Rx are co-located), the energy that is scattered in the inverse direction is of interest, and is known as backscatter. Depending upon the impedance contrast and the critical angle, the remaining part will penetrate the sediments and be backscattered by the inhomogeneity or sediment layers [Augustin et al., 1996]. The latter is also known as volume scattering [Jackson et al., 1986]. The amount of energy penetration in the seafloor will reduce with increasing frequency, as there is increased sediment attenuation. Quantitatively, typical penetration by 30 kHz frequency in low impedance sediment is often greater than 1m. The penetrated energy will be scattered back from the heterogeneities in the sediment structure [Novarini & Caruther, 1998].
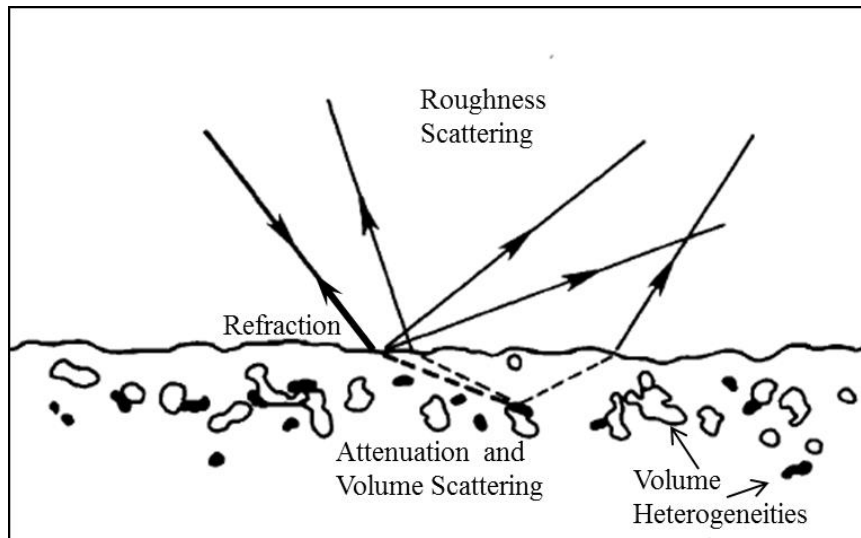
Figure 2.4: Bottom acoustic scattering mechanisms, including refraction and scattering at the water-bottom interface, attenuation, and volume scattering in the sediments from Jackson et al. [1986]

In the case of multibeam insonification, a range of incident angles are possible; different phenomena occur at specular, oblique, and beyond critical incident angles as illustrated in Figure 2.5. In the specular incident waves, the backscattering is due to macro-roughness or large scale roughness. At the oblique incidence, the backscatter is controlled by volume heterogeneity (for low impedance contrast) and to some extent by small-scale roughness. After the critical angle, the backscatter is purely due to the small-scale roughness as no energy is refracted into the sediments. The seafloor roughness in the case of scattering is a relative term as it depends on the scales of the sound wavelength with respect to seafloor roughness. Similarly, as the sediment attenuation is strongly frequency dependent and thus depth of penetration depends on frequency, the volume scattering will also be wavelength dependent.
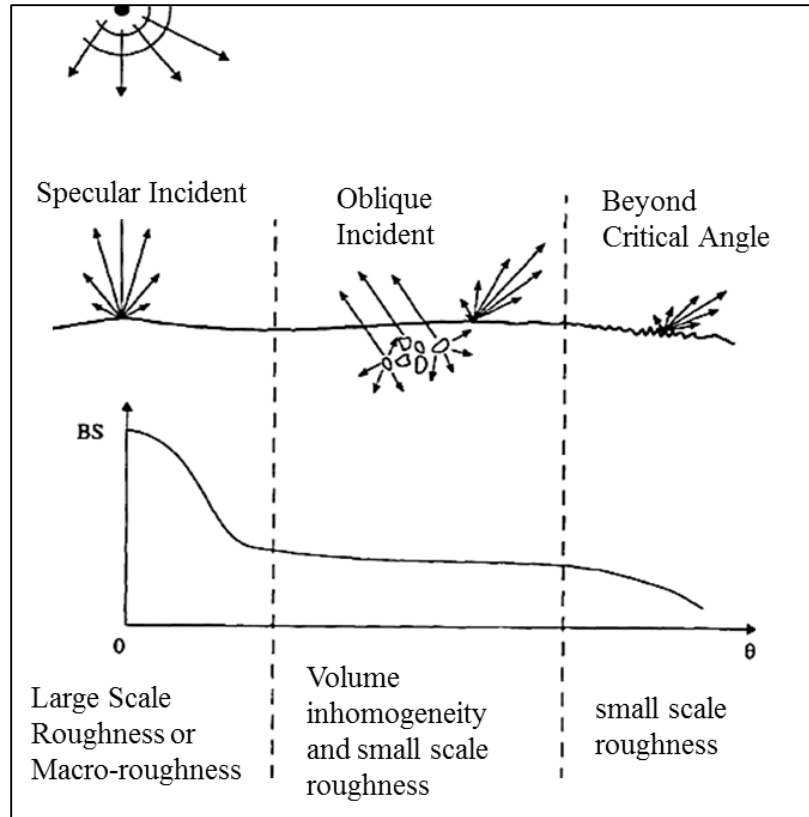
Figure 2.5: Typical backscattering coefficient and mechanisms responsible from
Augustin et al. [1996]

Ultimately, to have any backscattering signal at all there must be a roughness. That
roughness will exist over all lengths and scales (a spectrum). The two most common
ways to characterize the seafloor roughness is by using the roughness spectrum or by
using the probability density function (Rayleigh parameter) of seabed height. The energy
as a function of wavelength is a property of the interface, and its distribution will affect
the nature of the scattering. For modeling, the spectrum is usually partitioned into its long
and short scale surfaces by many researchers [Jackson et al., 1986; Lurton, 2002]. If the
radius of curvature of the seafloor is smaller than the wavelength used, then the seafloor
is considered to have a significant small-scale surface [Jackson et al., 1986]. If the radius

22

of curvature is larger than the wavelength used, the surface is considered to be dominated by large-scale surface and relatively smooth [Jackson et al., 1986]. This roughness characterization is commonly based on the incident wavelength, but also potentially by the available resolution of actual bathymetry. The high resolution of bathymetry obtained using very narrow beam widths and shorter pulse lengths will represent actual curvatures of seafloor more closely than bathymetry from interpolated single beam surveys or large beam width multibeam sonars. Nevertheless, typical multibeam sonars resolve horizontal wavelengths down to 2% of depth, thus in only 10m of water the minimum horizontal wavelength resolved is about 20cm, which is much greater than typical multibeam acoustic wavelengths.

There are a number of models proposed from the 1950s until today to approximate the physics of backscattering for rough surfaces. Three most commonly used models and basic theories are described in the following section. The first and simplest model of backscatter is Lambert's law [Lurton, 2002], shown in Equation 9, where BSn is the observed BS value at the nadir. It states that the returned intensity is proportional to the square of the sine of the GRA or square of the cosine of the incident angle. Lambert's law is an excellent first approximation, but its validity is restricted to oblique and grazing incidences for rough surfaces [Lurton, 2002].

$$BS(\theta_i) = BSn + 20\log(\cos\theta_i) \tag{9}$$

The Rayleigh-Rice theory [Strutt, 1945; Rice, 1951], also known as the small perturbation method, is the second theory dealing with scattering from randomly rough

23

surfaces, and incorporates the idea of Bragg scattering [Bragg & Bragg, 1913; Jackson et al., 1986]. In this approach, the surface roughness is considered to be a small perturbation to the case of a perfectly smooth surface (small-scale surface). The principal contributor to the backscattering is the roughness spectrum component given by the Braggs wavenumber. While the Rayleigh-Rice approach works well for small-scale surfaces, it is not readily applicable to large-scale surfaces. This theory is not well suited for backscatter near normal incidence, and its predicted frequency dependence is weak.

The third backscatter theory is the tangent-plane model based on the Kirchhoff approximation that incorporates the idea of scattering from facets. The surface is assumed to have multiple locally planar facets with a Gaussian distribution of the slope. The number of facets that contribute to backscatter grows exponentially smaller as the incidence angle deviates from the normal. Thus, the predicted response should drop off very rapidly away from normal incidence. As a result, this model is most applicable to high grazing angles, making it complimentary to the Rayleigh-Rice model. Though the Kirchoff approximation is frequency dependent, the tangent-plane model does not depend on the frequency of the incident wave [Lurton, 2002].

Jackson et al. [1986] have given an excellent review of previous models that explain backscattering by the seafloor roughness. According to them, a composite roughness model is universal as it avoids the shortcomings of the Kirchhoff and Rayleigh-Rice approximation. The composite roughness model uses the Kirchoff approximation for near normal incidence, preserving frequency dependence, while Rayleigh-Rice approximation

and volume scattering is used for oblique and low grazing angles. The volume scattering depends on the amount of energy that gets transmitted into the sediment, absorption coefficient of the sediment, and the volume backscattering strength from the hetorogenities inside the seabed [Lurton, 2002]. The most common model to compute the volume scattering is the Stockhausen model. This model considers transmission losses, refraction, and attenuation in the statistically homogeneous sediment with a flat interface [Stockhausen, 1963].

Elfouhaily and Guerín [2004] published a critical survey of approximate theories of scattering from random rough surfaces. They attempted to classify and characterize over 30 different approximate methods. All the methods were variants of the small perturbation method (Rayleigh-Rice), the tangent-plane method (Kirchhoff approximation), or the so-called unified methods that attempt to bridge the gap between the two classical theories.

Many models have been built to estimate the behavior of backscatter with different seafloor properties. The majority of high-frequency backscatter models consider two primary mechanisms. One is the roughness of the interface causing interface scattering and the second is volume inhomogeneity of the medium parameters causing volume scattering [Ivakin, 1998]. However, all models are based on some assumptions, and will work when those assumptions are met in specific conditions. The development in this area continues as it is important to relate the remotely sensed backscatter to seafloor properties without much ground truthing.

In the context of this research, the aim is to extract the actual backscatter strengths in the form of angular response curves with maximum possible accuracy. The extracted backscatter can then be used by others to try to apply these models to infer seabed properties. This research particularly focuses on beam pattern residuals that can significantly distort the slope of ARCs. That distortion could bias or flaw any attempt at inversion.

2.3   Use of Backscatter Strength for Seafloor Classification

2.3.1   Introduction

The least ambiguous methods of identifying seafloor characteristics is to do in-situ testing and bottom grabs, and then to examine the sediments in the laboratory for specific properties. These processes are expensive but useful for specific projects, such as drilling sites or offshore platform construction sites. However, these methods are financially impractical for large areas, and boundaries of the sediment changes are difficult to identify. The use of acoustic backscatter data promises advantages over in-situ testing by using a remote classification scheme. In the early 1950s and 1960s, researchers started to study the relationship between the acoustic backscatter and seafloor type [Urick, 1954; Urick, 1960; Patterson, 1963; McKinney & Anderson, 1964]. With the increasing

understanding of the backscatter phenomenon, many models have been built to describe backscatter from a real seafloor while considering a variety of physical properties.

2.3.2 Classification Using ARC

The previous review of scattering mechanisms and models has emphasized that the BS in the form of ARC is a primary key to seafloor classification. The conventional sidescan sonar, despite its inability to determine the across-track angles, is routinely being used to collect high-resolution backscatter data for identifying seafloor characteristics. Because of the low aspect ratio of these towed sidescans, they predominantly gather data at a small range of low GRAs, so variation in the backscatter with the GRA is negligible and difficult to quantify, and thus is usually ignored. However, at the small GRA range, different sediment types can produce the same mean backscatter values. The texture-based approach to classification is used to overcome this limitation. In texture-based classification, the mosaic or image of the backscatter data is used to find relative changes in the appearance of backscatter data [Pace & Gao, 1988]. On the other hand, the surface mounted multibeam sonar collects bathymetric and imaging data with a high aspect ratio, and covers a broad range of GRAs at the seafloor [Hughes Clarke et al., 1997]. The larger range of GRAs enabled researchers to build the ARC with the help of the acquired bathymetry.

Soon after the first attempts to extract BS from multibeam sonar [de Moustier, 1986], research was designed to assess whether the angular dependence of the acoustic backscattered energy can be used for seafloor classification. Questions addressed included, what are the parameters that control this angular dependence? Is surface roughness mostly responsible for the backscattered signal levels observed or does the volume scattering within the sediments play an important role [de Moustier & Alexandrou, 1991]?

Later research tried to establish correlations between the seafloor types and the backscatter angular response. Many researchers have successfully developed a local relationship between specific sediment types and the ARC using ground truth data [de Moustier & Alexandrou, 1991; de Moustier & Matsumoto, 1993; Hughes Clarke, 1994; Augustin et al., 1996]. Hughes Clarke and others [Hughes Clarke, 1993; Hughes Clarke et al., 1996] carried out experimental work to establish the relationship between different backscatter angular responses in shallow water where the actual seafloor could be examined at low tide. Known seabed types were insonified over a wide range of GRAs using multibeam sonar. The authors conclude that the multibeam sonar systems provide additional potential compared to deep-towed sidescan. The angular responses plotted as a function of a wide range of grazing angles can help differentiate between fine sand and mud that have similar intensities at a lower GRAs but have different intensities at higher GRAs. All of this, of course, requires the adequate reduction of received intensities to extract the ARCs, which is the aim of this thesis. Figure 2.6 shows typical backscatter ARCs.
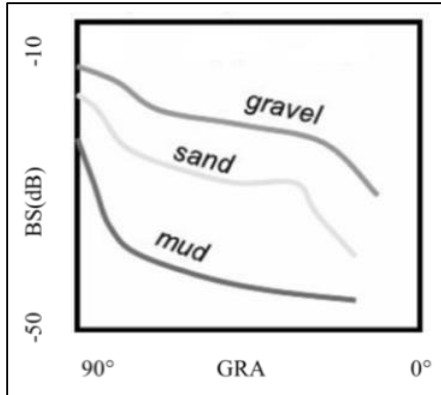
Figure 2.6: Typical ARCs for different seabed types from Hughes Clarke [2012]

2.3.3 Characterizing ARC

Since 1996, an increasing number of research papers have used ARCs for shallow water classification. Considerable research has been done to quantify the shape of ARCs. Early work before the multibeams in the 1980s [Boehme et al., 1985; Boehme & Chotiros, 1988] used static mounts using specially calibrated arrays. They used the shape, variance and magnitude of the curve for ARCs quantification. Hughes Clarke [1994] used mean backscatter strength, first order shape of ARCs (mean slope), the second order slope of ARCs (curvature) and coefficient of variation. The ARCs are divided into different zones for statistical clustering by some researchers [Hughes Clarke et al., 1997; Fonseca & Mayer, 2007; Lamarche et al., 2011]. Huang et al. [2013] have tested 7 different ARC feature analysis approaches by different researchers giving a good summary of ARC characterization.

29

2.3.4 Classification Using Mosaic

If the full variation in the backscatter strength with GRA is observed, the ARC holds the most potential. However, to minimize ship time most surveys only achieve 100% coverage and thus look at each location at just one particular GRA. Thus, angle invariant mosaics involving normalization of ARCs are used for classification. The mosaic of the multibeam seabed backscatter data is a geographically referenced compilation of multiple swaths of multibeam data that cover the entire survey area. Every single swath shows the angular variation having stronger backscatter from close to orthogonal GRAs and weaker returns with lower GRAs. To combine different swaths together, the angular variation covering swath widths has to be removed, without which the mosaic will look like an alternate pattern of dark and light intensities following the vessel tracks. The process of removing the angular variation is referred to as normalization. For normalization the shape of the angular variation has to be known. Generally in normalization, a statistical scheme is developed by using extracted ARC to reduce across-track intensity variation within a single swath by adjusting all observation to a reference GRA. Even though the ARC is removed, the resulting mosaics have been successfully used to classify sediments that clearly have very different properties like rock and mud.

While normalisation achieves an eye-pleasing mosaic, several researchers believe that by normalizing ARCs crucial information is lost, which cannot be retrieved from the mosaics [Fonseca & Mayer, 2007; Hughes Clarke, 2012]. The first disadvantage of the mosaicking process is that the shape of the ARC can vary at the nadir and small grazing

angles but still have same mid grazing angle shape. This variability, which is a means of additional discrimination, is lost in the mosaic. Then secondly during mosaicking the intensities from overlapping portions are obscured, further hiding the information from the interpreter. The third disadvantage is that the arbitrary choice of a single GRA used to normalize data is not a complete representation of the ARC [Fonseca et al., 2009].

As an ARC requires a wide range of grazing angles, when an ARC is computed by averaging the angular variation across the full width of a entire survey line, the classification is only applicable at the scale of the swath width of the sonar and thus reduces the effective spatial resolution of the classification. On the other hand, however, the normalized mosaics have a larger spatial resolution [Fonseca et al., 2009]. The other advantage of backscatter mosaics is that any sonar-related radiometric artifact that is present across the swath is minimized during the normalization process. Mosaics are mostly used for benthic habitat [Huang et al., 2012] and geological mapping of large scale areas [Augustin et al., 1994; Augustin et al., 1996; Potter & Shaw, 2010].

In recent years, researchers have become more involved in making automated characterization software. These algorithms can identify the seafloor types using pixel values from mosaics [Zhao et al., 2008; Preston, 2009; Huang et al., 2014]. Preston [2009] combined many different approaches including probability density functions, textures, and ARCs for classification. Even though these softwares evolve and get better in accuracy and processing, the mosaics that are used as an input still have inherited errors from the mosaicking process and normalization of angular response. The combined

approach of using ARC and mosaic data has been a point of recent research to minimize

the limited spatial resolution of ARCs [Fonseca et al., 2009; Hasan et al., 2012; Rzhanov

et al., 2012].

Table 2.1: Summary of advantages and disadvantages of different classification
approaches using backscatter data

Order	Step	Use	Advantages	Disadvantage
1	Backscatter data acquisition with real-time processing using first-degree assumptions	Can be used to identify significant differences in sediment type.	Real-time results.	Has many artifacts due to incorrect assumptions and beam patterns
2	Post-processing of backscatter data to adjust for any variations from first-degree assumptions	Used to better remove radiometric and geometric artifacts like beam pattern and actual ensonified area	User can correct for any violation of assumptions	Assumptions in the post-processing that may not completely remove the artifacts. Methodology limitations
3	Preparing the BS angular responses from processed data	Seafloor classification	Can give most detailed classification	Assumption of having same sediment type for area under consideration
4	Normalize the data from step 2 using angular responses from step 3 and make mosaic	Seafloor classification	Overall area visualization and classification	Loss of information due to techniques used in mosaicking.

Table 2.1 briefly summarizes the workflow and steps in using backscatter data for

classification by different approaches. As can be seen from Table 2.1, any errors in the

previous steps are embedded in the data resulting in errors in the consecutive steps. The

most important task is to correct the acquired data in post-processing with highest possible regard for the real radiometric and geometric situation. Once the right post-processing is done, the backscatter data can be used for seafloor classification, either in the form of ARCs or mosaics.

This thesis does not deal with the previously explained mosaicking errors; rather it focuses specifically on the issues explained in the following sections in the formation of the fundamental ARCs. The following section briefly explains how the instrument reported backscatter intensities are calculated and what assumptions are made.

2.4 Sonar Reported Backscatter

The fundamental backscattered signals from a multibeam echo sounder are the received intensities, not a fully reduced BS. Different manufacturers report these intensities in different ways. Two distinct cases are identified from the literature and the technical notes from the instrument manufacturers. In the first case, the system reports the measured absolute voltage or pressure recorded at the Rx. It is up to the user to convert received backscatter using estimated loss and gain in intensities to the BS values using generalized assumptions and parameters recorded at the time of data collection.

In the second case (that is dealt within this research), an estimate of the BS value is reported to the user. This BS value is corrected for predicted losses and gains in

intensities in real-time by the sonar system itself. These corrections are briefly explained in the following section and can be grouped into two categories: RBP corrections and geometric corrections. The RBP corrections include corrections associated with sonar properties such as Tx intensities, Rx sensitivity, and their angular variation. The geometric corrections are associated with the insonified area, ranges, and topography of the seafloor (local slopes). The parameters used for these corrections are recorded in the data telegram and assumptions are published in technical notes. Initially received voltage or pressure values are not reported to the user but, if the reduction is to be improved, they need to be back calculated. This thesis focuses on the second case data from one manufacturer, Kongsberg; hence their method is discussed in detail.

The complete picture of various corrections that need to be considered in the estimation of the BS can be given through the sonar equation. The sonar equation is compiled and presented (with all terms in dB units) as Equation 10 [Urick, 1983; Hughes Clarke, 1993; Hammerstad, 2000; Lurton, 2002; Augustin & Lurton, 2005];

$$EL = SL(Tr) + RS(Rc) - 2TL + BS + A \tag{10}$$

where, EL is received backscatter intensities, SL is maximum source level (radiometric) and Tr is the sonar-relative transmit source level variation (radiometric). RS is maximum Rx sensitivity (radiometric) and Rc is the sonar-relative Rx sensitivity variation (radiometric), both Tr and Rc are a function of along- and across-track angle from the Tx and Rx respectively. TL is the transmission loss (geometric) through the ocean medium. BS is the unknown value of backscatter strength which we wish to

34

extract. A is the insonified area (geometric) which is a function of grazing angle, pulse length, and Tx and Rx beam widths.

The actually reported intensities ($EL_{withassumptions}$) are the received intensities gained by the manufacturer TVG as shown in Equation 11.

$$EL_{withassumptions} = EL + TVG \tag{11}$$

TVG is a time varying gain applied by manufacturer to compensate for TL, angular variations in BS, estimated peak SL and RS, and varying insonified area.

The absolute or relative source level is the starting point of the calculation and, in the case of Kongsberg multibeam systems, this source level is not reported to the user; similarly the Rx sensitivity is also not reported. It is assumed that the reported intensities are normalized for SL and RS. The two-way transmission losses for the range R include the spherical spreading of the source intensities (40 log R), and the attenuation in the seawater (2 αR). For the spherical spreading computation, the source is assumed to be a small (point) and the medium is assumed homogeneous [Lurton, 2002]. The attenuation in the seawater is accounted for by calculating attenuation coefficient α. The attenuation coefficient is well studied and its relation to the frequency, salinity, and temperature is established [Francois & Garrison, 1982a; Francois & Garrison, 1982b]. It is assumed that the user is monitoring the survey area for any changes in oceanography and updating the attenuation coefficient as necessary. While a single α value is usually applied for a beam, in reality it is an integration of the changing α with temperature and salinity through the

water column to the depth of interest. Imperfections due to this have been explicitly addressed by de Campos Carvalho [2012].

The Tx beam pattern (Tr) refers to variations in the source level intensities along- and across the transmitted sector with respect to the peak level (SL). Similarly the Rx beam pattern (Rc) refers to variations in the Rx sensitivity with respect to peak sensitivity (Rs) along- and across the formed Rx beam. Taken all together they are herein referred to as the RBP. The across-track RBP is composed of across-track Rx sensitivity and across-track Tx intensity variation. The sonar manufacturers have a predicted RBP that is applied in real-time to normalize them. For recent editions of sonars like EM 710 and EM 302, however, recognizing that the predicted beam pattern is imperfect, Kongsberg has additional corrector functions that can be user modified to optimize real-time corrections. The major work in this research is to calculate any remaining residuals between actual and assumed RBP in both the along- and across-track directions.

These RBP corrector functions are stored in the transceiver unit in the file 'bscorr.txt'. For each sector a central beam pointing angle with respect to sonar is defined; the variations around the central beam pointing angle for each sector and each depth mode are defined in dB. For EM 302 and EM 122, the variation is given as a roll off by angle whereas for EM 710 it is defined at 10° intervals by default. The source level for each sector is also defined enabling the system to adjust for source level variation. Figure 2.7 shows the graphical representation of the manufacturer defined default RBP (Bscorr) for a single sector Very Shallow mode of an EM 710. The file contains only the

36

values that are shown by the nodes for each sector. No technical document was found during this research explaining how the transceiver applies these values during the backscatter data processing. It is assumed, from verbal discussions, that a spline is applied, and an interpolated function is used referenced to the sonar reference frame. The source levels for port, central, and stbd sectors are estimated as 217.6 dB, 217.4 dB, and 216.9 dB respectively. A Bscorr file for EM 710 is attached in Appendix 9.3.
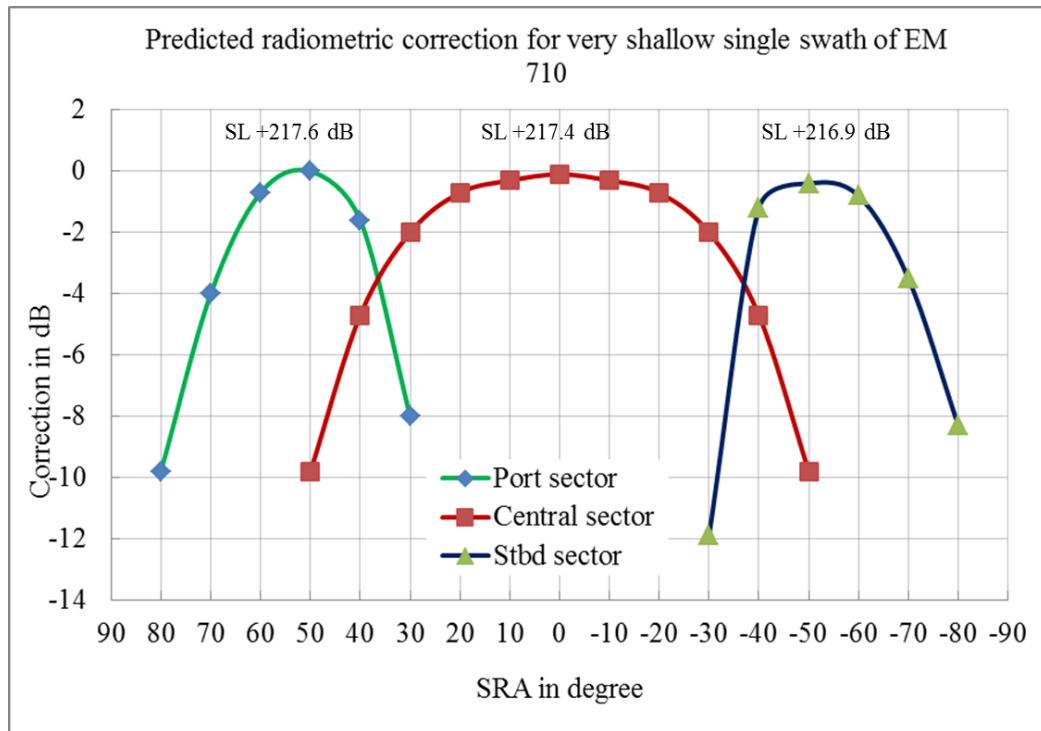
Figure 2.7: Graphical representation of radiometric correction from Bscorr file for Very Shallow single swath mode of EM 710

Even though the manufacturer has accounted for across-track Tx RBP (only) and developed a method to apply it during the backscatter data processing, the values that are in the Bscorr file can be updated by the user. There are no guidelines or field methods to compute these values and most of the users continue using the default file which may not

37

exactly account for the RBP of their unique sonar hardware combination. The aim of this research is to develop a simplified method for users to compute values of RBP for their individual sonar and software combination.

In the case of Kongsberg, a particular non-linear TVG-BS function is used to make the output backscatter image uniform across-track, by substantialy reducing the angular dependency of BS. This process is equivalent to normalizing the ARC to get a uniform mosaic of the survey area. To do this, the manufacturer estimates the shape of the ARC by fitting a simplified backscatter model as shown in Figure 2.8.

The model is derived based on predicted average BS value at nadir (BSn) and at predefined oblique angle (BSo) which is also called as crossover angle. Figure 2.8 shows the model, where the BSn is -25 dB, and the BSo is -31 dB at the crossover angle of 75°. In this model, the BSn is assumed to vary linearly with the grazing angle from BSn to BSo at a predefined crossover angle. The BS then changes nonlinearly using Lambert's law for grazing angles lower than crossover angle [Hammerstad, 2000]. The application of the TVG-BS along with TVG for transmission losses is done in real time to reduce the dynamic range of the data and to provide minimum variation across-track in the swath corridor. The angle to time conversion is done assuming a planar seafloor as shown in Figure 2.9 at normal distance equal to the actual minimum slant range. An estimate of BSn and BSo is derived dynamically from the immediately preceding recorded data in real time. The predicted values used in the model, however, are preserved so that the TVG-BS can be removed in post-processing.
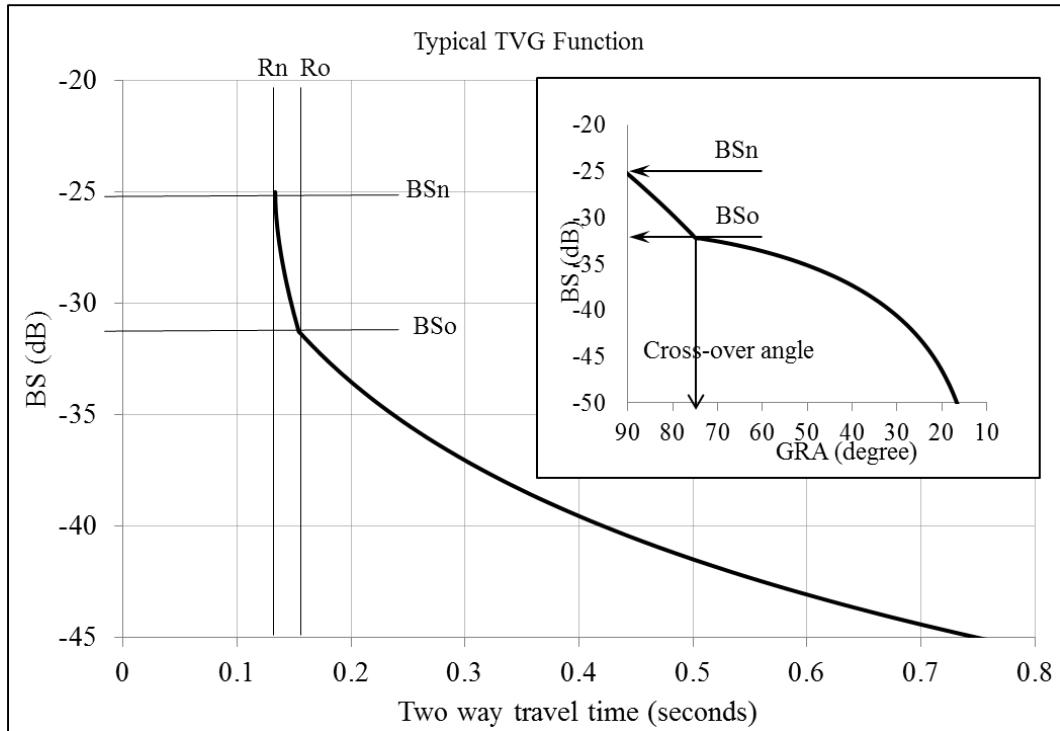
Figure 2.8: The manufacturer applied TVG to account for changing BS. The function is
computed for 100m depth with crossover angle of 75° (15° from nadir as reported)
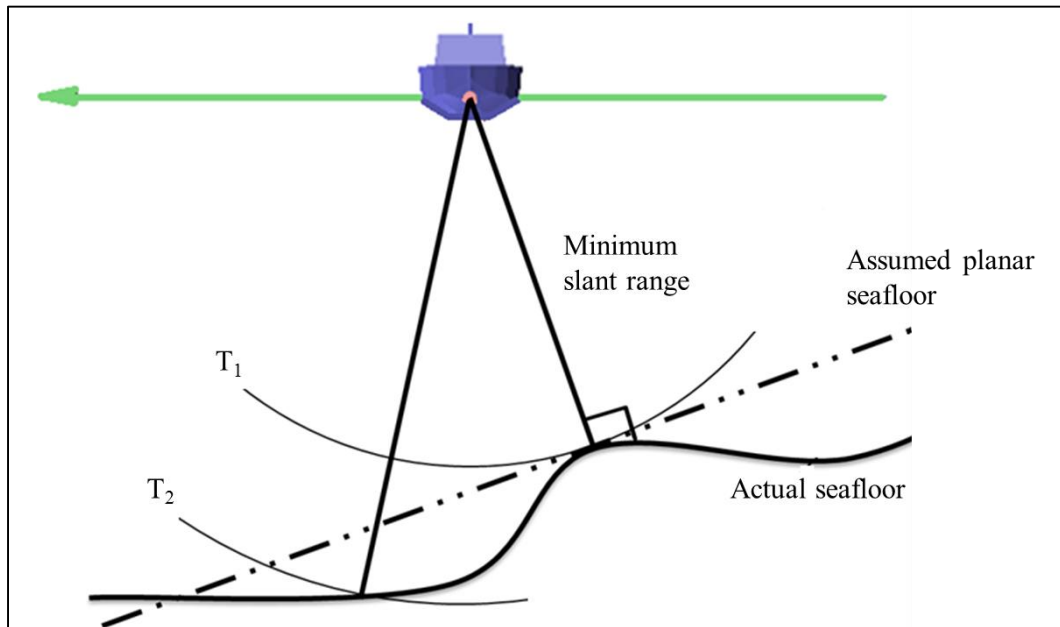
Figure 2.9: Minimum slant range and planar seafloor

39

The insonified area *A* depends on GRA, pulse length, and Tx and Rx beam widths as discussed earlier. As the exact topography is unknown in real time, a planar seafloor previously described is assumed at the minimum slant range and the approximate insonified area is computed. The slope of assumed seafloor depends on the minimum slant range; if the minimum slant range is not vertical the assumed seafloor is not flat as shown in Figure 2.9.

As seen from Equation 10, there are many terms that need to be accounted for to interpret the received intensities correctly. Before using the derived backscatter values, these corrections and the assumptions behind them need to be understood completely. In order to have the most accurate estimate of BS value, several researchers have attempted to understand the limitations of assumptions behind the corrections and implemented strategies to avoid those limitations [Beaudoin, 2005]. The most commonly used approach is to use the available across-track and along-track topography in post-processing. The next sections will describe the efforts implemented by other researchers and the current implementation in the Ocean Mapping Group (OMG) software pack.

2.4.1 Post-Processing of Backscatter Data.

The necessity of multibeam backscatter data post-processing is a well-accepted fact by researchers and the instrument manufacturers [Hammerstad, 1998; Hughes Clarke, 1993]. The post-processing corrections are left to the user because seafloor characteristics

and geometry cannot be predicted accurately in real time. Users have to be particularly careful in post-processing to confirm from the manufacturer's specifications, the assumptions about the real-time corrections, as not all corrections are applied by all the manufacturers [Beaudoin et al., 2002]. In the case of the Kongsberg systems, the received intensities are already approximately corrected for all the factors mentioned in Equation 10. The gain to account for energy losses, is automatically adjusted for the variation in peak source level, the estimated attenuation, and spherical spreading. Additionally the variation in the pulse length is accounted for and the intensities are corrected for the modeled seabed angular response [Hammerstad, 2000]. For all these reduction steps, the validity is only as good as the real-time assumptions of ARC, GRA, insonified area, attenuation, and predicted beam patterns.

The following corrections for further reduction of BS data are necessary before using it for any classification.

1) Measurement of the real seafloor slope to correct for actual insonified area [de Moustier & Alexandrou, 1991; Hughes Clarke, 1993; Hughes Clarke et al., 1996; Hellequin et al., 2003; Augustin & Lurton, 2005].

2) Account for the variation between actual and predicted transmit beam patterns [Hughes Clarke, 1993; Hughes Clarke et al., 1996; Hellequin et al., 1997].

3) Correcting variation between the apparent calculated and real grazing angle due to refraction [Mitchell & Somers, 1989; Hughes Clarke et al., 1996].

4) Irregular attenuation of the signal due to variation in the local water-mass properties [Hughes Clarke et al., 1996; Augustin & Lurton, 2005; de Campos Carvalho, 2012].

5) Removal of angle-varying correction based on Lambertian model (TVG-BS) [Hughes Clarke et al., 1996; Hellequin et al., 1997; Beaudoin, 2005].

6) Any aspherical spreading (focusing) of sound energy due to bending of sound waves [Mitchell & Somers, 1989].

7) Source level variation between sectors or sector-specific beam pattern [Augustin & Lurton, 2005; Llewellyn, 2006; Teng, 2011; Hughes Clarke et al., 2012].

It is important to mention that the required accuracy of the backscatter data depends on the purpose and degree of classification. For example, real-time data with just the simple assumptions can be used to successfully identify and classify the major seafloor types that have entirely different ARC, for instance, rock and mud. For detecting more subtle changes (such as muddy sand versus sandy mud) these simplified assumptions are inadequate. This thesis is intended to address these more demanding needs. The aim here is to compute the most accurate ARC as its shape provides valuable information about the seafloor properties. The maximum possible corrections are done in this research with a particular focus on radiometric and geometric corrections.

3   RADIOMETRIC BEAM PATTERN AND GEOMETRIC EFFECTS IN BACKSCATTER DATA

In Section 3.1 of this chapter, radiometric beam pattern (RBP) in backscatter data is briefly explained, followed by introduction of motion stabilization in Section 3.2. It is important to understand the motion stabilization mechanism in multibeam sonar, as it has complicated modulation of RBP on the backscattered data as explained in Section 3.3. The geometric effect is discussed in Section 3.4. Section 3.5 reviews the existing OMG algorithms. Section 3.6 reviews the existing methods of backscatter data reductions. Sections 3.7 and 3.8 present the research question and objective.

3.1   Radiometric Beam Pattern

3.1.1   Along- and Across-Track Transmitter Source Level Variation

The red half circle in Figure 3.1A shows the ideal transmit source level across the track. In reality, the intensity levels, shown by arrows in Figure 3.1A at 45°, 60°, and 70° with respect to nadir are smaller compared to the peak intensity at the nadir. The

approximate reductions in intensities shown in Figure 3.1A are taken from the manufacturer's technical notes [Hammerstad, 2005].
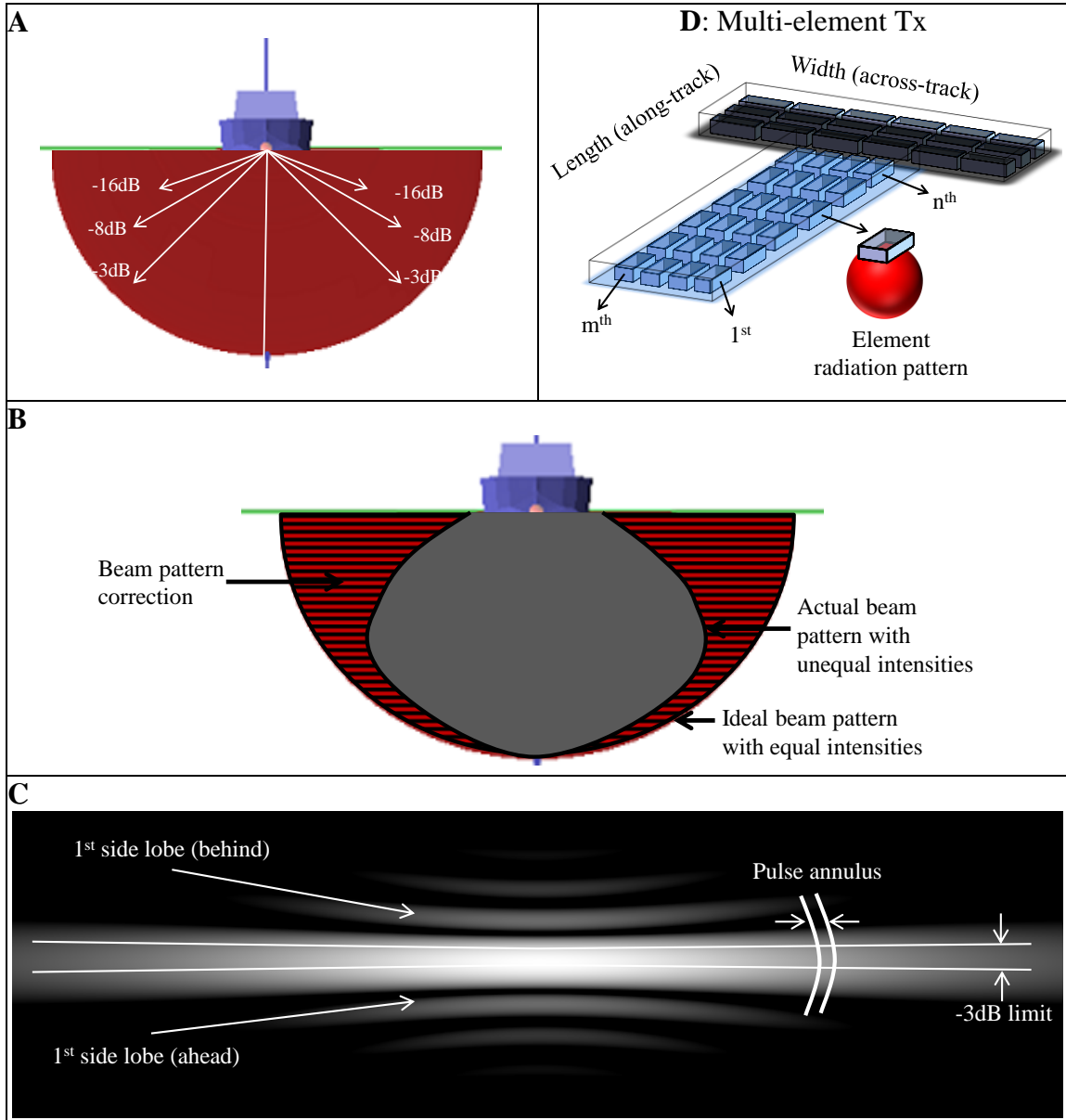
Figure 3.1: Tx source level variation: A: Variation in the source level across-track. B: Required across-track correction for beam pattern C: Fading across-track insonification due to variable Tx source level (vessel going down the page) D: Multi-element Tx

Due to this variation in the source level the seafloor is insonified at gradually changing intensities (Figure 3.1C) when referenced to SRA. The typical intensity variation in across-track direction is shown by the gray lobe in Figure 3.1B, with maximum intensity at nadir and reducing across-track, but it can be of any shape. The required correction is the difference between ideal (even) and actual intensities as shown by horizontal lines in Figure 3.1B. This required correction is always referenced by SRA as the beam pattern is relative to sonar.

The linear transmit array consists of many elements (m*n) as shown in Figure 3.1D, both in along- and across-track direction. These elements work in synchronization to form the desired across-track main transmit beam which is a product of individual element radiation pattern from 1 to n^{th} element and possibly includes any applied shading. The product also generates side lobes as shown in Figure 3.1C. The side lobes are in along-track direction and do not contribute to the across-track beam pattern (intensity variation). Each element has its inherent unique directional radiation properties which contribute to the final sum of directional actual beam pattern given by the product theorem [Urick, 1983]. It is important to note that this across-track reduction in intensities is not due to the attenuation or spherical spreading but because of beam forming resulting from the across-track dimension of the linear transmit array.

The transmitted intensities also show sharp variation in the along-track direction but are not significant to this discussion as, within a narrow time slice defined by the pulse annulus (Figure 3.1C), the intensities are integrated along the transmit beam. However,

45

when a transmit beam is steered in along-track direction it may have along-track variation in the transmitted source level with respect to unsteered beam due to reduced directivity. In this research, the along-track Tx beam pattern refers to the one caused by changing directivity.

3.1.2   Along- and Across-Track Receiver Sensitivity Variation

For each Rx beam, the peak sensitivity varies from beam to beam, generally dropping with steering due to a combination of both the individual element beam pattern and the drop in directivity of the formed beam due to its broadening with steering. Figure 3.2 shows exaggerated effects of increased beam width and reduced sensitivity due to beam steering (at nadir, 30°, and 45°).
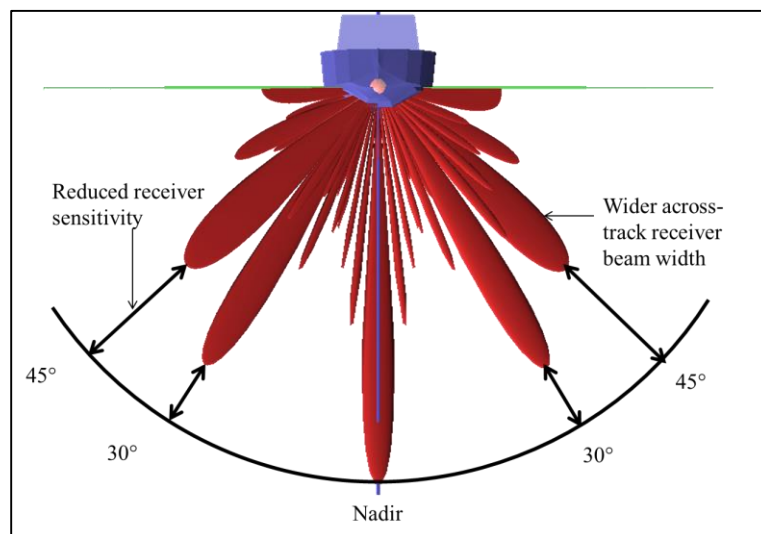
Figure 3.2: Rx sensitivity and beam width as a function of beam steering

A: Rx beam pattern oblique view	B: Front view of Rx beam pattern	C: Along- and across-track Rx sensitivity

D: Multi-element Rx

Width (across-track)

Length (along-track)

mth

nth

1st

Element radiation pattern

-3dB limit

1st side lobe (away from ship)

1st side lobe (towards ship)

E: Rx beam pattern side view

Beam pattern correction

Actual beam pattern with unequal intensities

Ideal beam pattern with equal intensities

Figure 3.3: A: Oblique view of Rx beam B: Side lobes in Rx beam pattern C: Fading along-track Rx sensitivity (starboard beam on vessel going down the page) D: Along-track Rx sensitivity variation

The Rx sensitivity variation is analogous to the Tx source level variation. The Rx sensitivity varies in both along- and across-track directions. The Rx uses the signal received by many elements (m*n in Figure 3.3D) placed across- and along-track in the Rx array to form a main Rx beam along with side lobes as shown in Figure 3.3A, B, and C. Each of the elements has its own inherent unique directional sensitivity pattern which again contributes to the final directional beam sensitivity as per the product theorem [Urick, 1983]. The along-track variation in sensitivity is a function of the fore-aft dimension (product of individual beam sensitivity pattern of element 1 to m^{th} in Figure 3.3D) of the Rx; the required correction is very similar to the across-track Tx beam pattern as shown in Figure 3.3E. Generally the width of the Rx fore-aft beam pattern is narrow as it only needs to account for changes in pitch between transmission and reception for single sector multibeam systems. As we shall see, for multi-sector systems with heavy transmit steering in the along-track direction, this has a big impact on received intensities.

Within a single beam, the across-track Rx sensitivity also shows sharp variation in the across-track direction. On reception, the across-track pattern within an individual beam is sampled many times (referred to as a snippet). This is not significant if beams are spaced across-track much tighter than 3 dB limit. However, when a Rx beam is steered in the across-track direction, it may have across-track variation in the Rx sensitivity with respect to unsteered nadir beam due to reduced directivity. In this research, the across-track Rx beam pattern refers to the one caused by changing directivity and individual element pattern.

48

3.1.3 Multi-Sector Transmit Beam Pattern

Some of today's multibeam sonars employ complete motion stabilization using multiple individual sectors as explained in Section 3.2. This introduces additional factors to be considered for beam pattern corrections. In an ideal situation, without any ship motion, when multibeam sonar employs multiple transmit sectors, two potential problems can occur. Firstly each sector may have different peak Tx source level and Rx sensitivity and secondly each Tx sector may have different source level and Rx sensitivity variation across- and along-track. The across-track component for multiple sectors is illustrated in Figure 3.4A. It shows a constant shift in peak sector source level at the sector boundaries. Also it shows transmit source level variation corrections which is different for each sector. Figure 3.4B shows the insonification geometry assuming no yaw or pitch and actual insonification at the seafloor; three sectors can easily be identified with maximum intensities at the center pointing angles (CPA) and fading away.

The Tx source level pattern and Rx sensitivity pattern can be modeled by knowing wavelength or center frequency, width and length of the physical array, the element pattern, and any shading function applied. The predicted models will always differ from actual patterns due to different inherent properties of individual elements. The only way to accurately define the patterns is to measure them in a perfectly known environment like a tank or estimate them using field methods like the one proposed in this research.
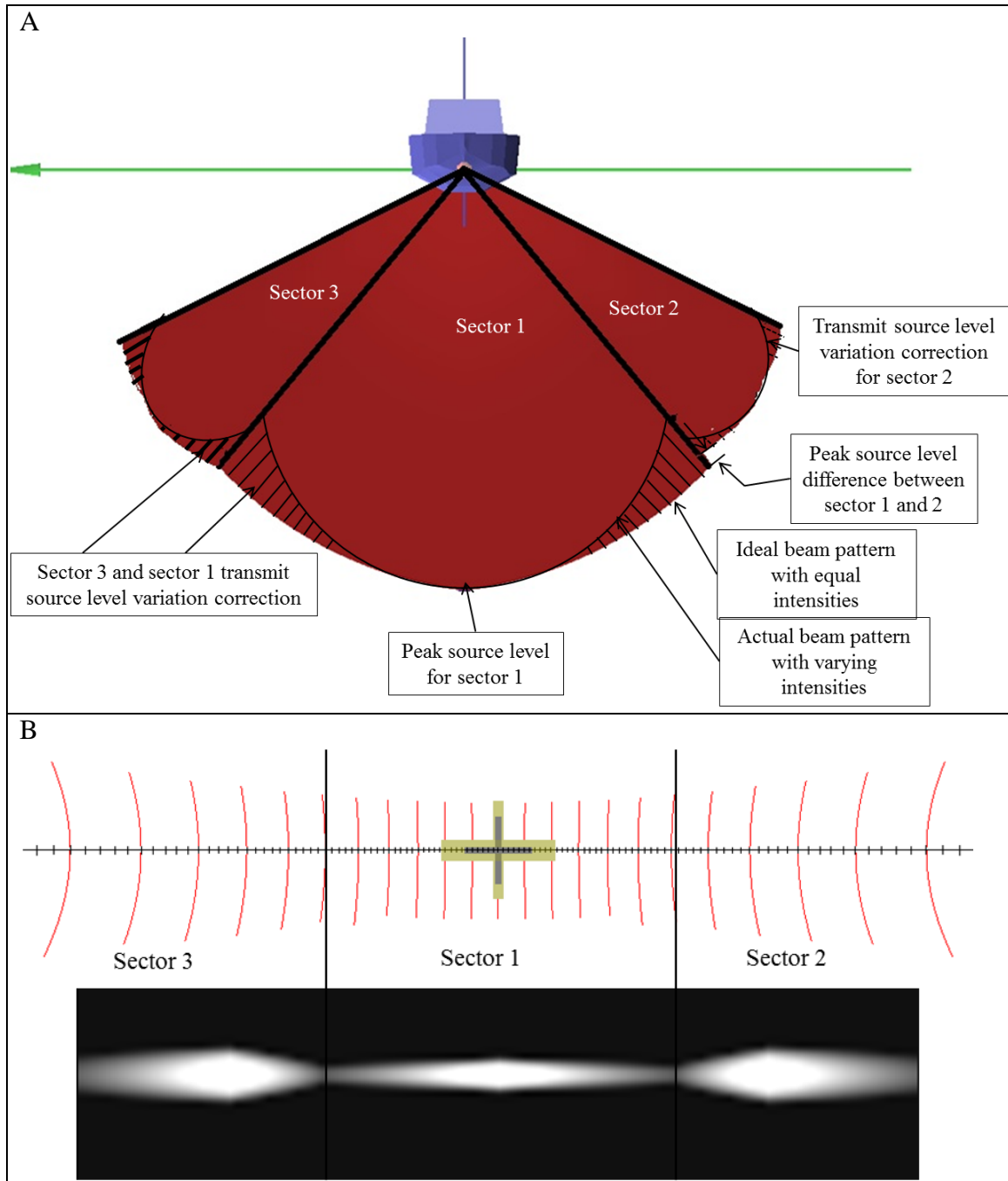
Figure 3.4: A: Tx source level differences and source level variation for multi-sector multibeam sonar B: multi-sector insonification

Although the across-track Tx and across-track Rx RBP are two different functions, they are dealt with together in this research because they cannot be unambiguously

50

separated. Additionally, the across-track Rx RBP varies much more slowly with angle, in contrast, as the transmit sectors are narrow across-track (for multi-sector systems), there variation is much more noticeable. For the case of along-track RBP, the along-track transmit RBP can be ignored as it is always integrated with along-track Rx RBP.

3.1.4 Across-Track and Along-Track RBP

As explained in the above section, there are two across-track RBP components, 1st is across-track Tx RBP and second is across-track Rx RBP. The first component is more dominant as it is result of deliberate narrowing of sector to accommodate multiple sectors in one swath, whereas the second component is just the result of more slowly changing directivity. Similarly there are two components for along-track RBP: 1st is along-track Rx RBP and 2nd is along-track transmit variation. The first component is more dominant as it is again a result of narrow along-track Rx beam pattern, whereas the 2nd component is the result of slowly changing directivity.

Though the across-track Tx and across-track Rx beam patterns, and along-track Tx and along-track Rx beam patterns can easily be explained separately, in reality they are hard to separate from each other. In shallow waters where the two-way travel time is very small (fraction of a second), the change in across- and along-track SRA between transmit time and receive time is not significant. Thus, their product as a single factor can be considered. However, this is not strictly adequate for the deep water situation where two-

way travel time can be few seconds, as it may involve large changes in SRA between transmit and receive time.

In this research they are dealt with together as a product, across-track RBP being dominated by across-track Tx RBP and along-track RBP being dominated by along-track Rx RBP.

3.2 Motion Stabilization

The evolution of motion stabilization methods reflects the result of continuous development to better meet the requirement of equal sounding density on the seafloor irrespective of ship's motion. This technology advancement was necessary to meet International Hydrographic Organization standards and also to increase acceptable survey line spacing and sounding density. This section briefly introduces the mechanism of motion stabilization followed by the section which will review the effect of motion stabilization on the RBP.

3.2.1 Roll Stabilization

Roll stabilization is common in all available Kongsberg multibeam echo sounders. Roll stabilization ensures swath coverage over a constant vertically referenced angle as

seen in Figure 3.5. Roll stabilization ensures a uniform swath corridor which thus helps to avoid any gaps between adjacent survey lines. This is achieved by dynamically altering the steering of the Rx channels with respect to the array. As a result, a given Rx channel will be sampling the seafloor illuminated by varying parts of the Tx beam pattern.

Roll stabilization allows continuous maintenance of a fixed width swath which helps to avoid any gaps between adjacent survey lines. However, it does not solve the along-track density issues caused by pitch and yaw as shown in Figure 3.6.
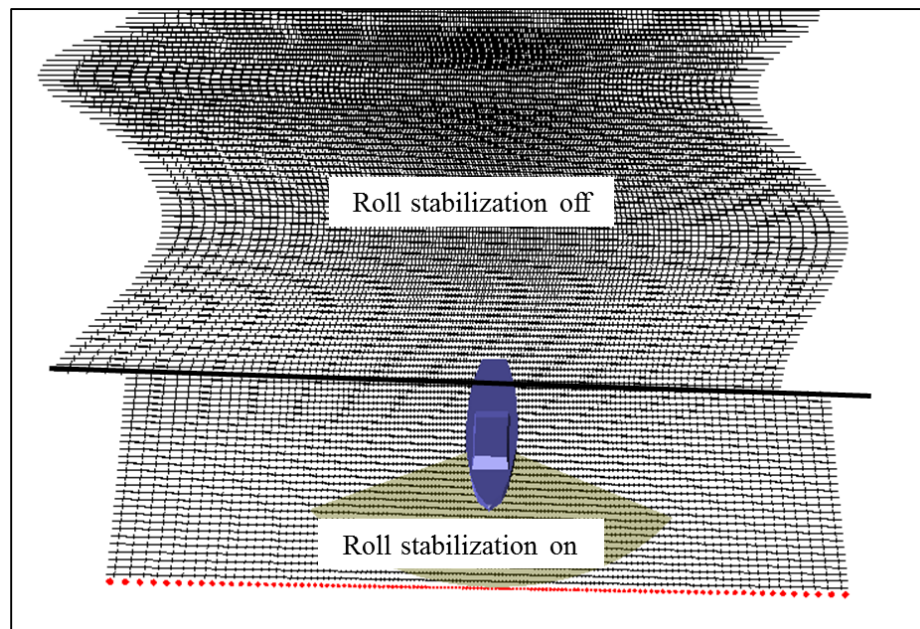
Figure 3.5: Constant angular coverage due to roll stabilization
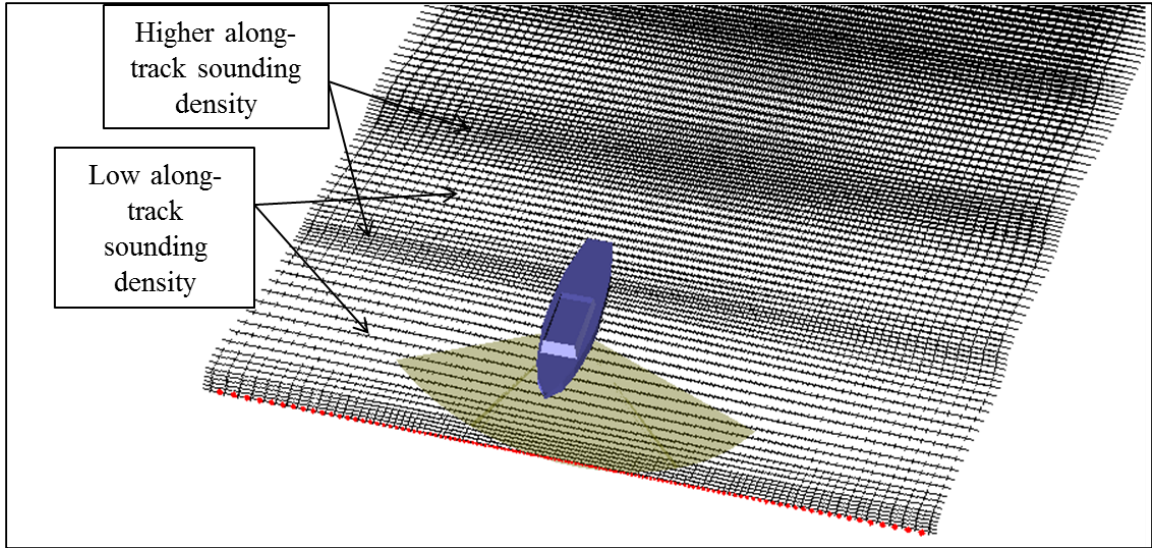
Figure 3.6: Along-track sounding density variations due to no pitch stabilization

3.2.2 Pitch Stabilization

The patches of high and low densities seen in Figure 3.6 can be more equally distributed by using pitch stabilization. Pitch stabilization can be achieved by steering the transmit beam forward or backwards as shown in Figure 3.7. It is important to note that the pitch stabilization is done by steering the transmit beam along-track, and no action is taken on the Rx beams. As can been seen in Figure 3.7, when there is no pitch stabilization, the Tx beam always intersects with the Rx beams in the center of the along-track Rx sensitivity pattern where it is at its maximum (in shallow water). The dotted vertical lines in Figure 3.7 show the across-track centerline of the unsteered transmitted beam and the received beams. Typical maximum pitch stabilization is about ±3°, which is a relatively small change in along-track Rx sensitivity considering how wide the along-

track Rx beam is. As the transmit beam is steered forward or backward, the transmitted beam may no longer intersect with the along-track center of the Rx beam (Figure 3.7 lower part), and this is a potential complication for backscatter data as explained in detail in the next section. Though pitch stabilization ensures the equal density around the reference angles, it causes higher or lower densities of soundings away from the reference angles due to single transmit sector as shown in Figure 3.8.
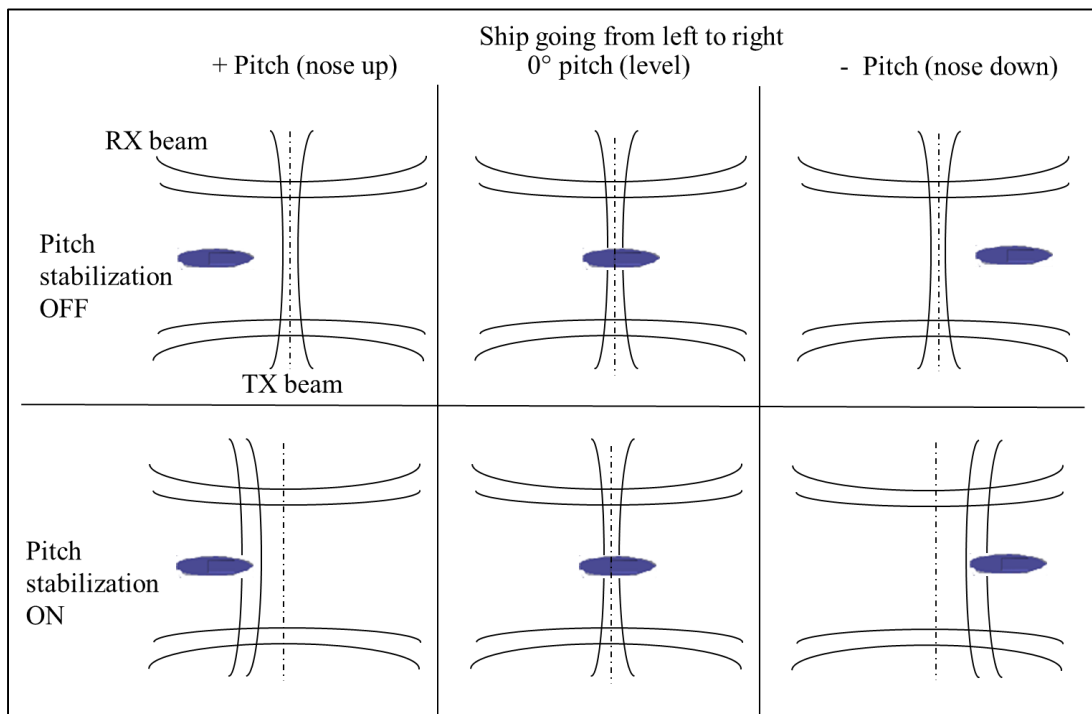
Figure 3.7: Transmit and receive beam geometry and pitch stabilization (dotted lines shows peak response of unsteered Tx and Rx beams).
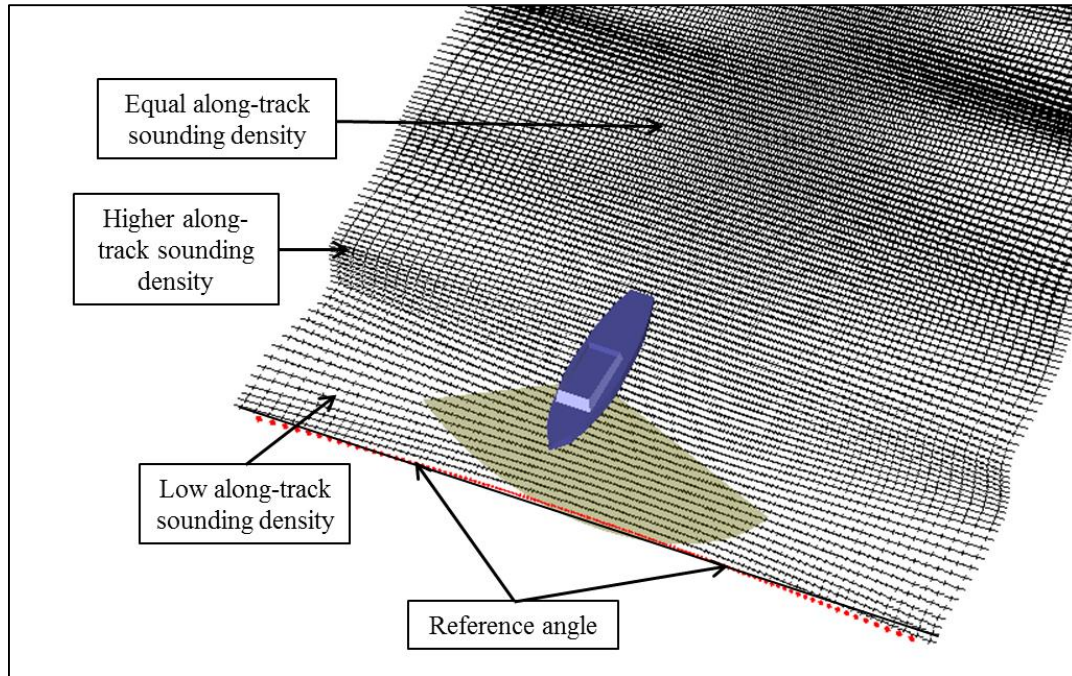
Figure 3.8: Single sector sounding density with roll and pitch stabilization without yaw stabilization.

3.2.3 Yaw Stabilization

For a single sector system, no yaw stabilization is possible for Kongsberg multibeam systems. Only by dividing a wide across-track transmit sector into multiple sub sections can yaw stabilization be achieved. With multiple transmit sectors, each sector can be steered forward or backward independently to achieve yaw stabilization as shown in Figure 3.9. Multiple sectors also help in more effective pitch stabilization by avoiding low and high density patches as shown in Figure 3.8.
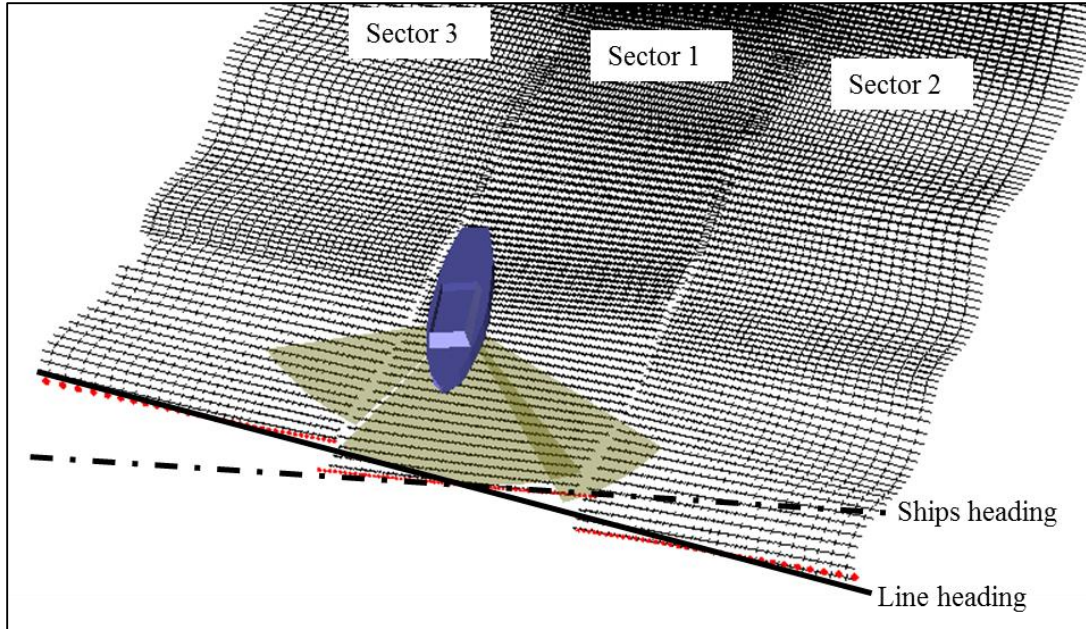
Figure 3.9: Multi-sector, all motion stabilized soundings with maximum equal density

The geometry of transmit sectors and Rx beams is shown in Figure 3.10. Similar to pitch stabilization, the yaw stabilization takes place with Tx beams only and no action is taken with Rx beams. In multi-sector systems, the typical extreme transmit sector steering during yaw stabilization is about $\pm10°$ compared to $\pm3°$ during pitch stabilization in single sector systems. As a result, the beams from different Tx sectors intersect Rx beams away from their along-track sensitivity center as shown in Figure 3.10. This complicates the final RBP as explained in the next sections.
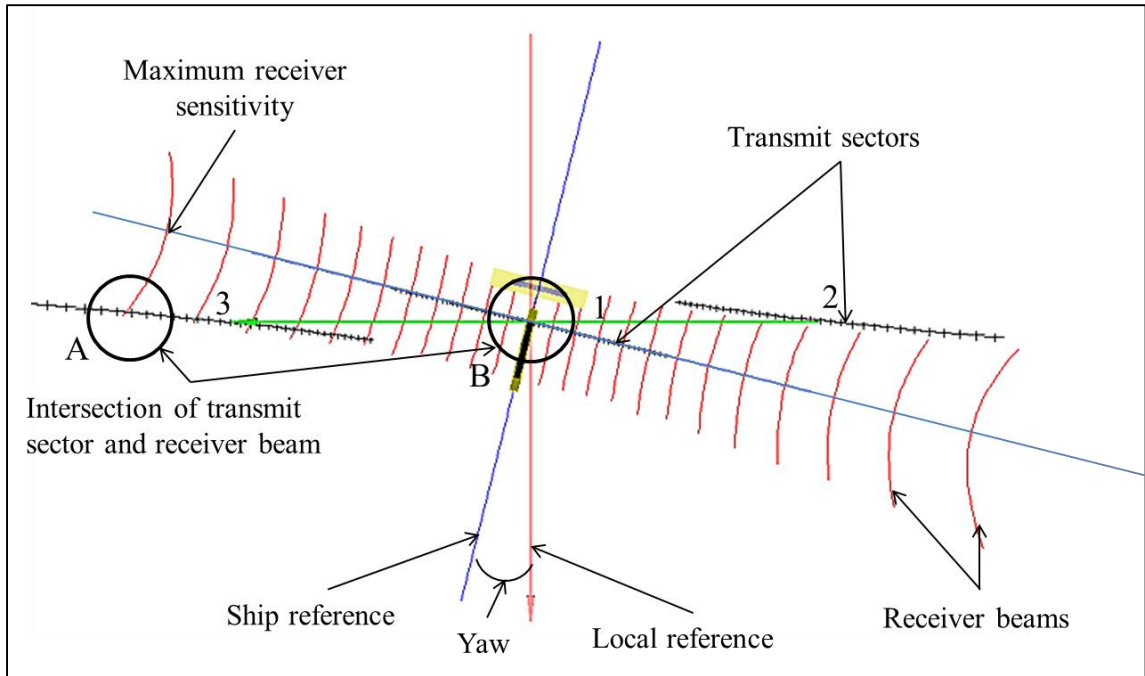
Figure 3.10: Multi-sector yaw stabilization geometry

As each transmit sector only needs to cover a subset of the full swath width, the across-track sector coverage by the transmitter can be minimized. This has the benefit of higher directivity and less sensitivity to noise coming from outside the sector of interest. But the difference is that the across-track transmit beam patterns roll off steeply with elevation angle resulting in more pronounced beam pattern residuals. Optionally the across-track steering could be roll stabilized and in that case the transmit beam pattern would be vertically referenced. But in the only operational case built by Kongsberg, the Tx beam patterns are reported to be unsteered and therefore sonar referenced.

3.3 Motion Stabilization and Radiometric Beam Pattern

In the previous section the Tx and Rx beam pattern were introduced along with motion stabilization mechanisms. This section reviews the effect of motion stabilization on backscatter data in order to explain the imposed RBP on the actual seabed backscatter caused by motion stabilization.

3.3.1 Multi-Sector Transmit Beam Pattern and Roll Stabilization

In roll stabilization, no action is required on the transmission cycle. The sectors are transmitted with the predefined sector center pointing angle (CPA) shown in dashed blue lines in Figure 3.11A, B, C. The CPAs are relative to the sonar Tx active surface (i.e., in the sonar reference frame) irrespective of the instantaneous roll. The sectors are transmitted with peak intensity at the CPA and the intensity reduces away from the CPA. There are no actual sector boundaries and all the sectors overlap. For illustration purposes, however, approximately -8 dB sector boundaries at about 30° [Hammerstad, 2005] from the CPA are shown by dotted color lines for each sector in Figure 3.11A, B, C. The vertically referenced Rx sector boundaries are shown in continuous dark black lines which constrain the portion of the transmitted sector that is received to be used for sonar operations (bathymetry and imaging). These vertically referenced sector boundaries

are defined on reception of the signal by roll-stabilized Rx beams tuned to the specific
frequencies of the desired sector.
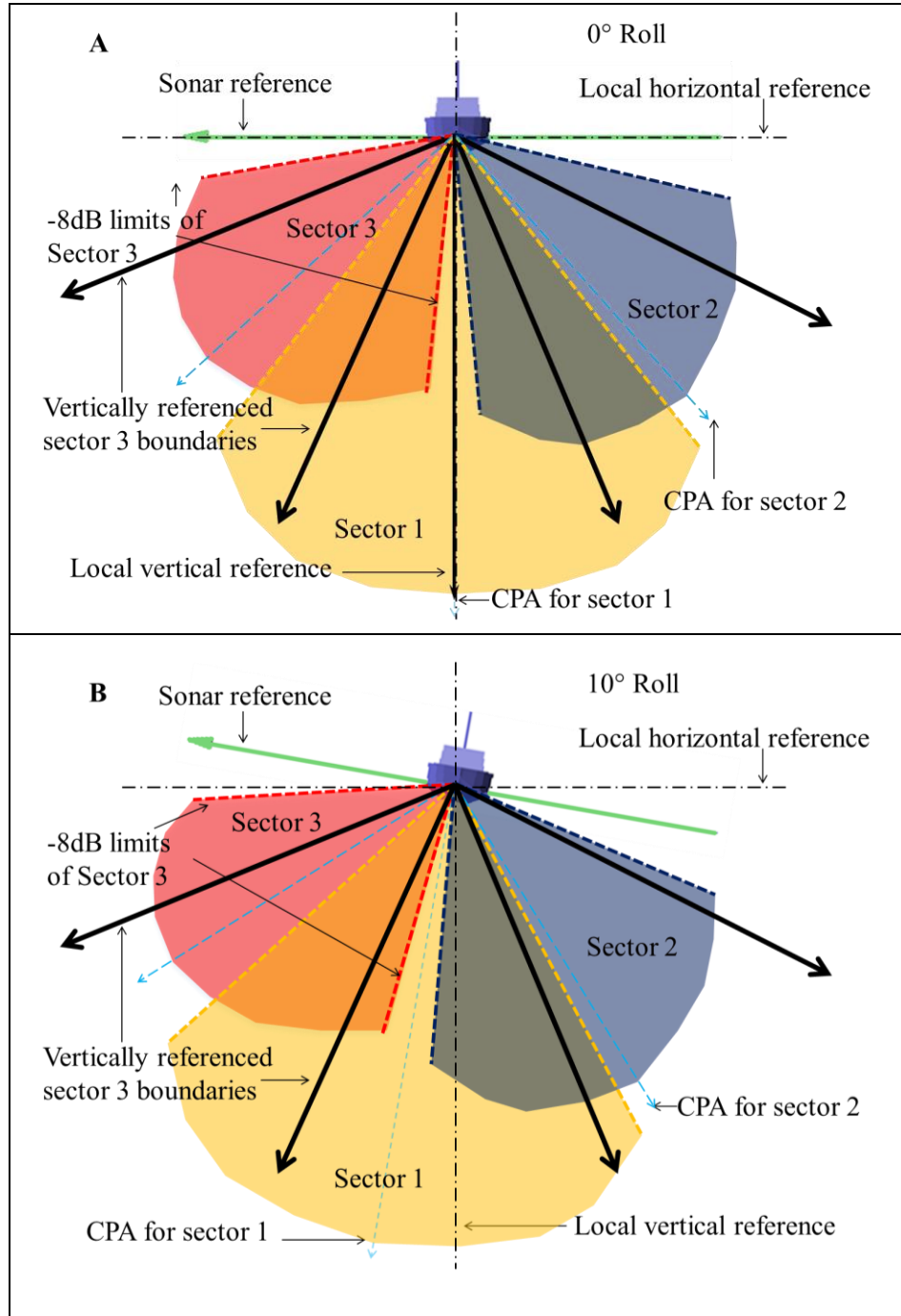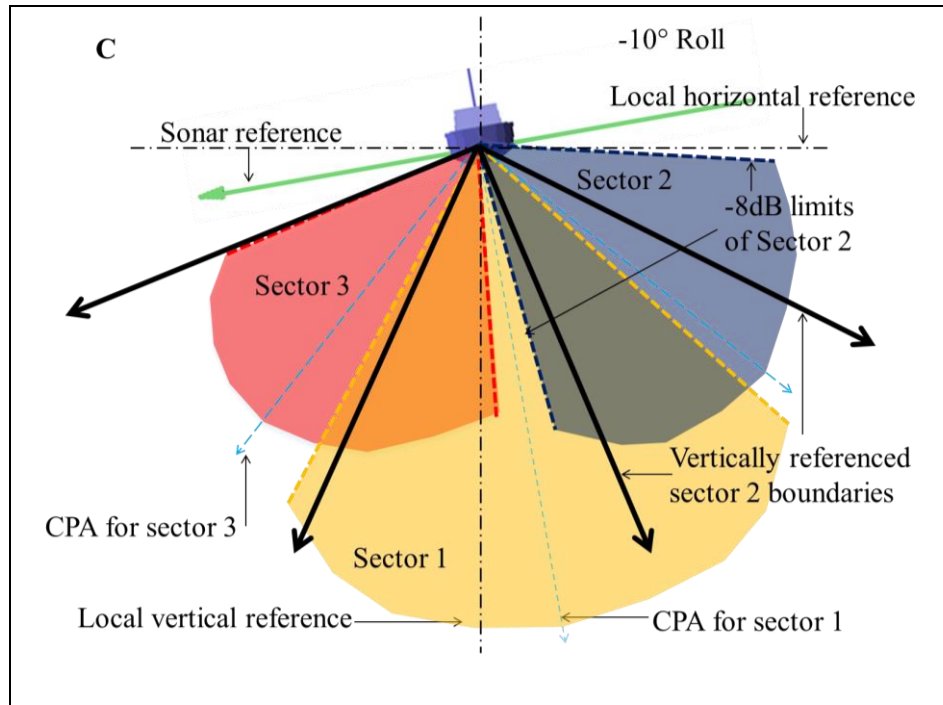
Figure 3.11: Multi-sector transmit beam pattern and roll stabilization

In Figure 3.11A the ship is perfectly aligned with local reference and roll is 0°. When the vessel rolls, the sector CPA (dashed blue lines in Figure 3.11) rolls with the vessel as they are sonar relative, but the boundaries that define the utilized portion of the transmitted sector (dark black lines in Figure 3.11) are vertically stabilized and do not roll with the ship. This is explained in Figure 3.11B with 10° of vessel roll and in Figure 3.11C with -10° of roll.

The roll stabilization achieved in this manner thus uses a different portion of the transmitted sector for bathymetry and imaging depending on vessel roll. The consequence of this stabilization is that the vertically referenced sectors experience different source levels within the sector as the vessel rolls. This is shown using a synthetic model (Figure

3.12) created using heavily scaled up ship motion on a flat seafloor for illustration. The model uses the beam pattern shown in Figure 3.4A.
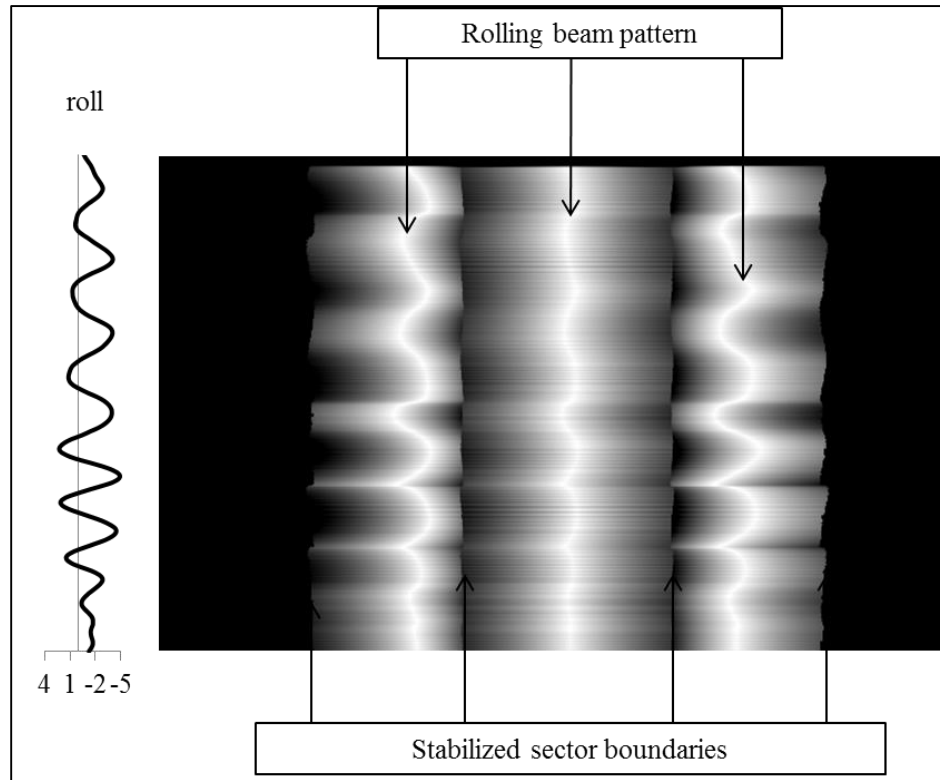
Figure 3.12: Multi sector Tx insonification and complications with roll stabilization

Figure 3.13 shows an actual backscatter image which is compensated for seabed angular response and transmission losses. The manufacturer's predicted beam pattern correction function was scaled for specific sectors to magnify the effect of rolling on the Tx beam pattern.
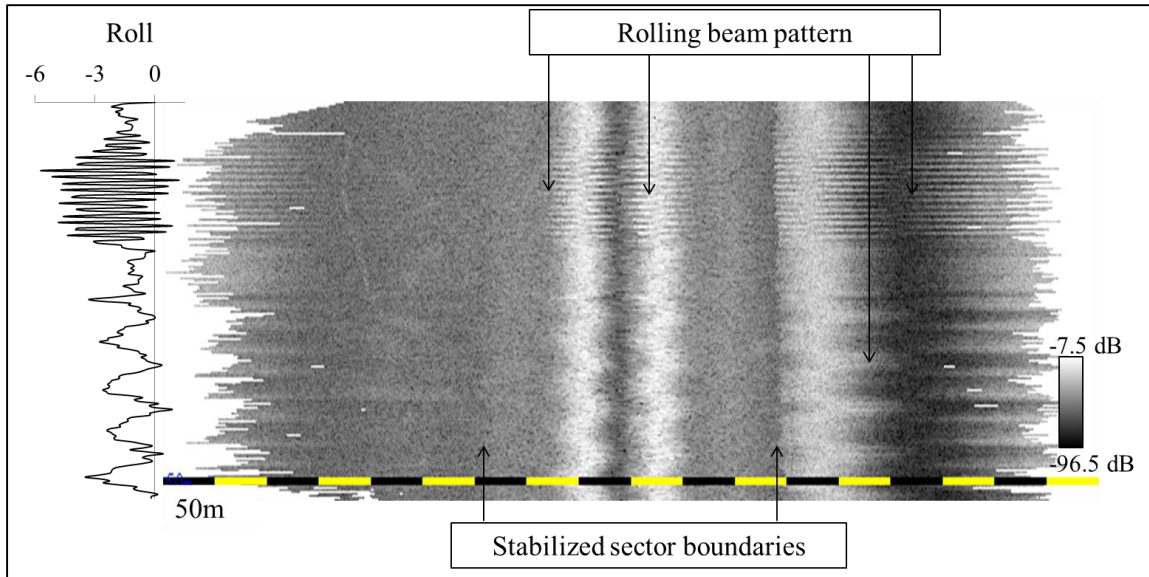
Figure 3.13: Multibeam backscatter data (EM 710, ≈200m water depth) showing across-track beam pattern due to rolling

3.3.2 Multi-Sector Receiver Beam Pattern and Yaw, Pitch Stabilization

As explained in previous sections, active yaw and pitch stabilization is done using multiple transmit sectors steered forward or backward. The Rx, however, continues to detect the echo using a single sector which is not steered along-track. This geometry is explained in Figure 3.7. The yaw and pitch both cause the intersection of Tx beam with the Rx beam to deviate away from the along-track center of the Rx beam pattern. This means that the Rx sensitivity varies as the vessel pitches or yaws. As a result of this mechanism, the received backscatter displays strips of strong and weak intensities as shown in Figure 3.14. In the case of heavy yaw stabilization, the outer Rx beams will show along-track changes in the intensities.

Figure 3.14 shows the actual data collected with a three sector system under heavy yaw stabilization. The multibeam backscatter image shows the bright and dark pattern on the outer sectors due to changing along-track Rx sensitivity.
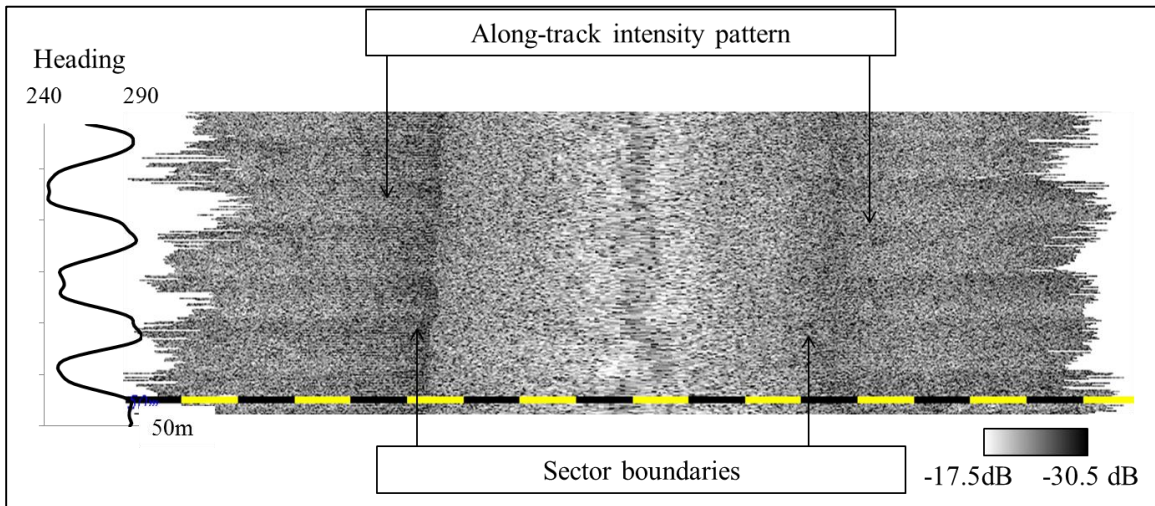
Figure 3.14: Multibeam backscatter data (EM 710, ≈200m water depth) showing along-track beam pattern due to yaw stabilization

3.4   Geometric Effect in Backscatter Data

The geometric effect is an artifact in the multibeam image data due to the geometry of the intersection of the pulse annulus and the shape of the seafloor. For a nearly flat seafloor, the specular echo (shortest range) is very close to nadir beams under the ship. If the variations in the slope of the seafloor changes the geometry, as in the case of a ridge or sand wave field, the specular echo is no longer from nadir beams but can be anywhere in the swath. In the case of fore-aft slope of the seafloor there may be no specular echo at all. As a result of this, the high and low intensity pattern appears proportional to low and

high grazing angle respectively as shown in Figure 3.15. This pattern is a projection of ARC that is modulated by local changes in grazing angle.
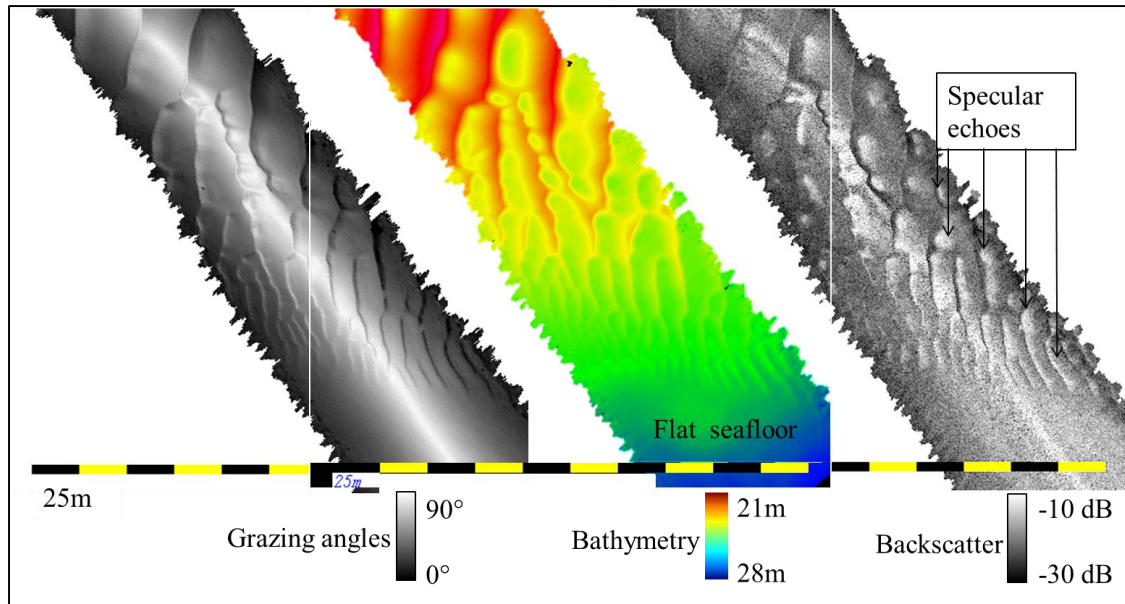
Figure 3.15: Geometric effect on backscatter intensities

In an earlier empirical beam pattern correction algorithm (OMG1 in section) the apparent across-track intensity modulations due to changing geometry have been unavoidably mixed with the projected radiation patterns. The real time TVG for minimizing angular variation applies corrections to the backscatter data assuming planar seafloor and thus fails in the case of uneven seafloors such as in Figure 3.15. The geometric effect will be different on the same rough seafloor if surveyed using different line bearings because of different along- and across-track slopes of the seafloor relative to the beam vector.

This geometric effect in backscatter data can be removed by first removing the manufacturer-applied real-time TVG for angular variation of BS (TVG-BS) and then

normalizing the data by grazing angles using the empirical method of generating ARC. This method is successfully used for a single sector system, and results for a sand wave field are demonstrated by Hughes Clarke [2012].

3.5   Review of Current OMG Algorithms

This section discusses current methods employed in OMG algorithms to do post-processing corrections to multibeam backscatter data listed in Section 2.4.1.

3.5.1   Source Level

The source level is assumed to be constant for the duration of the survey and the effects of any changes in the source level variation are assumed negligible. The relative changes in the source level are more commonly due to depth mode changes where the pulse length is changed and the area calculation does not exactly compensate for it. In the case of the Kongsberg system, these relative changes in pulse lengths are recorded in the runtime telegram, but compensated only to a first order by the manufacturer's TVG in real time. Often this compensation is imperfect. OMG algorithms have an option to calculate any residual apparent change in BS level before and after a pulse length change and apply them after according to the recorded setting. The relative source level between

the sectors may be different and adjusted by taking the mean of the differences during the process of normalizing the image data to form a mosaic. For a survey to survey comparison, a stable seabed reference is required. Using that, overlapping segments of successive surveys can be used to calculate inter-survey differences.

3.5.2 Measurement of True Seafloor Slope

In the literature, many authors (starting with [de Moustier, 1986]) have mentioned the importance of calculating the actual seafloor slope that is required to compute the actual GRA at which the incident sound wave strikes the seafloor. At this point, it is important to describe the different angles involved in the multibeam geometry.

Referring to Figure 3.16, incident angle θ_i (range from port to stbd is -90° to 90°) is the angle of incident sound wave referenced from the vertical at the source; sometimes it is referenced from the horizontal (90° at nadir and +/- 0 at port/stbd). The important thing to notice is that θ_i is independent of seafloor geometry. In the OMG algorithm this incident angle is calculated by a simplified assumption (ignoring along-track distance and refracted ray path) and is equal to the inverse tangent of the ratio of the depth to seafloor (excluding sonar draft) to the across-track distance of the bottom detection. The across-track distance is commonly stored with respect to the reference point (RP) and hence before the angle computation the offset between the RP to sonar is accounted for. In reality the θ_i at the sonar surface may be different from θ_i at the seafloor due to

refraction of the ray along its path. At the moment this refraction is ignored in the OMG incident angle calculations.

θ_s is the sonar relative angle; it is the angle between the normal axis (single dotted line in Figure 3.16) of the sonar and the beam. The SRA depends neither on the vessel roll nor on the seafloor geometry. The SRA can be further divided into SRA at the time of transmission and SRA at the time of reception; the Rx formed beam angle (SRA at the time of reception) is stored for each beam in the reported telegram. In the current OMG algorithm as a simplification, this angle is assumed equal to the incident angle of the beam plus vessel roll at the time of reception of the beam. As with θ_i, this does not precisely reflect refracted angles and fore-aft distortions. The vessel roll at the time of transmission and reception is assumed to be the same, but for deeper seafloor this may not be a valid simplification and proper adjustment may be required. For this research SRA plays a very important role and new methods are implemented in OMG algorithms to precisely define the SRA at Tx and Rx by using ship orientation and without using θ_i and hence avoiding the refraction issue. The detailed discussion is presented in the methodology chapter.

The GRA (θ_g) for the seafloor is the angle of intersection between the assumed planar seafloor (double dotted line in Figure 3.16) and the incident wave. θ_G for actual seafloor can be very different from θ_i as it depends on along- and across-track seafloor slope. Figure 3.16 shows a simplified case with across-track slope only. In ideal conditions

where the seafloor is flat and horizontal and there is no roll or refraction, all angles will be same for a given beam.
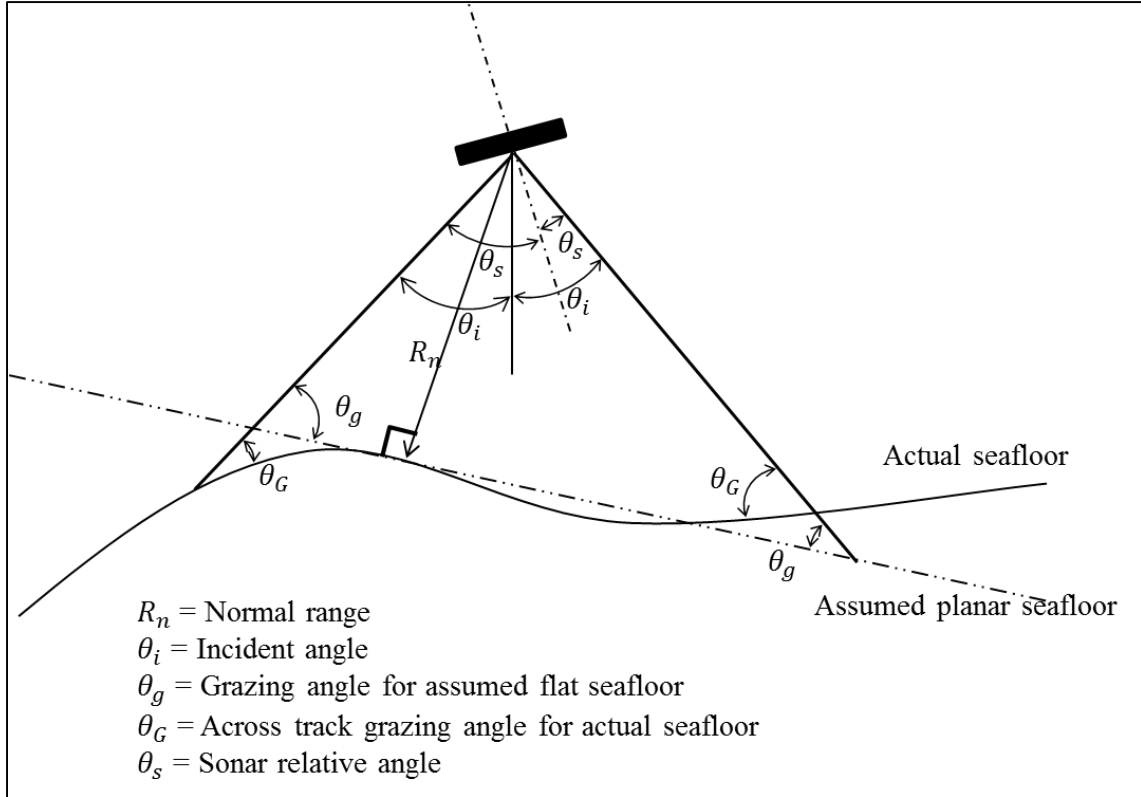
Figure 3.16: Grazing angle geometry

The true slope can be calculated using measured bathymetric data. The OMG currently have an algorithm that calculates the GRA accounting for along- and across-track slope. In short this correction is incorporated in the OMG backscatter processing algorithm. The quality of the real surface normal is degraded by noisy soundings. Adjustments and improvements to this algorithm are attempted as a part of this research. As we shall see, the backscatter data is sorted in $1°$ bins by these angles in the developed method and also for composing ARCs. Hence accurate computation of all the angles is

necessary. A detailed discussion of the computation of these angles is provided in Chapter 4 and Appendix 9.1.

3.5.3 Variation between the Apparent Calculated and True Grazing Angle due to Refraction

Figure 3.16 assumes homogeneous seawater in which the incident ray is not refracted. In reality, layered seawater can bend the ray inward or outward affecting the actual GRA.

Figure 3.17 shows the two different layers that refract the beam inward and outward making θ'_G different from θ_G. The magnitude of the difference will depend on how wide is the swath and how much variation is in the water column. Currently in the OMG software, this correction is implemented and used during this research. Knowing the sound speed at the surface and at the sediment water interface, the alteration of θ_i can be estimated. θ'_i is then combined with the seabed normal vector to compute the refraction corrected grazing angles.
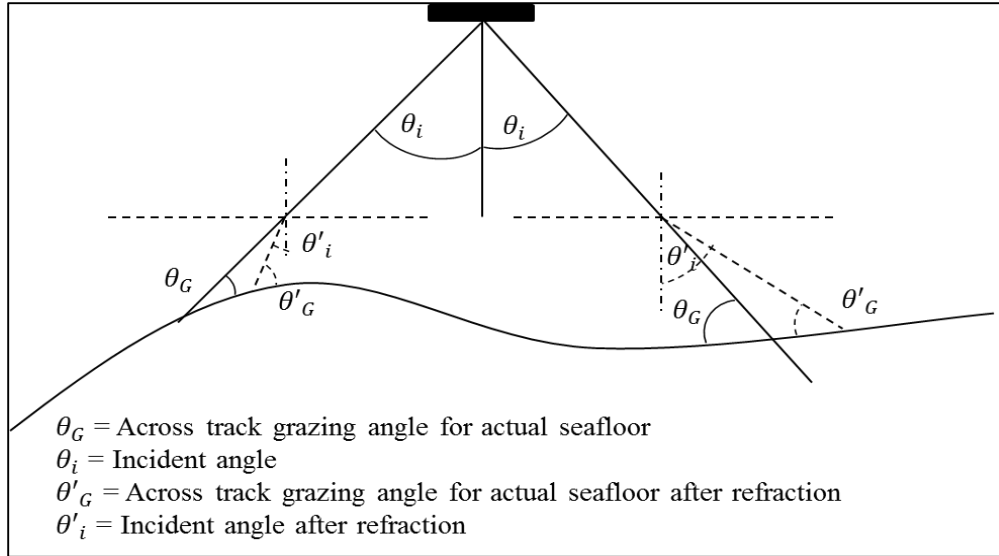
Figure 3.17: Effect of refraction on grazing angle.

3.5.4 Correction for Attenuation

As noted in the previous section, the attenuation is sensitive to frequency and changes with salinity, temperature, and pressure. The temperature and salinity changes are a function of depth. In current practice, Kongsberg's EM 710 applies sector-specific attenuation considering the different operating frequencies and depths given the correct salinity and temperature profile. In the case of wrong attenuation coefficient being used in real-time, the OMG software is capable of correcting the backscatter data using true value of attenuation coefficient in post-processing. The detailed work has been completed on sector-specific attenuation by the OMG group [de Campos Carvalho, 2012; de Campos Carvalho et al., 2013].

3.5.5 Removal of Angle-Varying Correction (TVG-BS)

In order to get the ARC, the manufacturer-applied TVG-BS has to be removed. The manufacturer-provided specifications and the parameters stored in the datagram are used to undo the compensation. The current OMG software has an algorithm that addresses the specifics of the manufacturer's function [Beaudoin, 2005] but more rigorous testing is performed as a part of this research to gain confidence in the ARC. Specifically improved insonified area calculations coping with local seafloor slope and varying beam width with sector steering is attempted.

3.5.6 Compensation for Pulse Length

In order to keep the signal to noise ratio high while keeping the maximum possible range resolution, sonar systems can increase or decrease the pulse length of the signal. The change in pulse length changes the insonified area that has to be included in the calculation of the BS. The effect of changing pulse length in the calculation of the insonified area is currently implemented in the OMG software pack. As a part of this research, this algorithm (particularly the crossover from beam width limited to pulse length limited case) was carefully reviewed and no significant updates are required.

3.5.7 Variation between Actual and Predicted Beam Pattern

In the OMG algorithm, there are two methods currently employed to deal with beam patterns. In the first method, the residual beam pattern is removed along with the normalization of the combined product of ARC and RBP. The multibeam backscatter image made after the normalization has minimum residual RBP and minimum angular response of BS. The first method, which dates from the early 90's is an empirical method used by researchers to ensure removal of the combined effect of actual angular response and residual beam pattern [Hughes Clarke, 2012]. The normalized data are then mosaicked and used for the sediment characterization. The changing angular response with different sediment types is handled by separating the statistics for different sediment types from either a priori knowledge or using a rolling average looking at the responses with a local area. The detailed description of this can be found in Hughes Clarke [2012]. An extension to the first method was developed by Teng [2011], which separates the residual beam pattern for each distinct sector.

In the second case, the product of ARC and RBP is compared to an ARC generated using a model for the known (or guessed) sediment type. The difference between the product of ARC and RBP and the model ARC is attributed to the combined Rx and Tx RBP [Hughes Clarke et al., 1997]. This estimated RBP is then removed from all data, and ARCs with minimized effect of rbp are thereby obtained.

The third and most recent method has been developed by Tamsett and Hogarth [2016]. This is a method to estimate the combined Tx and Rx beam pattern using a rolling motion of the vessel rather than using the generalized model. The rolling motion allows separation of ARC from RBPs. The obtained sonar functions (RBP) are used to correct all the data, and then ARCs are obtained that can be used for classification.

3.6   Removing the Beam Pattern from ARC: Problem Statement

As described in the literature review (section 2.3), backscatter-based seafloor classification is typically done using either ARC or mosaics of multibeam backscatter data. In any case, it is crucial that ARCs are estimated with the highest accuracy. The required post-processing of the reported multibeam backscatter data to obtain the ARC was also summarized in the literature review. In order to use the backscatter data for identifying small changes in the sediment type either temporally or spatially, processed backscattered data with least remaining artifacts has to be obtained. One of the major remaining sources of ambiguity in the processed data is the improperly corrected effect of RBP [Lurton & Lamarche, 2015]. The last section described the intricate overprint of RBP on backscatter data due to motion stabilization. This section reviews the current methodologies for removing RBP and seabed angular variation from reported backscatter data. Three different approaches were identified in the review and are presented below.

3.6.1   OMG Method 1

In this method dating from the early 1990's, the algorithm deals with the radiometric, geometric, and BS angular variation effect in a single bundle in which a combined product of ARC and RBP is estimated. The basic assumption in this method is that, averaged over a time period (thus over a large area), the average differences between SRA, VRA, and GRA tends to zero and thus the combined RBP and angular variation can be approximated as a constant for the area considered for the calculation. The removal of RBP and ARC happens when the backscatter data are normalized relative to either VRA, GRA or SRA using the product of ARC and RBP. This method was originally applied to single-sector multibeams, but can also be applied separately to the individual sectors of multi-sector multibeams [Teng, 2011]. The result of normalization is a combined RBP and ARC minimized mosaic of backscatter that then can be used for the classification using spatial variation in the angle-normalized backscatter intensities. Some error will remain where locally there is significant ship motion and/or local seafloor slopes that cause SRA, VRA and GRA to diverge.

An example of this methodology was shown by Hughes Clarke [2012]. In this method, it is possible to suppress the dominant effect (radiometric or geometric) in the mosaic. Using this method Brucker et al. [2007] demonstrated successful removal of dominant geometric effect in Howe Sound by removing the combined product of RBP and angular variation referenced to GRA. Using the mosaic produced from this method, Hughes Clarke [2012] was able to identify sediment changes in the Bay of Fundy off

Margaretville using data collected in 1994 and 2007. In an extension of this method, it is possible to compensate for changing ARC within a survey line by using the sequential local computation of angular variation [Hughes Clarke, 2012].

3.6.2 OMG Method 2

The second existing approach in the OMG algorithm is to estimate the RBP by first extracting the GRA referenced signature of an ARC using a model of the backscatter response for an estimated sediment type. After the model ARC is applied using the grazing angle, the remaining angular variation can be assumed to be just the residual RBP effects. Once estimated, RBP can then be enforced with respect to SRA to remove the radiometric effect from other data where the ARC was not previously known. These estimates of ARCs that now do not have a significant RBP overprint can then be used for characterization. In this method, the user is required to have excellent a priori knowledge of the seafloor backscatter response for at least a small subset of the survey area. The difference in actual seafloor properties and the properties used to form the model of backscatter response will improperly attribute some GRA effect to RBP or vice versa. Also, the estimated RBP is the product of along- and across-track RBP and separation between them had not implemented in this method.

Despite these limitations, the ARCs produced by this method were successfully used by Hughes Clarke et al.[1997]. The authors applied this method to the old EM 1000,

which was a single sector system using a curved array. The EM 1000 was unique in that the system's RBP was dominated by variations in the Rx electronics. The Rx channels were roll stabilized, and thus the apparent RBP was applied vertically referenced to get ARCs for classification. For the more recent systems like EM 710 and EM 2040, which are multisector systems, the RBP is dominated by variations in the Tx source level. For these sonars, the obtained RBP by this method was applied relative to sonar and then subsequently the ARC was obtained and used for classification by Hughes Clarke [2015].

Similar method has been applied by SonarScope, commercial software developed at French research Institute for Exploitation of the Sea dealing with multibeam backscatter data processing. In this software, a measured product of ARC and RBP is compared to the model of the ARC for given sediment and RBPs are estimated. A parabolic curve is fitted to the estimated RBP for each sector and a modeled (radiation) directivity pattern is obtained [Lurton & Lamarche, 2015]. The offset values of RBP are obtained by visually checking continuity of sectors and symmetry of response around a nadir region [Beaudoin et al., 2012; Lurton & Lamarche, 2015]. As a good estimate of the model of ARC for the seafloor is required, it is recommended that this process is done by a well-trained person. Augustin and Lurton [2005] have also used the same method and demonstrated the results.

3.6.3 Tamsett and Hogarth Method

This method has been very recently developed for swath bathymetric sidescan sonar systems [Tamsett & Hogarth, 2016]. The authors recognized that the RBP is sonar relative and rolls with the sonar. This relationship is used to estimate the sonar beam pattern without requiring the use of any models of backscatter ARC. The basic idea followed in this approach is that for a homogeneous seafloor, at a given GRA, the seafloor backscatter strength is constant and that any roll driven variations in the intensity at that GRA thus can be solely attributed to the sonar (Tx and Rx) RBP.

This method is the first step towards unambiguous separation between the radiometric effect and the ARC without requiring any assumptions about the shape of the ARC. Of the three reviewed methods, this method should be the most efficient in minimizing the effect of RBP on ARCs obtained. It has the particular advantage that, unlike the OMG Method 2, it requires no a priori knowledge of sediment type. However, it needs to be modified and further developed to accommodate the additional complications due to the multi-sector motion stabilization mechanism and its overprint on the received backscatter intensities.

As this method was developed for bathymetric sidescan sonars, it bundles the Tx and Rx beam pattern together. It is a fair assumption as the Tx and Rx are parallel and mounted together and share similar beam patterns in the case of a bathymetric sidescan sonars. However, in the case of a multibeam multi-sector system, Tx and Rx beam

patterns would ideally be calculated separately as the Tx and Rx are separate physical arrays which are mounted orthogonally and may have very different intensity and sensitivity variations respectively.

The authors recognize that the method does not differentiate between the roll at the time of transmission and the roll at the time of the reception of the signal. The transmit beam pattern signature is imprinted according to the roll at the transmit time, whereas the Rx beam pattern signature is imprinted according to the roll at the reception time. This will introduce some errors into the calculation of beam pattern, and the extent of that error will depend on two-way travel time and rate of vessel roll. Thus for shallow water and short travel times the assumption may be adequate, but for deeper water this may be a limitation.

3.7   Research Questions

Over the past 20 years, multibeam bathymetry and backscatter have provided amazing insight into the geographic distribution of morphology and sediments on the ocean floor. Today, however, going beyond just identifying the seabed type to tracking seabed changes is the new paradigm. Given how the seabed used to look at one epoch, can we detect whether it has changed since? The use of bathymetry from repetitive multibeam surveys to identify changes in the geometry of a seafloor over short temporal separation (a few hours to a few days) has been successfully demonstrated [Hughes

Clarke et al., 2012]. The confidence in these changes is directly associated with how accurately the bathymetry is measured using the integrated system for each survey. The increased accuracy in positioning, orientation, tide models or measurements, and sound speed profilers have contributed to increased accuracy of bathymetric measurements. The available motion stabilization in multi-sector multi-swath multibeam systems assures the highest and most consistent density of soundings giving reliable bathymetry with maximum coverage. The high range and angular resolution multibeam systems available further fulfill the bathymetric resolution requirements for repetitive mapping.

In a similar way, multibeam backscatter data have been successfully used for seafloor classification. For a single survey, relative seabed changes can be discriminated even with imperfections in the absolute accuracy of the backscatter data. Identifying smaller temporal and spatial sediment changes is still a challenge. There are few examples of sediment change identification with large temporal gaps [Hughes Clarke et al., 2012]. In order to address the question of whether backscatter data obtained during the repetitive surveys with shorter temporal separation (1 year to few hours) can be used for identifying changes in the sediment types, backscatter data with least possible artifacts has to be obtained. In this regards, this research focuses on reducing radiometric beam pattern in the backscatter data to highest possible value.

The hypothesis that is being tested in this research is unambigious along- and across-track RBPs can be extracted from strategically collected backscatter data utilizing ship's motion. With the improved accuracies and confidence on the extracted RBPs, more

confident ARCs can be obtained. The extra information that is provided by an ARC allows a more detailed representation of the seafloor compared to angle normalized mosaics. If ARCs can be computed with maximum accuracies with minimal residual RBP for backscatter data then smaller spatial or temporal sediment changes in the sediment properties may be more confidently identified.

The corrections applied to multibeam data are reviewed in the previous section. The new improved motion stabilization has significantly complicated the effect of RBP in the backscatter data. RBPs need to be taken out completely in order to access the uncontaminated backscatter signal from the data. The unambiguous separation of the Tx and Rx RBP, as well as the separation of RBP from the ARC has not yet been achieved; however existing methods can be modified and further developed to achieve this separation. The available three methods to remove beam patterns achieve approximate estimation and eliminate the beam pattern up to a certain degree. These methods are only acceptable for the large-scale classification of seafloor and to identify large temporal changes in the sediment type.

3.8   Research Objectives

The aim of this research is to improve the fidelity of backscatter data by minimizing artifacts due to RBP. To achieve the objective, understanding the logical workflow of the existing OMG software packages is important as they will be used as a platform for this

research. The modules or subroutines that have been developed to date need to be reviewed for any embedded inadequate assumptions or subtle programming errors. Then new methods need to be implemented within the already available framework of the OMG software. The research objectives are divided into two parts as described below.

3.8.1 Reviewing and Refining Existing Backscatter Data Post-Processing Algorithms

All the corrections that are applied to the backscatter data need to be understood and discussed in more detail. However, it is not possible to evaluate algorithms for all and every aspect of the corrections applied. As part of this research, the computation of grazing angle, insonified area, and removal of manufacturer-applied gain is critically examined. However, the recently studied and modified correction algorithms for applying correct attenuation coefficients to multi-sector multibeam sonar are believed to be accurate and thus are not critically reviewed. In short, the following are the objectives to minimize the error in backscatter data post-processing.

1) Review and refinement of the algorithm that computes actual grazing angles and modifying it to consider refraction in the water column.
2) Review, refinement, and encapsulation of the algorithm (deTVG) that removes manufacturer-applied gain to remove angular variation of BS.

3.8.2 Developing New Method for Radiometric Beam Pattern Removal

Development of this new method and its implementation in the OMG algorithms is a significant contribution of this research. The limitations of the Tamsett and Hogarth [2016] method to compute the RBP are discussed in the review section. A method to overcome those limitations and to cope with the complications of multibeam multi-sector sonar is attempted. This development can be divided into two parts.

1) Developing an algorithm to compute Tx beam pattern (across-track RBP) from backscatter data using the rolling motion of the ship by extending the Tamsett and Hogarth method to multi-sector multibeam sonars.

2) Developing an algorithm to compute Rx beam pattern (along-track RBP) from backscatter data using the transmit steering due to the yawing motion of ship for multibeam sonars.

Both the above objectives have been achieved during this research and the next chapter describes the detailed methodology that is used in this research.

4 METHODOLOGY: DEVELOPING NEW METHOD TO EXTRACT RADIOMETRIC BEAM PATTERN

The methodology to achieve the research objective is divided into two major sections. The first section describes the fundamental principle underlying this research; it also describes the preprocessing required on the backscatter data before it is used for actual RBP extraction. The second section describes the core methodology of this research; it is further divided into two sub-sections, one describing the procedure of extracting across-track RBP and the other describing the procedure of extracting along-track RBP.

4.1 Fundamental Principle and Preprocessing before RBP extraction

This section is divided into four sub-sections. The first describes the data collection strategy and the basic principle used in this research. The second discusses the required preprocessing of the backscatter data which includes removal of manufacturer-applied TVG-BS and corrections for geometrical effect with review and refinement of existing OMG algorithms. The third describes how different angles are computed and how the pre-processed data are sorted using those angles. The fourth describes the cleaning of backscatter data by removing outliers.

4.1.1   Fundamental Principle

The backscatter strength for a given area containing homogeneous sediment type at a specific GRA is constant and should not change with the motion of the vessel; this is the fundamental principle used in this research. The RBP is independent of GRA and its effect only depends on SRA. The motion of the ship changes the SRA and hence the effect of RBP on the backscatter data also changes proportional to the ship's motion. In this research the method is developed to extract this SRA dependent RBP by carefully separating and sorting the backscattered data by the sector, GRA, and SRA.

During a regular survey campaign, initially collected survey data was visually analyzed to decide the patch of area that is suitable for the required data collection. For example in Bute (2014) the data collected in the first few days was used to identify locations with reasonably homogeneous material on a fairly flat seafloor. A similar strategy was used for the Squamish dataset in 2015. An area containing homogeneous material is required in order to fulfill the fundamental principle used in this method. The data has to be collected while underway to allow rolling, yawing, and pitching. If the material is changing within the survey line extent, the same grazing angle may have different BS along the length of the line, which will introduce an error in the RBP data extraction. The chosen test areas have gentle topography and any abrupt geometry was avoided. Test areas were surveyed several times with different sonar settings and appropriate depth modes (different pulse lengths and frequencies). The survey lines were

run in opposite directions in order to distribute the effect of any slight sediment differences in the test area throughout entire swath width of the sonar.

For along- and across-track RBP extraction described latter in this chapter, data were collected as described above and shown graphically in respective sections. Then the backscatter data are preprocessed for RBP extraction in three steps (see Figure 4.1). The very first step is to remove manufacturer-applied TVG-BS corrections to the backscatter data and apply corrections for actual insonified area accounting for the geometric effect. For this step, algorithms that have been developed previously in the OMG are used. A critical review and tests are performed to ensure the correctness. The second step is to sort the backscattered intensities by sector, GRA, and SRA. The third step is to remove any backscatter intensities (outliers) that are distinct from all other sorted backscatter intensities from step two.

```
┌─────────────────────────────┐
│       Data collection        │
└─────────────────────────────┘
              │
              ▼
┌─────────────────────────────────────┐
│  Remove manufacturer applied TVG-BS, │
│                                      │
│           Compute GRAs               │
│                                      │
│   Correct for actual insonified area │
└─────────────────────────────────────┘
              │
              ▼
┌─────────────────────────────────────┐
│   Compute SRAs (SRA-Ts and SRA-Rs)   │
│                                      │
│       Backscatter data sorting       │
└─────────────────────────────────────┘
              │
              ▼
┌─────────────────────────────────────┐
│   Backscatter data outlier removal   │
└─────────────────────────────────────┘
```
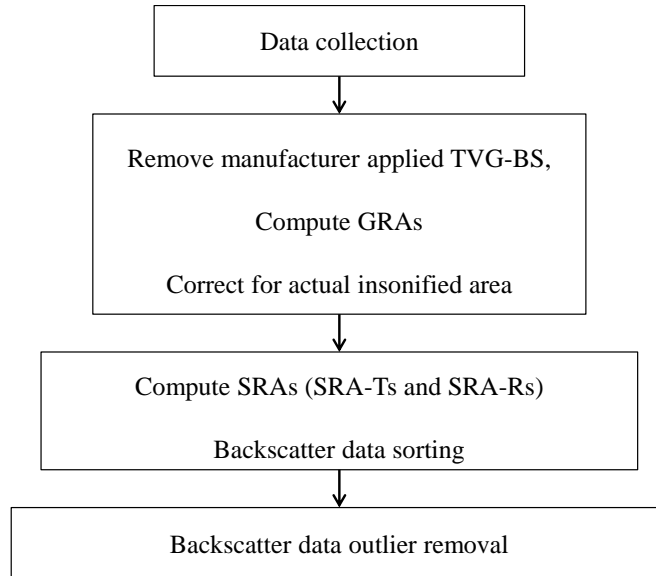
Figure 4.1: Flowchart showing major steps in backscatter data preprocessing

4.1.2 Removing Manufacturer-Applied TVG-BS and Correcting for Geometric Effect

The first algorithm at The University of New Brunswick (UNB) for removing manufacturer-applied TVG-BS was written in 2005 [Beaudoin, 2005]. The algorithm used system parameters that are stored in the data telegrams and the details from technical notes [Hammerstad, 2000] to compute the real-time TVG-BS applied by the system. This TVG-BS was then subtracted from the backscatter data in order to get the TVG-BS free backscatter data. During this research the existing algorithm is encapsulated to enable detailed testing and integration using a graphical user interface developed as part of this research. The interface helped to visualize components of TVG-BS and geometric correction.

87

Removing the geometric effect involves computation of true GRA and correcting the intensities for actual insonified area. Both the above steps are performed inside a single OMG algorithm (deTVG). The latest update of deTVG algorithm includes 1) exact resolution of ranges and TVG-BS function parameters like BSn, BSo, and range to normal incident as reported in datagrams; 2) Computation of TVG function once per beam instead of once per sample; 3) fixing a small error which was computing wrong sample numbers in some cases. Figure 4.2 shows the TVG-BS magnitudes subtracted from the reported data. The figure is for a single profile collected using EM 710 at about 250m depth.
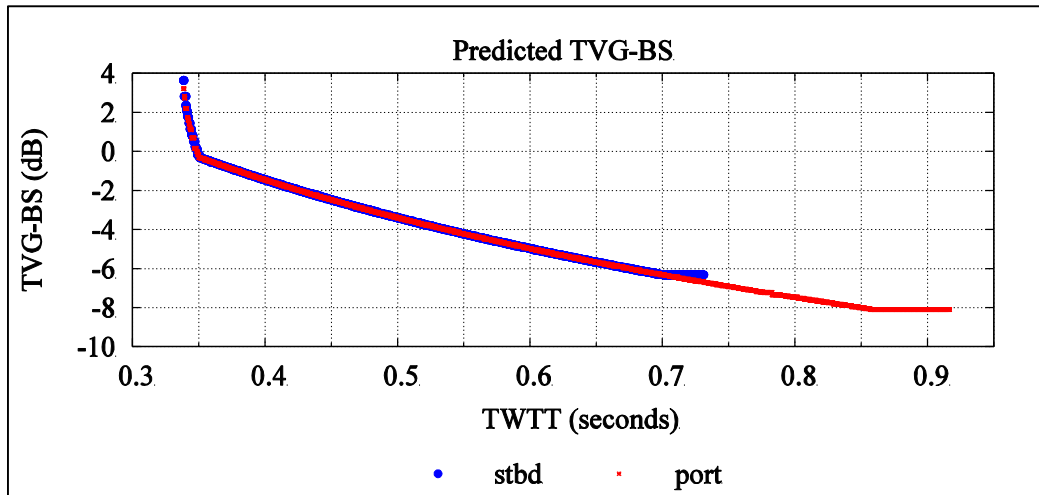
Figure 4.2: Manufacturer applied TVG-BS for a single profile.

In order to compute actual insonified area, the true GRA was first computed. A detailed discussion of the GRA computation is given in the Appendix 9.1. The insonified area calculation is explained in section 2.1.4 and the existing OMG code is used to correct for the geometric effects. Figure 4.3 indicate the magnitudes of these corrections

88

by comparing the manufacturer predicted corrections assuming flat seafloor at the normal incidence with the actual bathymetry of the computed insonified area.
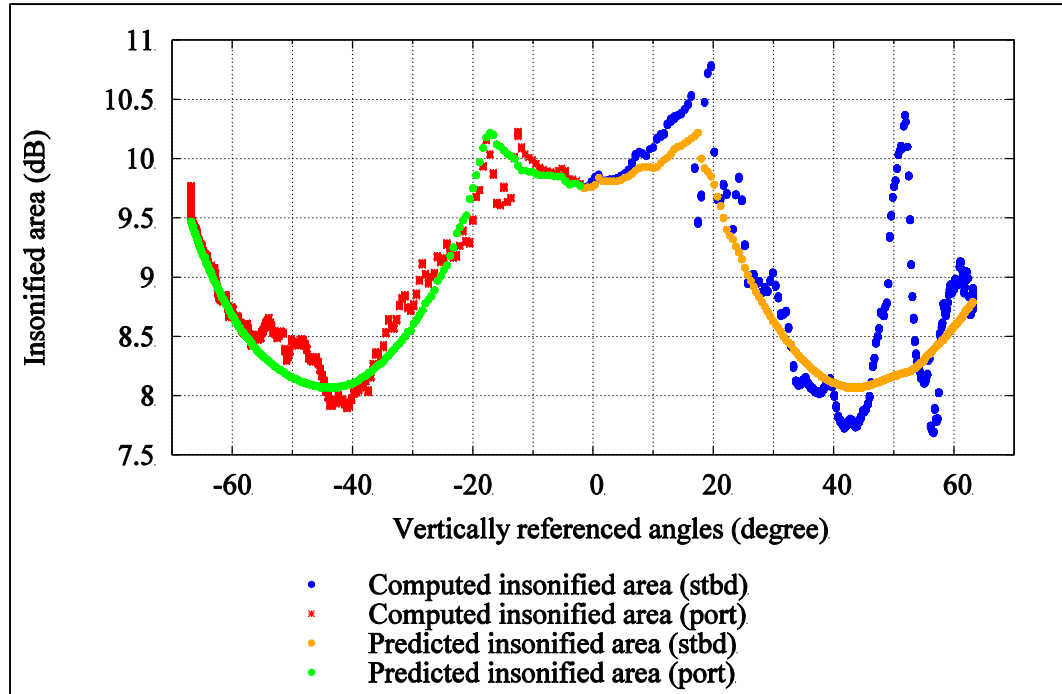
Figure 4.3: Magnitude of insonified area correction for a single profile on undulating seafloor

Figures 4.4 to 4.7 show the TVG-BS free and geometrically corrected backscatter intensity data along with the curves that are the products of ARC and RBP for various test survey lines. The intensity variation visible along the drawn lines in the backscatter images is the result of overprinted RBP; this intensity variation is used in the developed method to extract the RBP. The aim of this research is to unambiguously separate the RBP (along- and across-track) from the product of ARC and RBP in order to obtain the true ARC. The data shown in Figures 4.4 to 4.7 were collected for this research and the RBP can be seen in the form of backscatter images and the curves as well.

89
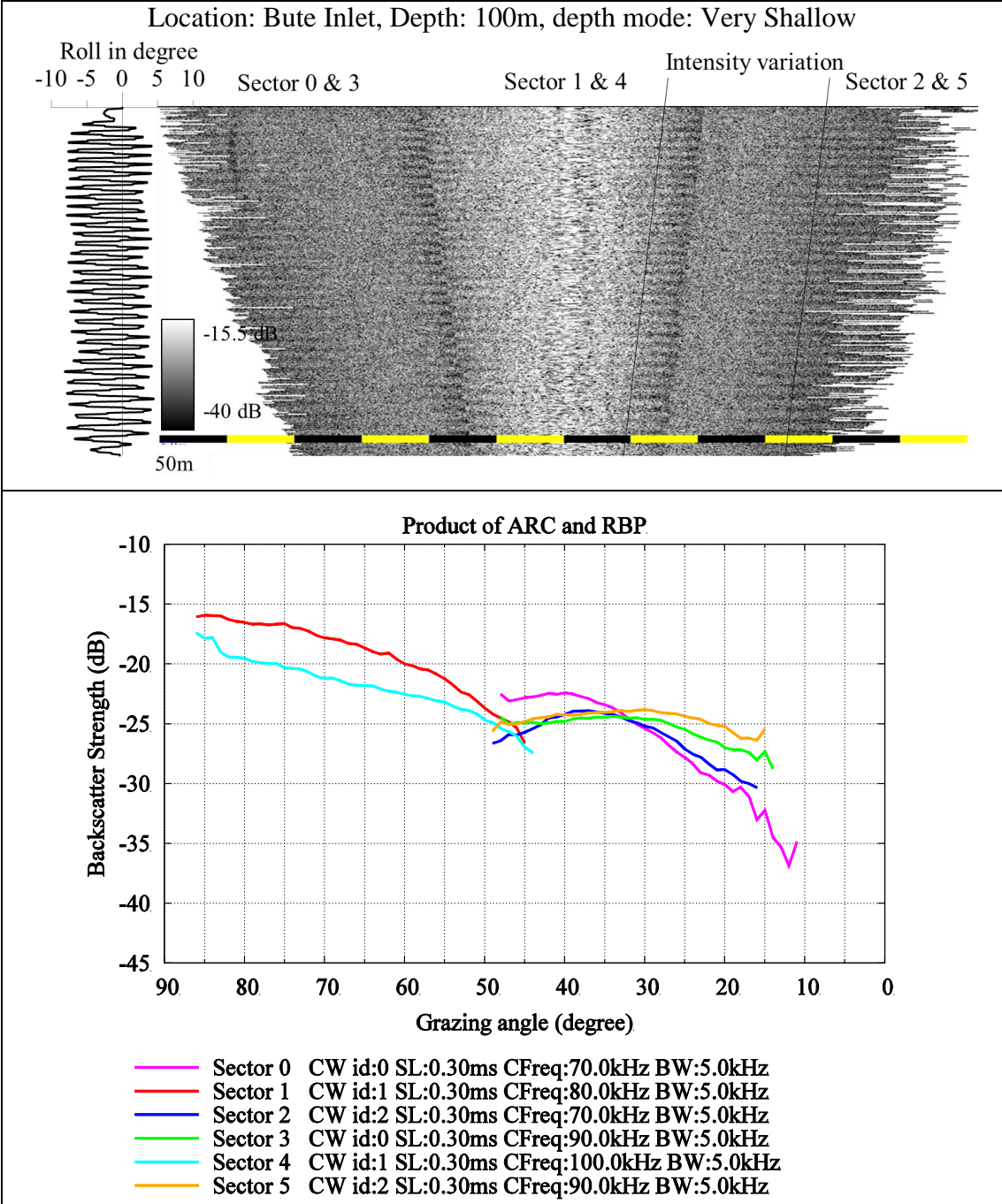
Figure 4.4: TVG-BS-free backscatter intensities with dominant across-track RBP collected in Bute Inlet with heavy roll
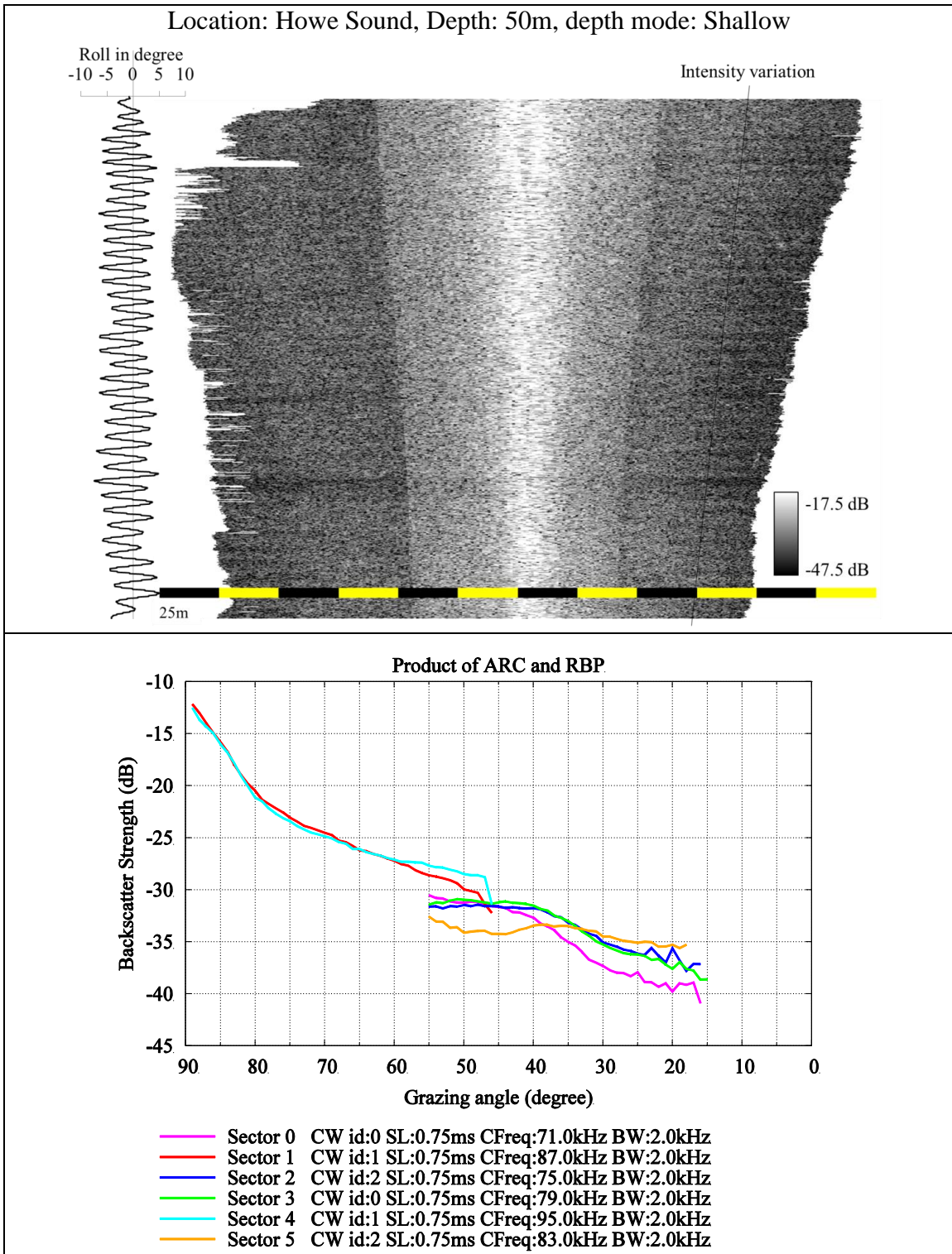
Figure 4.5: TVG-BS-free backscatter intensities with dominant across-track RBP collected in Howe Sound (Squamish) with heavy roll
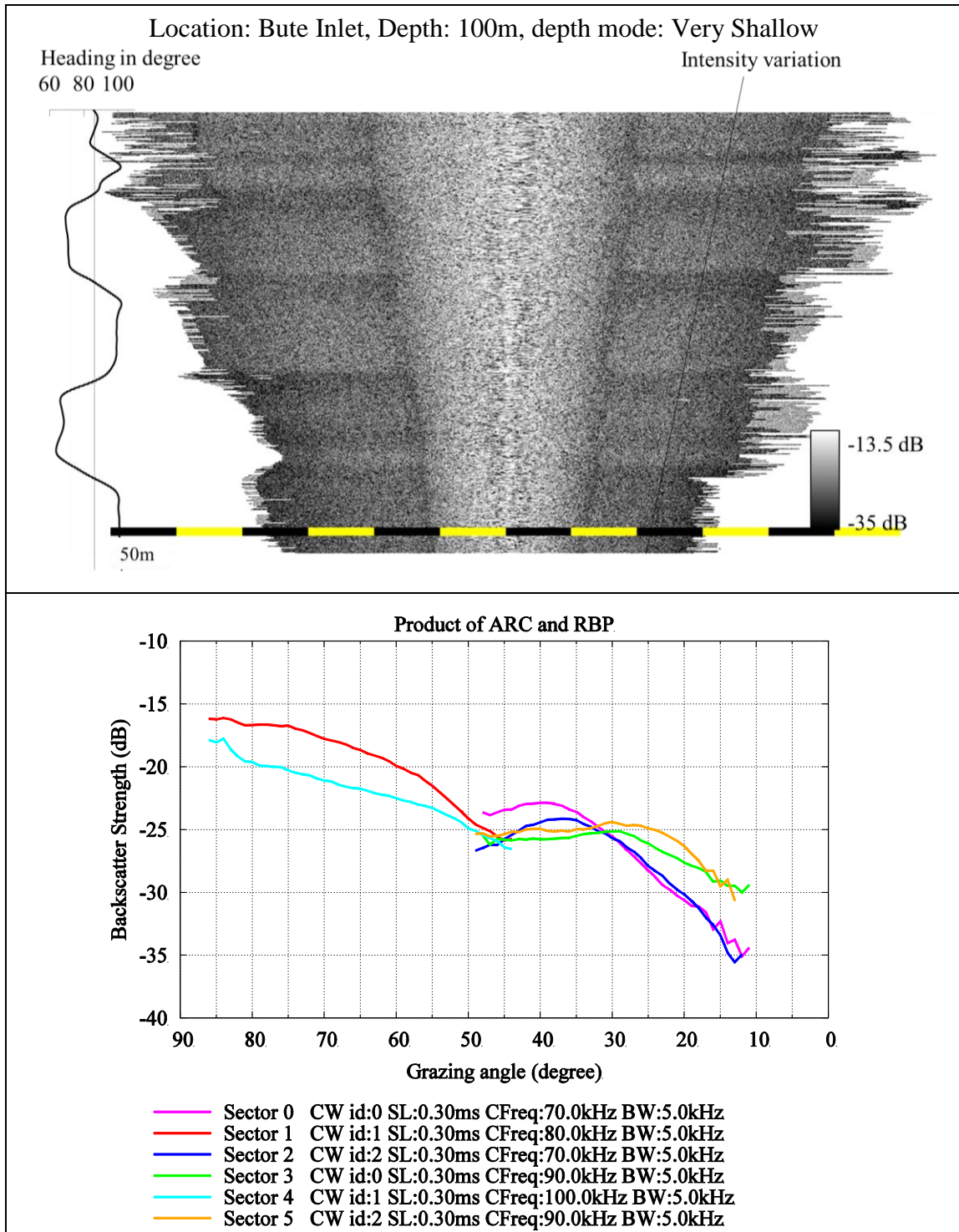
Figure 4.6: TVG-BS-free backscatter intensities with dominant across- and along-track RBP collected in Bute Inlet with heavy yawing
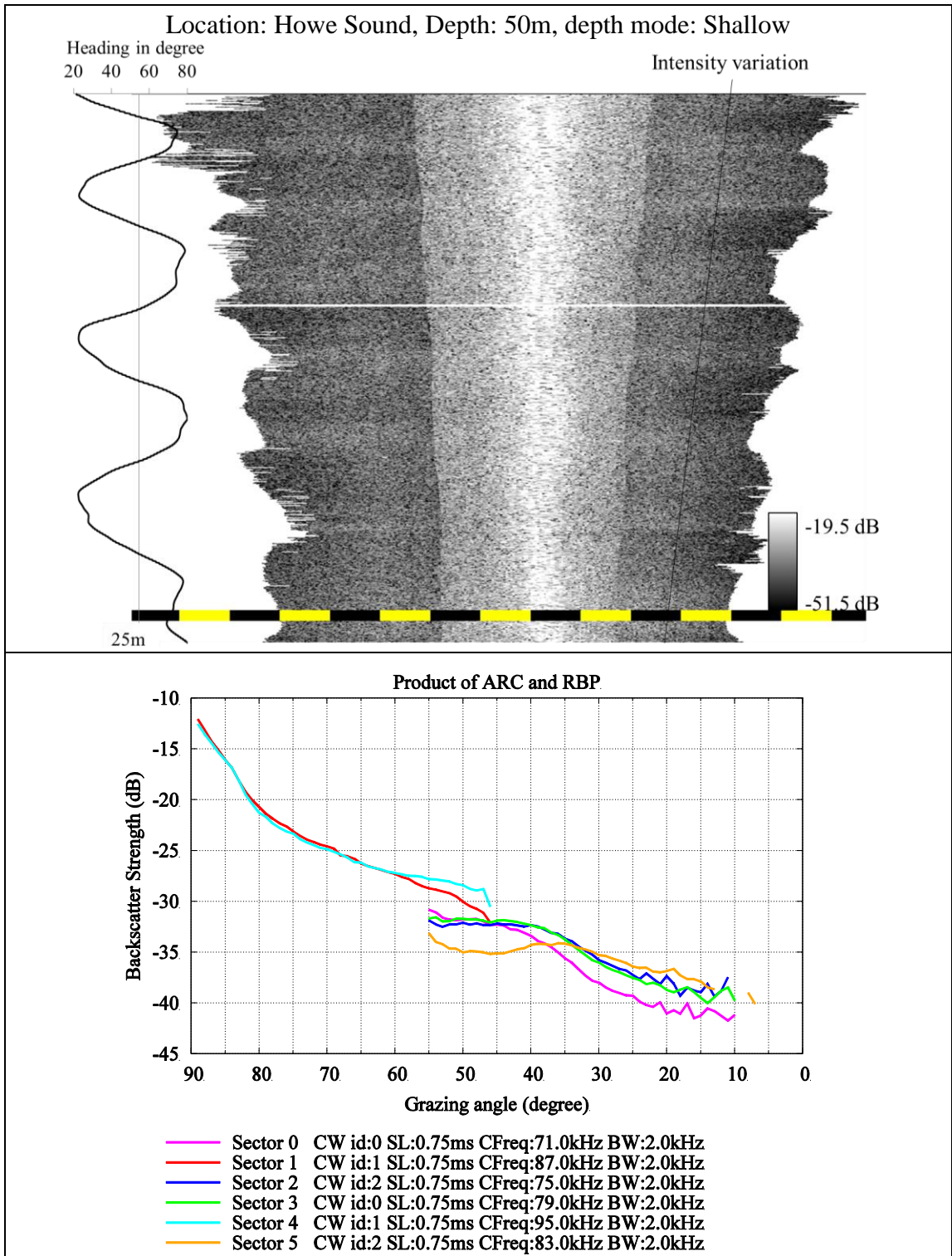
Figure 4.7: TVG-BS-free backscatter intensities with dominant across- and along-track RBP collected in Howe Sound (Squamish) with heavy yawing

93

4.1.3 Data Sorting

This section discusses how and why the data are sorted by different parameters. The first sorting parameter is the sectors. As discussed in Section 3.2, the latest multibeam sonar systems use multiple sectors and multiple swaths and different modes for improving bathymetric accuracies and coverage. The sectors are differentiated from each other by center frequency, pulse length, pulse type, and bandwidth. For example EM 710 can have 3 sectors in one swath, for a total of 6 sectors in dual swath mode. The system can operate in dual swath modes for 4 different depth modes. In the OMG software suite each sector is identified by comparing the above mentioned differentiation parameters and a unique sector number starting from 0 is assigned for all sectors encountered [Teng, 2011]. The algorithm continuously checks each beam of all profiles for any change in the differentiating factors. As discussed in Section 3.1.1 a single element may exhibit different radiometric properties for different frequencies within its bandwidth. The amount of source level put in for each individual sector may also vary. The backscatter data coming from different sectors thus have different RBP and hence sectors are used as the first sorting parameter and all the data are separated under a unique sector number.

Further sorting is then done for each sector considering the SRAs and GRAs related to each sample of backscatter data. As discussed in Section 4.1.1 the data from a specific GRA with different SRAs will be compared during the RBP extraction process. In order to have maximum confidence in the extracted RBP it is important to compute the SRAs and GRAs with maximum possible accuracy. The details discussion on how GRA is

computed and the modifications done in the algorithm during this research are described in Appendix 9.1. The following section describes how SRAs are computed.

4.1.3.1 Computation of SRAs

As stated earlier, the across-track RBP is dominated by the sonar relative across-track Tx RBP. Hence it is important to compute the SRAs at the time of transmission to correctly account for the across-track RBP. The existing OMG algorithm to compute SRAs is based on the simplification (Section 3.5.2) of a straight beam vector from sonar to detected bottom, just adjusted by the roll at the reception. No allowance was made for actual sonar relative steering and it was assumed that there was no significant roll between the transmission and reception. This was adequate as it was never required to compute precise SRAs. Hence a new algorithm is developed to compute across-track SRAs at the Tx at the time of transmission (SRA-T) as a part of this research.
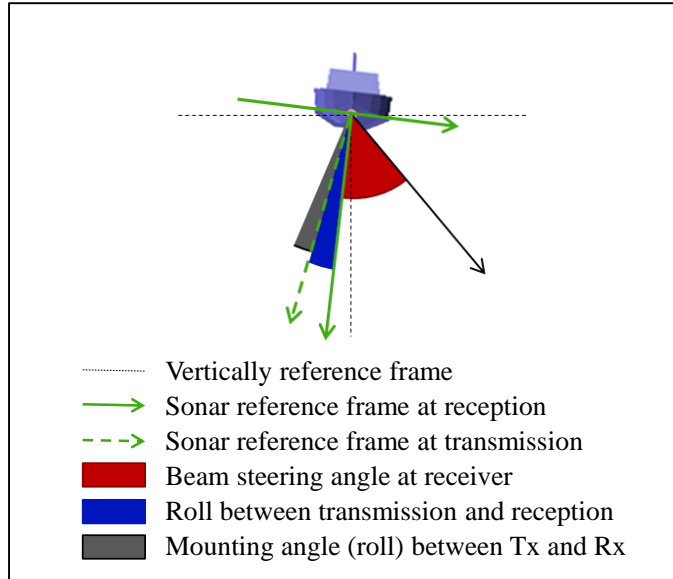
Figure 4.8: Simplified imaging geometry of SRA-T computation

The imaging geometry of computing SRA-T is shown in Figure 4.8 for a single beam pointing angle presented by black continuous line. The algorithm computes SRA-T by adding (considering proper signs) three different angles; first angle is an Rx beam steering angle at the time of reception of the beam shown in red in Figure 4.8, which is read from the raw range and angle 78 telegram. Second angle is the difference between the roll of the ship at the time of transmission and reception (in other words, amount of ship roll between the transmission and reception) shown in blue in Figure 4.8. The third angle is Tx mounting angle (roll) with respect to the ship reference frame shown in gray in Figure 4.8 which is accounted to consider any sonar mounting misalignment.

The challenge is to compute the roll of the ship at the time of the Tx as it is not recorded in any telegram. A linear interpolation is done to compute the roll at the time of Tx by computing the exact time of Tx and using the high frequency motion data. The

exact time of the first transmit sector is computed from the raw range and angle 78 telegram, and then for consecutive sectors within the same swath and the second swath by properly adding the transmit sector offsets stored in the telegram. The exact time of reception for each beam is computed by adding two way travel time to the transmit time. This way of computing SRA-T is unambiguous as it does not use any detected positional information and hence free from refraction problem and works with the same efficiency in shallow and deep waters. The range of computed SRA-Ts is from -90° on port side horizontal to +90° on stbd side horizontal.
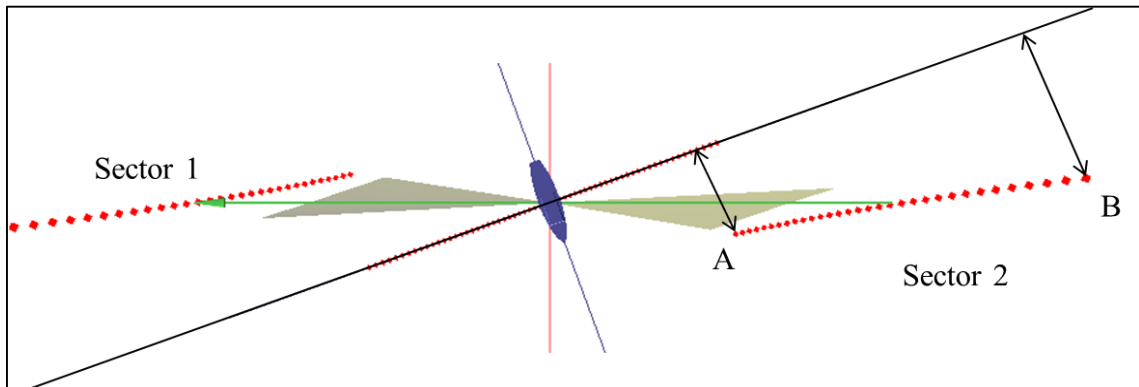
Figure 4.9: Circular projection of detected beams due to steered Tx sectors and Rx beams

In the case of along-track RBP, the RBP is dominated by the along-track Rx RBP and hence it is important to compute the along-track SRA at the Rx at the time of reception (SRA-R). Now the only along-track SRA stored in the telegram is the sector transmit steering angle at the time of transmission for each sector. This angle is a rough approximation of the SRA-R but cannot be directly used for two reasons: 1) the orientation of the ship will be different at the transmission and reception and the magnitude of the difference will depend on the rate of change of orientation and the depth

and, 2) Each beam from a single sector, though steered at same along-track transmit sector steering, gets projected in a circular way about the along-track axis as shown in Figure 4.9 and this complex geometry of the steered beams is not considered. This complex geometry is result of the Tx cone to Rx cone intersection. In Figure 4.9 the along-track distance for the first beam in the outer sector (shown by A) is not equal to the last beam of the same outer sector (shown by B) even though the sector steering is of the same magnitude. More details of this geometry are discussed by Hamilton et al. [2014].
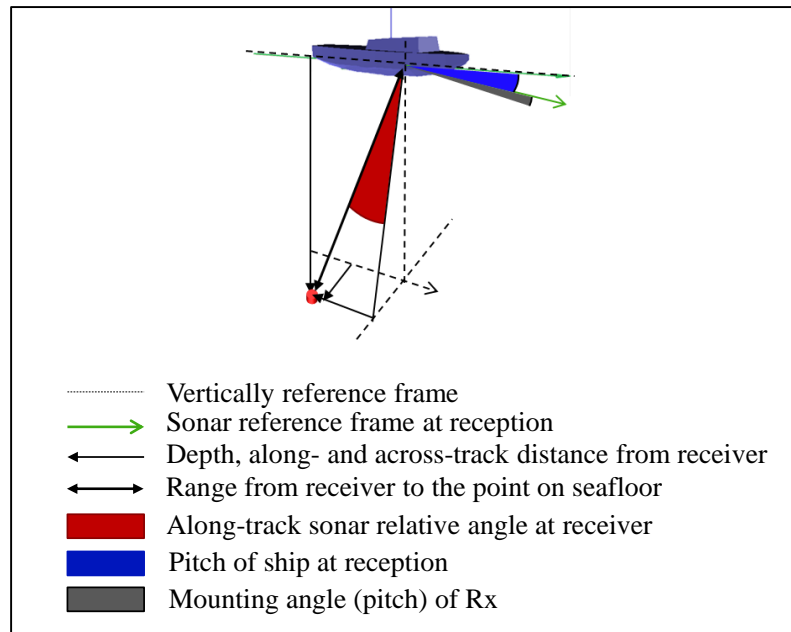
Figure 4.10: Simplified imaging geometry of SRA-R computation

The developed algorithm in this research computes the SRA-R by using positional information (depth, along- and across-track distance). To illustrate this method, a simplified imaging geometry is shown in Figure 4.10. The depth, along- and across-track distances are generally reported relative to the positioning system in the ship reference frame. The algorithm first recalculates the positional information relative to the receiver

accounting for leaver arms and instantaneous orientation. Then a range to the detected depth from the receiver is computed. Next the algorithm computes SRA-R by adding (considering proper sign) three different angles: 1) an inverse tangent trigonometric function of range and along-track distance, shown in red in Figure 4.10, 2) the pitch at the time of reception, shown in blue in Figure 4.10, 3) the along-track Rx mounting angle (pitch) with respect to the ship reference frame shown in grey in Figure 4.10. The pitch at the time of the reception is computed by linear interpolation using the high frequency motion data and the exact time of the reception of the signal. The maximum sector steering in modern multi-sector systems is $\pm 10°$ (positive being steered forward and negative is steered backward). The expected range of computed SRA-Rs is slightly greater than $\pm 10°$.

Once the GRAs, the across-track SRAs at Tx (SRA-Ts), and the along-track SRAs at Rx (SRA-Rs) are computed, backscatter data for each sector are sorted using 1° integer bin of all of GRAs, SRA-Rs and SRA-Ts. The order of sorting is arbitrary and it was chosen to be as shown in Figure 4.11 for computational simplification in the developed algorithm. In the specific case of EM 710 in this research, the entire backscatter data is sorted in 6 bins by sectors, and then backscatter data in each of those 6 bins are sorted by SRA-R into 21 bins. The sorting process continues further as shown in Figure 4.11 considering GRA and then SRA-T. As we shall see this separation of BS data in millions of bins based on the angles is the key to this research.

Step	Parameter	Parameter range	Total number of bins	
				Backscatter data
1	Sector	6 for dual-swath EM 710	6	**Sector**
2	Along-track SRA-R	-10° to +10° (21°)	126 (6*21)	**SRA-R**
3	GRA	Port 0° to stbd 0° (181°)	22,806 (126*181)	**GRA**
4	Across-track SRA-T	-90° to +90° (181°)	4,127,886 (22806*181)	**SRA-T**
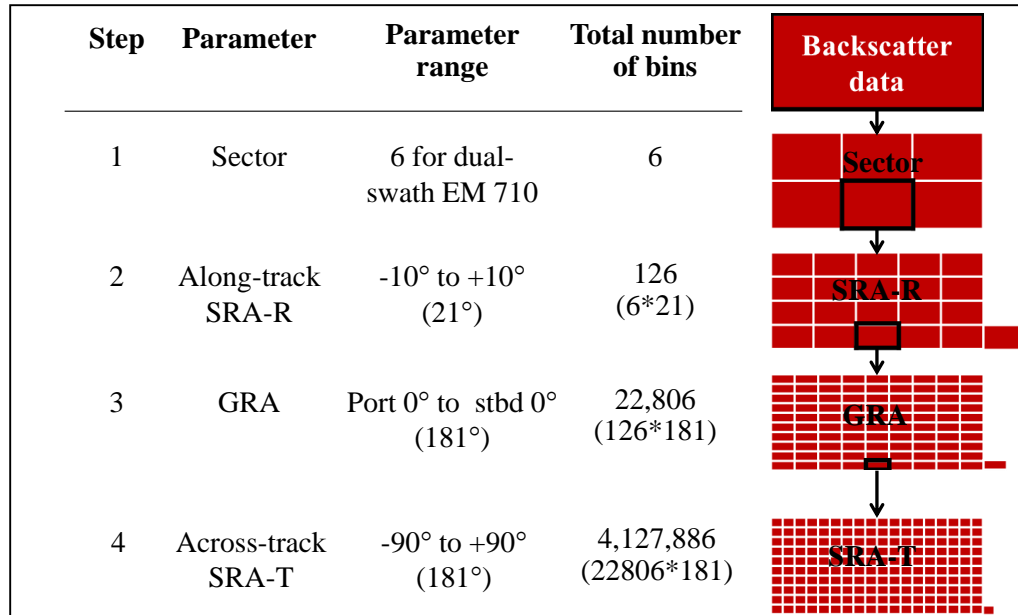
Figure 4.11: Summary of backscatter data sorting

4.1.4 Backscatter Data Handling and Outlier Removal

The actual received intensities (linear values, specifically voltages or pressure fluctuations) are never reported to the user in any telegram. The reported intensities are in dB as they are already reduced using an arbitrary SL and Rx sensitivity and hence can only be adjusted in a relative framework. The intensities in dB are converted back into relative linear intensities (RLI), relative to the unknown arbitrary reference. All the RLI that fall under a single SRA-T are then checked for any unexpected values (outliers) that are too small or large compared to the average value. The outliers can be due to many reasons such as random noise, system noise, spikes, etc. (this research does not look into the details of the cause of noise). However, they are identified and excluded as they can

distort the RBP calculations and also cause higher standard deviation (SD). All the RLIs in each SRA-T bin are checked for outliers.

Figure 4.12 shows the RLI distribution of backscatter intensities that falls in the bin under sector 5, SRA-R of 0°, GRA of +60° (port), and SRA-T of +65°. The distribution of backscatter intensities is assumed to be Rayleigh distributed [Lurton, 2002]. The histogram shows number of samples that fall in the bin size of 0.00001. During the experiment it was found that few intensities near the tail of the distribution induces biases and higher SD on the final extracted RBP, hence these randomly higher intensities were eliminated. The initial average of RLI values is computed and all the values that are higher or lower than two times the SD from the average value are removed and the average is recalculated. If the lower cutoff limit falls below zero, then it was considered to be 0.0 as the RLI cannot be negative. In the particular example shown in Figure 4.12, out of 3676 samples 348 samples (≈ 10%) were rejected. The final RLI average and SD are then stored for each across-track SRA-T for further computation.
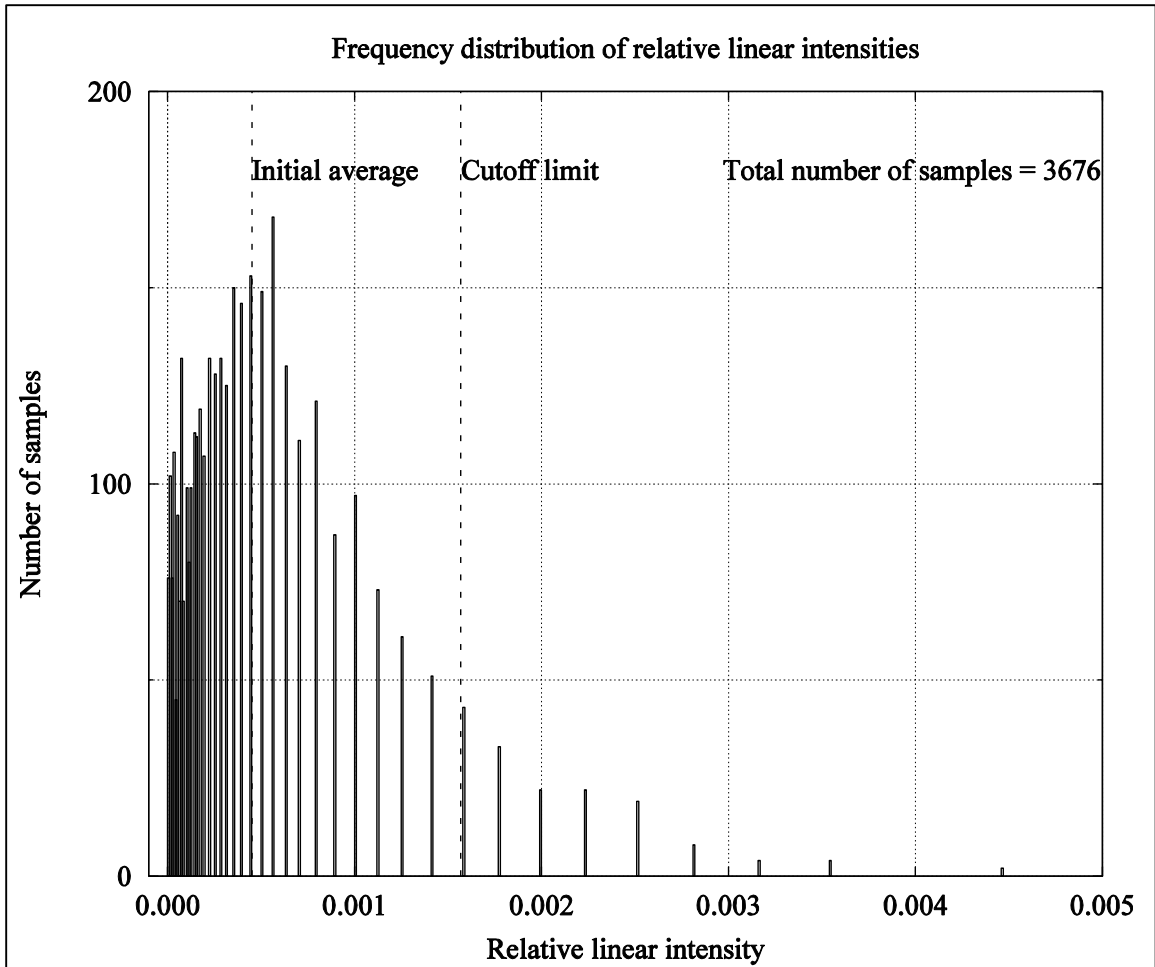
Figure 4.12: Histogram showing distribution of RLIs at across-track SRA-T +65°

4.2　Extraction of Radiometric Beam Pattern

Once all the required preprocessing on the backscatter data is done the process continues to follow the core methodology of this research for extraction of RBP. The complete RBP is extracted in two components: first the across-track RBP and then the along-track RBP is extracted.

To better explain the computation of across- and along-track RBP an example dataset is used. The RBP extraction process is explained using the intermediate results for the example dataset which was collected in April 2015 near the Squamish River Delta at 50m water depth. EM 710 in Very Shallow mode was used to collect the backscatter data.

4.2.1 Extracting Across-Track RBP

This section is divided into 6 sub-sections. The first describes how a specific test data was collected for the extraction of across-track RBP. Sub-sections 2 to 5 describe four major steps to extract across-track RBP. The last sub-section describes how the extracted across-track RBP is applied to the backscatter data to obtain the final results.

4.2.1.1 Data Collection Strategy for Across-Track RBP Extraction

The data that are required to extract the across-track RBP are collected by changing SRA-T at a specific GRA by deliberately rolling the vessel and maintaining minimum yaw. As the vessel rolls, a specific GRA on a homogeneous test site is illuminated by different across-track SRA-Ts. A simplified imaging geometry for a single sector system is shown in Figure 4.13.
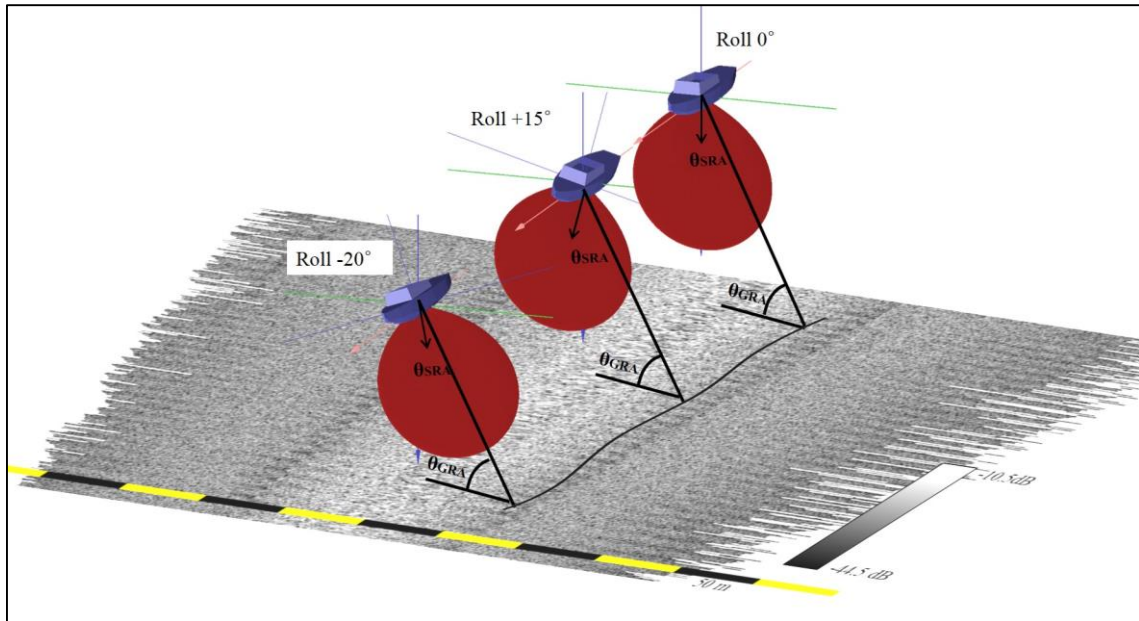
Figure 4.13: Simplified imaging geometry for the data collection

Any across-track variations in the received intensities due to rolling of the vessel are solely accounted for by corresponding variations in the across-track RBP. Figure 4.14 shows the actual reported backscatter intensities for one of survey line from the example dataset. The intensity variation along the drawn line can be clearly seen. The across-track RBPs are relative to across-track SRA-T so their effect is proportional to the roll of the ship; which creates the alternate strong and weak backscatter intensities along-track as the ship moves forward while rolling. The manufacturer-applied across-track RBP corrections (from Bscorr file) explained in section 2.4 were applied during the example data collection. Even with the application of the corrections, the along-track alternate pattern and the across-track intensity variations at the sector boundaries are visible, indicating insufficient corrections.
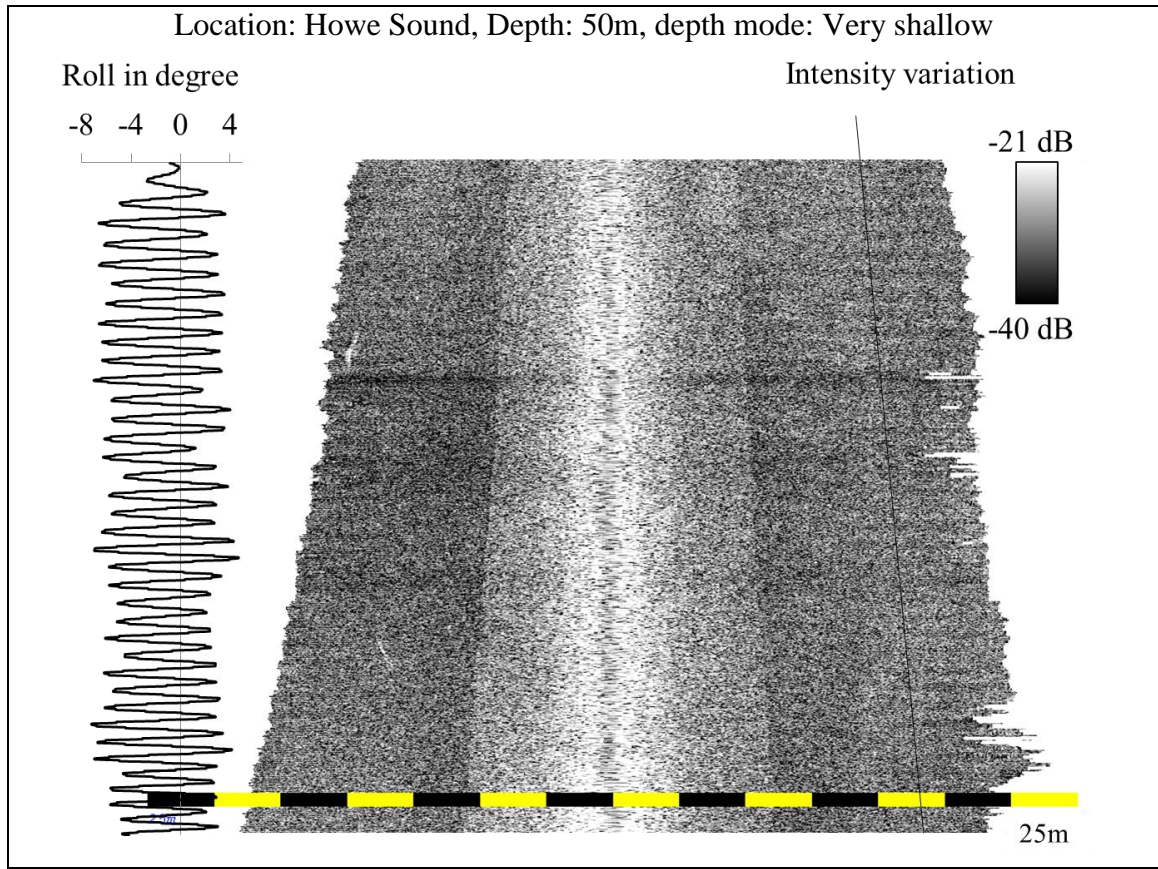
Figure 4.14: Showing received intensities for across-track RBP extraction from one of the test survey lines

Once these specific test data were collected, the 1st step in preprocessing was done by removing manufacturer-applied TVG-BS and correcting for geometric effects. There are no significant geometric effects seen in the original backscatter image shown in Figure 4.14 as the selected test site did not have any sudden geometric changes. Figure 4.15 shows the TVG-BS-free backscatter intensities; the along-track intensity variation along the drawn line is still visible in Figure 4.15.

105
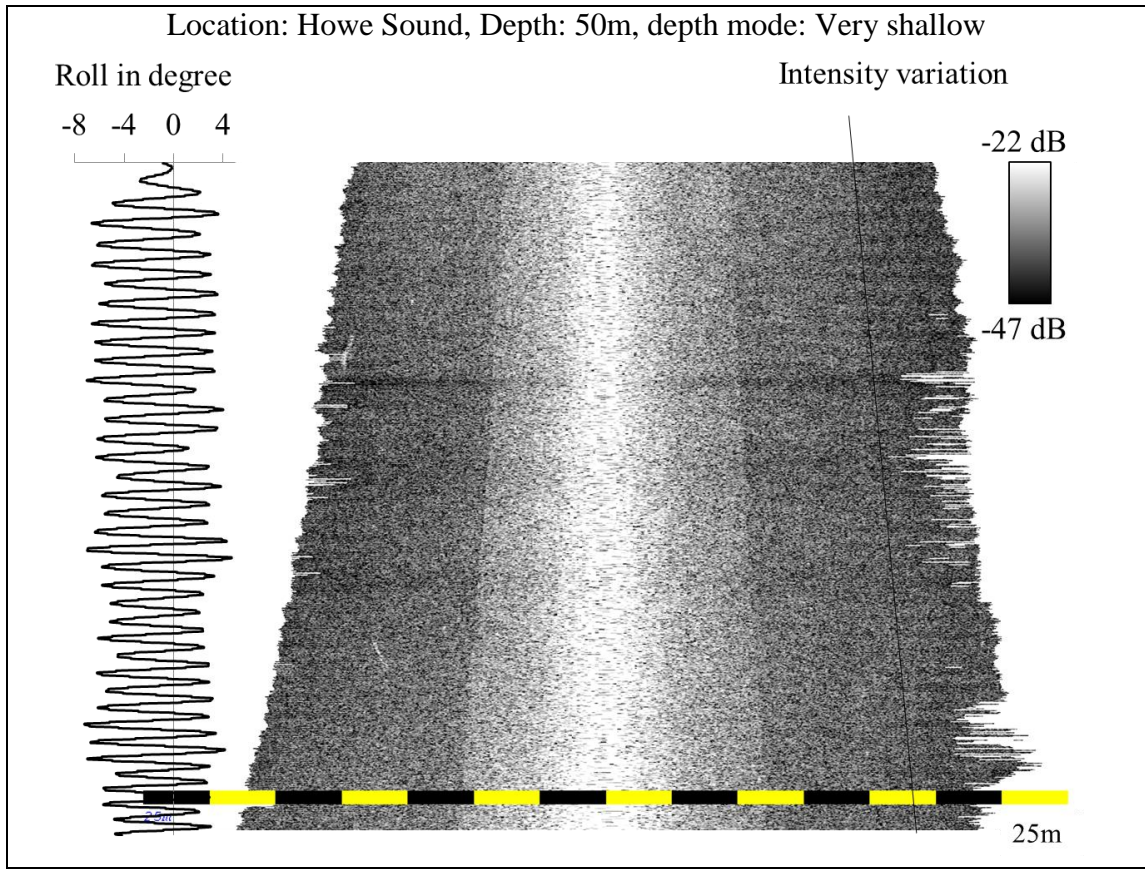
Figure 4.15: TVG-BS and geometric effect free backscatter intensities

Figure 4.16 shows the backscatter strength curves which are products of actual ARC and across-track RBP. The aim of this research is to unambiguously separate the RBP (along and across) from the product of ARC and RBP in order to obtain true ARC.
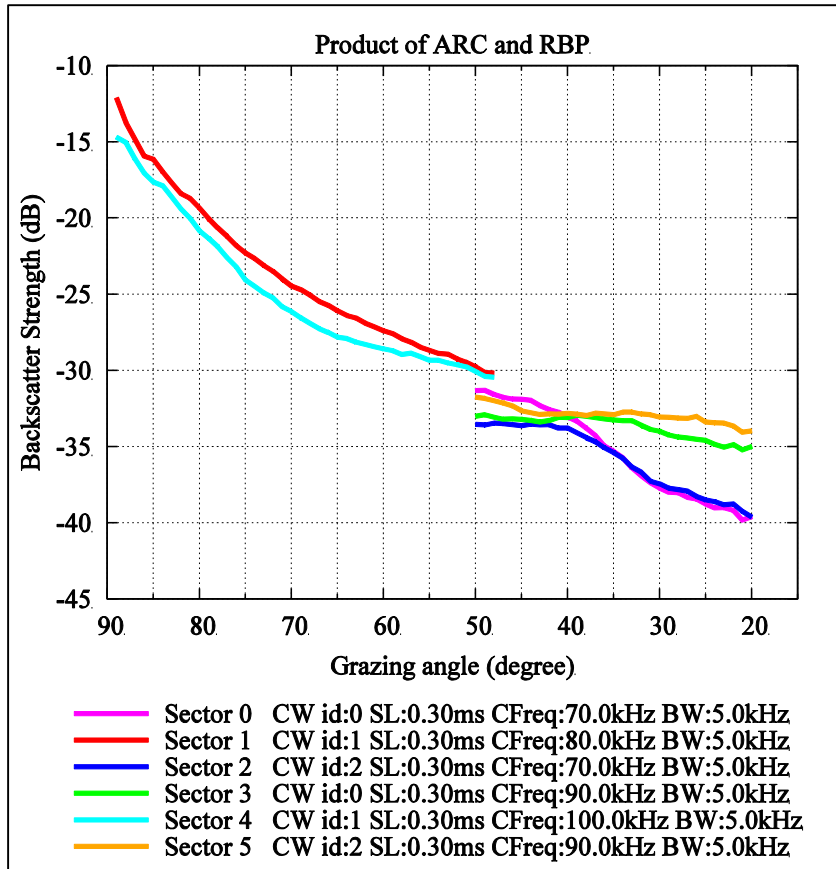
Figure 4.16: Backscatter strength curves showing product of RBP and ARC for the test dataset

Once the geometric effect and TVG-BS are removed, the backscatter data (each sample for all snippets) are sorted into different bins and outlier backscatter samples are removed as explained in Section 4.1.4. The extraction of across-track RBP is divided into three major steps as follows,

1) Extracting across-track RBP sub-functions at each across-track SRA-T.

2) Stacking the extracted across-track RBP sub-functions to get the across-track RBP functions (one for each sector).

107

3) Adjusting the across-track RBP functions with respect to the chosen reference SRA-T to obtain final across-track RBP master function for entire single or dual swath.

Figure 4.17 shows the overall workflow of across-track RBP extraction process.

```
┌─────────────────────────────────┐
│    Strategic data collection    │
└─────────────────────────────────┘
                 ↓
┌─────────────────────────────────┐
│    Preprocess backscatter data  │
└─────────────────────────────────┘
                 ↓
┌──────────────────────────────────────────┐
│ Extract across-track RBP sub-functions at each SRA-T │
└──────────────────────────────────────────┘
                 ↓
┌──────────────────────────────────────────┐
│ Compute across-track RBP functions for each sector │
└──────────────────────────────────────────┘
                 ↓
┌────────────────────────────────────────────────────┐
│ Compute across-track RBP master-function for entire imaging coverage │
└────────────────────────────────────────────────────┘
```
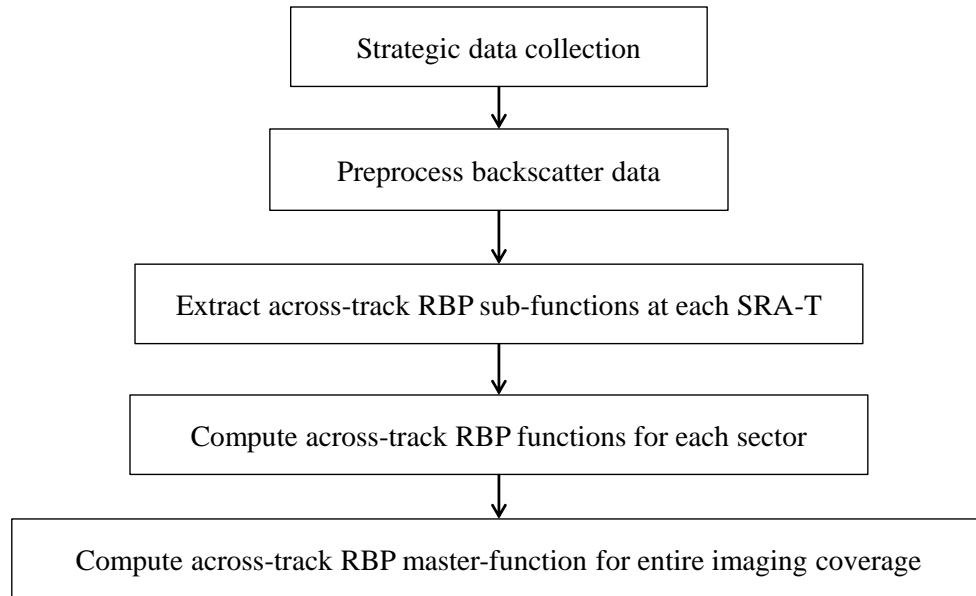
Figure 4.17: Workflow for across-track RBP extraction

4.2.1.2 Extracting Across-Track RBP Sub-Functions at each SRA-T

In order to compute the across-track RBP sub-function at SRA-T -60° (sector 0) as shown in Table 4.1, the RLI at SRA-T -60° is taken as reference and the intensities from all other SRA-Ts (from -73° to -54°) that have a GRA of 30° at the seafloor are used. The selection of the reference is arbitrary as, at this point, the aim is to find the relative across-track RBP sub-function. The shape of the variation sub-function or the ratios of

the intensities relative to each other will remain the same irrespective of the reference chosen.

Next the variations of RLI around a chosen reference SRA-T are computed by comparing the intensities from neighboring SRA-Ts (from -73° to -54°) that have the same GRA (30°). Table 4.1 presents sample data for sector 0, along-track SRA-R of 0°, GRA 30°, and across-track SRA-T ranging from -73° to -54°. This dataset is used to compute the across-track RBP sub-function around SRA-T -60°. The intensity at GRA 30° and across-track SRA-T of -60° is assumed as reference (ratio=1.0). The average RLI for all the other SRA-Ts is divided by intensity at the SRA-T -60°. The derived ratios in column 5 of Table 4.1 are the intensity variations (multipliers) around SRA-T -60° referenced at SRA-T -60°. The propagated uncertainties in the RLI ratios of the computed sub-function are shown in column 6 of Table 4.1. The details about the SD propagation are given in Appendix 9.2.

Table 4.1: Across-track RBP sub-function extraction
at SRA-T -60° referenced at SRA-T -60°

GRA (degrees)	Across-track SRA-T (degrees)	Average RLI*10^4	Uncertainty in RLI*10^4	Across-track RBP sub-function (ratios) at SRA-T -60°	Propagated uncertainty in sub-function
30	-73	0.65	0.34	0.38	0.28
30	-72	1.16	0.61	0.69	0.51
30	-71	0.81	0.43	0.48	0.35
30	-70	0.74	0.39	0.43	0.32
30	-69	1.00	0.52	0.59	0.44
30	-68	1.12	0.59	0.66	0.49
30	-67	1.03	0.54	0.61	0.45
30	-66	1.10	0.57	0.65	0.48
30	-65	1.21	0.64	0.72	0.53
30	-64	1.25	0.65	0.74	0.54
30	-63	1.41	0.74	0.83	0.61
30	-62	1.40	0.73	0.82	0.61
30	-61	1.56	0.82	0.92	0.68
30	-60	1.70	0.89	1.00	0.74
30	-59	1.80	0.94	1.06	0.78
30	-58	2.02	1.06	1.19	0.88
30	-57	2.34	1.22	1.38	1.02
30	-56	2.51	1.31	1.48	1.09
30	-55	3.64	1.90	2.14	1.58
30	-54	2.40	1.26	1.42	1.05

This process is repeated for every possible SRA-T in all sectors. Figure 4.18 shows the across-track RBP sub-functions extracted for a few SRA-Ts.
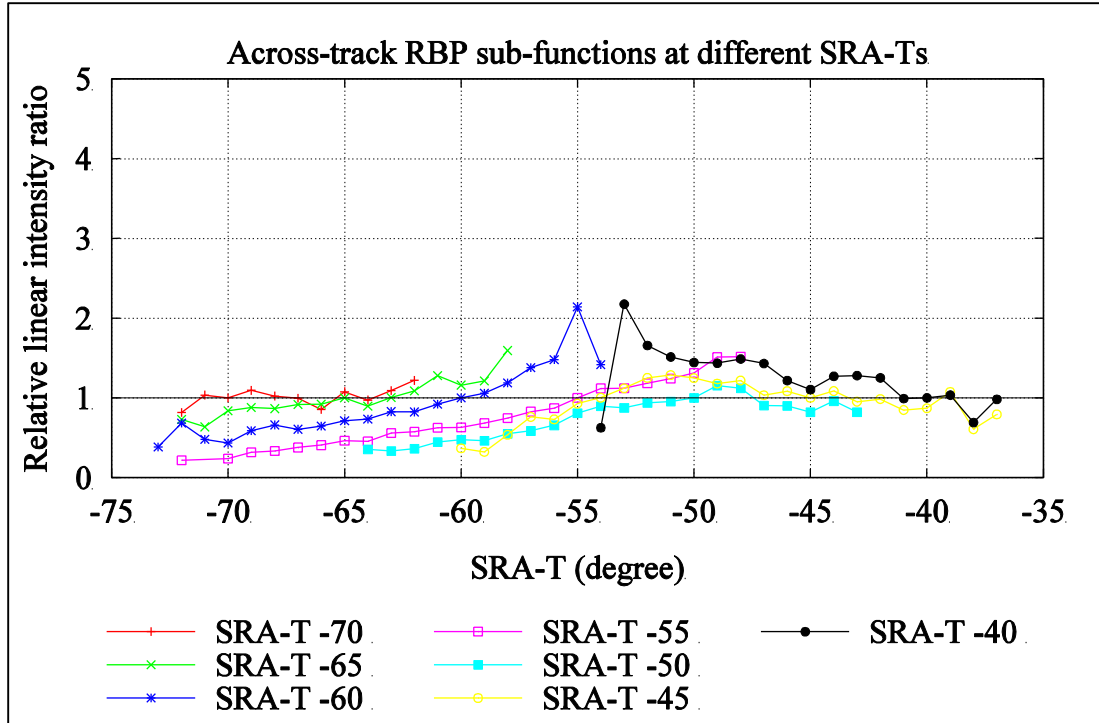
Figure 4.18: Few across-track RBP sub-functions from sector 0 with individual reference SRA-T. The ratio at the reference is 1.

4.2.1.3 Computing Across-Track RBP Function for each Sector

The extracted across-track RBP sub-functions for each SRA-T in the previous step have overlap between adjacent SRA-Ts as seen in Figure 4.18. This overlap is used to compute the across-track RBP function for the entire sector. The extent of overlap depends on the amount of rolling performed during data collection. As the vessel rolls the GRAs that are close to the middle of sector is illuminated by a number of SRA-Ts limited primarily by the magnitude of rolling. However for the GRAs those are close to the sector boundaries, the illumination by number of SRA-Ts is limited by the actual transmit sector

111

boundary, which normally exceeds the system reported sector boundary by a few degrees. As a result, the overlap is maximum at the middle of the sector and it decreases towards the sector boundaries. For example, the overlap between the across-track RBP extracted at SRA-T -60° and -59° is about 15° as a result of ±6.5° of roll during data collection. Detailed analysis is presented in Section 5.2 to discuss the effect of different magnitudes of roll on the developed method.

In order to compute the across-track RBP function for a single sector, the sub-functions are stacked with respect to a single reference for each sector. This stacking process is divided into the following three steps.

1) Choosing the reference sub-function for each sector.
2) Stacking all the sub-functions for each sector.
3) Averaging sub-function values at each SRA-T to get the across-track RBP function for each sector referenced to its respective reference sub-function.

1) Choosing the reference sub-function for a sector

During the stacking process, the individually referenced across-track RBP sub-functions will be stacked to relate all sub-functions to a single reference sub-function. In the developmental stage of the research, this reference sub-function was arbitrarily chosen to be at the SRA-T that has maximum number of samples. The stacking process is carried out from the reference sub-function to end of sectors in port and stbd direction. As shown in Figure 4.19, low number of samples close to nadir compared to port and stbd

sides of the central sectors decreases the confidence in the stacking process. Hence all the central sectors (two for dual swath system) are divided into two sub-sectors (port and stbd) and treated independently for all further steps.
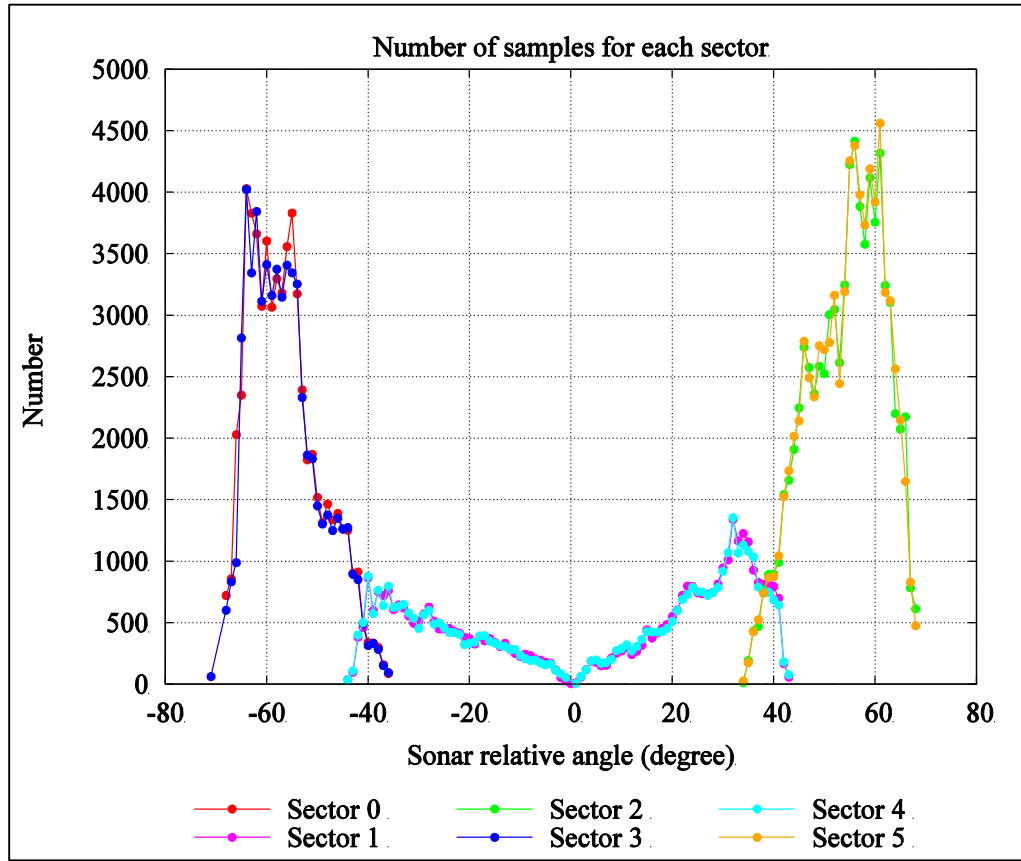
Figure 4.19: Sector-specific number of samples after sorting the backscatter data

The arbitrarily chosen reference sub-function (SRA-T value) in this step should not affect the final shape of the across-track RBP function. The reference only defines SRA-T that will have no change in intensities by having RLI variation ratio equal to 1. Later a detailed analysis (as discussed in section 5.1) is carried out to test the effect of the selection of the reference sub-function on the final across-track RBP function and master function. Table 4.2 shows the chosen references for the sample dataset.

113

Table 4.2: Chosen reference sub-functions (SRA-T) for each sector

Sector	Reference sub-function SRA-T	Side
0	-63°	port
1.0 (port sub-sector of sector 1)	-40°	port
1.1 (stbd sub-sector of sector 1)	35°	stbd
2	56°	stbd
3	-50°	port
4.0 (port sub-sector of sector 4)	-40°	port
4.1 (stbd sub-sector of sector 4)	34°	stbd
5	56°	stbd

Figure 4.20 shows the chosen reference sub-function in dark blue along with the few sub-functions previously shown in Figure 4.18.
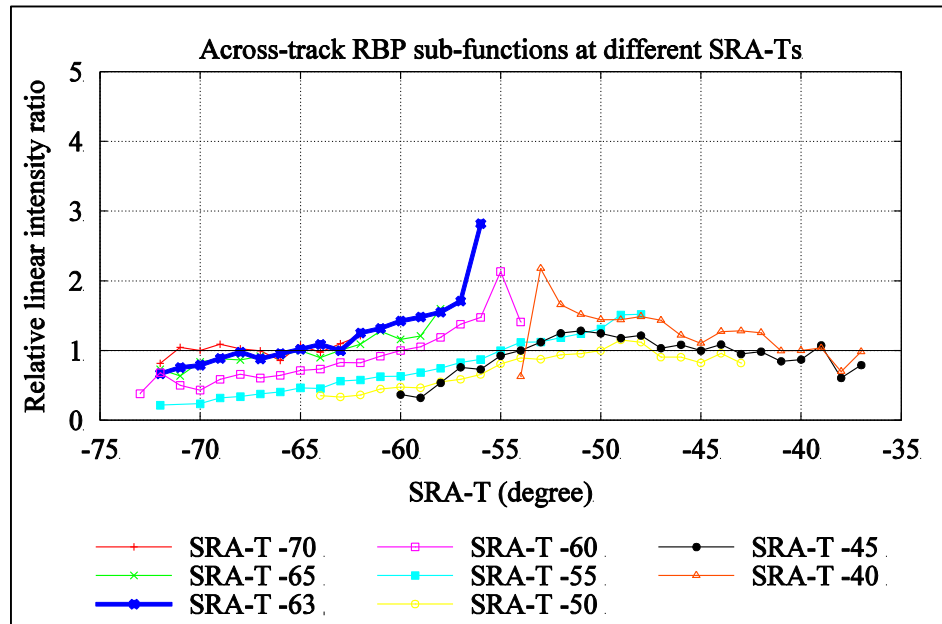
Figure 4.20: Across-track RBP sub-functions with chosen reference sub-function at SRA-T -63° for sector 0 of example dataset

2) Stacking the sub-functions for each sector

The stacking process for all the sectors (8 in total) is done in four loops. In the first loop, the adjacent sub-functions are stacked starting from reference sub-function and going towards the SRA-T -90° for all the port sectors. In the second loop, for the same port sectors, the adjacent sub-functions are stacked from reference sub-function to the nadir (0°), completing the stacking process of port side sectors. The 3rd and 4th loop do the stacking in the same way for stbd sectors.

In the stacking process common SRA-Ts from adjacent sub-functions are compared. As a result of vessel roll during the data collection each adjacent sub-function will have a range of SRA-Ts and hence for a subset of their range, they will share a common range of SRA-Ts as shown in Figures 4.18 and 4.20. At the beginning, the common range of SRA-Ts between the reference sub-function and its adjacent sub-function (ports or stbd depending on the loop) is compared. The comparison yields an offset and propagated SD for each SRA-T within the common range. A single offset along with its SD between the sub-functions is then computed by averaging offsets from the entire common range of SRA-Ts after removing any outliers. The computed average offset is used to shift the sub-function under consideration, so as to be referenced with the reference sub-function. During shifting of the sub-function, the SDs of the sub-function are updated considering the SD of the computed offset. Then, that shifted sub-function is compared to its adjacent sub-function to compute the average offset and its SD for sub-function under consideration. The process continues till the last sub-function is referenced with the

115

reference sub-function. As computation of each offset builds on the previous referenced sub-function, starting at the reference, the whole sector now has a common reference and concludes the stacking process for that sector. As the SDs are propagated during the stacking reference, the confidence in the iteratively stacked RBP function can be assessed.

The stacking process is explained between the reference sub-function at SRA-T -63° and sub-function at SRA-T -64° in Figure 4.21, Tables 4.3 and 4.4. In Figure 4.21 the black arrows indicate the single offset (column 4 Table 4.3) between each common SRA-T (from -72° to -56°) indicating the differences in the RLI ratios. The red sub-function referenced at SRA-T -64° is shifted by the computed single average offset (column 5 of Table 4.3) and referenced wrt sub-function at SRA-T -63° and shown in dark red (column 6 of Table 4.3).
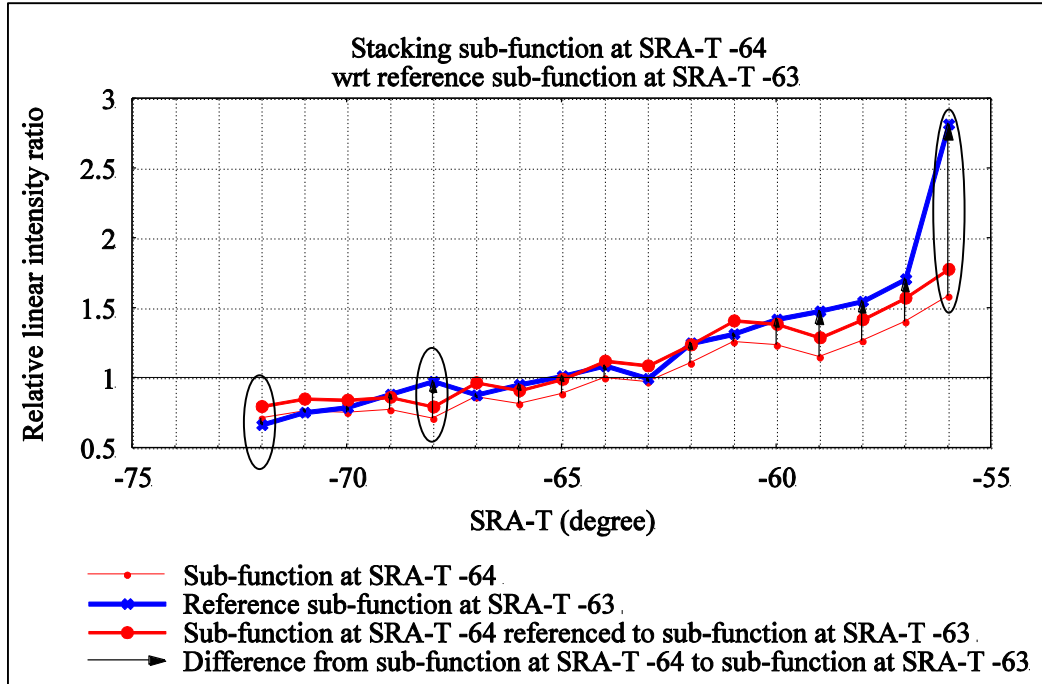
Figure 4.21: Stacking process for sub-function at SRA-T -64° wrt sub-function at SRA-T -63°. Circled values were detected as outliers

The initial average offset is computed and all the offsets that are higher or lower than two times the SD from the average offset are neglected (strike through offsets in Table 4.3) and then final average offset (column 5 of Table 4.3) is computed. Table 4.4 illustrates the propagation of SD during this stacking process. The details of the statistical processes used are summarized in Appendix 9.2. Each sub-function has related SDs that contributes to the final SD of the average offset. As the sub-function is shifted, its SDs are propagated considering the SD of the computed offset. As the computation of each successive offset and stacking process builds on the previously referenced sub-function, starting at the reference, the SDs are also propagated accordingly.

Table 4.3: Stacking of sub-function at SRA-T -64° wrt sub-function at SRA-T -63°

Common SRA-T	RLIs (ratio) of reference sub-function* 10^4 (SRA-T -63°)	RLIs (ratio) of port adjacent sub-function * 10^4 (SRA-T -64°)	Offsets	average offset	RLIs (ratio) of stacked SRA-T -64° sub-function ref to SRA-T -63°
-72	0.67	0.71	0.94		0.80
-71	0.79	0.76	1.00		0.86
-70	0.79	0.75	1.05		0.85
-69	0.89	0.77	1.15		0.87
-68	0.98	0.71	1.38		0.80
-67	0.88	0.86	1.02		0.97
-66	0.96	0.81	1.18		0.92
-65	1.02	0.89	1.15		1.00
-64	1.09	1.00	1.09	1.13	1.13
-63	1.00	0.97	1.03		1.09
-62	1.25	1.11	1.14		1.24
-61	1.32	1.26	1.05		1.42
-60	1.43	1.24	1.15		1.39
-59	1.48	1.15	1.29		1.29
-58	1.55	1.27	1.23		1.42
-57	1.71	1.40	1.22		1.58
-56	2.82	1.58	1.78		1.78

Table 4.4: Propagation of SD during stacking of sub-function at SRA-T -64° wrt sub-function at SRA-T -63°

Common SRA-T	SDs of reference sub-function (SRA-T -63°)	SDs of port adjacent sub-function (SRA-T -64°)	SDs of offsets	SD of average offset	SDs of stacked SRA-T -64° sub-function ref to SRA-T -63°
-72	0.50	0.53	~~0.98~~		0.63
-71	0.56	0.56	1.04		0.68
-70	0.59	0.56	1.10		0.67
-69	0.66	0.57	1.20		0.69
-68	0.72	0.52	~~1.44~~		0.63
-67	0.65	0.64	1.07		0.77
-66	0.71	0.60	1.23		0.72
-65	0.75	0.65	1.20		0.79
-64	0.81	0.74	1.14	0.36	0.89
-63	0.74	0.72	1.08		0.86
-62	0.93	0.82	1.19		0.98
-61	0.98	0.93	1.10		1.12
-60	1.05	0.91	1.21		1.10
-59	1.10	0.85	1.35		1.02
-58	1.15	0.94	1.28		1.13
-57	1.27	1.04	1.28		1.25
-56	2.09	1.17	~~1.86~~		1.41

It should be noted that this process is done for adjacent sub-functions at SRA-T for each 1° bin and Figure 4.22 shows the computed average offsets between adjacent sub-functions and their SD. The relative standard deviation (RSD) of the offset is the ratio of the SD and the offset. RSD is used to enable direct comparison with other offsets and their SD.
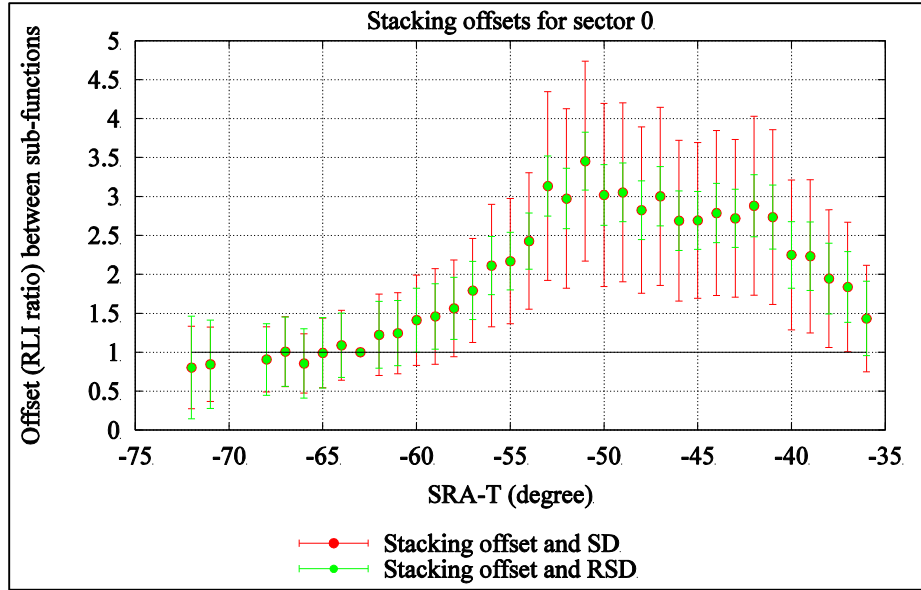
Figure 4.22: Stacking offsets and their SDs for all sub-functions of sector 0

The individually referenced sub-functions shown in Figure 4.20 are referenced to the common reference sub-function at SRA-T -63° after the stacking process (see Figure 4.23), compared to Figure 4.20.
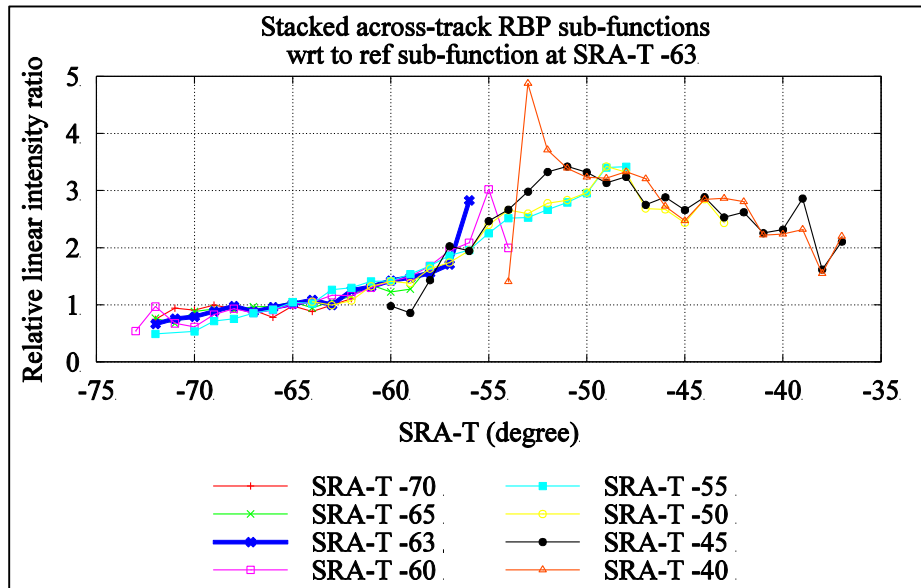
Figure 4.23: Few of the stacked sub-functions from sector 0

Figure 4.24 shows all the across-track RBP sub-functions after stacking for the sector. This stacking process is repeated for all the sectors of entire swaths.
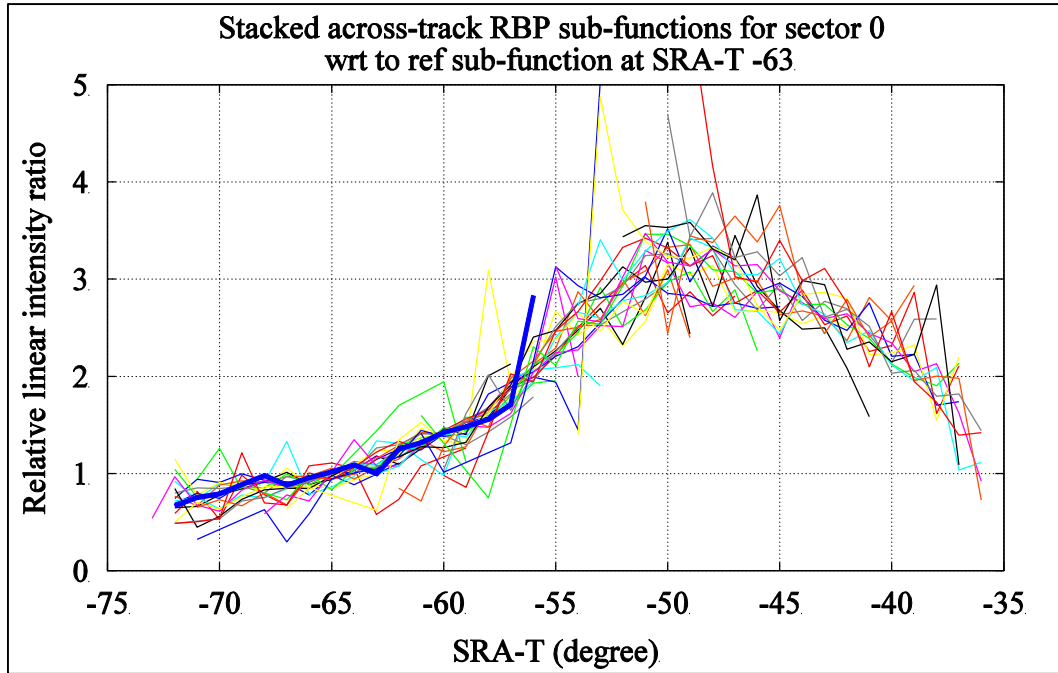
Figure 4.24: Stacked sub-functions for entire sector 0 wrt reference sub-function at SRA-T -63° shown in dark blue

3) Computing average across-track RBP function for each sector

Once the stacking is done, the next step is to arrive at the single value of RLI variation ratio (across-track RBP function) at any given SRA-T. After the stacking process, there are multiple sub-functions that contribute to the single SRA-T due to the overlap. For example in Figure 4.24, at SRA-T -63° there are multiple RLI variation ratio values. In this step, all those values and their SDs are considered for averaging. The initial average value is computed and all the values that are higher or lower than two times the SD from the average offset are neglected. The final average value is then

121

computed using qualified values and their SD is also computed accordingly. Use of SDs as weights during the averaging process is particularly avoided in this research for the reason specified in Appendix 9.2. Figure 4.25 shows the computed average across-track RBP function for sector 0.
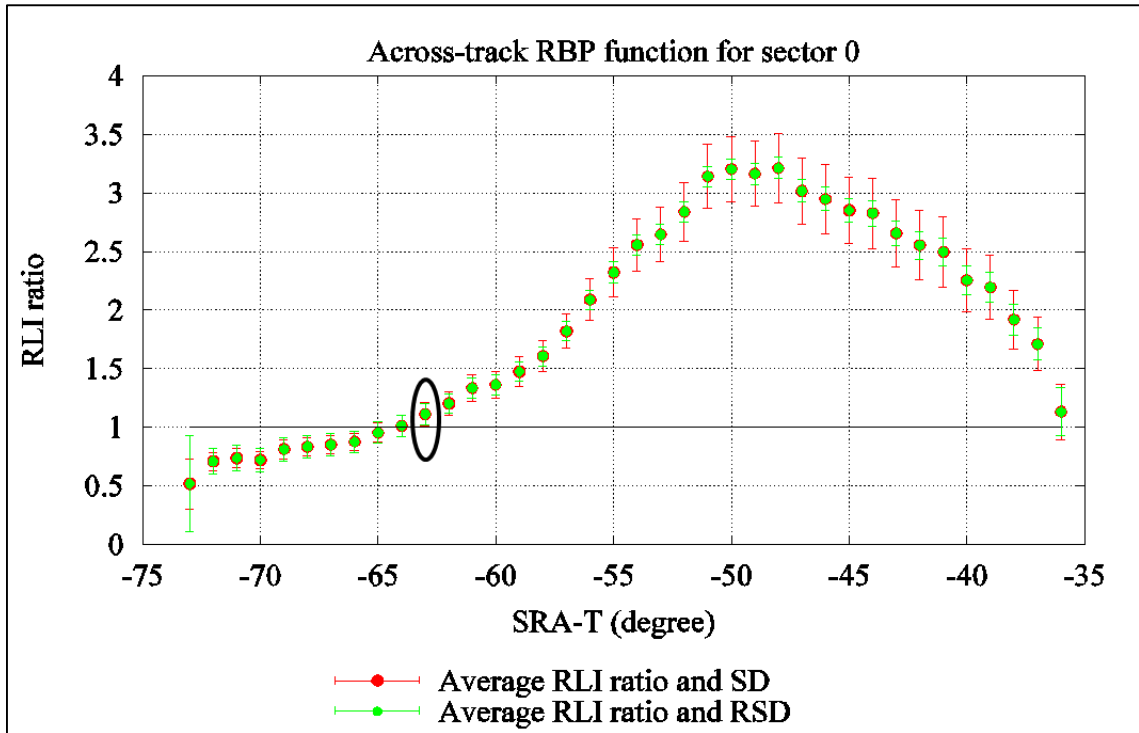
Figure 4.25: Computation of average across-track RBP function for sector 0

During the averaging process it is possible to have the reference deviate from the ratio of 1.0 as a result of averaging. In Figure 4.25 the averaged RLI ratio at reference SRA-T (circled) is slightly higher than 1.0. This averaging process is continued for all the sectors and Figures 4.26 and 4.27 show the average across-track RBP functions for swath 0 and 1 respectively. These across-track RBP functions are referenced to individual SRA-T for each sector, and the average RLI ratio value at the references are close to 1.0.
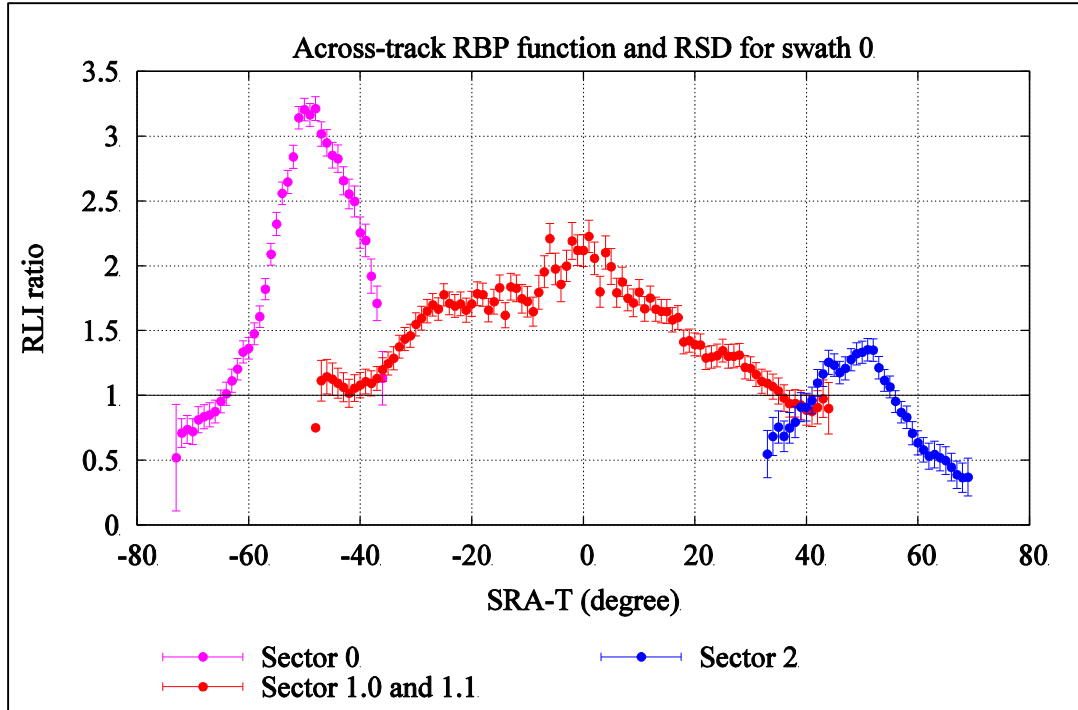
Figure 4.26: Average Across-track RBP function for all sectors in swath 0 referenced to respective sector-specific SRA-T
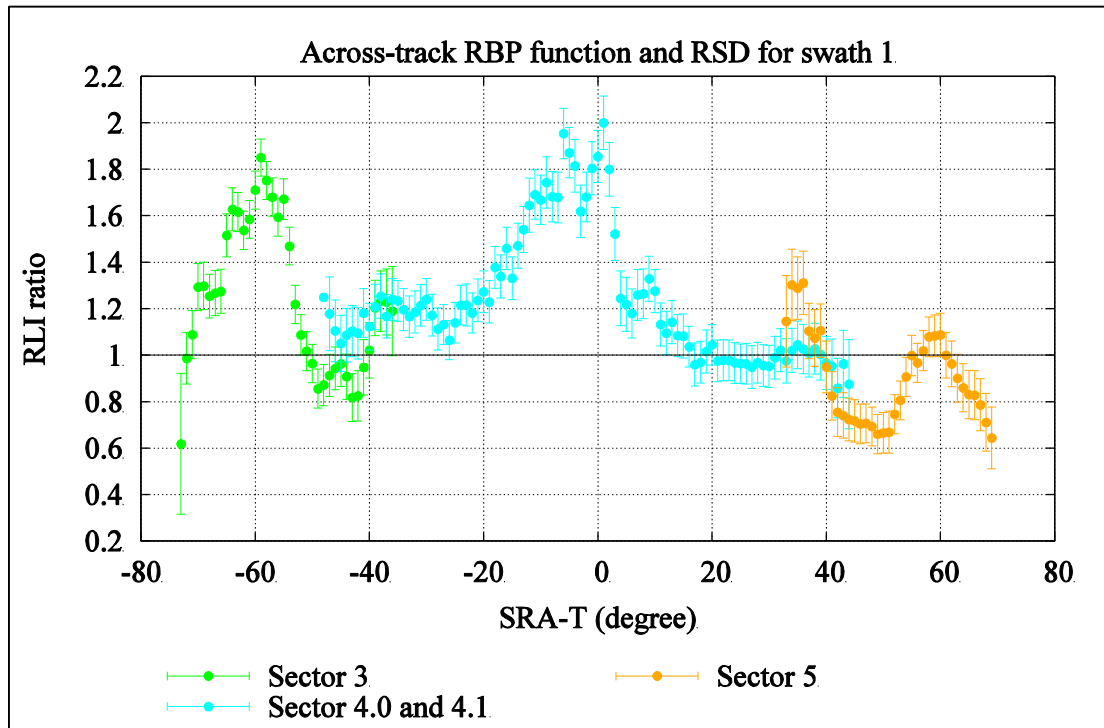
Figure 4.27: Average across-track RBP function for all sectors in swath 1 referenced to respective sector-specific SRA-T

123

The extracted across-track RBP functions shown in Figures 4.26 and 4.27 are the final sector-specific across-track RBP functions between the adjacent SRA-Ts for each sector. The shape of these curves should remain the same irrespective of the reference chosen within the sector (as shown in Section 5.1). The next step is to correlate these sector-specific functions with each other and obtain the across-track RBP master function valid for an entire profile.

4.2.1.4 Computing Across-Track RBP Master Function for the Entire Imaging Coverage

In order to eliminate the intensity offsets due to source level differences between different sectors, the across-track RBP functions need to be associated with a common reference for the entire imaging coverage (2 swaths, each with 3 sectors). To establish an inter-sector and inter-swath association, the fundamental principle explained in Section 4.1 is used. The intensities at the same GRA from different sectors and swaths should be the same for a homogeneous seafloor. Although different sectors operate at different center frequencies and the seafloor response for different frequencies is slightly different, for this research the response from limited common GRAs from different sectors is assumed to have similar return intensities. The effect of this assumption depends on differences in the frequencies used and the response for them from different seafloor types. The effect of this assumption is tested in detail in Section 6.2.

The computation of the across-track RBP master function for the entire profile is divided into the following steps

1) Computing the average modified relative linear intensities (MRLI) using the across-track RBP function.

2) Computing an offset by comparing average MRLI at the same GRAs from different sectors.

3) Adjusting the sector-specific across-track RBP functions using computed offsets and obtaining the final across-track RBP master function for the entire imaging coverage.

1) Computing the average MRLI using across-track RBP function derived for each sector

The extracted sector-specific across-track RBP functions are used to correct the RLIs and to obtain MRLIs for each SRA-T of each sector. The initial RLIs are corrected by the across-track RBP function value at given SRA-Ts to obtain MRLIs. This is done by multiplying the average RLI for each across-track SRA-T bin by the across-track RBP function value for the respective SRA-T (from the same sector). As the MRLIs are corrected for across-track RBP function, at a given GRA all SRA-Ts have identical MRLIs and any across-track variation by GRA can be assumed as true angular variation (ARC). Figure 4.28 shows the initial RLIs and MRLIs for sector 0. Bunching up of MRLIs suggests the successful removal of the across-track RBP function and the variation in the MRLIs by GRA is due to the true angular response from the sediment.
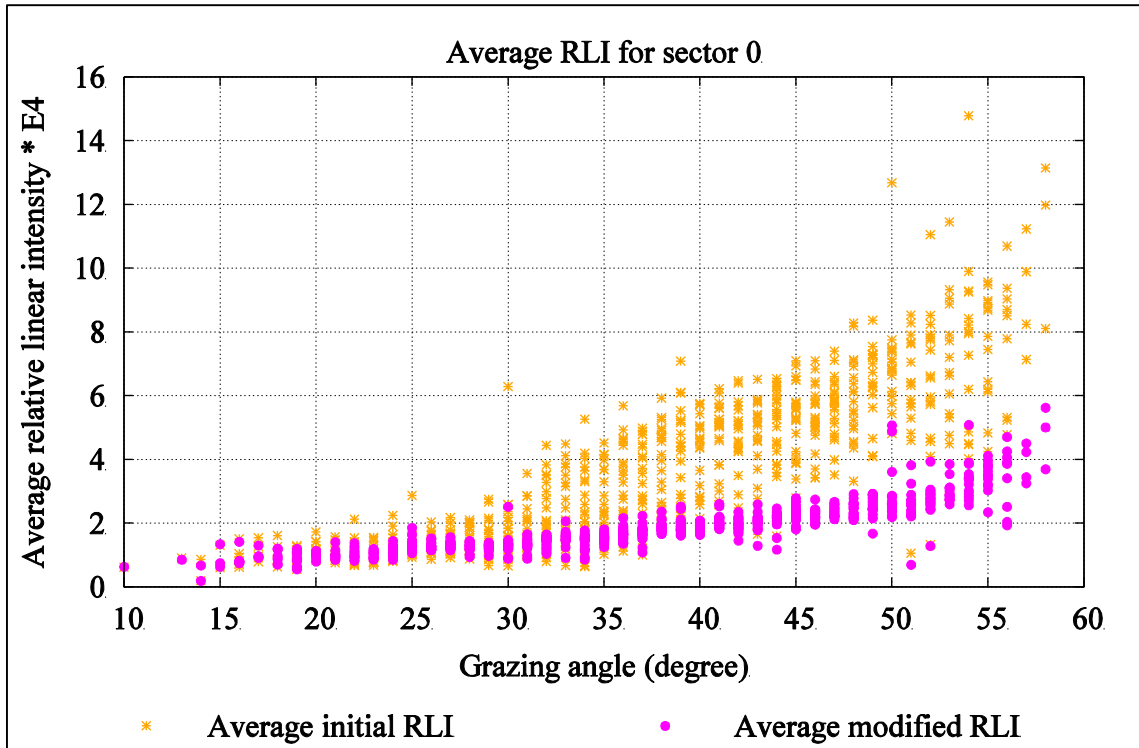
Figure 4.28: The average initial RLIs and MRLIs for sector 0

Along with average MRLIs, their SDs are also computed by propagating the SDs of the initial average RLIs and the corresponding across-track RBP function values. Each average MRLI has an associated SD which is higher than the corresponding average RLI due to the additional SD of the corresponding across-track RBP function value.

As a result of gentle slopes in the seafloor and natural undulations, there are some GRAs common between adjacent sectors. The extent of these common GRAs will depend on amount of seafloor slope; more details are discussed in Section 5.3. Figure 4.29 shows the average MRLIs for sector 0 and 1 which have common GRAs ranging from 46° to 59°. These average MRLIs are free from across-track RBP and hence the MRLIs at any given GRA should be the same irrespective of sector (and source level). A

126

clear offset can be seen in Figure 4.29 between the average MRLI of sector 0 and 1.0; computing that offset is the next step.
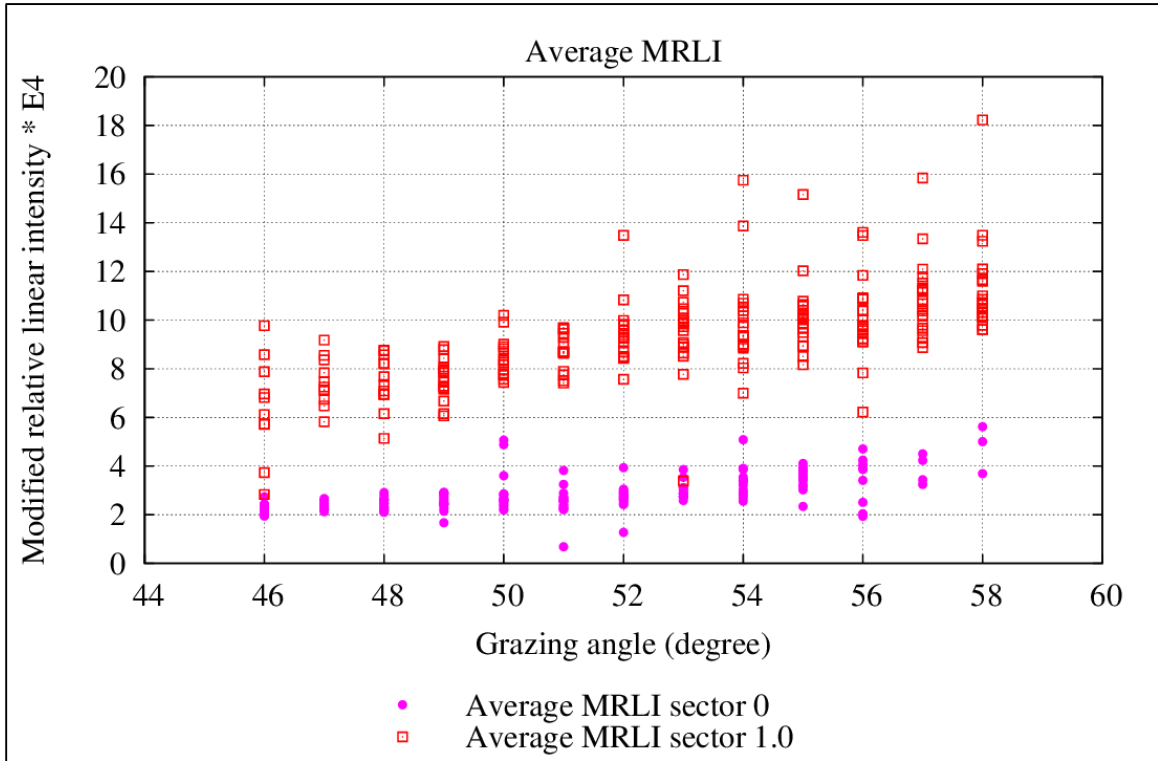
Figure 4.29: Average MRLIs for sector 0 and sector 1.0

2) Computing the offsets between the sectors

The algorithm follows a step by step process to compute the single offset values between reference sector 0 and other sectors along with propagated related SDs. Sector 0 is arbitrarily selected as reference from the outer sectors as they have a relatively high number of samples compared to central sectors. Once the common GRAs are selected, the computation is done in the following three steps.

Step 1: Computing average of average MRLIs at given GRA.

As the average MRLIs are free from across-track RBP, at a given GRA there should be only one value of average MRLI. This value is computed for each GRA of each sector under consideration; in Figure 4.30 single average value is computed at GRA 46° of sector 0 (shown by black solid circle for all GRAs) and for the same GRA 46° of sector 1.0 (shown by black hollow square for all GRAs). Before the averaging the outliers are removed following the standard process explained in Appendix 9.2. The SDs of the average MRLIs are propagated in the computation of the average values. This process is continued for all the overlapping GRAs (from GRA 46° to 58° in Figure 4.30) between two sectors and associated SDs are computed.
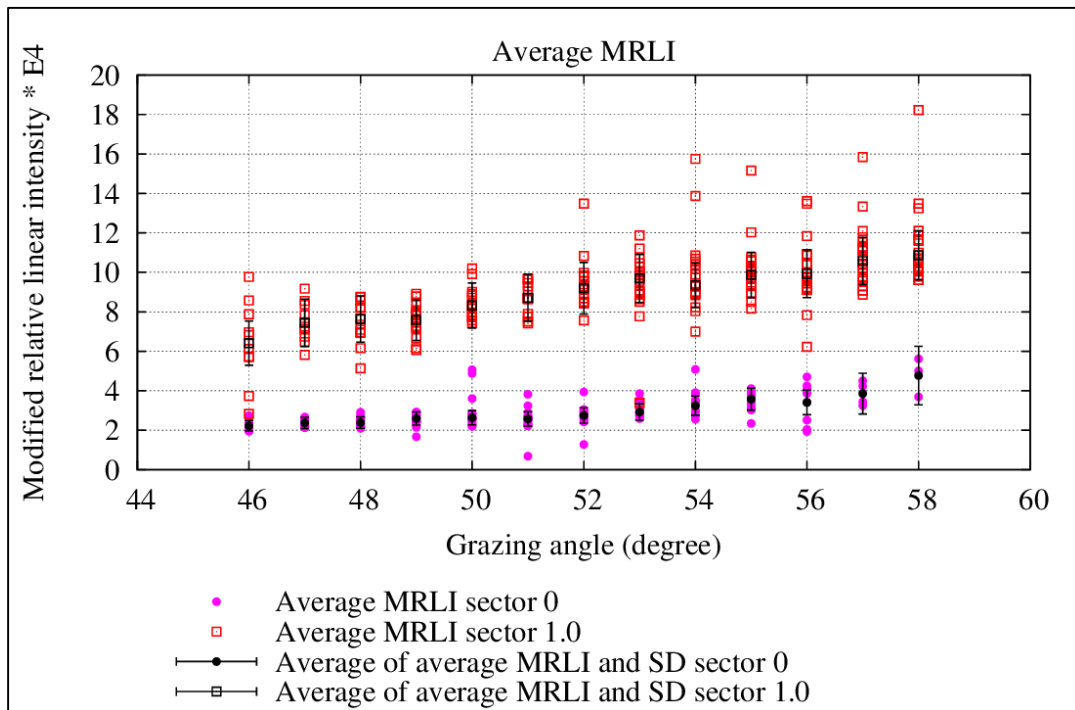
Figure 4.30: Computation of average of average MRLIs and their SDs

Step 2: Computing the offsets for each common GRA

An offset between two sectors for each common GRA is computed by dividing the average of average MRLI computed in step 1. The outliers are removed before the averaging following the standard process. Each average of average MRLI has its associated SD and it is propagated during the computation of individual offset. Figure 4.31 indicates each computed offset at common GRA between sector 0 and sector 1.0 by a thin black asterisk.
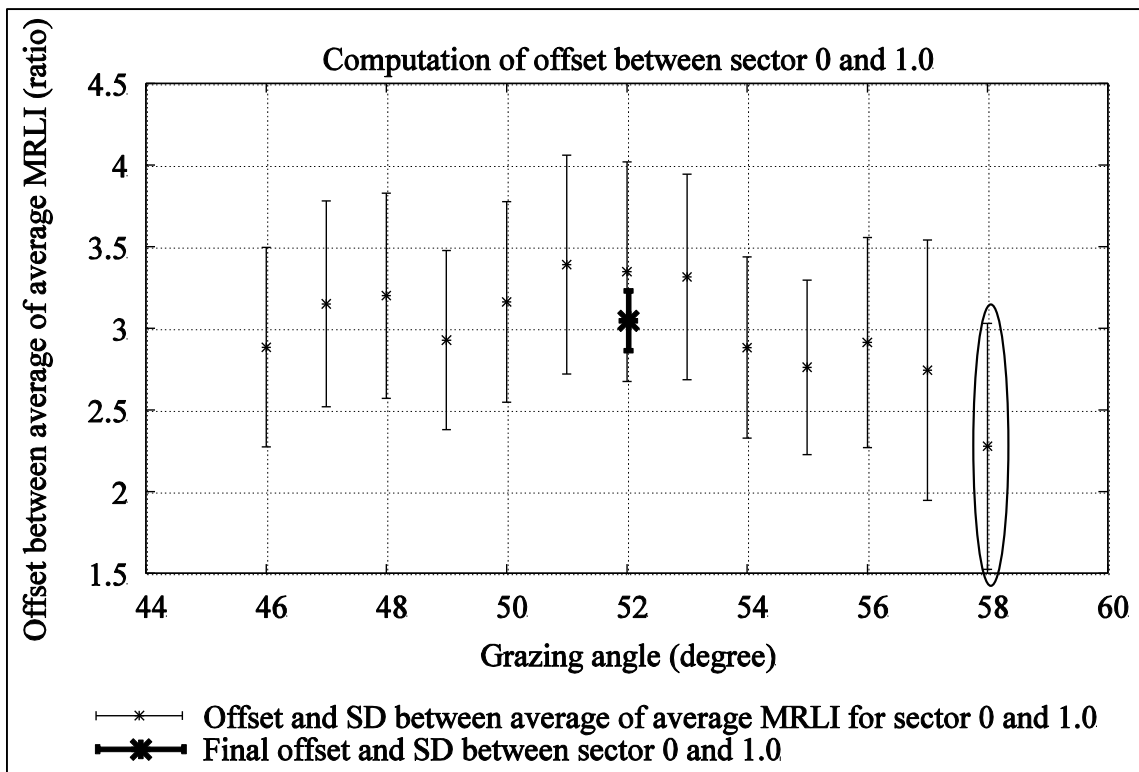
Figure 4.31: Computation of single offset between sector 0 and sector 1.0 by averaging multiple offsets as a result of overlapping GRAs.

Step 3: Computing a single offset between two sectors.

Multiple offsets (multipliers) are obtained in step 2 as there are multiple common GRAs between the sectors. In the 3rd step the average is taken from the multiple offsets to get a final single offset representing the shift between the two sectors (shown by a thick black asterisk in Figure 4.31). Any outliers (circled in Figure 4.31) are removed before the averaging process. The associated SDs of the offsets are propagated during the averaging process and SD of final offset is obtained. Table 4.5 lists the final offsets from reference sector 0 to other sectors and associated RSDs.

Table 4.5: Final computed offsets (multipliers) from reference sector 0 and related RSDs

Sector	Offset (Multipliers)	RSD	Side
0 (reference)	1	NA	port
1.0 (port sub-sector of sector 1)	3.261423	0.088311	port
1.1 (stbd sub-sector of sector 1)	4.386254	0.084296	stbd
2	1.775952	0.047975	stbd
3	1.917583	0.046857	port
4.0 (port sub-sector of sector 4)	2.911456	0.088355	port
4.1 (stbd sub-sector of sector 4)	3.955934	0.103177	stbd
5	3.444485	0.048599	stbd

3) **Obtaining the final across-track RBP master function for the entire imaging coverage**

The computed offsets and their SDs from the previous step are then used and all the sectors are adjusted to bring them into agreement with reference to the RBP function of

130

sector 0. The average across-track RBP functions shown in Figures 4.26 and 4.27 are multiplied by the respective sector offset computed in the previous step and related SDs are propagated. Figure 4.32 shows the RBP function and SD for the entire imaging coverage (2 swaths, each with 3 sectors) after adjusting the inter-sector and inter-swath offsets.
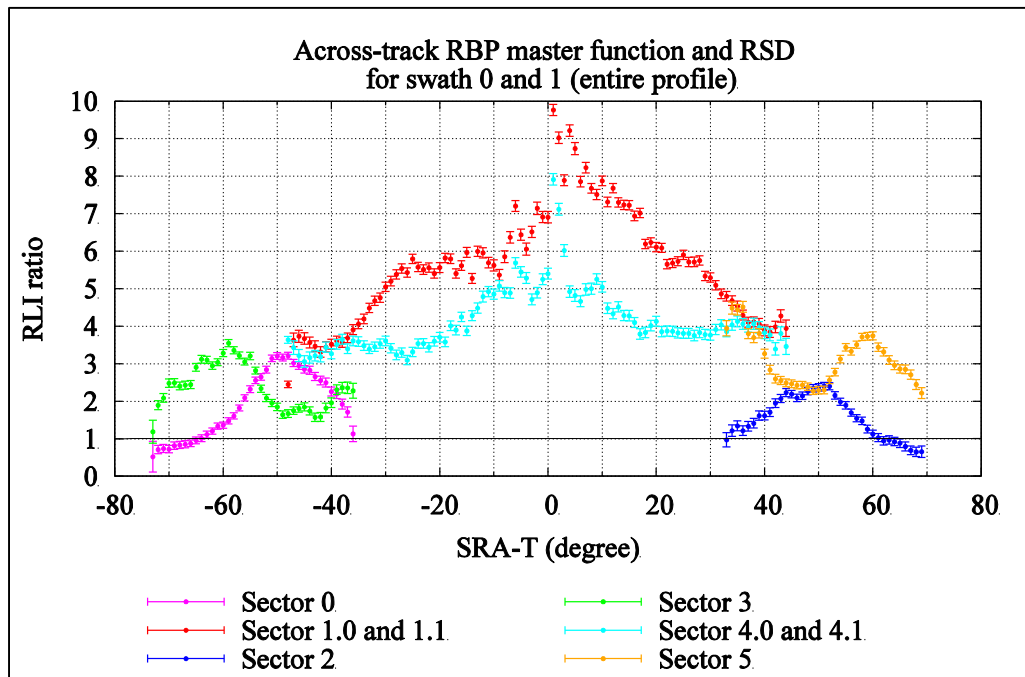
Figure 4.32: Across-track RBP master function referenced to SRA-T -63° of sector 0

As sector 0 is the reference sector, its across-track RBP function values (and SDs) have not changed after the application of the sector offsets. However other sectors now have a specific position wrt sector 0 after the application of the sector offset, causing increased SDs as a result of additional SDs of the sector offsets computed in this section of the process.

4.2.1.5 Shifting Across-Track RBP Master Function to another Reference

In Figure 4.32 the across track RBP master function is referenced to the reference sub-function SRA-T of sector 0 which in this case is SRA-T -63° and most of the values are above 1. With this reference, if the across-track RBP master function is used to correct the backscatter data, it will bring the backscatter intensities to a very low level; as during the application of the RBP, the intensities at SRA-T -63° will be taken as the reference (unchanged) and the intensities at SRA-Ts that have across-track RBP master function value of more than 1 will be reduced. This will create very dark backscatter intensity images and very low backscatter strength values in the ARC. The selection of the reference will not, however, affect the shape of the ARCs.

To avoid this problem there are two options: 1) chose the reference at the maximum intensity SRA-T of sector 0 or 2) shift the reference chosen to the maximum intensity SRA-T. The algorithm is capable of shifting the reference to any sector and any SRA-T as required. For this example the master reference is chosen at SRA-T -50° of sector 0. More discussion on the selection of this final reference and its effects is done in Section 5.1.

The master reference shift process involves the division of all across-track RBP master function values by the single value at the new master reference. Figure 4.33 shows the across-track RBP master function referenced at SRA-T -50° of sector 0. It should be

noted that this step can be completely avoided if the initial SRA-T sub-function reference during the stacking process is chosen at the desired final RBP master function reference.
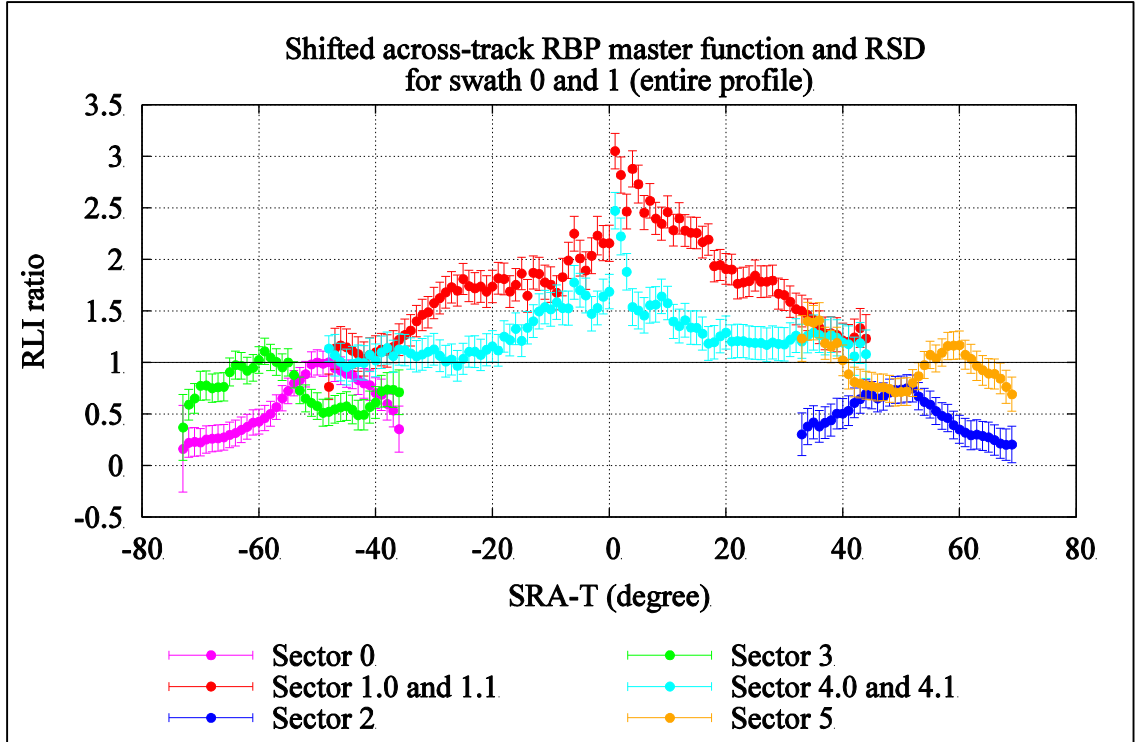
Figure 4.33: Across-track RBP master functions referenced to SRA-T -50° of sector 0

The next step is to express the master function values in decibel units (dB) along with the related SDs as shown in Figure 4.34. The reference ratio of 1 when converted to dB gives a reference value of 0. The conversion process and the propagation of SD are explained in Appendix 9.2.
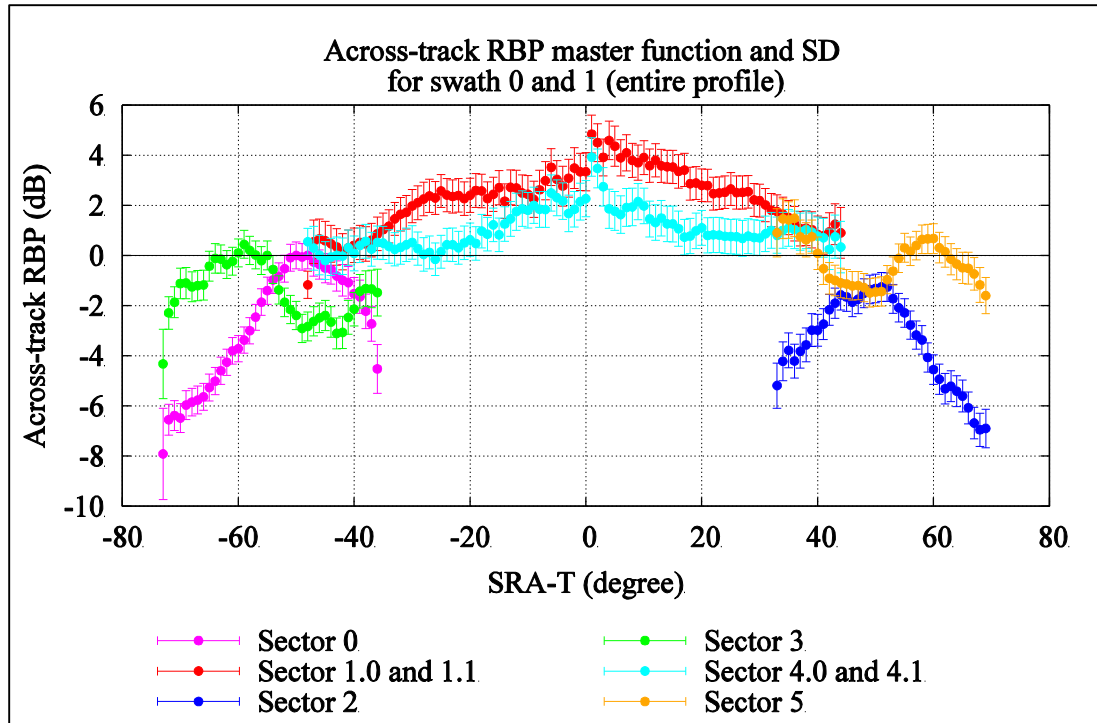
Figure 4.34: Across-track RBP master function in dB

During the development of this method it was noticed that extracted across-track RBP at nadir can be noisy and result in unrealistically high values depending on the amount of the survey data available. The high intensity values can be attributed to the relatively small number of samples at nadir ($\approx$ 2.5% of those available at SRA-T $\pm50°$) and any unknown errors during removal of manufacturer-applied TVG-BS. Given the design of the Tx array, it is considered unlikely that there would be rapid variation in the intensities around nadir. In order to avoid the noisy results at nadir, the algorithm has an option to interpolate values using up to 5th order weighted polynomials fitted to the central sectors. The inverses of variances are used as the weights during the polynomial fit. The effect of this interpolation on the final ARC was studied and a difference of less than 1dB was observed at the nadir region. It should be noted that this step is optional and required only

in the case of noisy data at nadir. Figure 4.35 shows the across-track RBP master function with interpolated values at nadir (±15°).
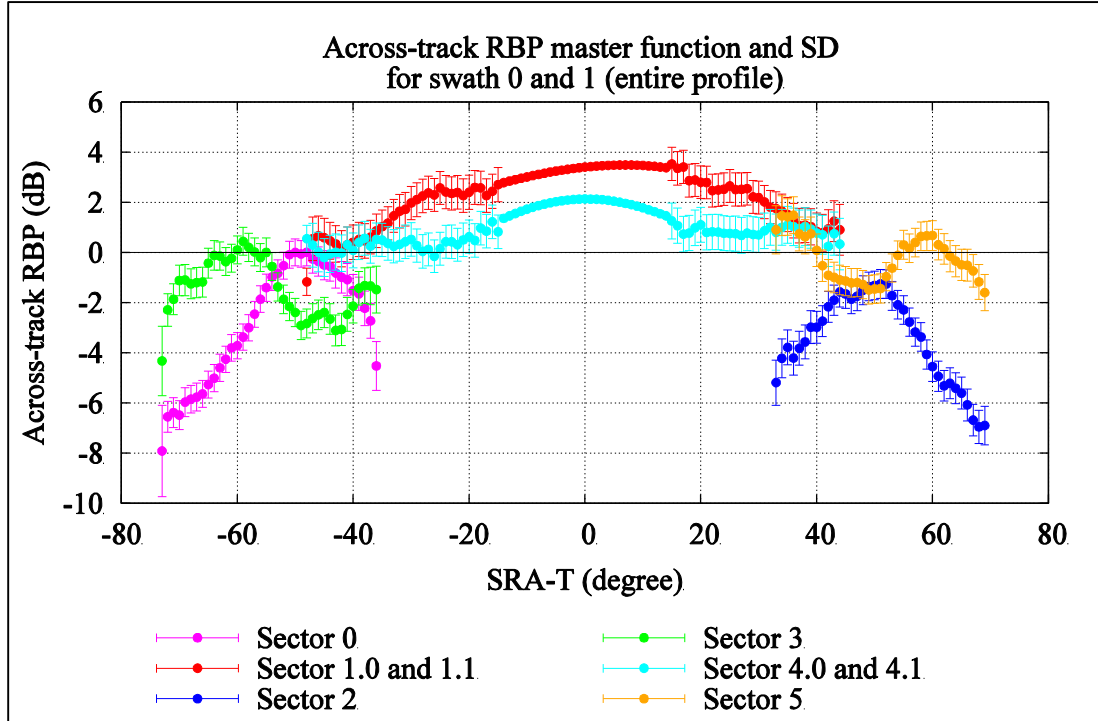
Figure 4.35: Across-track RBP master function with interpolated values at nadir

This concludes the extraction of the across-track RBP master function. The following section shows how this master function can be applied to the backscatter data to obtain ARC and corrected backscatter intensities.

4.2.1.6 Application of Extracted Across-Track RBP

Once the across-track RBP master function is extracted for each depth mode of multibeam sonar, they can be applied to any backscatter data collected with any

orientation over bathymetrically and geologically changing seafloor. To briefly demonstrate the results, the same test backscatter data that were used for the extraction of the across-track RBP in the above sections are used. The existing OMG algorithms are modified to apply the extracted across-track RBP to obtain ARC and corrected backscatter images.

The across-track SRA-T for each beam of the original backscatter data is first computed. Then the backscatter sample intensities from that beam are corrected by the corresponding across-track RBP correction value. Then in order to derive the ARC, the corrected values are sorted by the GRA in 1° bins (from 0° to 90°) and average values are plotted as ARC (shown as after RBP removal in Figure 4.36). Producing these corrected ARCs, is the main aim of this research. The developed method has unambiguously removed the across-track RBP from the initial ARC and RBP product curves (shown in Figure 4.16 and reproduced as before RBP removal image in Figure 4.36). These ARCs can now be directly used for seafloor classification with more reliability.

Before RBP removal

Product of ARC and RBP

After RBP removal

Angular response curve

Sector 0   CW id:0 SL:0.30ms CFreq:70.0kHz BW:5.0kHz
Sector 1   CW id:1 SL:0.30ms CFreq:80.0kHz BW:5.0kHz
Sector 2   CW id:2 SL:0.30ms CFreq:70.0kHz BW:5.0kHz
Sector 3   CW id:0 SL:0.30ms CFreq:90.0kHz BW:5.0kHz
Sector 4   CW id:1 SL:0.30ms CFreq:100.0kHz BW:5.0kHz
Sector 5   CW id:2 SL:0.30ms CFreq:90.0kHz BW:5.0kHz
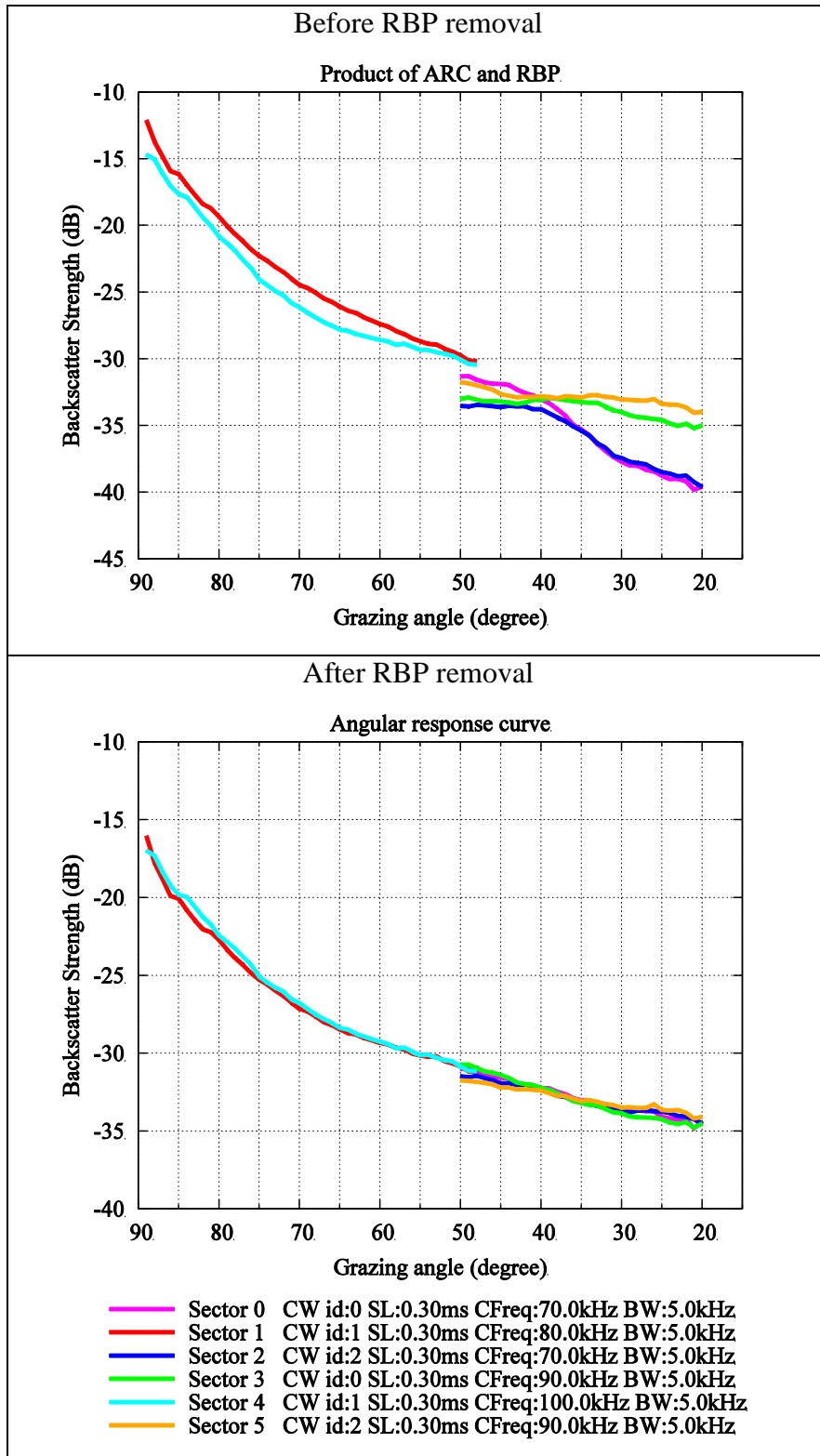
Figure 4.36: Extracted true ARC after removing RBP

To obtain the corrected backscatter images, the corrected backscatter intensities are sorted in bins determined by the user defined pixel values and then average values are formed into an image or mosaic as shown in Figure 4.37 (after RBP removal). Compared to the backscatter image with across-track RBP in Figure 4.15 (reproduced as before RBP removal in Figure 4.37), the changes in backscatter intensities due to rolling of the vessel and the intensity offsets between the sectors due to source level differences are now corrected and not visible in the backscatter image.

Roll in degree

-8 -4 0 4

Before RBP removal

Intensity variation

-22 dB

-47 dB

25m

Roll in degree

-8 -4 0 4

After RBP removal

No Intensity variation

-24 dB

-47 dB

25m

Location: Howe Sound, Depth: 50m, depth mode: Very shallow
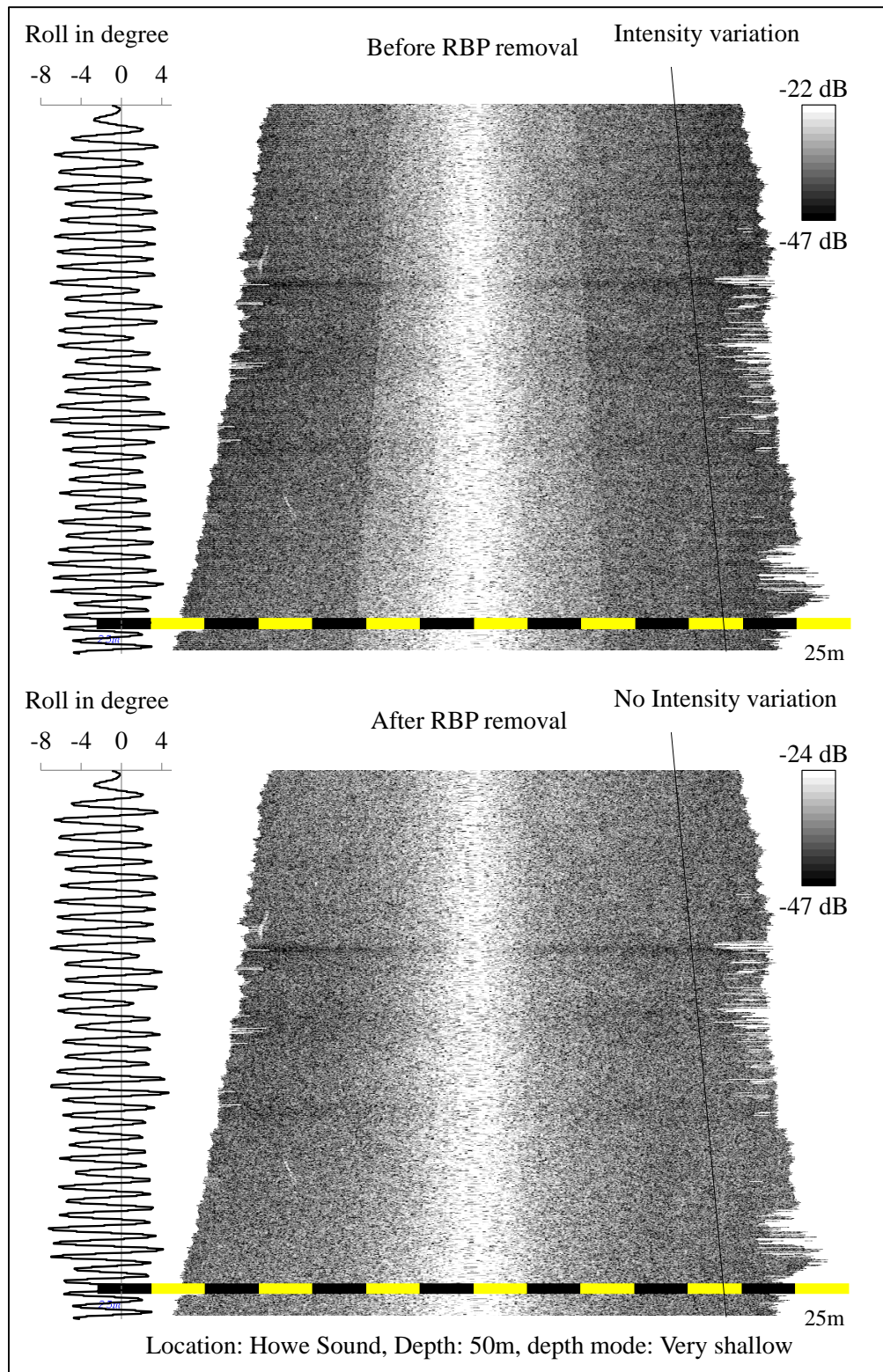
Figure 4.37: Backscatter intensity image before and after RBP removal

139

This section described in detail the methodology used for the across-track RBP extraction along with the example dataset. The next section explains the strategies used for the along-track RBP extraction.

4.2.2 Extracting Along-Track RBP

The second component of RBP is the along-track RBP, and this section describes how the required test data are collected and along-track RBPs are extracted using the test data. Figure 4.38 shows the brief workflow of this extraction process.
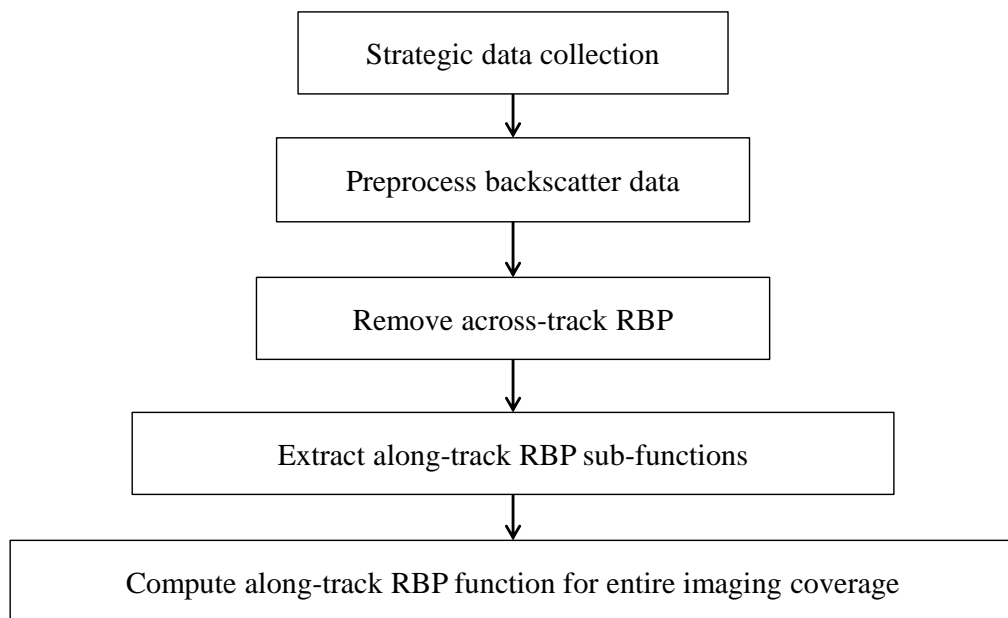
Figure 4.38: Workflow for along-track RBP extraction

4.2.2.1 Data Collection Strategy for Along-Track RBP Extraction

The along-track beam pattern appears in the backscatter data when the vessel is yawing heavily with active yaw stabilization, and also, to a lesser extent when applying pitch stabilization. During heavy yaw, the along-track steering of the outer transmit beams is at a maximum. In this situation, the along-track pattern of strong and weak intensities can be seen in backscatter data. This pattern is also sonar relative but reflecting variation in the Rx sensitivity in the along-track direction.
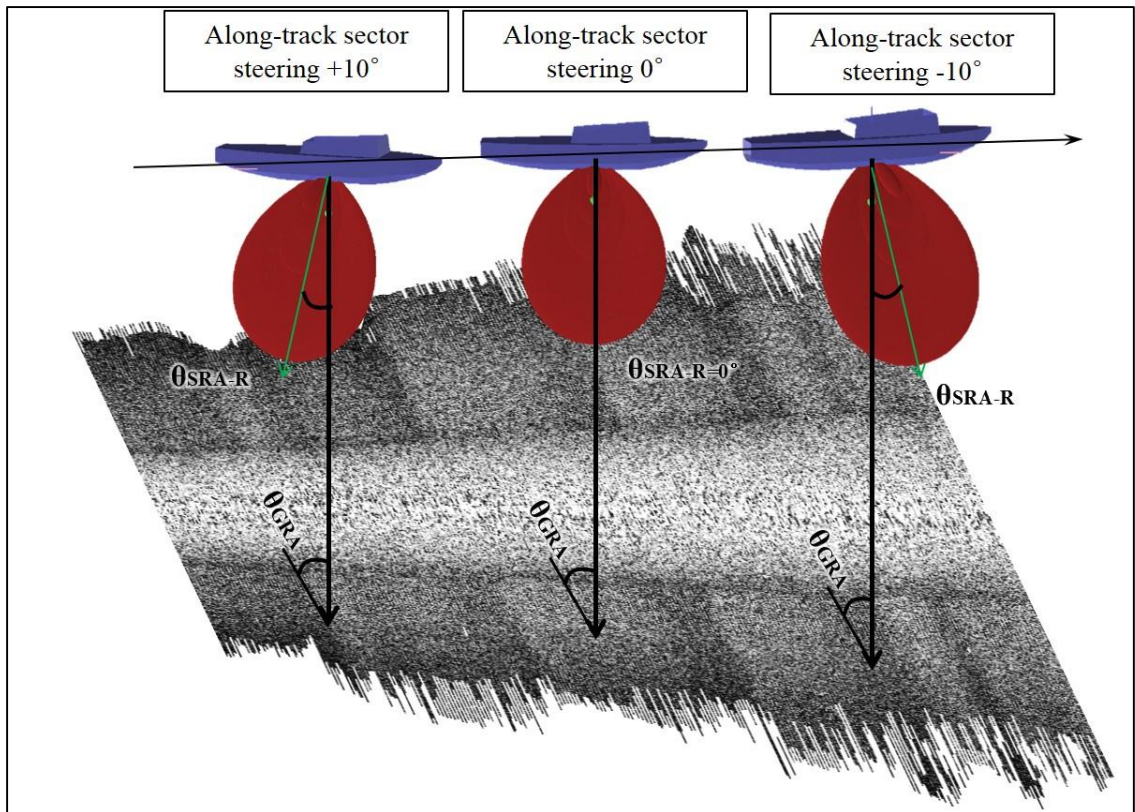
Figure 4.39: Simplified imaging geometry for data collection for along-track RBP extraction.

The data that are required to extract the along-track RBP are collected by deliberately yawing the vessel with active yaw and pitch stabilization on and maintaining minimum roll. As the vessel yaws, the returning signals from a specific GRA are received at different along-track SRA-Rs (see Figure 4.39). If the received intensities are corrected for across-track RBP, then any variations in the intensities from a particular GRA as the vessel yaws can be attributed solely to the along-track RBP.

Figure 4.40 shows the actual reported backscattered intensities of one of the test survey lines collected. The across-track and along-track (along the line) intensity variation can be clearly seen in the image.
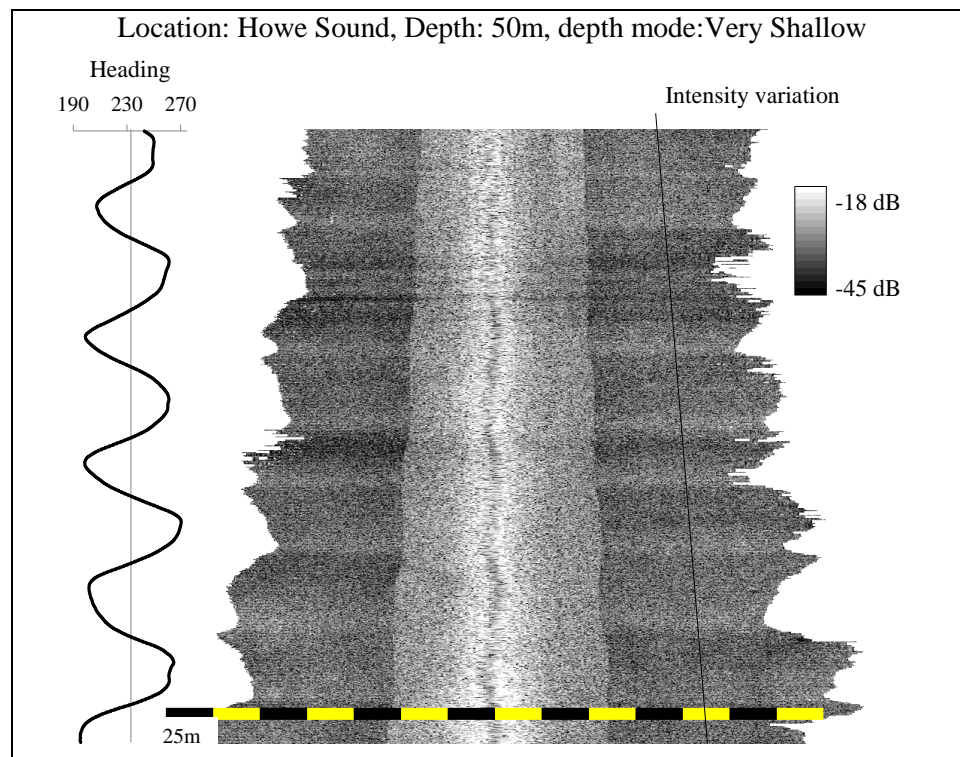
Figure 4.40: Showing received intensities for along-track RBP extraction from one of the test survey lines

The manufacturer-applied TVG-BS is removed in a data preparation stage; Figure 4.41 shows the TVG-BS free intensities. The along-track intensity variation due to yawing of vessel can be seen in TVG-BS free data along the drawn line; also across-track intensity variations can be seen, particularly at the sector boundaries.

Figure 4.42 shows the backscatter strength curves which are products of actual ARC and RBP (along and across).
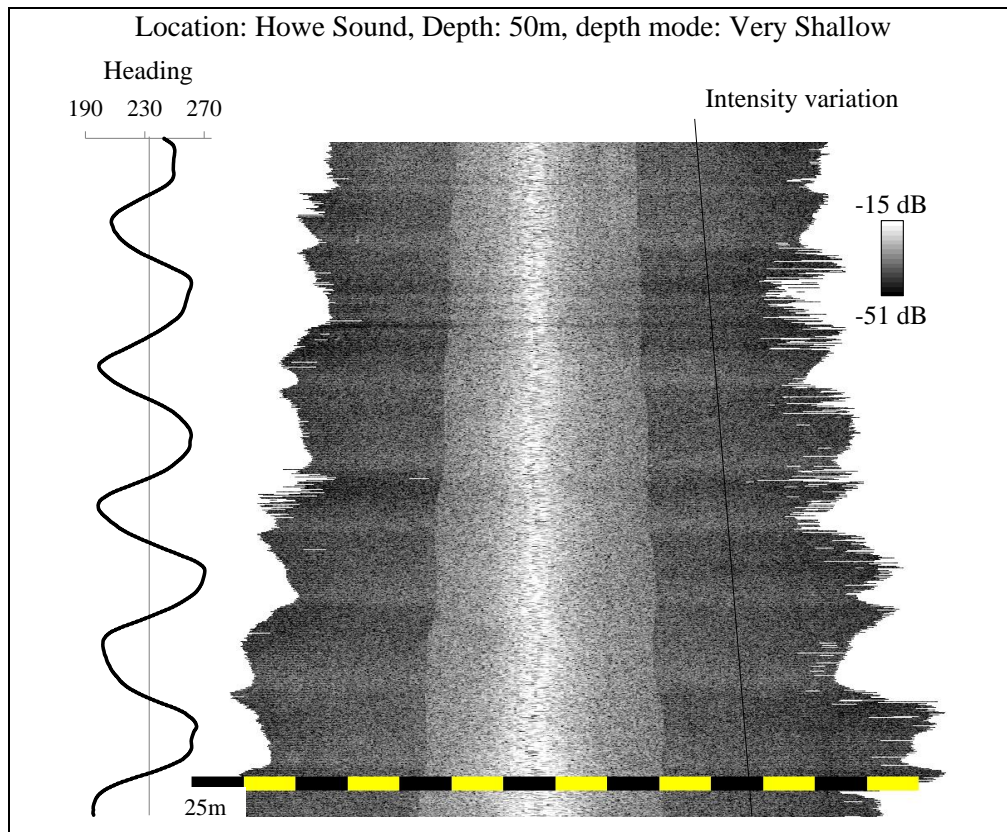
Figure 4.41: TVG-BS-free backscatter intensities
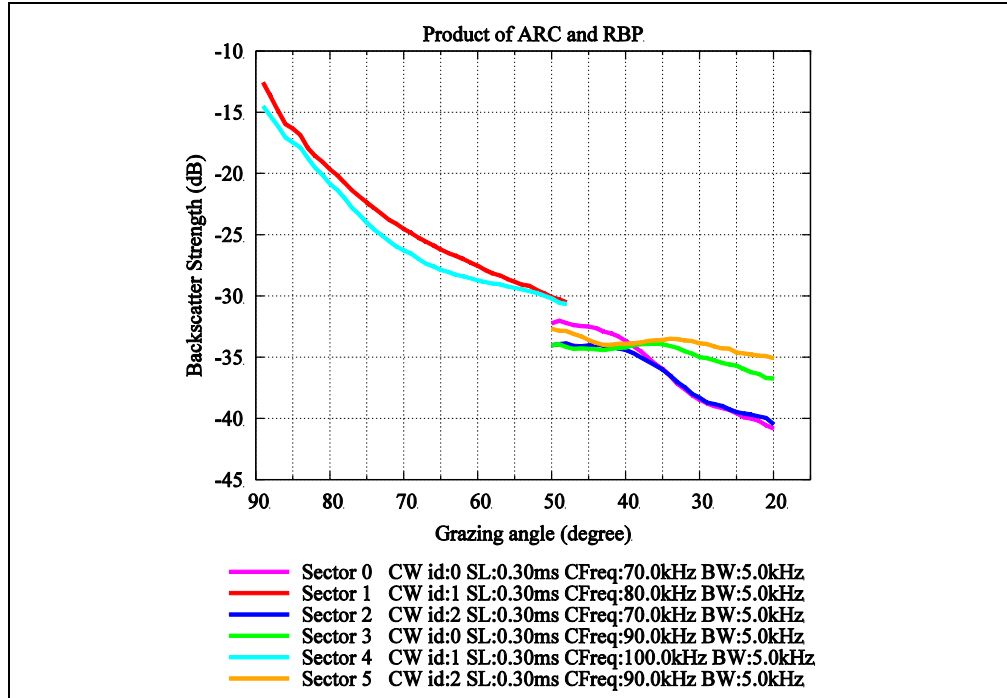
Figure 4.42: Backscatter strength curves showing product of ARC and RBP

Once the geometric effect and TVG-BS are removed, the backscatter data are sorted into different bins and outlier backscatter samples are removed as explained in Section 4.1.4. The extraction of along-track RBP is divided into two major steps:

1) Removing the across-track RBP.

2) Computing final along-track RBP function for each sector.

4.2.2.2 Removing the Across-Track RBP

The test data collected for the along-track RBP extraction has the across- and along-track RBP superimposed on the actual backscatter intensities as seen in Figure 4.41.

When a specific GRA is illuminated by a specific across-track SRA-T, it has been affected by the across-track RBP at that SRA-T; when the affected signal is received at a specific along-track SRA-R it is again affected by the along-track RBP at that specific along-track SRA-R. Hence, the across-track RBP must first be correctly accounted for before extracting the along-track RBP. The removal of the across-track RBP is explained in Section 4.2.1.6. Once the across-track RBP is removed, at the specific GRA there should be no variation in the intensities due to the rolling of the vessel (or due to different across-track SRA-T illuminating the GRA).

Figure 4.43 shows the backscatter image of the test dataset that is corrected for across-track RBP. The across-track RBP extracted for Very Shallow mode from the previous section shown in Figure 4.34 was used for the correction. The related SDs of the extracted across-track RBP are propagated with the SDs of the average RLIs to obtain SDs of across-track RBP free average MRLIs. The across-track variation at the sector boundaries visible in Figure 4.43 is due to very different along-track SRA-R between the sectors as the central sectors do not attempt yaw stabilization. As a result, the across-track variation at the sector boundary is not constant and almost absent between the sectors when the outer sectors are slightly or not steered at all.
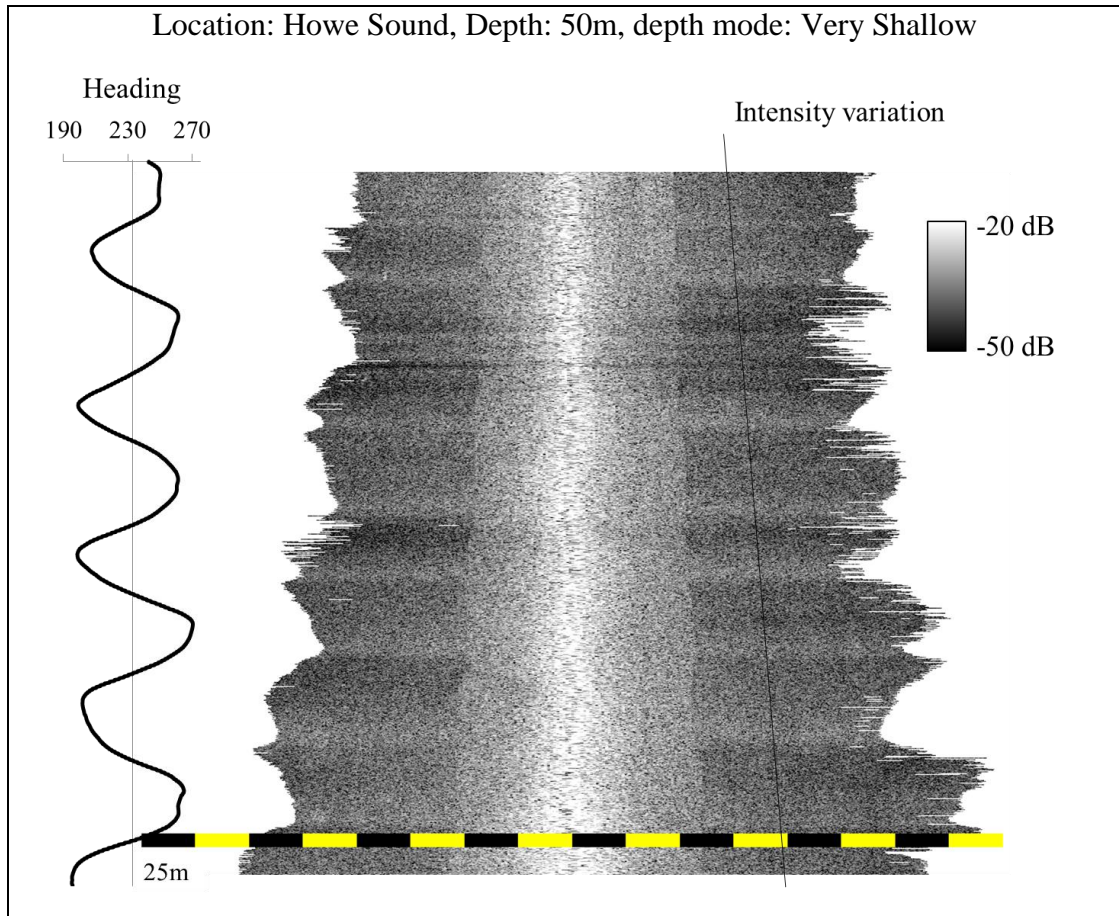
Figure 4.43: Across-track RBP free backscatter intensities

Figure 4.44 shows the product of ARC and along-track RBP. The aim of this part of the research is to use the data shown in Figure 4.43 and extract the along-track RBP. The next section describes the process of extracting the along-track RBP.
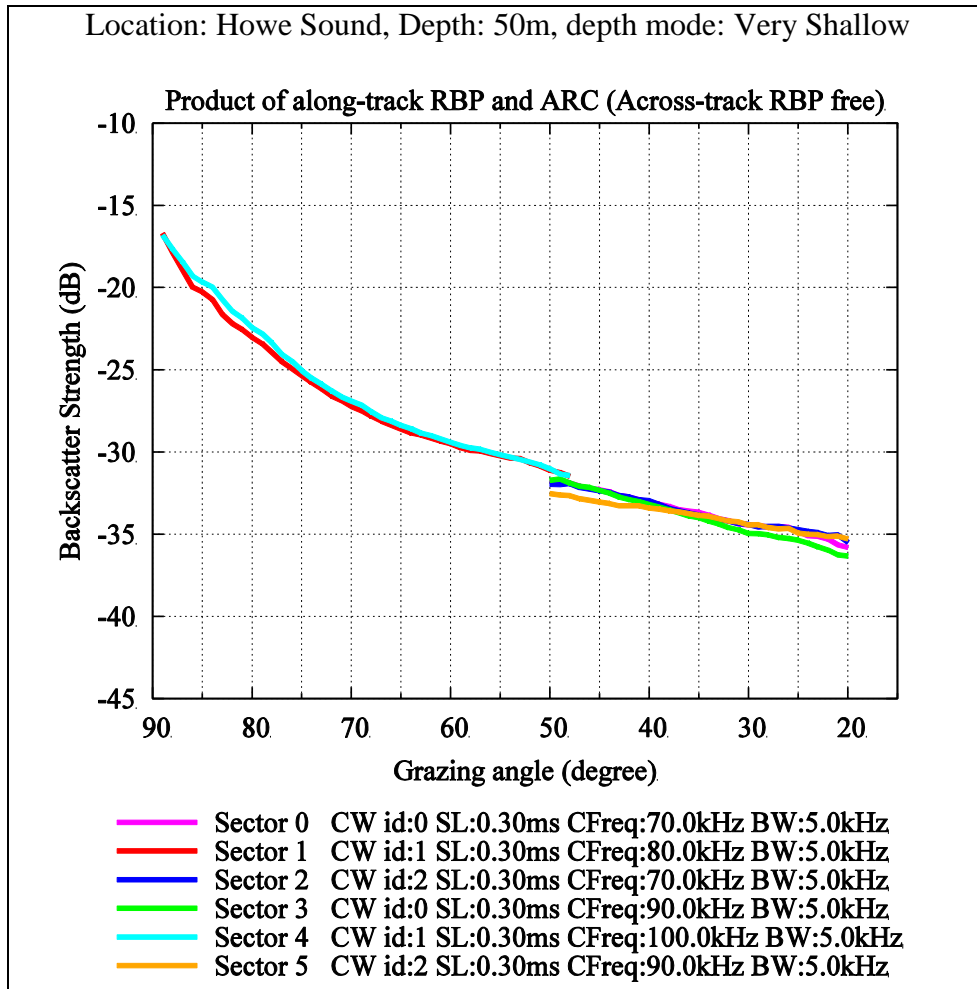
Figure 4.44: Backscatter strength curves showing product of ARC and along-track RBP

4.2.2.3 Extraction of Along-Track RBP

The extraction process of along-track RBP is divided into two major steps: 1) extraction of along-track RBP sub-functions 2) averaging sub-functions to obtain along-track RBP function

147

1) Extraction of along-track RBP sub-functions

After removing across-track RBP, the obtained average MRLIs from all across-track SRA-Ts that fall under a bin for specific GRA and along-track SRA-R are averaged and one value of the average of the average MRLIs is obtained for each bin of along-track SRA-R and GRA. The SD of the average of the average MRLI is also computed during this process.

Table 4.6: Along-track RBP sub-function computation example

SRA-R (degree)	Average of average MRLI $*10^4$	SD of average of average MRLI $*10^4$	Along-track RBP sub-function at GRA 40° (ratio)	SD of sub-function
-9	0.17	0.04	0.46	0.16
-8	0.22	0.05	0.57	0.21
-7	0.25	0.06	0.65	0.23
-6	0.27	0.07	0.71	0.28
-5	0.29	0.07	0.77	0.28
-4	0.30	0.07	0.78	0.29
-3	0.32	0.09	0.84	0.33
-2	0.31	0.08	0.82	0.31
-1	0.32	0.08	0.83	0.31
0	0.38	0.11	1.00	0.40
1	0.32	0.07	0.85	0.30
2	0.36	0.09	0.95	0.35
3	0.34	0.08	0.90	0.34
4	0.32	0.08	0.84	0.32
5	0.38	0.11	0.98	0.41
6	0.34	0.08	0.88	0.33
7	0.28	0.08	0.73	0.29
8	0.28	0.06	0.72	0.26
9	0.24	0.08	0.63	0.28

The along-track RBP sub-functions are extracted with reference to the 0° along-track SRA-R value for each possible GRA. Table 4.6 shows the calculated values for one such sub-function and its SD at GRA 40°. Similar calculations are performed for each possible GRA for all sectors obtaining multiple sub-functions for each sector. Figure 4.45 shows all the extracted sub-functions from the test data for sector 0 (colors indicate sub-functions for different GRAs). Unlike the across-track, these sub-functions do not have to be stacked. It is assumed that the along-track RBP is the same for all the across-track elevation angles within the sector. A single function is obtained by simply averaging these sub-functions as shown in the next step.
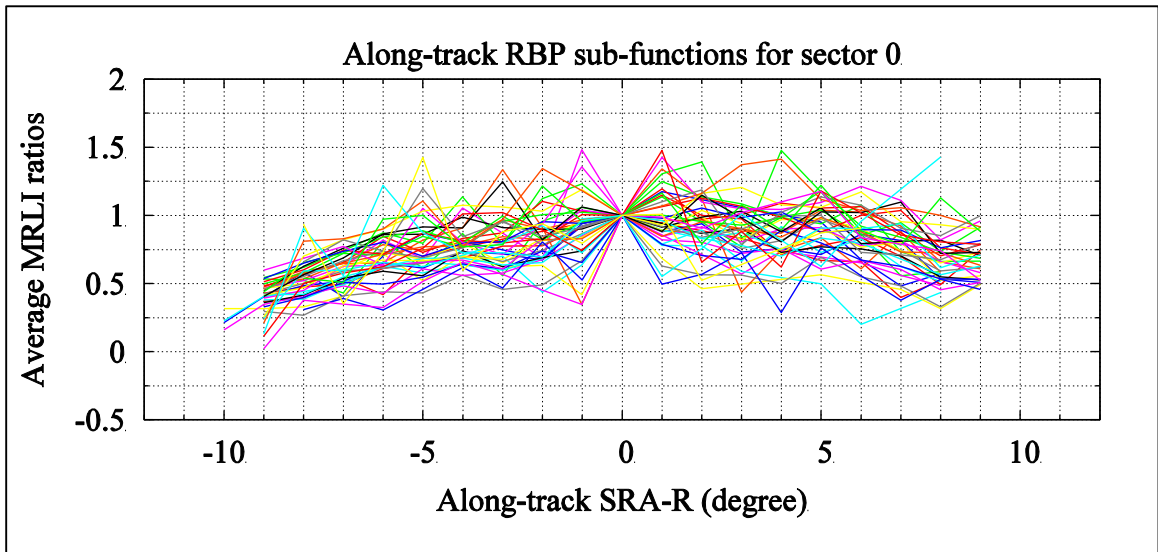
Figure 4.45: Multiple along-track RBP sub-functions for sector 0

2) Obtain along-track RBP function

The along-track RBP function and its SDs are obtained by averaging the sub-functions at each along-track SRA-R. Figure 4.46 shows all the sub-function values

(average of average MRLI ratios) for along-track SRA-R of -8°. There are a total of 42 sub-functions extracted for this particular test dataset for sector 0 ranging from GRA of 7° to 56°. An average, along with its SD is obtained after outliers in these values are eliminated as shown in Figure 4.46.
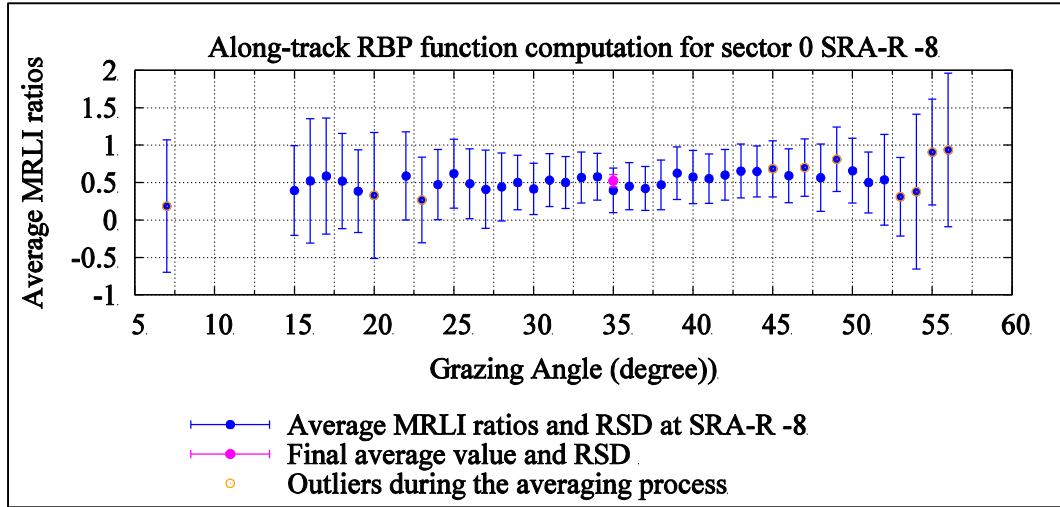
Figure 4.46: Computation of along-track RBP function value at SRA-R -8°by averaging sub-function values from all possible GRAs

The averaging process is repeated for each along-track SRA-R to obtain a single along-track RBP function value along with its SD for all SRA-R in the sector. Figure 4.47 shows the complete along-track RBP function along with the sub-functions in the background for sector 0.
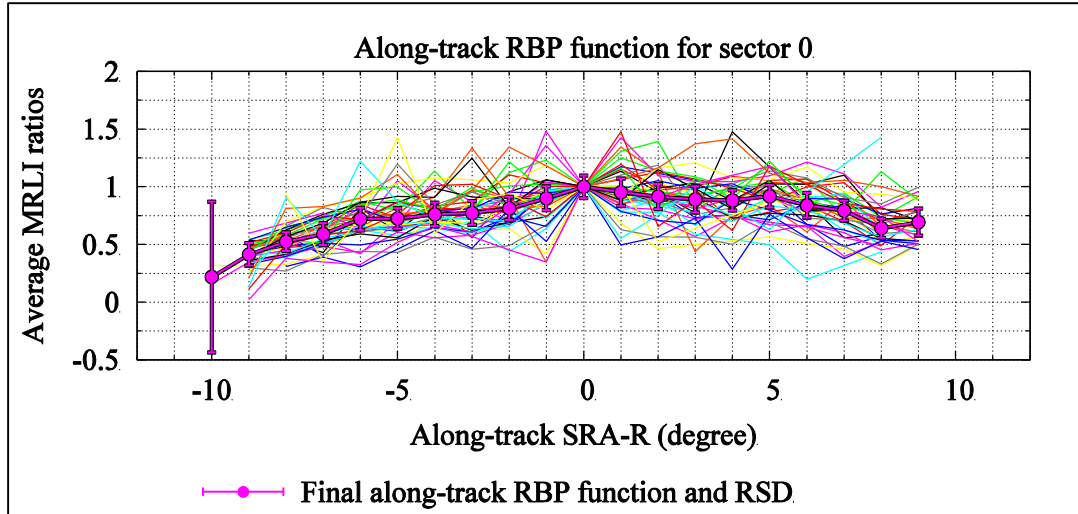
Figure 4.47: Final along-track RBP function with RSDs for sector 0

This final along-track RBP function is then converted in dB along with its SDs. Figure 4.48 shows the along-track RBP function in dB for sector 0 and Figure 4.49 shows the along-track RBP function for all sectors with their SDs.
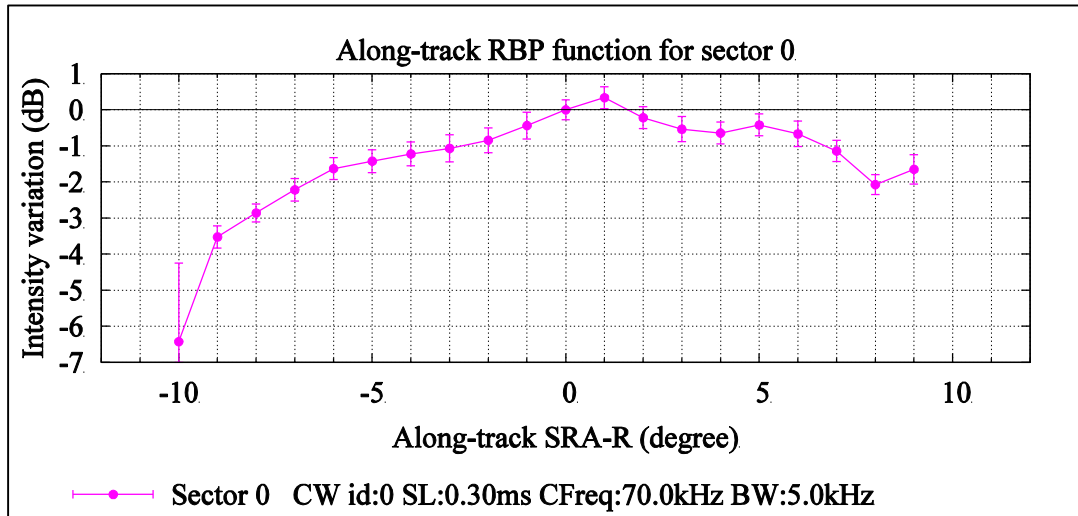
Figure 4.48: Final along-track RBP function with SD for sector 0 in dB
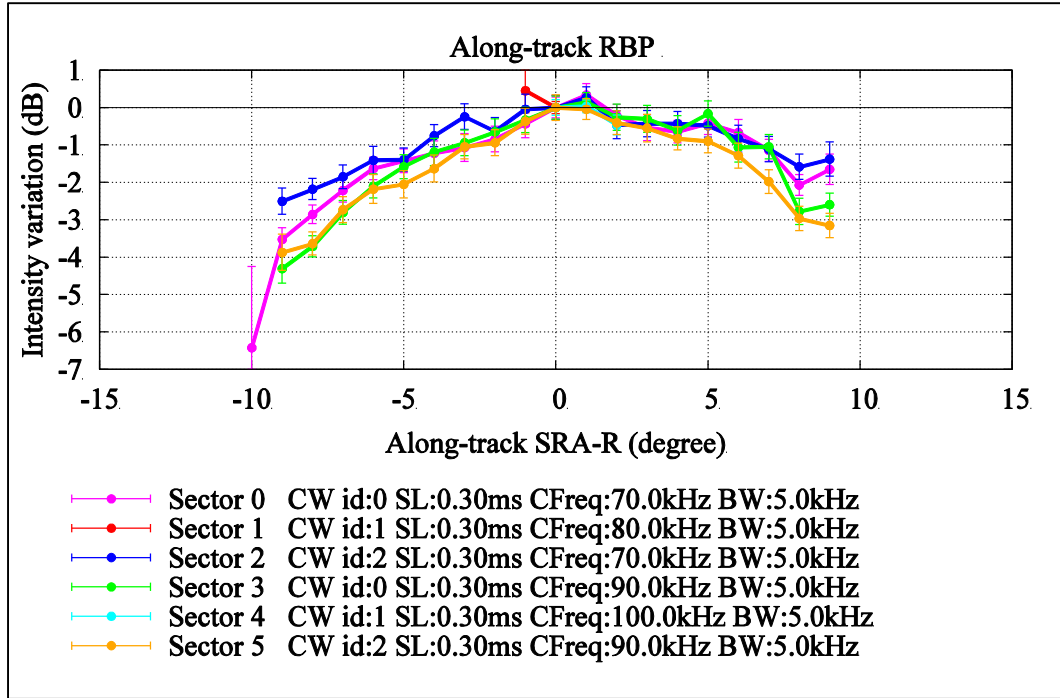
Figure 4.49: Final along-track RBP function with SDs for all sectors in dB

As can be noted in Figure 4.49, for the central sectors no along-track RBP was extracted due to lack of data at SRA-R beyond $\pm 1°$. The central sectors were not steered forward or backward during the heavy yawing. The steering is done only during pitch stabilization (maximum of $\pm 3°$) and it was not possible to induce heavy pitch motion during the data collection. In the absence of the data a generalized function can be used to predict the along-track RBP considering the general shape of along-track RBPs of other available sectors (see Figure 4.50). A more sophisticated approach can be used by relating the change of slope of along-track RBPs to the used frequency, number of elements, and their spacing. It is apparent from Figures 4.49 and 4.50 that the along-track RBP function for low frequency sectors (i.e. sector 0 and 2 at 70 kHz) are flat compared to the high frequency sectors (i.e. sector 3 and 5 at 90 kHz). This can be attributed to the wider Rx beams of low frequency compared to high frequency beams for the same sonar.
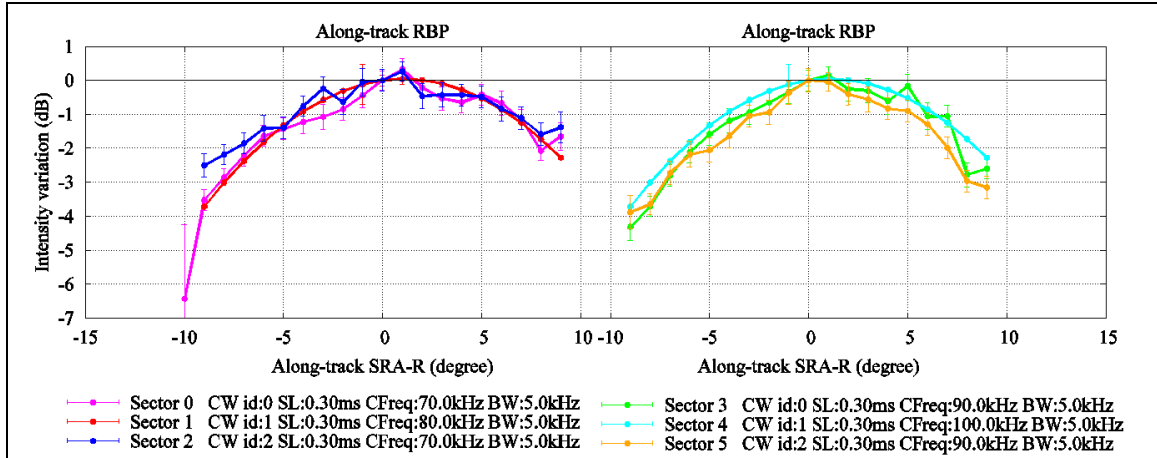
Figure 4.50: Predicted along-track RBP functions for central sector

The along-track RBP is the variation in the intensities due to the Rx sensitivity. All the elements present on the Rx are used for the reception of the incoming signal. As different sectors use different frequencies, the variation in the sensitivity of the Rx between the sectors is caused by two factors: 1) effect of different frequencies on the physically fixed element spacing and number of elements, 2) different sensitivity response of the elements for different frequencies.

The expected offsets between the sectors have already been accounted for during the master function computation of the across-track RBP, where the differences between received intensities of different sectors were adjusted. These inter-sector differences in received intensities (sector offsets) are due to different transmit source levels as well as Rx sensitivity for different sectors. When the across-track RBP master function was used to correct the backscatter data before along-track RBP correction is extracted, the offsets due to different sensitivities between the sectors were also accounted for. Hence the computed along-track RBP functions are already referenced to the common reference and

153

should not have any offsets between them. Thus the computation of the master function is not necessary in the case of along-track RBP. This is also evident from the RBP free backscatter data as presented in the next section.

4.2.2.4 Application of Along-Track RBP

The existing OMG algorithm to correct for the beam pattern is modified in order to apply extracted along-track RBP. The application process is very similar as explained in Section 4.2.1.6. For the along-track RBP application, the intensities from the data are separated by along-track SRA-Rs and SRA-Ts. In this case the along-track RBP functions shown in Figure 4.49 were applied to the backscatter intensities corrected for across-track RBP previously shown in Figure 4.43. Figure 4.51 shows the backscatter intensities before and after RBP removal; there are no intensity variations in along- as well as across-track direction after the RBP removal. The only variations visible in the backscatter intensities are due to the bubble wash under the ship which spans across the swath irrespective of sectors and ship orientation.
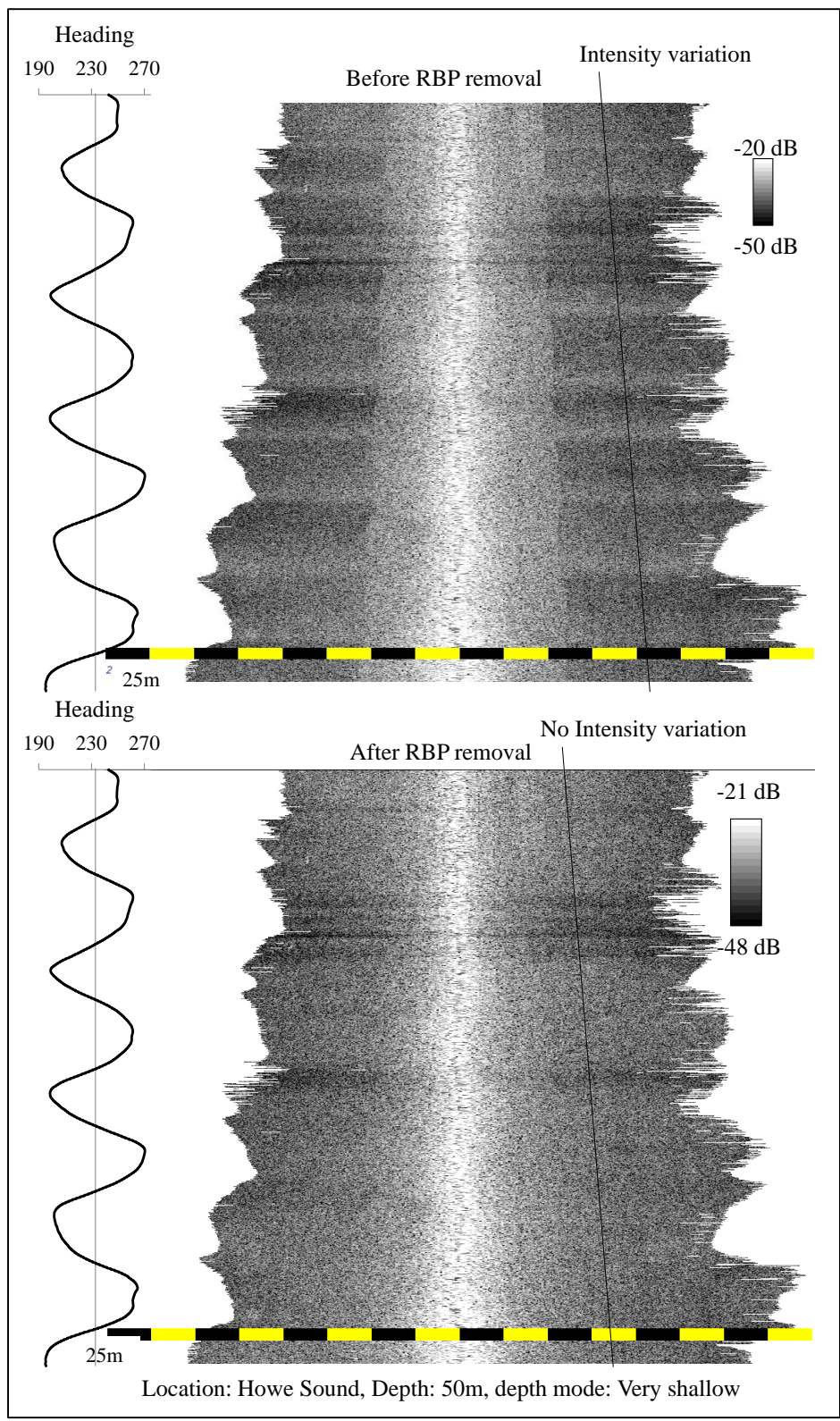
Figure 4.51: Backscatter intensities before and after RBP removal

The corrected backscatter intensities for RBPs shown in Figure 4.51 are used to compose the ARCs shown in Figure 4.52 (after RBP removal). These ARCs are free from along-track and across-track RBPs and can be further used for the seafloor classification with higher accuracy. Obtaining such ARCs was the aim of this research and with the developed RBP extraction methods the most accurate RBP free ARCs can now be obtained irrespective of ship orientation and seafloor slope.

This chapter has demonstrated that the methodology developed in this research can successfully extract across-track and along-track RBP from strategically collected test data. The backscatter data, once free from the extracted RBPs, give confident and reliable ARCs as seen in the results. The next chapter is intended to analyze the developed methodology for its sensitivity towards four important factors. It is important to understand the factors that control the extracted RBPs and their SDs.
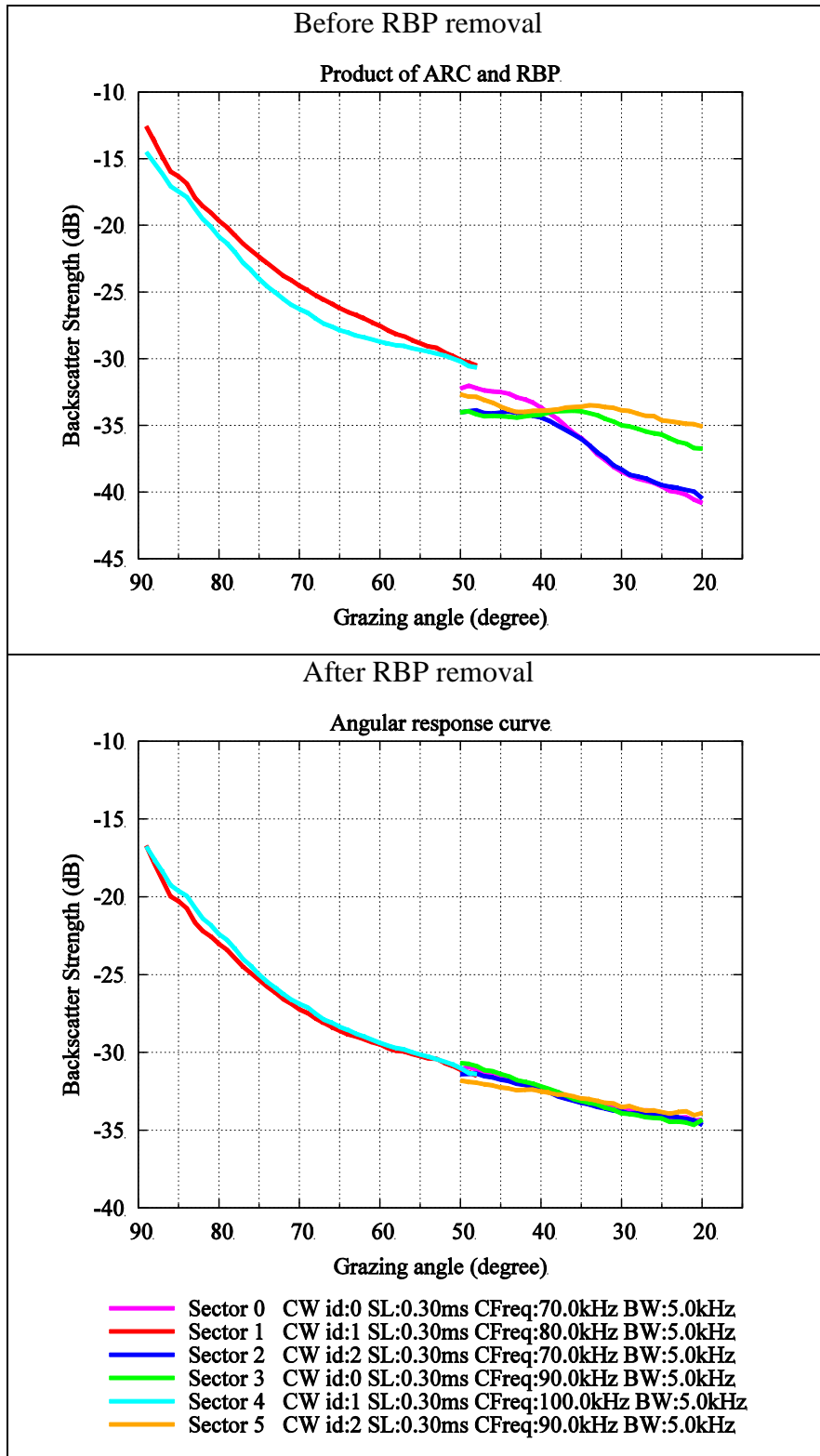
Figure 4.52: True ARC after RBP removal

5   SENSITIVITY ANALYSIS OF RBP EXTRACTION METHOD

Chapter 4 explained the detailed methodology of across-track and along-track RBP extraction method. This chapter examines the conditions under which the extraction of RBP is most reliable by analyzing the sensitivity of the RBP extraction method to four important factors as mentioned.

1) Stacking references: This analysis looks into the effect of choosing different across-track RBP function references on the across-track RBP master function and corrected backscatter data.

2) Magnitude of roll: This analysis looks into the effect of different magnitudes of roll of the survey data on the SD of extracted RBP master function. As not all vessels can be forced to roll with equal magnitude.

3) Survey test site, direction and data size: How the amount, location (slope distortion), and direction of backscatter data affects the final RBP master function was analysed in this part. This was analysed to obtain recommendations for the optimal data collection strategies required for the extraction.

4) Distribution of along-track sector steering: How the distribution of magnitudes of along-track sector steering of outer sectors affects the extracted along-track RBP was analysed and presented in this section. This was analysed to help optimize the test data collection for along-track RBP extraction.

5.1 Sensitivity to Choice of Across-Track RBP Function References Angle

During the development of the across-track RBP extraction, the stacking reference SRA-T was selected arbitrarily. In order to test how the selection of the stacking reference affects the across-track RBP function computation, three different cases as shown in Table 5.1 were studied. The criteria were chosen to spread the choice of the references covering wider sector width. The same data were used for three cases ensuring the same magnitude of roll and number of profiles, avoiding any effect due to these factors. The final master reference for computing across-track RBP master function was selected at the reference SRA-T of sector 0 in all three cases.

Table 5.1: Reference selection criteria for sensitivity analysis

Case	Criteria
Case 1: Outboard from center of swath	Reference selected at SRA-T having maximum number of backscatter samples
Case 2: At the middle of sector	Selected at the geometrically central SRA-T of the sector width.
Case 3: Inboard from center of swath	References selected at SRA-T halfway from center of sectors towards the center of swath, expect for the central sub-sectors.

Figure 5.1 shows the selected references for each sector along with typical sector coverage indicated by horizontal lines. As explained in chapter 4, both central sectors were divided into two sub-sectors at the nadir and hence sector 1 and 4 in Figure 5.1 have

159

two sets of references, one on each side of nadir (SRA-T 0°). The references for both the sub-sectors of the central sectors in case 3 were selected at the middle of the sub-sectors as the nadir data always has fewer samples compared to the off nadir data. During this analysis it was realized that the references for the central sub-sectors cannot be taken too close to nadir (± 20°) due to insufficient data.

In order to understand the effect of the reference selection all three cases were compared with each other and results are discussed in the next section.
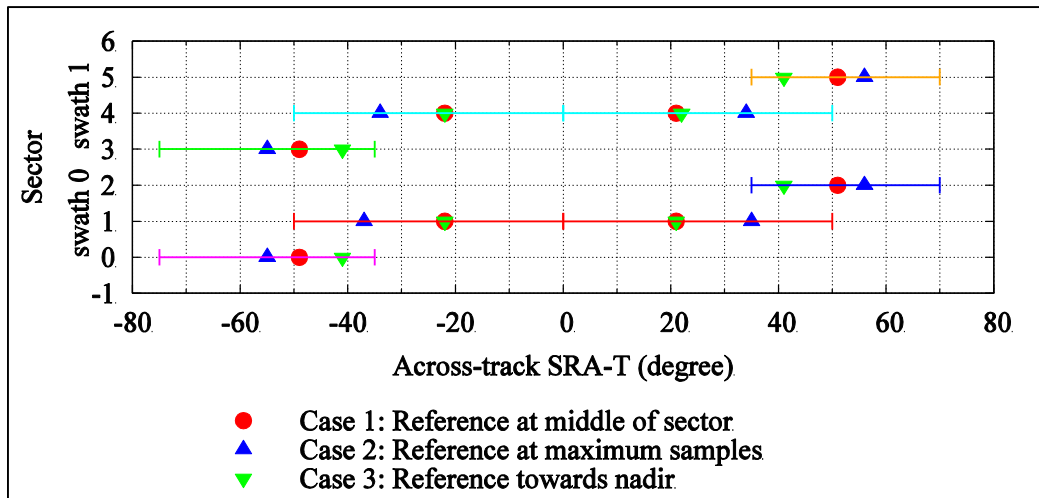
Figure 5.1: Across-track RBP function references selected for three different cases

5.1.1 Effect on Across-Track RBP Master Function.

Figure 5.2 compares SDs of across-track RBP master function for sector 0 which clearly indicates no effect of selection of different references on the confidence of extracted RBP master function values. Similar results were obtained for other sectors.
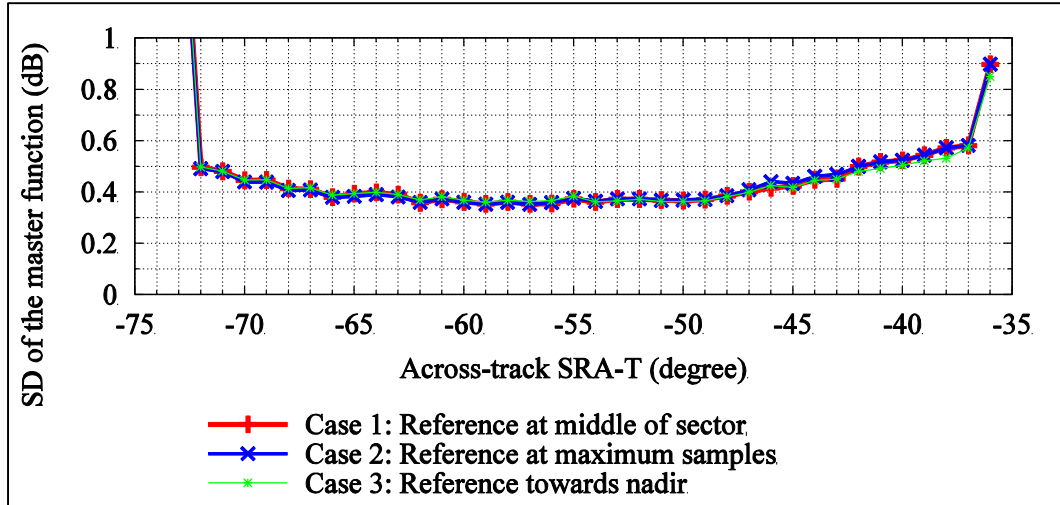
Figure 5.2: Absolute SDs of master function for sector 0 for three cases.

The final extracted RBP values are compared in Figure 5.3. The identical shape of the functions in all three cases indicates that the relative across-track RBP values are similar in all three cases. Considering equal SDs and shape of final across-track RBP master function, it is concluded that the selection of a specific across-track RBP function reference does not have any influence on the shape and magnitude of functions and master functions. Therefore any arbitrarily chosen reference SRA-T (except close to nadir) can be used for the across-track RBP extraction.

While shapes are independent of references, an offset between three cases is observed. As the master reference SRA-Ts for three cases were selected at the reference SRA-T for sector 0, three cases had different reference intensity causing offsets between RBPs. All other sectors were referenced to sector 0 and hence they have the same scaling effect.

161
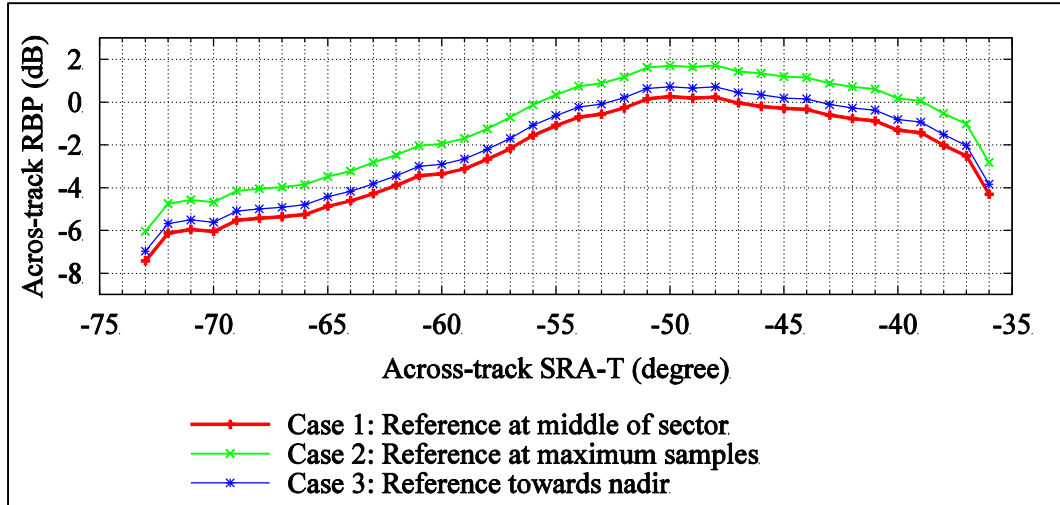
Figure 5.3: Scaled across-track master function for sector 0 for the three cases.

The scaling factor (addition in case of dB units) between case 1 and case 2 is about 1.7 dB as seen in Figure 5.3. The next section describes the effect of this scaling on the corrected backscatter data.

5.1.2 Effect on Corrected Backscatter Data

In this analysis the master function is referenced to the reference SRA-T of across-track RBP function of sector 0. The result of this is scaled across-track RBP master functions where the magnitude of the scale depends on the ratio between the final reference the initial reference for across-track RBP function of sector 0. This does not have any effect on the shape of corrected backscatter data within the sector and between the sectors as the shape of the across-track RBP functions and their magnitudes relative to other sectors are not affected. However, the scaling does affect the absolute magnitude of

the corrected backscatter data. Similarly the change in the absolute magnitude of the backscatter data shifts the ARCs without changing their shape (see Figure 5.4). Comparing the ARCs in the figure, the backscatter strengths in case 2 are approximately 1.8 dB lower than in case 1.
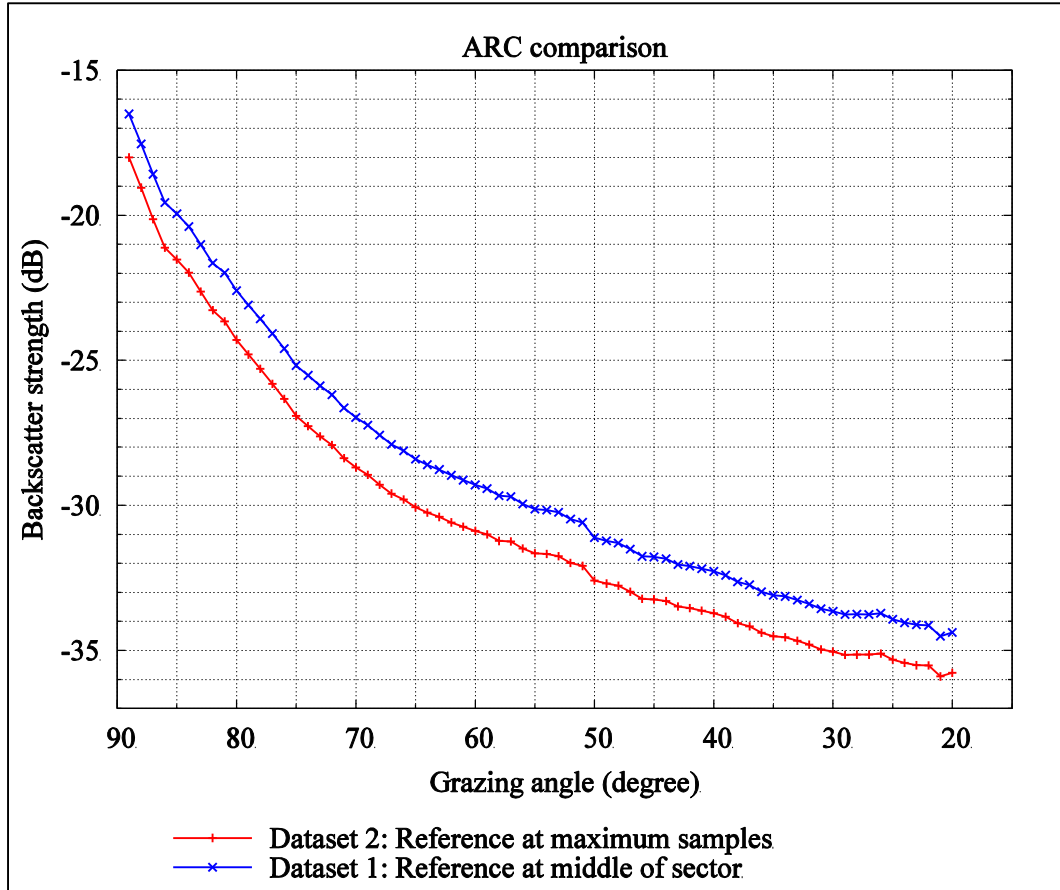
Figure 5.4: Similar ARCs with different absolute backscatter strength obtained in case 1 and 2

For the case of backscatter images, the change in absolute intensity will make the image darker or lighter. The manufacturer claims a specific source level but, as seen in this research, it varies across-track. The SRA-T at which that specific level is corrected is

not reported. Hence delivered backscatter intensities remain only a relative value, free from radiation-induced angular variations and the true values are unknown.

In this situation the user has to choose the reference for across-track RBP master function arbitrarily. In this thesis it is recommended that the maximum transmit intensity SRA-T should be chosen as the master reference. The central sectors near nadir are expected to have the highest transmit intensities. However, due to relatively less samples and relatively higher SDs in that region, the SRA-T with highest transmit intensity from the outer sectors was chosen as the master reference.

In conclusion for this analysis, the selection of a specific across-track RBP function reference does not have any significant effect on the shape of the function, their relative magnitudes, and propagated SDs. The choice of master reference will, however, arbitrarily shifts the whole pattern. In the absence of knowledge of the SRA-T at which the source level really is the stated value, this is unavoidable. For the reasons described in the last paragraph, the references and master reference were chosen at the peak intensity SRA-T of the sectors for further analysis.

5.2   Sensitivity to Magnitude of Roll during the Data Collection

As explained in the data collection strategy section, the test data required for the extraction of the across-track RBP were collected by deliberately rolling the vessel. As

not all vessels can be rolled deliberately with same magnitude, this analysis was performed to test the effect of different magnitudes of rolling on the extracted RBP. For this analysis, three different datasets were used. For each case, the number of profiles in each dataset was very similar (696±1) thus having the same influence in all the cases. The datasets were collected on the same test site with the same geometry and the true backscatter strength of the seafloor, thus their effects were equal for all three cases. All three cases have their references for the functions at exactly the same SRA-T (selected at the middle of the sectors). The three cases are described in Table 5.2.

Table 5.2: Description of datasets used for the three cases

Case	Description
Case 1: Heavy roll	A dataset used was collected under heavy roll. Frequency distribution of the roll is shown in Figure 5.5.
Case 2: Moderate roll	A dataset used was collected under moderate roll. Frequency distribution of the roll is shown in Figure 5.5.
Case 3: Light roll	A dataset used was collected under light roll. Frequency distribution of the roll is shown in Figure 5.5.

Using the data from case 3, it is apparent that this did not properly extract the RBP. This indicates that with roll less than ±3°, extraction of the RBP was not viable on that particular test site. Two important observations were made during this analysis as explained in the following sections.
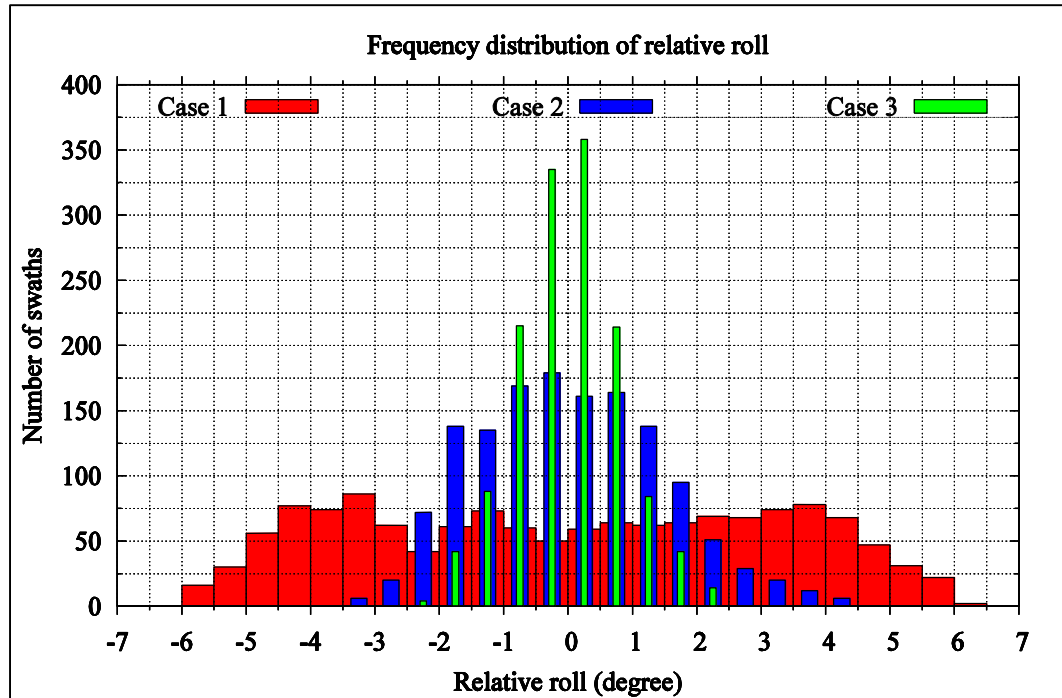
Figure 5.5: Frequency distribution of relative magnitude of roll in cases 1, 2, and 3

5.2.1 Angular Coverage of Sub-Functions and Functions

In the analysis it was found that the propagated SDs of the extracted across-track RBP master function were directly related to the magnitude of the roll; indicating that the extracted RBP is degraded with less roll. Figure 5.6 compares the absolute SDs for sector 0 for three cases. Similar results were seen for all other sectors.
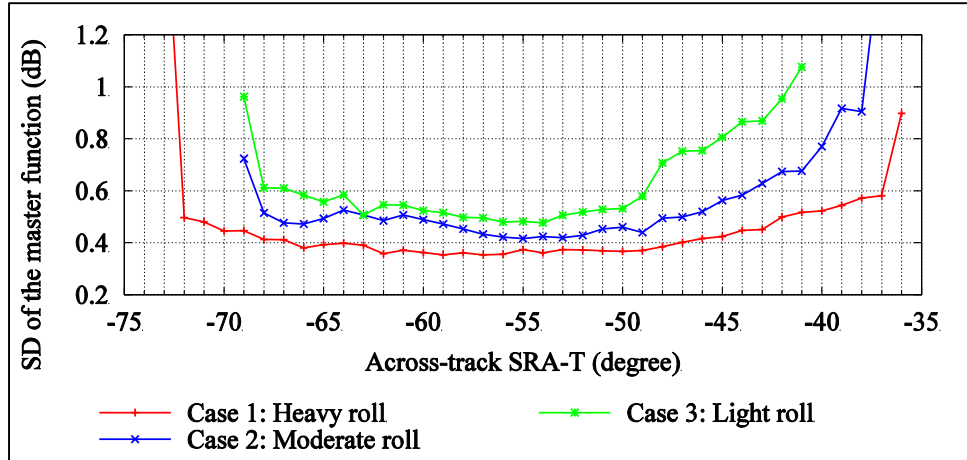
Figure 5.6: Absolute SDs of extracted across-track RBP master function for sector 0 indicating clear relation with magnitude of roll

The ultimate reason behind the degrading of the SDs was directly related to the angular coverage of the sub-functions extracted at the beginning of the process. A specific GRA at the seafloor was illuminated by a wider range of SRA-Ts if the magnitude of roll was higher and vice versa. For example, the sub-function at SRA-T -61° for sector 0 has angular coverage of 19° in case 1, 15° in case 2, and 12° in case 3 as shown in Figure 5.7.
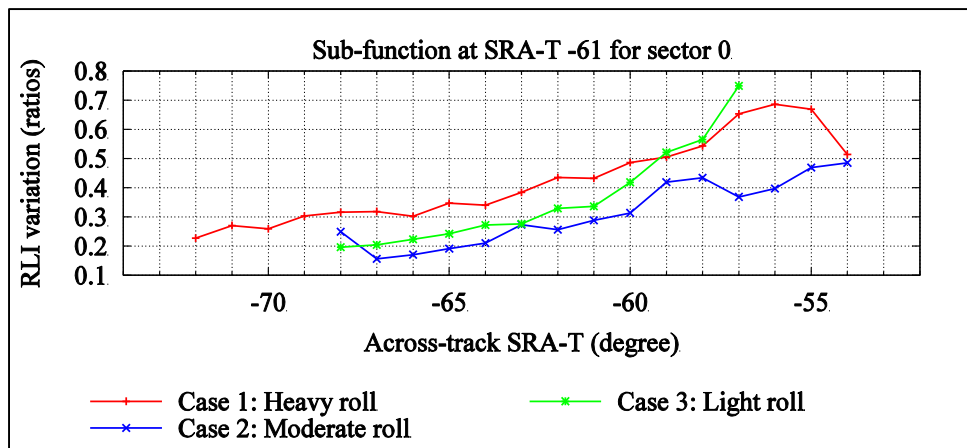
Figure 5.7: Wider angular coverage of sub-function in case 1.

The wider range of SRA-Ts facilitates wider angular coverage of across-track RBP sub-function; which increases the precision in two ways: 1) by increasing number of common SRA-Ts used for the computation of the stacking offsets between the sub-functions, and 2) by increasing the number of sub-functions used in the computation of the function for the sector. Figure 5.8 shows the number of common SRA-Ts used after the outlier removal for the stacking process, while Figure 5.9 shows the number of sub-functions that were used for the averaging process.
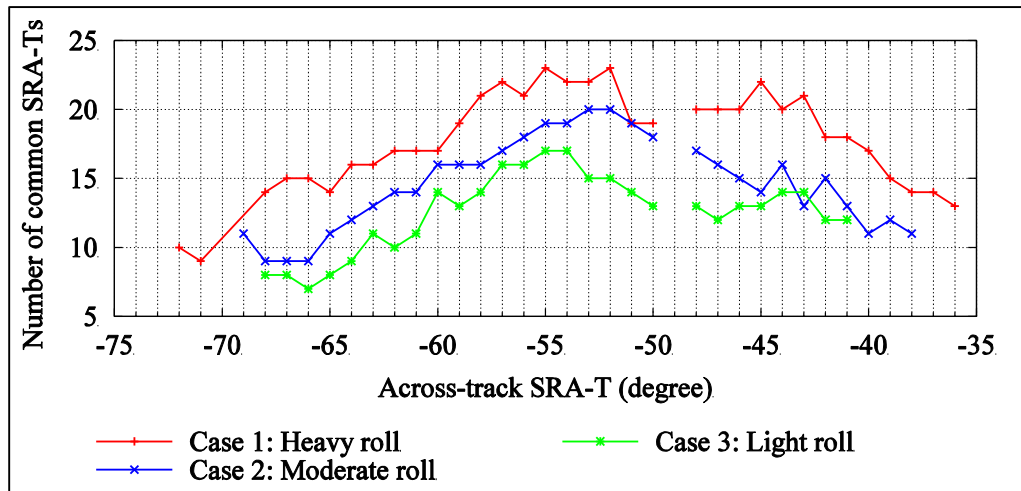
Figure 5.8: Number of SRA-Ts used for the computation of offset between the sub-functions for stacking process (sector 0).

The second benefit of heavy roll is the overall wider angular coverage of the RBP extraction. As shown in Figure 5.10, the across-track RBP function for sector 0 in case 1 has coverage from -73° to -34° SRA-T, while in case 3 the extraction was possible only from -69° to -41° SRA-T. In other words, if the RBPs were extracted from data with moderate magnitude of roll and, subsequently during routine data collection the vessel rolls heavily, then there would be no computed RBP available at that extreme SRA-T.

168

This problem can be avoided by extrapolating the extracted RBP with moderate roll data to wider range of SRA-Ts. The developed algorithm is capable of doing least square regression to fit a polynomial of up to 5th order of magnitude. Depending on the shape of the extracted RBP function the order of magnitude of polynomial fit can be selected.
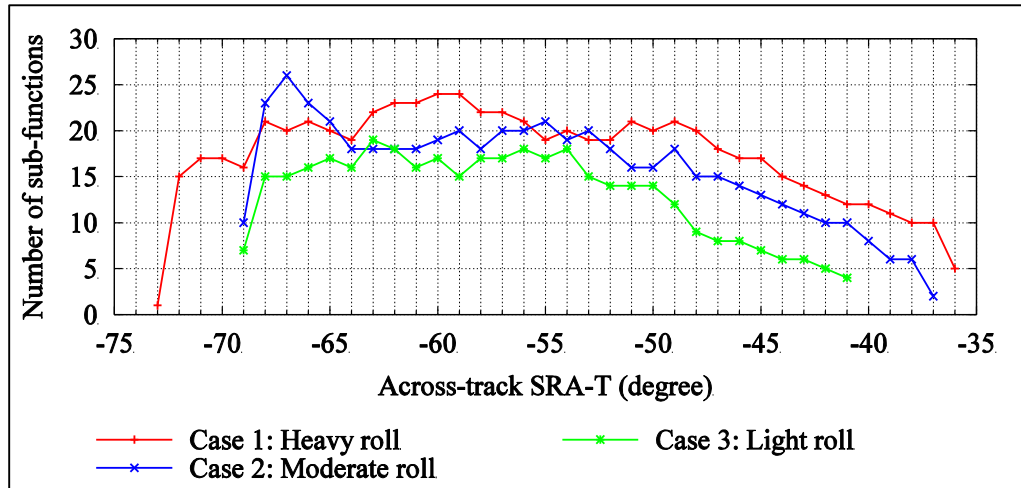
Figure 5.9: Number of sub-functions used for computing the function during the averaging process (sector 0).
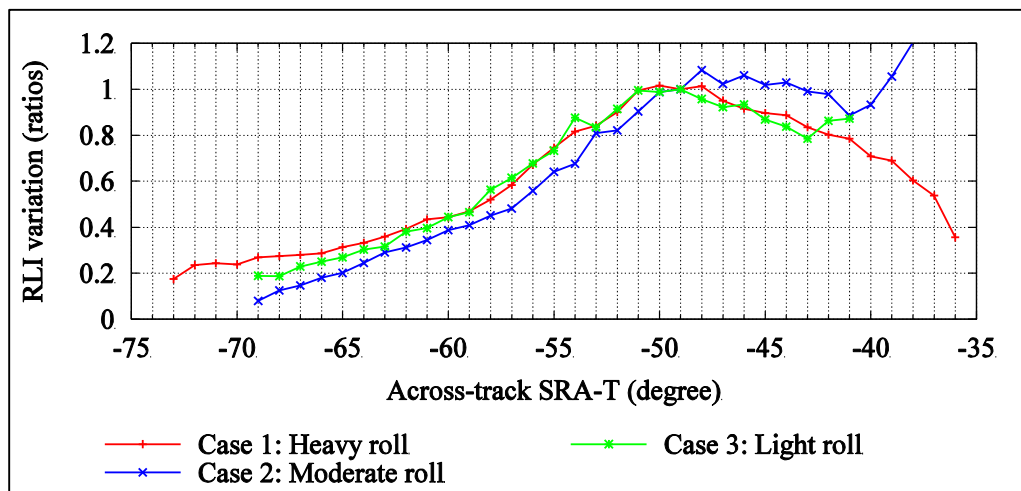
Figure 5.10: Across-track RBP master function sector 0

169

5.2.2   Common GRAs between the Sectors and Magnitude of Roll.

In order to compute the sector offsets relative to sector 0, a significant number of common GRAs are required between sector 0 and those other sectors. These offsets relate all the functions to the function of sector 0 in order to obtain the master function. The observations in this analysis indicate no relationship between number of common GRAs and magnitude of roll. At first thought it might be expected that number of common GRAs between the sectors will increase with the magnitude of the roll. As the sector boundaries are roll stabilized, however, the magnitude of the roll will not have any relation to the number of common GRAs. Figure 5.11 shows the number of GRAs used in all three cases. In contrast, for the case of roll stabilized sector boundaries the only way to generate common GRAs is for the seafloor slope to vary. This is explained in Section 5.3.1.
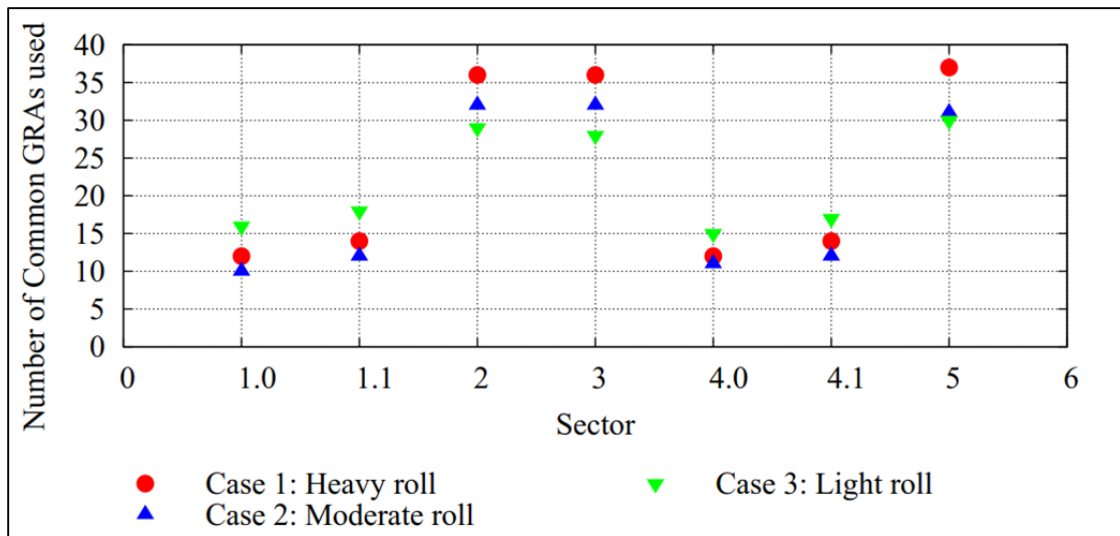
Figure 5.11: Common GRAs between sector 0 and other sectors

In this analysis, two important aspects were found. First, with high magnitude of roll more precise sector–specific RBPs with wider angular coverage can be obtained. Secondly, the magnitude of roll does not play any role in the computation of offsets between the sectors, as sector boundaries are roll stabilized. Clearly another mechanism than roll, is needed to provide the common GRAs from adjacent sectors. The only way to do this is to vary the seafloor slope.

5.3   Sensitivity to the Topographic Character (Slope Distribution)

This analysis examined the effects of test site seafloor slope variation on the extraction of RBP. For this experiment a common dataset collected over a single test site was divided into three cases as shown in Table 5.3.

Table 5.3: Data selection criteria used for the slope analysis

Case	Criteria
Case 1: 350 profiles in both direction	Used all the profiles from two survey lines collected in opposite directions. (Total number of profiles used was 700; with dual swath system, total number of swaths was 1400)
Case 2: 175 profiles in both direction	Used every alternate profile from the same two survey lines used in case 1. (Total number of profiles used was 350; with dual swath system, total number of swaths was 700)
Case 3: 350 profiles in same direction	Used all the profile from a single survey lines from the two survey lines used in case 1. (Total number of profiles used was 350; with dual swath system, total number of swaths was 700)

171

It should be noted that the data used in three cases were collected on the same test site ensuring the same seafloor geometry and backscatter strength. All three cases have their references for the functions and master reference at exactly the same SRA-Ts, which were selected at the middle of the sectors. For three cases it was necessary to have the same magnitude of roll in order to eliminate any effect due to different magnitudes as seen in the previous section. In Figure 5.12 it is evident that all the three cases have almost identical distribution of roll in the utilized swaths.
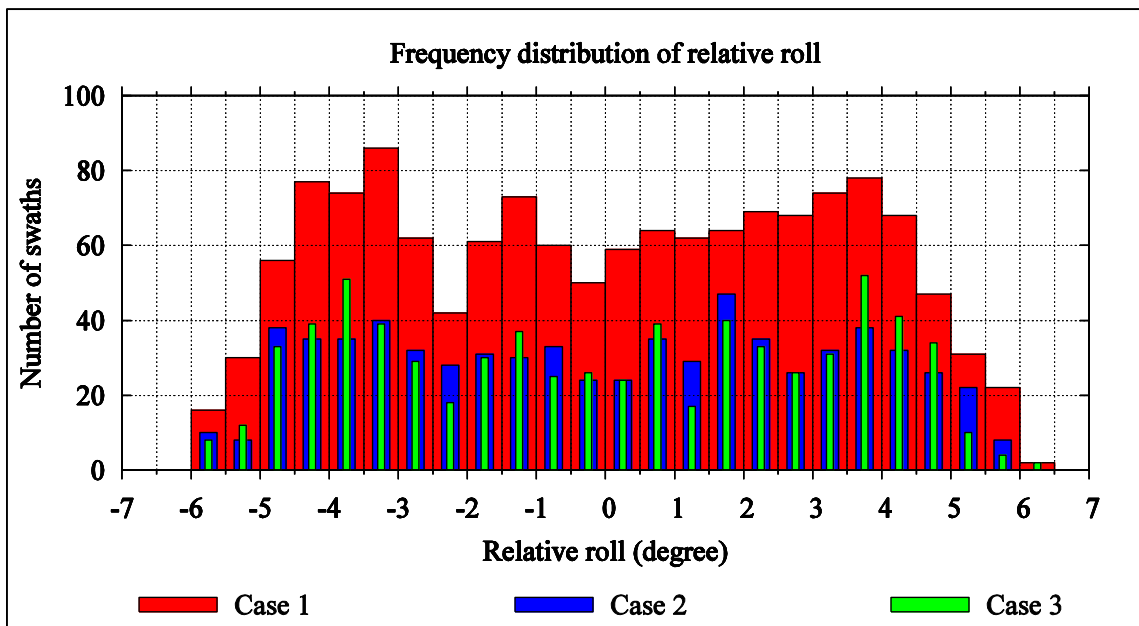
Figure 5.12: Frequency distribution of relative roll in cases 1, 2, and 3

At the end of the analysis, the across-track RBP master function was successfully extracted only in case 1 and 2. The ARCs extracted using these across-track RBP master functions are shown in Figure 5.13. The ARCs are similar indicating that reliable across-track RBP can be extracted even with just 350 profiles collected on that particular test site.

Case 3 could not produce the final across-track RBP master function despite having the same number of profiles as in case 2. However case 3 successfully extracted the across-track RBP functions for each sector. The detailed analysis gave insight into the data collection strategies that need to be implemented in order to extract the RBPs more effectively.
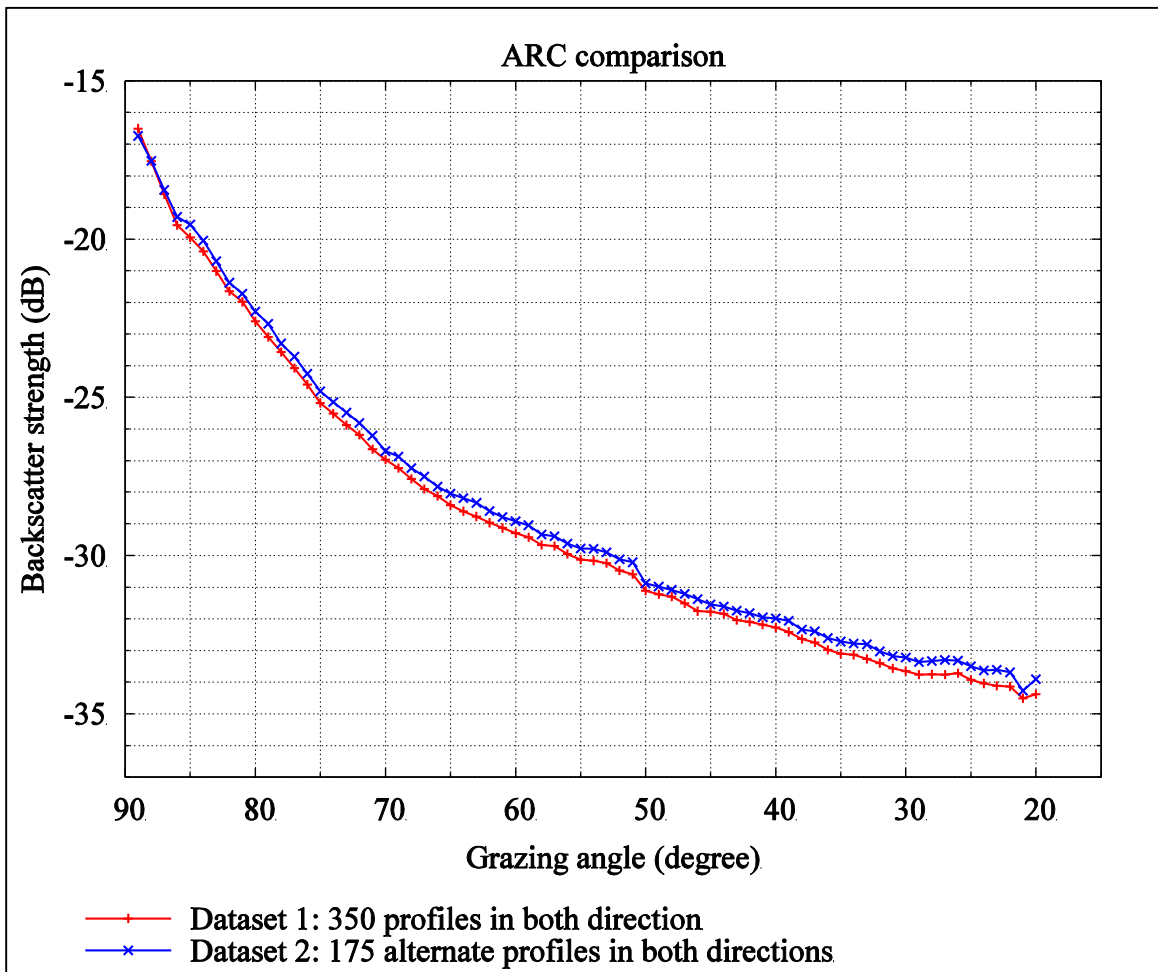
Figure 5.13: Similar ARCs obtained in cases 1 and 2

5.3.1 Failure to Compute Sector Offsets

Case 3 produced across-track RBP functions but failed to compute the sector offsets required to compute the final master function. The failure was due to having only one common GRA available between sector 0 and sector 1.1 and 4.1 (stbd sub-sector of sector 1 and 4). Figure 5.14 shows the numbers of common GRAs used for the computation of the sector offsets for three cases; the number of common GRAs was lowest for case 3. In case 3, sector 1.1 and 4.1 had only 1 GRA common with sector 0 which led to the failure of the extraction process.
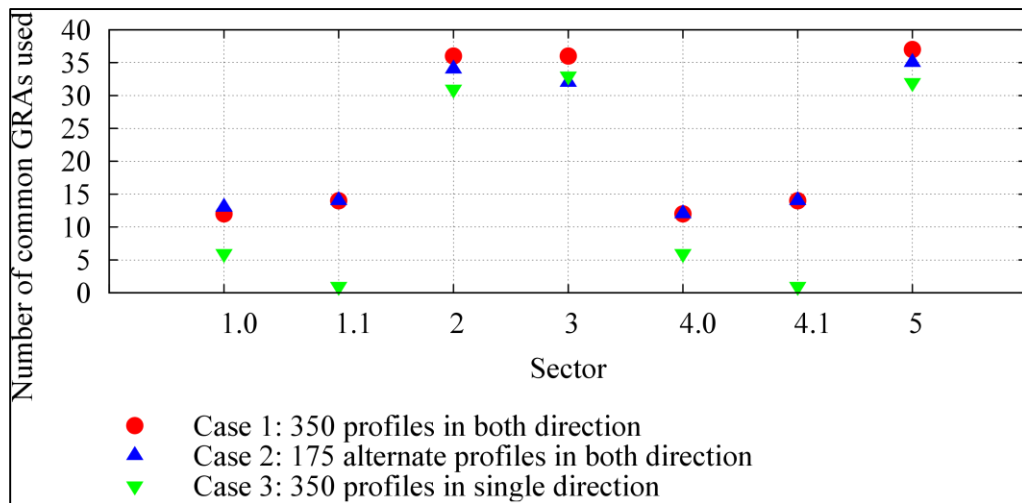
Figure 5.14: GRAs common between sector 0 and other sectors

Two points can be made from Figure 5.14. 1) Case 1 and case 2 have identical numbers of GRAs despite case 2 having half the number of profiles as used in case 1. 2) Case 3, while having a similar number of profiles as case 2, has the lowest number of common GRAs. Primarily this indicates that the number of common GRAs does not depend on the amount of data used. In the previous section, which looked at the effect of

magnitude of roll, it was concluded that the number of common GRAs did not depend on the magnitude of roll.
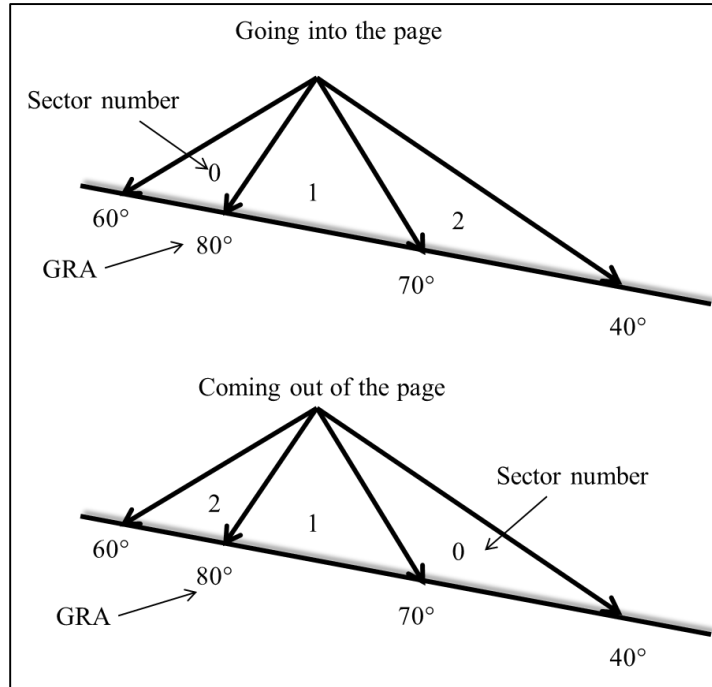
Figure 5.15: Seafloor geometry and direction of survey line affecting total GRA coverage

As GRA is defined relative to the seafloor surface and not to the sonar reference frame, the numbers of common GRAs solely depend on the seafloor slope, its variability, and the orientation of the survey lines. The test site that was used to collect the dataset was planar with about 5% of gradient perpendicular to the direction of the survey lines. As illustrated in Figure 5.15, in case 2, with survey lines in both directions, each sector covers a wider range of GRAs compared to data collected in single direction only (case 3). Even if multiple lines of data are collected on a gently sloping seafloor, running the survey lines in only one direction will result in fewer common GRAs compared to the lines collected in both directions. On the other hand, in the case of a seafloor with an

175

undulating surface or with variability of seafloor slope, data collected only in a single direction can still result in a sufficient number of common GRAs between sectors.

5.3.2   The Angular Coverage of Sub-Functions

In case 3 the across-track RBP functions were successfully extracted. However, it was noticed that their SDs were higher than in case 1 and 2 as shown in Figure 5.16. As concluded in section 5.2, the range of sub-functions was directly related to the magnitude of roll and the greater range of the sub-function resulted in higher precision of the functions. However, the magnitude of the roll was similar for all three cases and the reduced precision in case 3 is related to seafloor slope.

In case 3 fewer sub-functions (as shown in Figure 5.17) were available to compute the functions for each sector by averaging. As previously stated this was due to the smaller angular range of sub-functions.
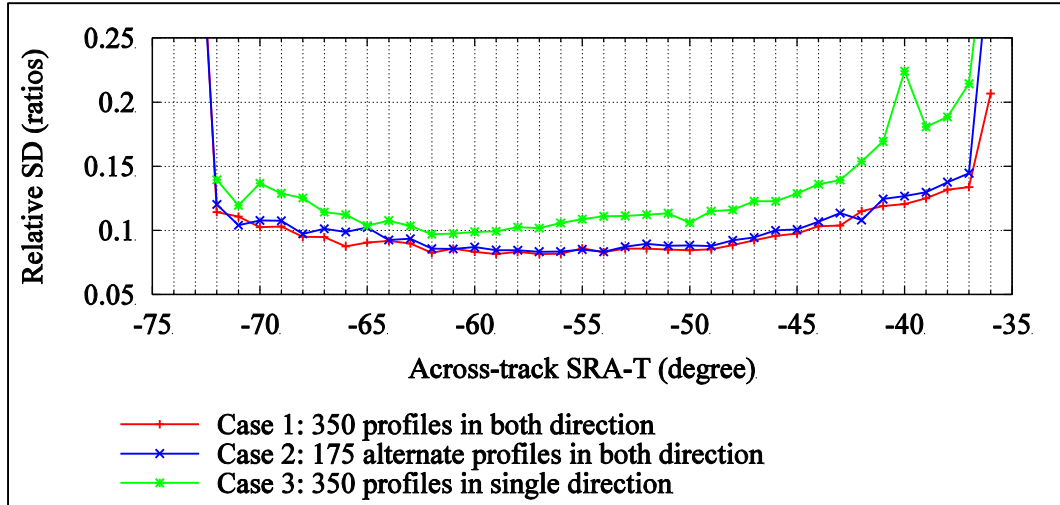
Figure 5.16: RSDs of across-track RBP function (sector 0) showing higher uncertainty for case 3.
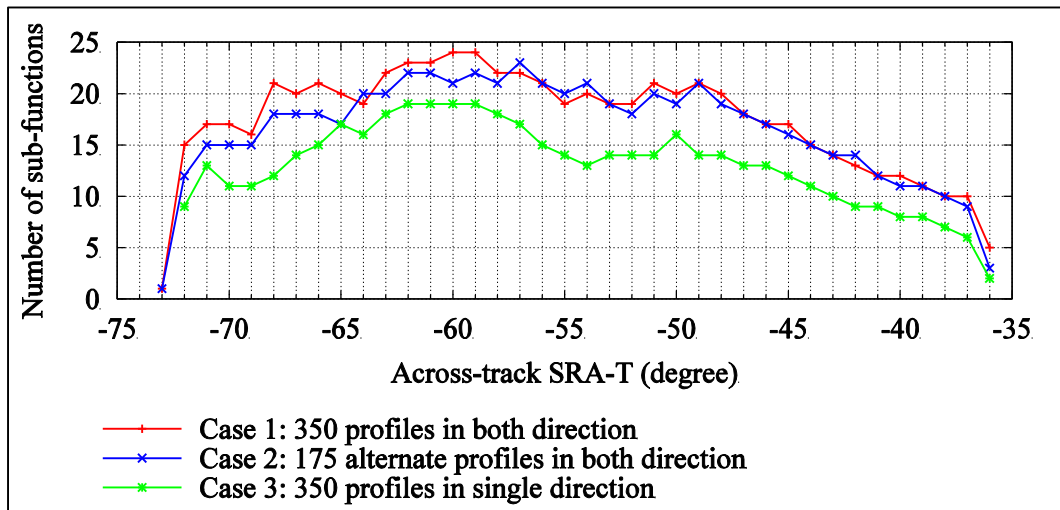
Figure 5.17: Fewer sub-functions contributing to the averaging process for case 3

The angular coverage of the sub-function not only depends on the magnitude of the roll but also depends on the slope of the seafloor. This is explained using Figure 5.18. If the data are collected perpendicular to the slope of the seafloor and going in both directions, a single GRA of 60° is illuminated with the wider range of the SRA-Ts which increases the angular coverage of the sub-function extracted at SRA-T -60°. The factors

which contribute towards wider angular coverage for sub-functions includes: A) the seafloor slope, B) survey lines parallel to seafloor slope contours, and C) collection of the data in both directions. Case 3 exhibited reduced angular coverage thus reduced precision due to the lack of factor 3.
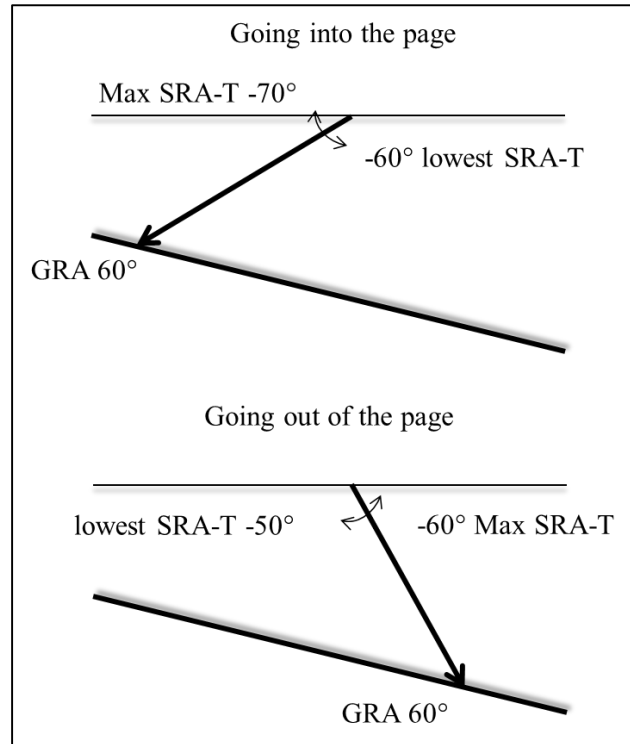
Figure 5.18: Seafloor geometry increasing the range of SRAs illuminating a GRA.

In the conclusion of this analysis two important points concerning seafloor slope can be made. Firstly the common GRAs between sector 0 and other sectors do not depend on magnitude of roll or number of profiles. Rather it depends on the slope of the seafloor (and its variability) and the direction of the survey. On a flat seafloor a GRA will not have SRA-Ts from adjacent sectors even with heavy roll. Hence some other means of varying GRA for a given SRA-T is needed. One way of achieving this range of SRA-T is

178

using natural slope variability. Very gentle regional slope may be insufficient to have enough range of SRA-Ts. Reversing the survey azimuth on the same sloping seafloor or using undulating seafloor increases the number of common GRAs. Without common GRAs insufficient inter-sector overlap exists and thus the master function cannot be obtained. Hence it is crucial to have a gently sloping test site for the data collection.

Secondly if the data is collected on the sloping seafloor in both directions some range of SRAs within the sector can be obtained without rolling. More undulating seafloor will increase the range of SRAs looking at a GRA enabling extraction of sub-functions. This is important, as not all vessels can be induced to roll. However, care must be taken to ensure homogeneous sediment type on the entire test site. Changing steep slopes normally tends to result in different sediments. Different sediments at the same GRA will contradict the fundamental principle of the extraction method.

5.4   Factors Affecting the Along-Track RBP Extraction

As found in previous sensitivity analysis, seafloor slope is crucial for across-track RBP extraction as it is necessary to obtain common GRAs between sectors in order to compute sector offsets to relate the across-track RBP functions to a common reference. However, the extracted along-track RBP sub-functions for each sector are already referenced to a common reference (the across-track RBP has accounted for this) and there is no need to compute the sector offsets. This eliminates the need for common GRAs

179

between the sectors. Hence, in the case of along-track RBP extraction, the test site can have minimal or no slope. It also eliminates the need for collecting data in the reverse direction.

The magnitude of roll is irrelevant in the case of along-track RBP. The intensities at a specific GRA from any available range of SRA-Ts due to rolling are already corrected for across-track RBP and only the average value of the corrected intensities is considered for along-track RBP extraction. Hence there is no effect of any roll during the data collection on along-track RBP extraction.

While seafloor slopes and roll are not important, the availability of along-track steering is important. In order to obtain the full range of along-track RBP functions, the dataset must be collected utilizing maximum allowable sector steering (typically up to $\pm 10°$). The range of extracted along-track RBP function is directly proportional to the magnitude of along-track sector steering. If the sectors were steered only $\pm 5°$ during the data collection, then the along-track RBP functions can only be extracted up to $\pm 5°$.

The following analysis examines the effect of the frequency distribution of the sector steering on the extracted along-track RBP function. For this experiment three different cases were selected based on the distribution of the along-track sector steering within the available maximum range as indicated in Table 5.4. All data used in this analysis were collected on the same test site.

Table 5.4: Different criteria for the sensitivity analysis

Case	Criteria
Case 1: Higher number of swaths at maximum SRA-R	The dataset was collected with heavy yawing. The outer sectors were continuously steered either forward or backward at maximum values resulting in the frequency distribution shown in Figure 5.19.
Case 2: Higher number of swaths at maximum and zero SRA-R	This dataset was obtained by adding survey lines with no sector steering to the dataset in case 1. The obtained frequency distribution is shown in Figure 5.20.
Case 3: Distributed swath frequency for all SRA-R	This dataset was obtained by adding survey lines that were collected with slow yawing to the dataset in case 2. The obtained frequency distribution is shown in Figure 5.21.
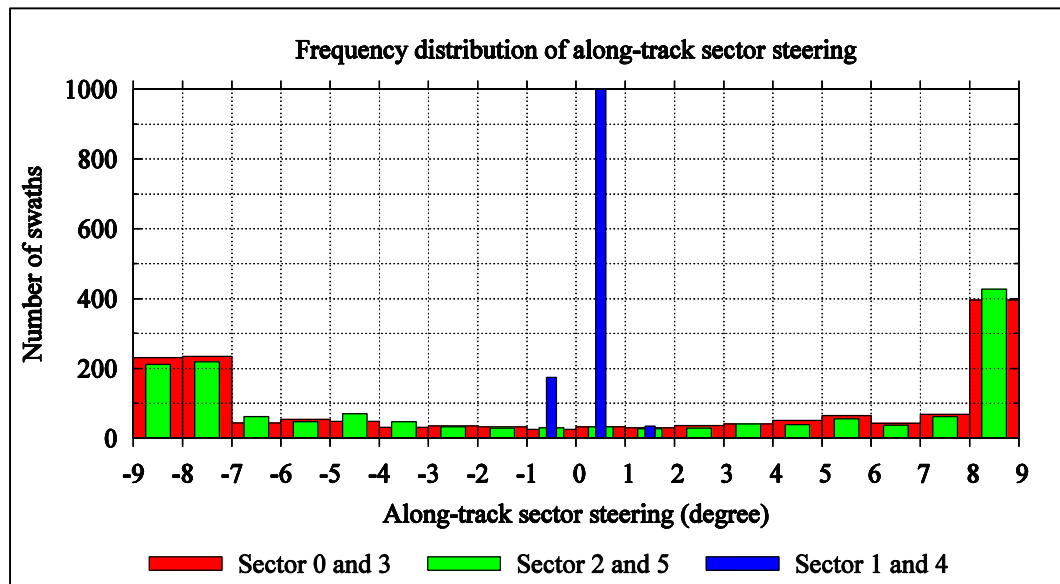
Figure 5.19: Along-track sector steering frequency distribution in case 1
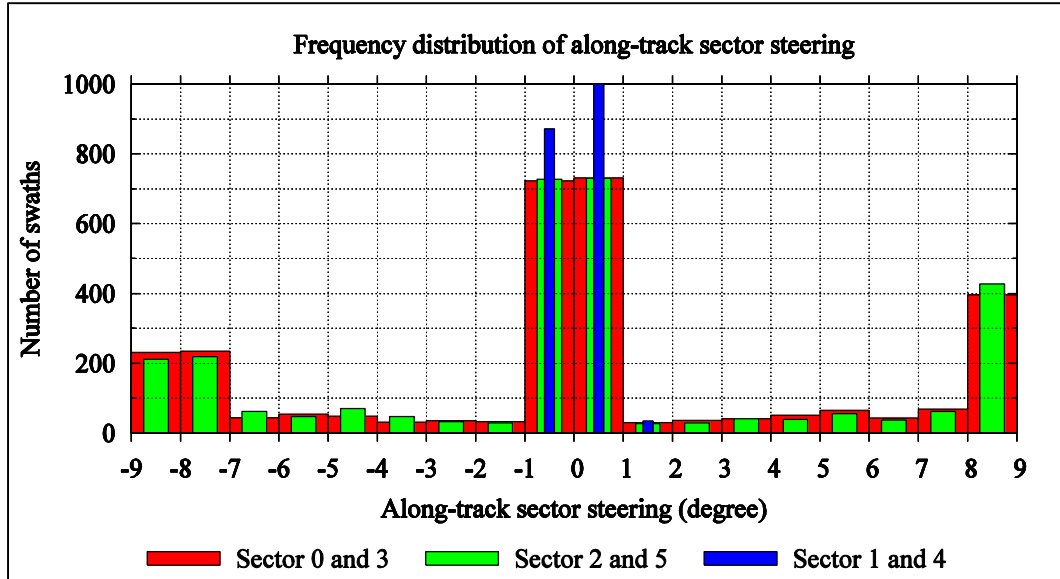
Figure 5.20: Along-track sector steering frequency distribution in case 2
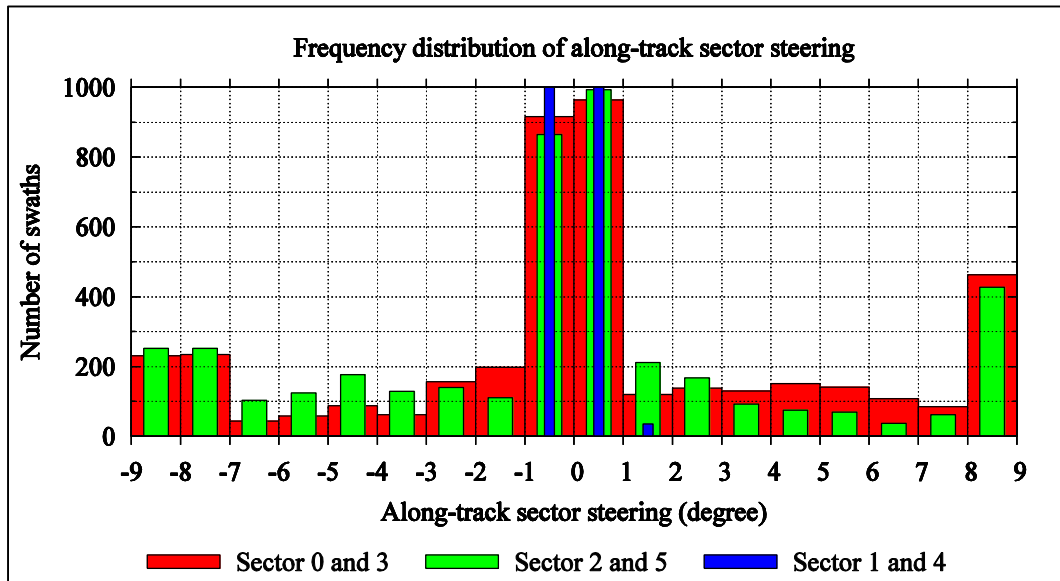
Figure 5.21: Along-track sector steering frequency distribution in case 3

In all three cases the along-track RBP and ARCs were successfully obtained. However some differences in the magnitude of extracted along-track RBP functions were noticed as shown in Figure 5.22.

182

In Figure 5.22, even though the differences between the extracted along-track RBPs in the three cases are less than 1 dB, Case 2 has less variation compared to case 1, while case 3 has the least amount of variation. The sudden decrease or increase in the value of intensity variations cannot be real given the design of the Rx array. Thus it is the result of noise in the data used. This noise is least for case 3 as it experiences less variation. Apart from being more reliable, case 3 has the highest precision as shown in Figure 5.23.
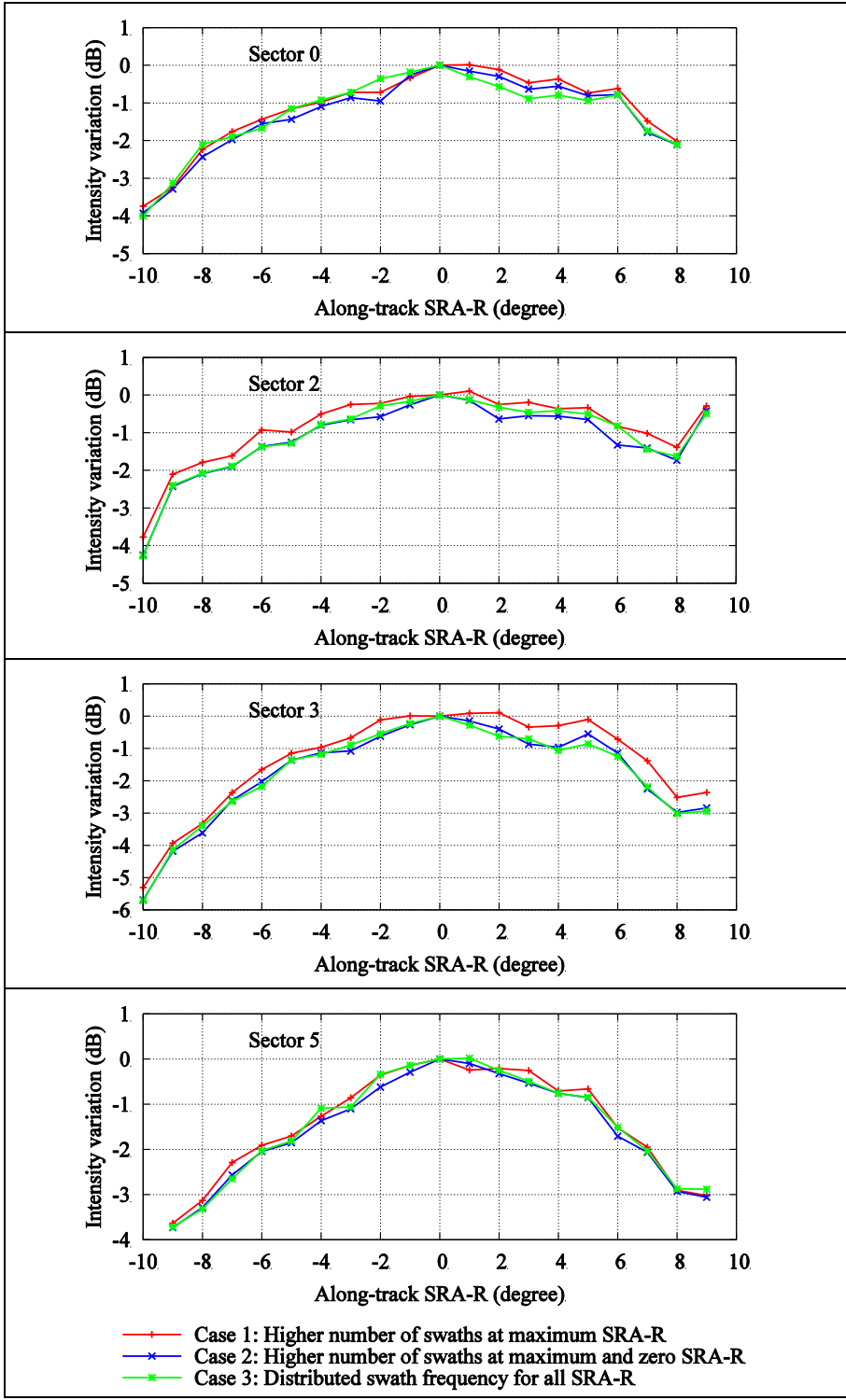
Figure 5.22: Comparison of along-track RBP for sectors 0, 2, 3, and 5
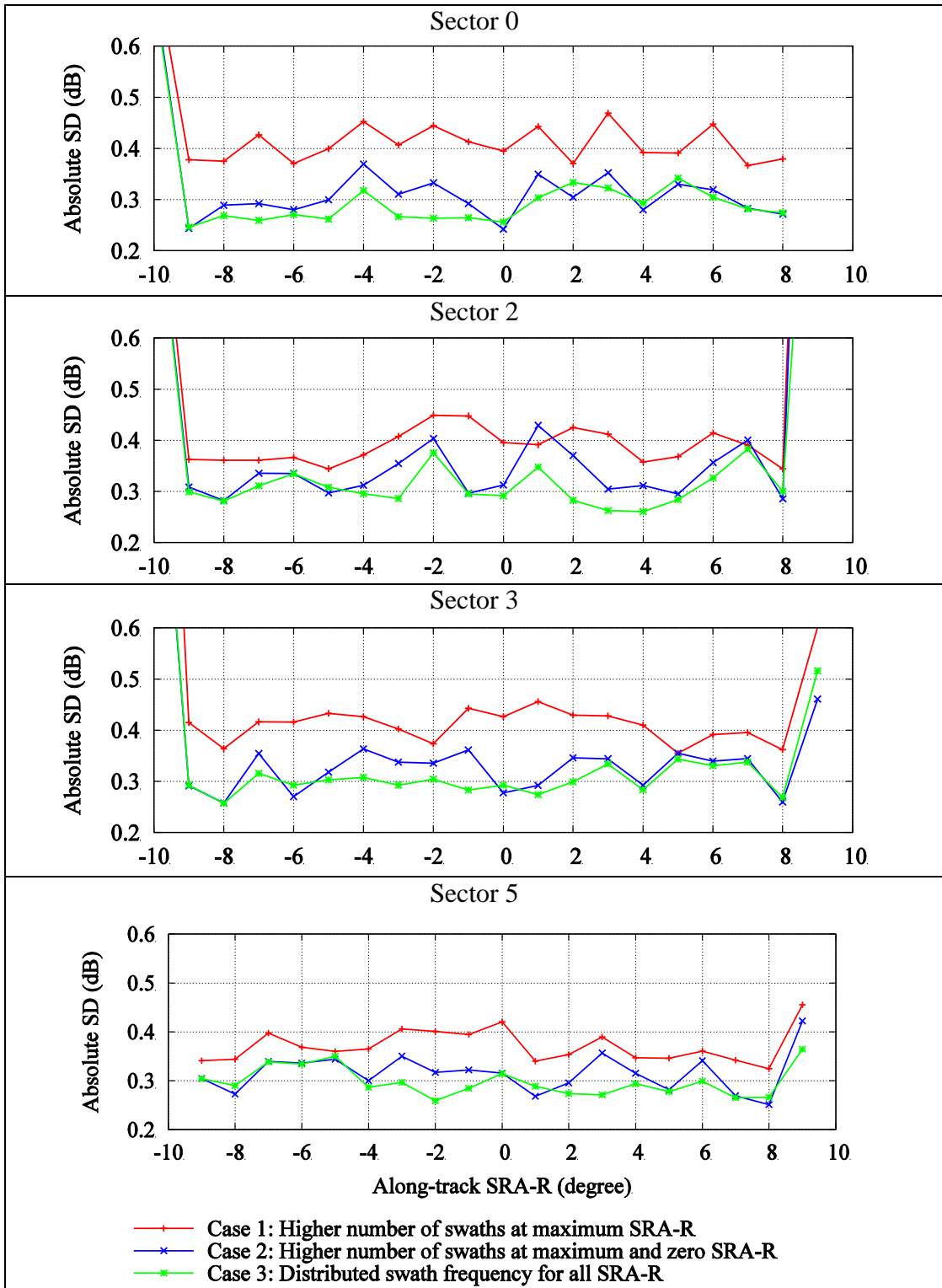
Figure 5.23: Comparison SDs of along-track RBP for sectors 0, 2, 3, and 5

The effect of number of swaths and distribution of along-track sector steering on the SDs of the extracted along-track RBP is important to understand. During the data collection with heavy yaw, the outer sectors were steered either forward or backwards for the majority of profiles and very few profiles were obtained close to 0° along-track sector steering as shown in Figure 5.24 (case 1).
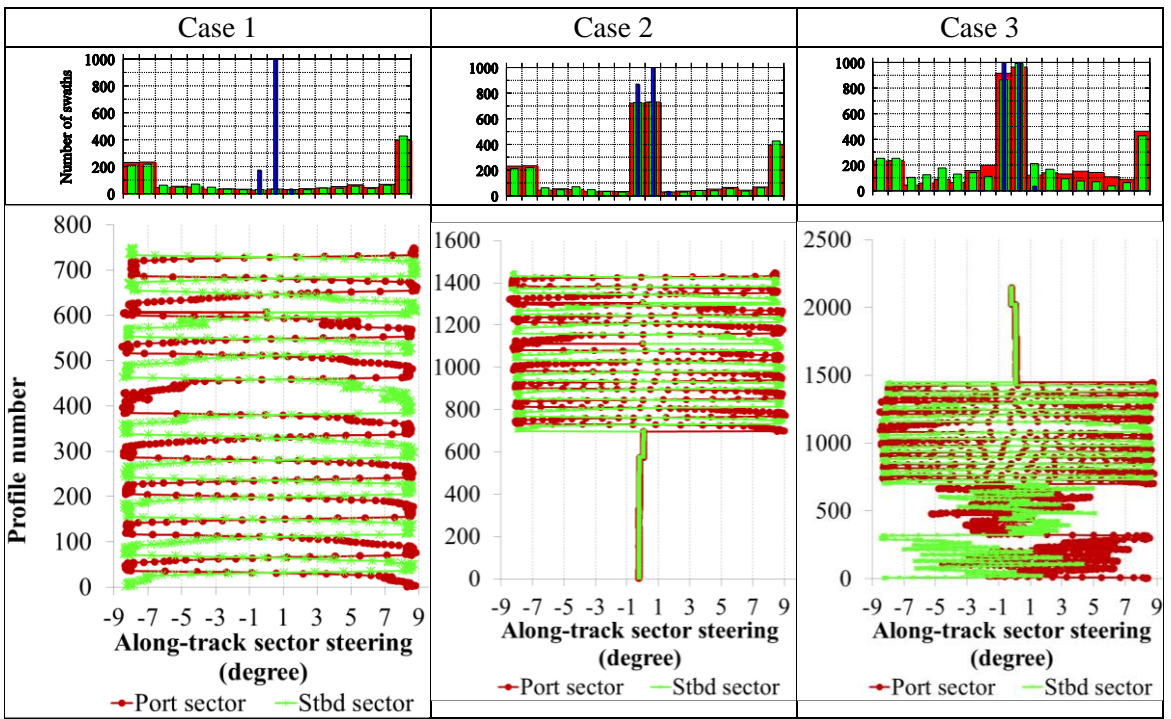
Figure 5.24: Distribution of profiles for cases 1, 2 and 3.

In the developed method, reference for along-track RBP is taken at SRA-R of 0° and typical data collected with yawing motion will not result in sufficient number of profiles at SRA-R 0°. To partially address this drawback in case 1, survey data with no yawing were added to the data with heavy yawing (case 2 Figure 5.24). However the best dataset should be case 3 where equal distribution of swaths over the full range of SRA-R was attempted as shown in Figure 5.24. The better distribution of number of swaths affects

186

the computation of along-track RBP and related SDs in two ways as explained in the next sections.

5.4.1   Increasing SD of the RLI Values

The increased numbers of swaths at zero sector steering added many observations in the GRA and SRA-T bins that fall under the reference SRA-R (0°) bin. In the developed method, these observations were corrected for across-track RBP and then an average RLI was calculated at the reference SRA-R for each GRA. Due to increased number of the observations in SRA-T bins, the average RLI value at the SRA-R bin had higher precision. These more precise reference RLI values were used to compute more precise along-track RBP sub-function values (one for each GRA) by dividing RLIs at other SRA-Rs. The net result is that the SDs of all the computed function values at all SRA-Rs were lowered by using the reference RLI intensities with increased precision. In Figure 5.25, the RSDs of along-track RBP sub-function values at all possible GRAs for SRA-R 0° are shown; the increased precision (decreased RSD values) is apparent for case 2 and 3.

As case 2 and 3 have a large number of swaths at SRA-R 0°, they do not show any further improvement in RDs, suggesting that sufficient swaths have been collected at the reference SRA-R. However Case 3 has the highest number of swaths at SRA-R 3°. This increases the precision of the average RLI values at SRA-R 3° compared to case 2 and 1

for the reasons discussed in the previous paragraph. The increased precision at SRA-R 3°
and increased precision at reference SRA-R results in higher precision of along-track
RBP sub-function values for all GRAs at SRA-R 3°. This increased precision for case 3
at SRA-R 3° is shown in Figure 5.26.
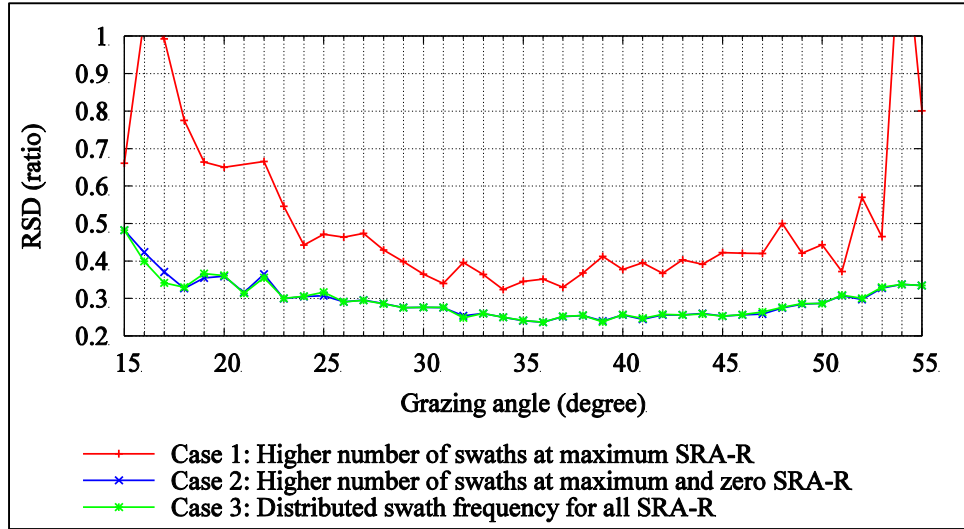
Figure 5.25: RSDs of along-track RBP sub-function values at SRA-R 0° for sector 0
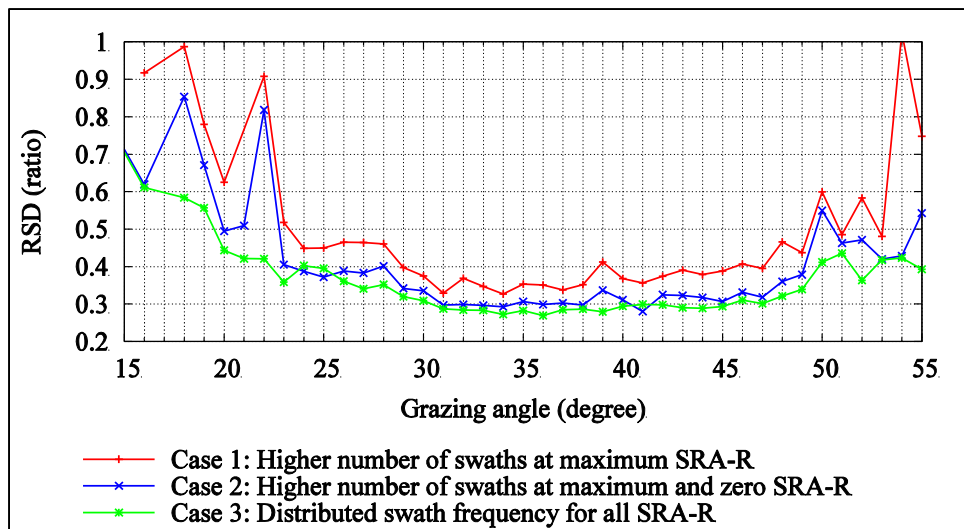
Figure 5.26: RSDs of along-track RBP sub-function values at SRA-R -3° for sector 0

188

5.4.2 Increasing Number of Sub-Functions

In the developed method, along-track RBP sub-functions are computed for each available GRA within a sector. Then available values of sub-functions (from all GRAs) at each SRA-R are averaged to obtain the value of the function at that SRA-R. Increased sub-function values will increase the precision of the computed values of the along-track RBP functions. There are two ways by which increasing the number of swaths can increase the number of sub-functions: A) Utilizing all the available range of GRAs to compute sub-functions and, B) increasing the range of GRAs.

Comparing case 1 and 2 specifically at all non-zero SRA-R values, there was no increase in number of swaths; thus both the cases had same numbers of GRAs available for the sub-function computation for each SRA-R; still an increased numbers of sub-functions at all non-zero SRA-R values can be observed in Figure 5.27. This increase was due to reason A explained above. The computation of sub-functions is not possible if the reference SRA-R values are unavailable for the GRAs. The increased number of swaths at reference SRA-R for case 2 increased the number of reference SRA-R values available for computation of the sub-functions for all the available SRA-Rs. With more available reference SRA-R values, more sub-function values were computed at all non-zero SRA-Rs from the same available range of GRAs.

Further comparing case 3 to case 2 specifically at all non-zero SRA-R values, the higher number of swaths increased the range of GRAs available at all the non-zero SRA-

Rs. This increase led to computation of more sub-function values at all non-zero SRA-R as seen in Figure 5.27, ultimately increasing the precision of across-track RBP functions in case 3 as seen in Figure 5.26. This further highlights the importance of having a significant number of swaths at the reference SRA-R.
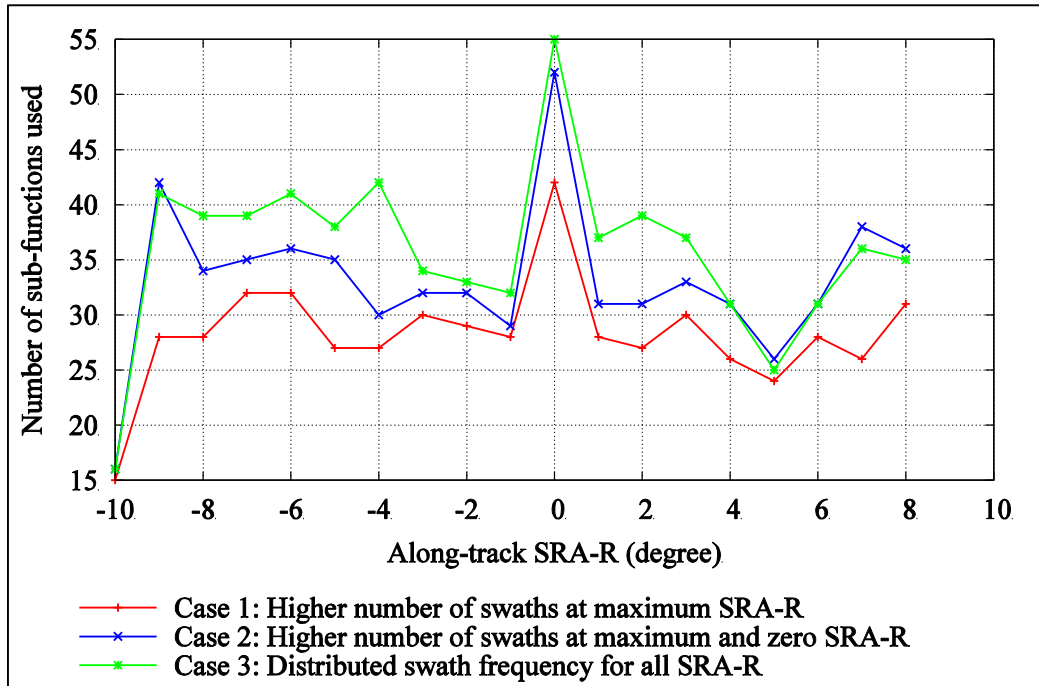
Figure 5.27: Number of sub-functions used for the computation of along-track RBP function for sector 0

The above analysis highlights the necessity of higher and equal number of profiles at all SRA-Rs. However in reality, during the collection of yawing data (as in case 1) it is not always practical to smoothly vary the along-track sector steering throughout the full range without concentrating at the ends of the range. Better data (case 2 and 3) can be obtained by simply adding more survey lines on the same test site without yawing the vessel at the full range.

6   VALIDATION OF THE METHODOLOGY

Chapter 4 has explained the detailed methodology of across- and along-track RBP extraction. Factors affecting the quality of the RBP extraction were discussed in Chapter 5. This chapter validates the reliability and repeatability of the RBP extraction method by comparing results obtained at different test sites and at different times. The developed method is the first direct measurement method for the across- and along-track RBP; no feasible alternate methods of computing the RBPs are available (other than prohibitively expensive far-field direct measurements), hence no direct comparison is possible. In order to validate the proper working of the RBP extraction method, three approaches are used.

The first approach will confirm the reliability of the developed RBP extraction method by comparing ARCs produced for the same test site from four different datasets. The ARCs must be identical for the same test site irrespective of the sonar operating mode and ship's motion. The second approach will confirm the repeatability of the developed RBP extraction method for different seabed types, by comparing extracted across-track RBPs (for Shallow mode, for 2014 datasets). The extracted RBPs must be identical for the sonar (hardware and software) and operating mode irrespective of the underlying seabed type. The third approach will confirm the repeatability of the developed method over a longer time period by comparing extracted across-track RBPs at

different times and different areas (for Very Shallow mode, for 2014 and 2015 datasets). The results of all three approaches are discussed in the following sections.

During this research, datasets were collected in two specific areas with different sonar settings and ship motion. The first area is located in Howe Sound at Squamish River Delta, British Columbia; the second area is located in Bute Inlet, British Columbia, Canada. The across-track RBPs in this chapter are extracted by taking the function reference SRA-Ts at the middle of the sectors for all the cases. It was not always possible to collect the same number of profiles due to time constraints; hence some datasets have different numbers of profiles. The magnitude of the roll also varied between the datasets as heavy roll was induced by rolling the boat manually. In the case of along-track RBP extraction, data with a maximum possible number of swaths and equal distribution of along-track sector steering were used. The effects of these factors on the extracted RBPs have already been discussed in the previous chapter. The best available datasets were used for the validation process in order to confirm the reliability and repeatability of the developed method.

6.1   Validation 1: Reliability of the Developed Method

From many datasets collected at the same test site with different sonar settings and ship motion, four datasets (two survey lines in opposite directions) were selected for this validation approach. During the collection of these datasets, the manufacturer-estimated

RBP corrections were applied. Thus the RBP corrections extracted from these datasets were the remainder of the actual RBPs after the manufacturer's corrections. All four datasets, as described in Table 6.1, were collected on the same test site and hence it is a valid assumption that if the across-track RBP corrections are removed correctly, all four datasets should produce identical ARCs. Only a slight variation is expected in ARCs obtained using different sectors as different frequencies are used in different operating modes by the sonar.

Table 6.1: Selected datasets collected in 50m water depth at Squamish River Delta

Dataset	Sonar mode	Dominant motion	Pulse length	Band width
1	Very Shallow	Rolling	0.3 ms	5.0 KHz
2	Very Shallow	Yawing	0.3 ms	5.0 KHz
3	Shallow	Rolling	0.75 ms	2.0 KHz
4	Shallow	Yawing	0.75 ms	2.0 KHz

6.1.1 Preprocessed Data

Figure 6.1 shows the preprocessed data (one of the two lines) in the form of backscatter images while Figure 6.2 shows the extracted product of ARC and the RBPs.

Test site at Howe Sound, Squamish, depth 50m, year 2015, Manufacturer's RBP corrections applied, Sonar EM 710	
Very Shallow mode	**Shallow mode**
Dataset 1 with dominant rolling motion	Dataset 3 with dominant rolling motion
Dataset 2 with dominant yawing motion	Dataset 4 with dominant yawing motion
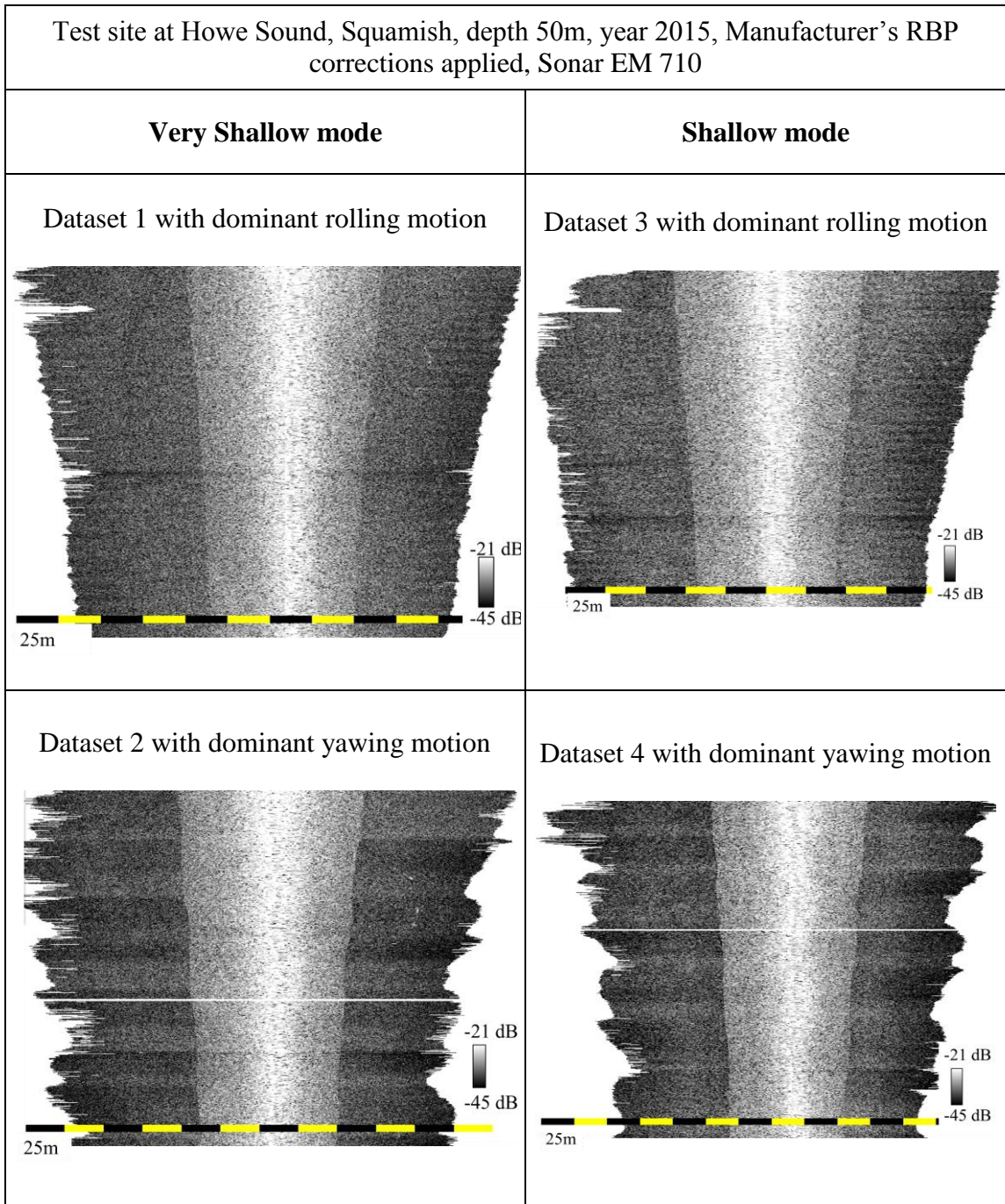
Figure 6.1: Backscatter data after removal of manufacturer-applied TVG-BS for cases 1, 2, 3 and 4.
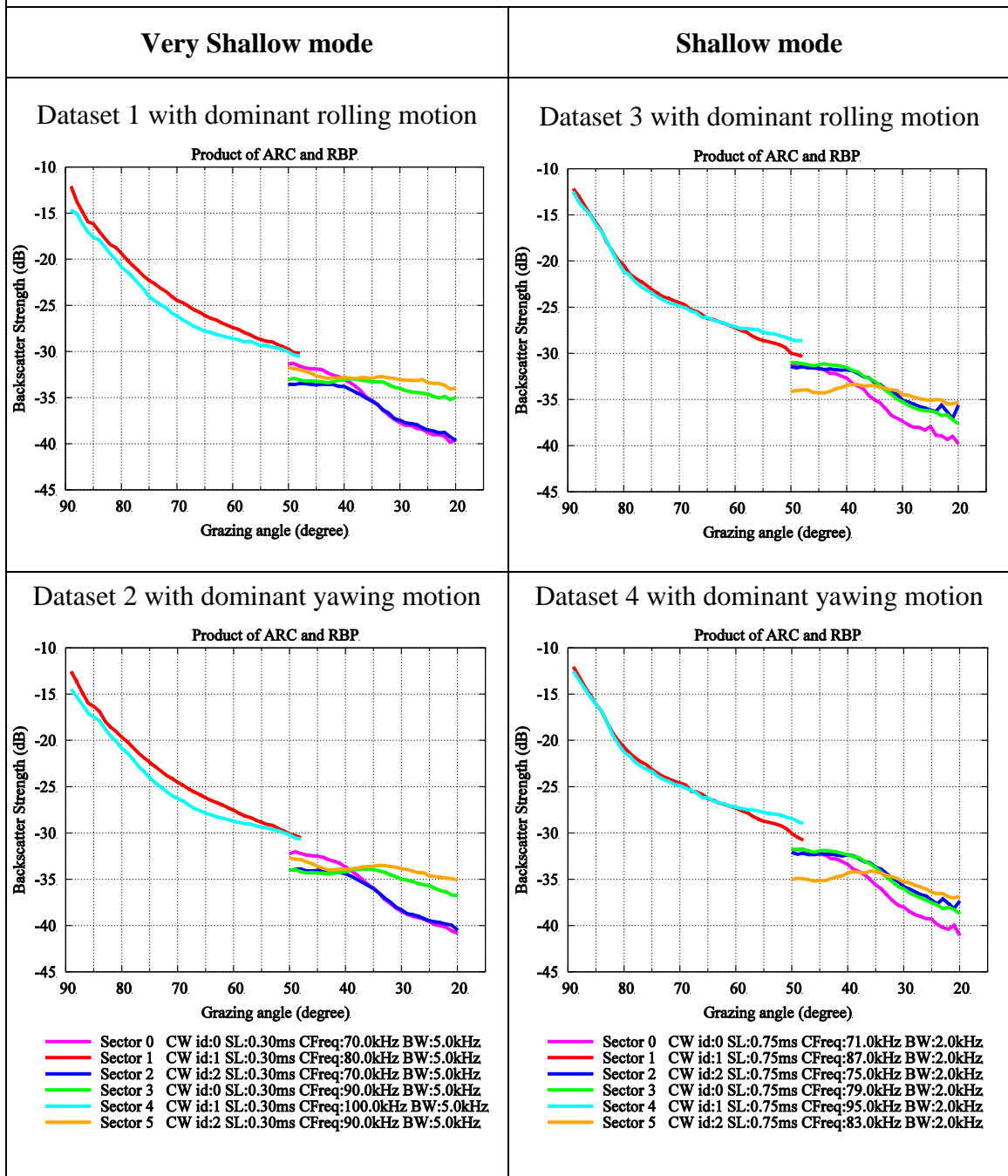
Figure 6.2: Product of ARC and RBP for cases 1, 2, 3, and 4

6.1.2 RBP Extraction

For the Very Shallow mode datasets (1 and 2), the across-track RBP was extracted using dataset 1 as shown in Figure 6.3A. The extracted across-track RBP was removed from dataset 2 and then along-track RBP was extracted as shown in Figure 6.3B. The RBPs for Shallow mode (Figures 6.3C and D) were extracted following a similar process for dataset 3 and 4.

As a side note, when across-track RBPs for Very Shallow and Shallow modes are compared to each other it can be noticed that the different center frequency of the sector can change the shape of the across-track RBP function. This change is greater in the case of sector 1 (80 kHz in Very Shallow mode vs. 87 kHz in Shallow mode), sector 3 (90 kHz in Very Shallow mode vs. 79 kHz in Shallow mode), and sector 5 (90 kHz in Very Shallow mode vs. 83 kHz in Shallow mode) as they have maximum difference in the center frequency between the modes.
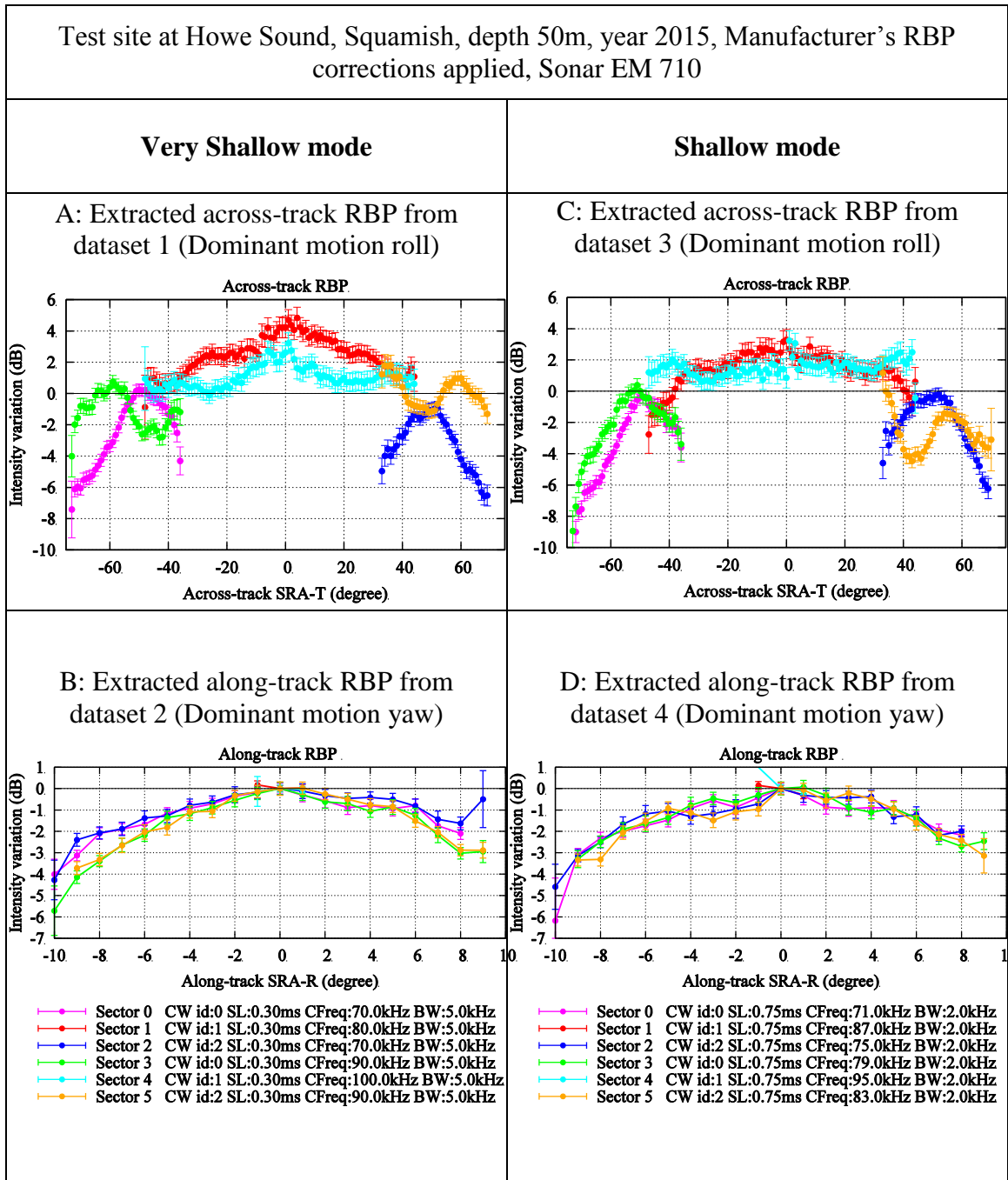
Figure 6.3: Extracted along- and across-track RBPs for cases 1, 2, 3, and 4

6.1.3 Corrected Backscatter Image Comparison

The backscatter intensities were corrected using the corresponding RBPs and corrected backscatter images were obtained. These corrected backscatter images should not have any artifacts related to ship motion; also there should not be any across-track intensity differences between the sectors. Figure 6.4 shows one of the two corrected survey lines from all 4 datasets.

Test site at Howe Sound, Squamish, depth 50m, year 2015, Manufacturer's RBP corrections applied, Sonar EM 710	
Very Shallow mode	**Shallow mode**
Dataset 1 with dominant rolling motion	Dataset 3 with dominant rolling motion
Dataset 2 with dominant yawing motion	Dataset 4 with dominant yawing motion
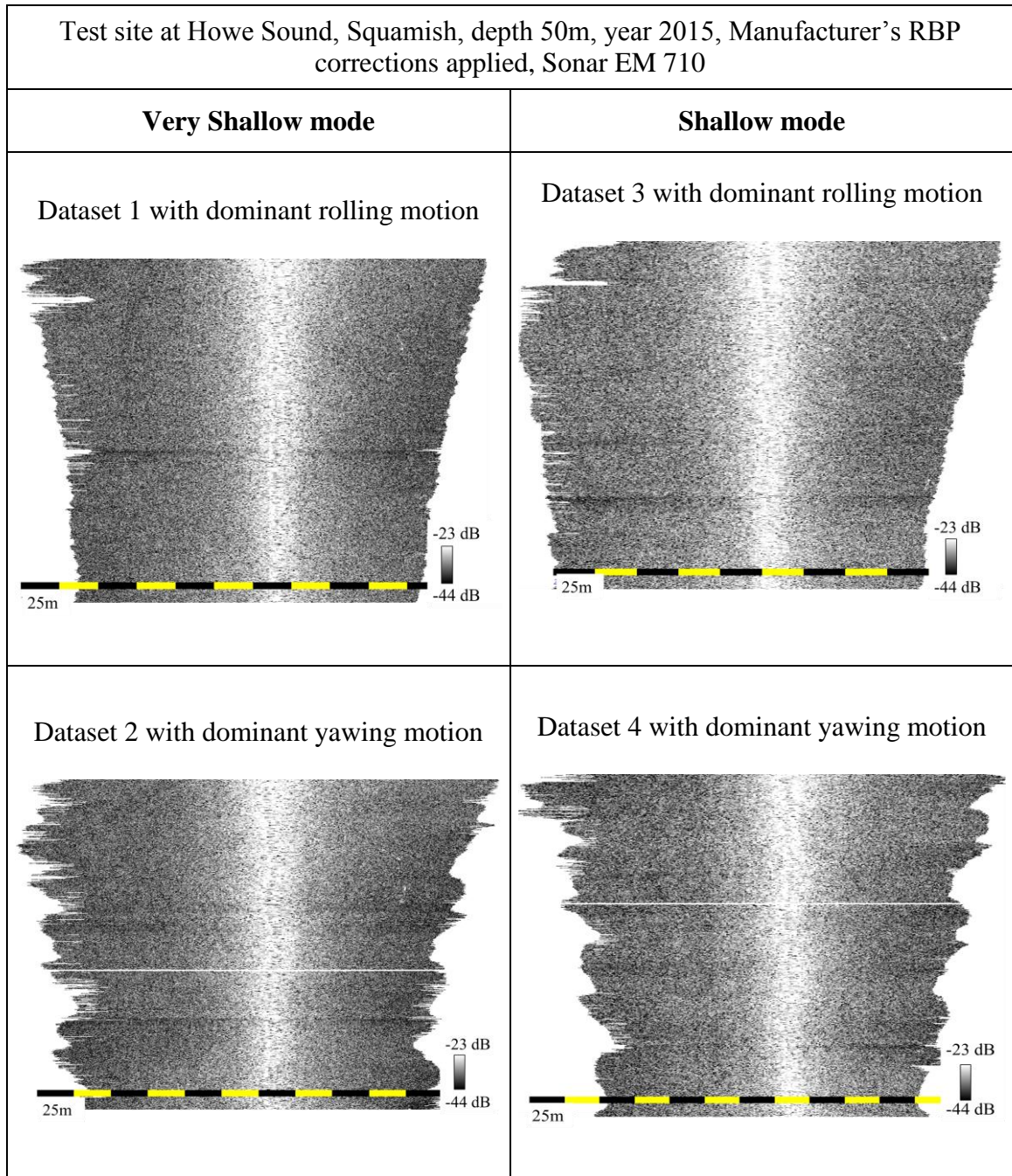
Figure 6.4: RBP corrected backscatter intensities for all 4 cases

Figure 6.4 shows identical backscatter images without any along- or across-track intensity variation (except angular variation and bubble wash) indicating correct removal and extraction of RBPs.

6.1.4 Comparison of ARCs

The ARCs from each dataset were obtained by removing respective operating mode specific across- and along-track RBPs extracted in the previous step. These extracted ARCs from all 4 datasets must be identical as they are for the same homogeneous seafloor. An average of backscatter strengths at each GRA from available sectors was taken and ARCs for each dataset are plotted in Figure 6.5. The sector-specific ARCs for each dataset are presented in Figure 6.6.
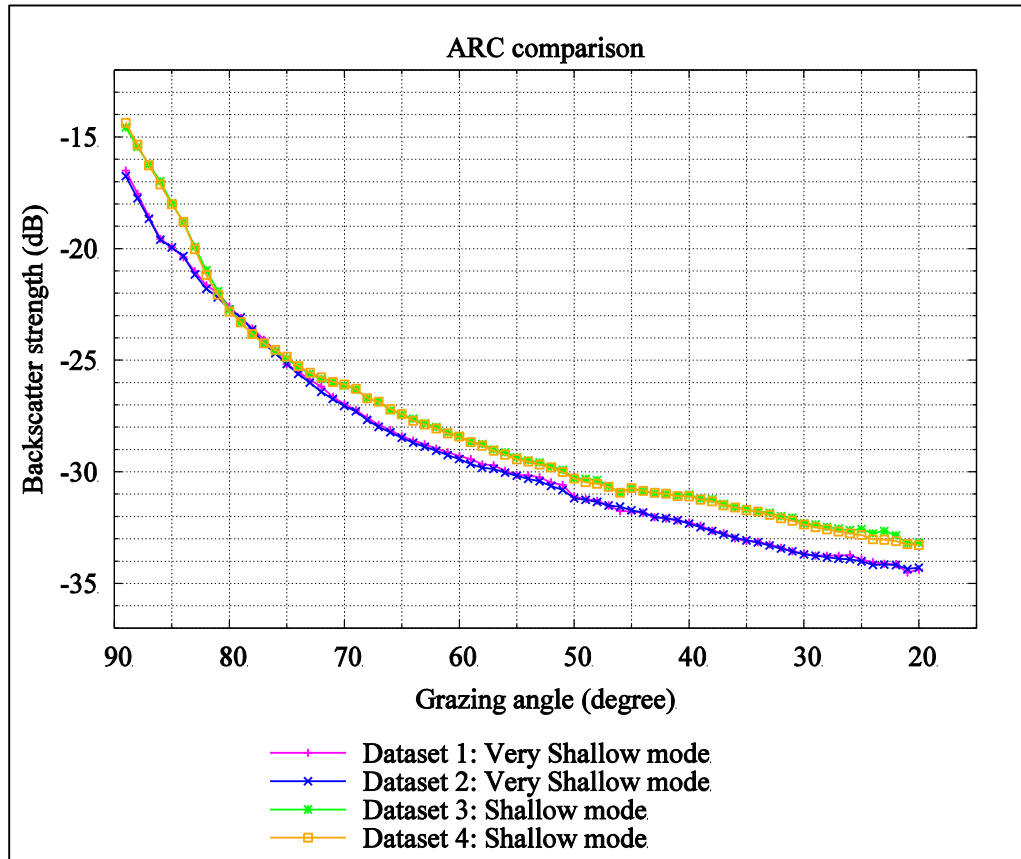
Figure 6.5: Comparison of ARCs between datasets 1, 2, 3, and 4

Test site at Howe Sound, Squamish, depth 50m, year 2015, Manufacturer's RBP corrections applied, Sonar EM 710

Very Shallow mode	Shallow mode

Dataset 1 with dominant rolling motion

Dataset 3 with dominant rolling motion

Dataset 2 with dominant yawing motion

Dataset 4 with dominant yawing motion

	Very Shallow mode legend
Sector 0	CW id:0 SL:0.30ms CFreq:70.0kHz BW:5.0kHz
Sector 1	CW id:1 SL:0.30ms CFreq:80.0kHz BW:5.0kHz
Sector 2	CW id:2 SL:0.30ms CFreq:70.0kHz BW:5.0kHz
Sector 3	CW id:0 SL:0.30ms CFreq:90.0kHz BW:5.0kHz
Sector 4	CW id:1 SL:0.30ms CFreq:100.0kHz BW:5.0kHz
Sector 5	CW id:2 SL:0.30ms CFreq:90.0kHz BW:5.0kHz

	Shallow mode legend
Sector 0	CW id:0 SL:0.75ms CFreq:71.0kHz BW:2.0kHz
Sector 1	CW id:1 SL:0.75ms CFreq:87.0kHz BW:2.0kHz
Sector 2	CW id:2 SL:0.75ms CFreq:75.0kHz BW:2.0kHz
Sector 3	CW id:0 SL:0.75ms CFreq:79.0kHz BW:2.0kHz
Sector 4	CW id:1 SL:0.75ms CFreq:95.0kHz BW:2.0kHz
Sector 5	CW id:2 SL:0.75ms CFreq:83.0kHz BW:2.0kHz

Figure 6.6: ARCs obtained after removing extracted RBPs for datasets 1, 2, 3, and 4

Figure 6.5 indicates that the ARCs for the same mode are similar and no difference in either slope or absolute BS can be observed. Comparing ARCs between Very Shallow and Shallow mode, three differences can be observed: 1) change of slope between GRA 8° to 15°, 2) average difference of 0.75 dB in absolute intensity level and, 3) Difference of 2 dB between GRA 0° to 5°. These differences can be partially attributed to differences in operating frequency and total energy between the two modes. The Shallow mode transmits higher energy by using longer pulse length (signal length = 0.75ms) compared to short pulse length (signal length = 0.30ms) of very shallow mode. The bulk shift of (0.75 dB) could not be prevented using the developed method as it does not test for absolute levels. A spread between the overlapping sectors of ARC can be observed for all the cases in Figure 6.6. The greatest variability is always at the inboard edge of the outer sectors.

The absence of significant differences ($<\pm$ 0.5 dB estimated) between the ARCs from four different datasets validates the reliability of the developed RBP extraction method.

6.2   Validation 2: Repeatability of Extracted RBPs at Different Locations

The next step is to validate the repeatability of the developed RBP extraction method. This will be tested in two ways, first by comparing RBPs (Shallow mode) extracted from two datasets collected on two different test sites but at the same time. Secondly (Section

6.3) the repeatability will be tested over a period of a year in which it is possible that the hardware could change. For the first comparison, two of the datasets detailed in Table 6.2 were selected. The datasets were collected using the same multibeam sonar (EM 710) in Shallow operating mode with heavy rolling motion at two different test sites in Bute Inlet, BC on June 13th 2014. The manufacturer's corrections were not applied during the data collection at these sites; hence stronger intensity variations can be seen in this validation. The test sites differed in geometry and the sediment type. Both the sites, however, had homogeneous sediments as a basic requirement of the developed methodology. The across-track RBPs extracted from both the datasets should be identical as the datasets were collected in the same operating mode by the same sonar (and the same software operating the sonar transceiver) despite differences in sediment type and geometry of the test sites. The type of sediment at the test site should not have any effect on the extracted RBP, as the RBPs are characteristic of the sonar (and its operating mode).

In the following sections, first the preprocessed data in the form of backscatter images are presented, then the corrected backscatter data after removing the extracted RBP are presented, and finally the extracted RBPs are compared sector by sector.

Table 6.2: Selected datasets (Bute Inlet 2014) in Shallow operating mode with heavy roll

Dataset June 13th 2014	Depth	Number of profile	Test site depth
1	100m	371	100m
2	200m	203	200m

6.2.1 Corrected Backscatter Data

Two survey lines in opposite directions with heavy roll were collected at each test site at different depths. For both the datasets across-track RBPs were extracted using the developed method. The stacking references were chosen at the middle of the sector for each sector. The extracted across-track RBP was then removed from the preprocessed backscatter data and backscatter data free from RBP were obtained. Figure 6.7 shows one of the survey lines from each dataset in the form of backscatter images. The ARCs for both the sites were obtained from the RBP-free backscatter data (see Figure 6.8).

From the ARCs in Figure 6.8 it is apparent that the sediments present at site 1 with 100m depth was very different then at site 2 with 200m depth as the ARCs have very different slope and absolute backscatter intensity levels. In both ARCs within 5° of normal incidence, fewer samples were obtained resulting in random backscatter strength values. These values were not plotted in Figure 6.8.
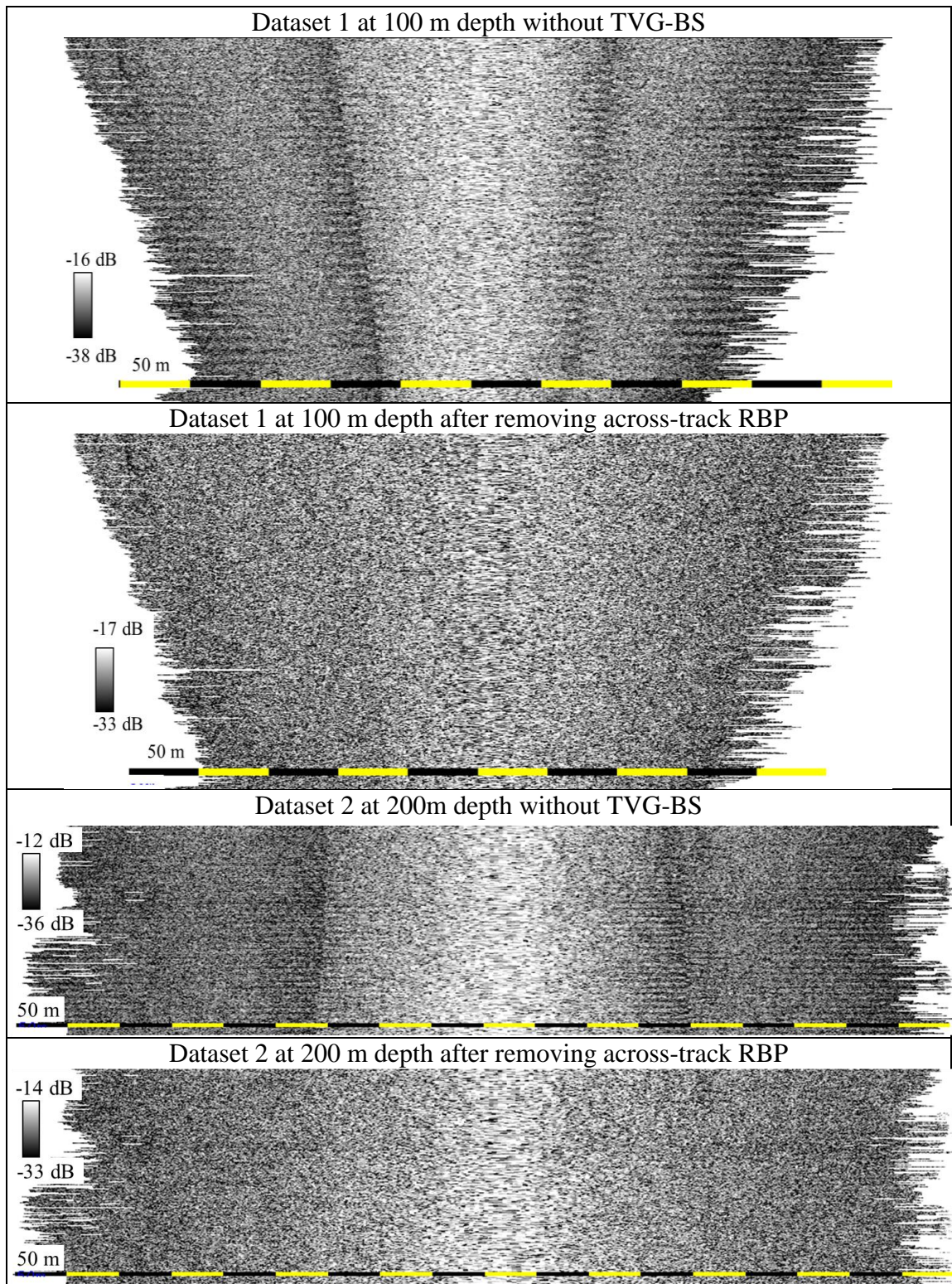
Figure 6.7: Backscatter data before and after RBP correction for both datasets
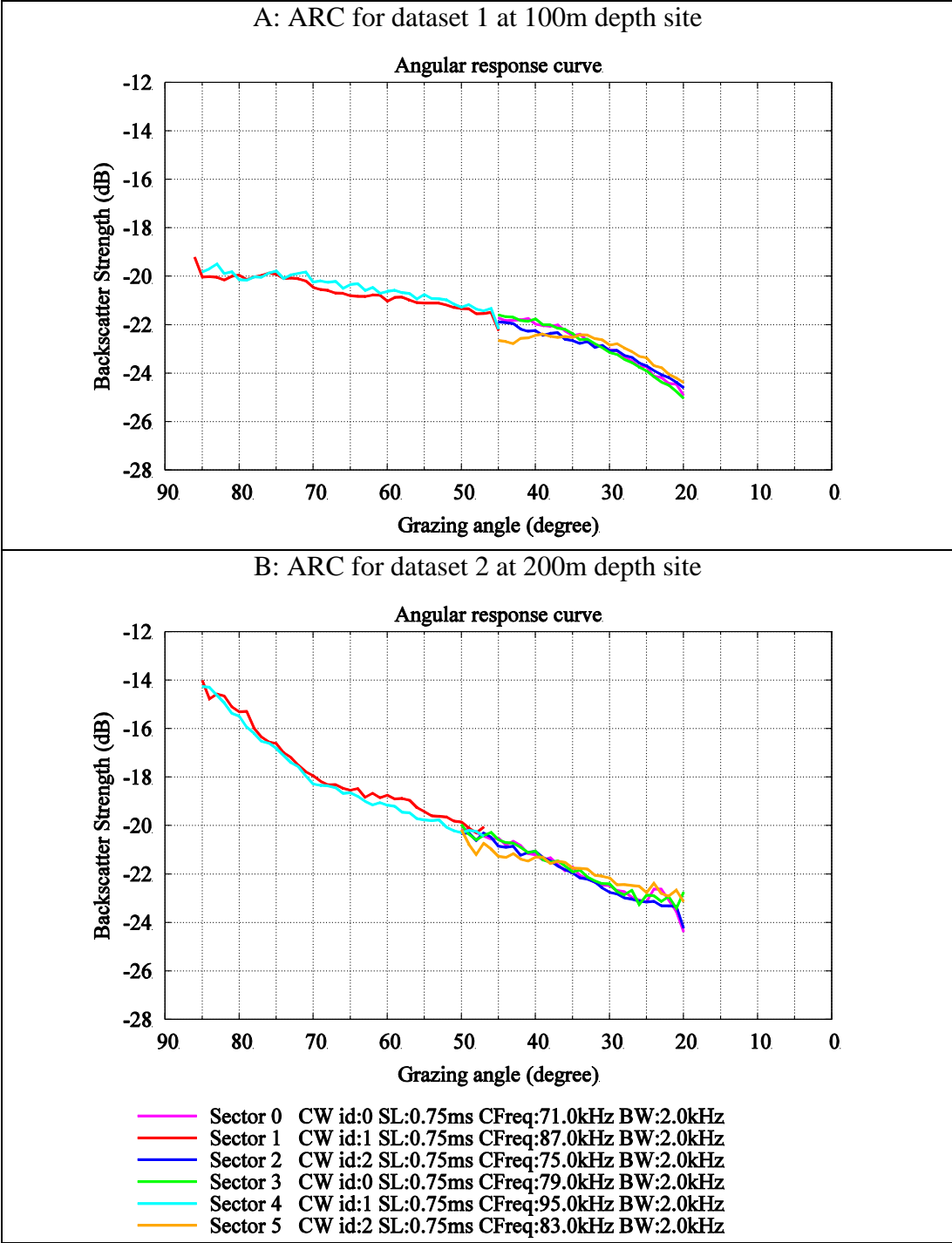
Figure 6.8: ARCs indicating different sediment types at two test sites

6.2.2 Comparing Across-Track RBPs

This section compares the extracted across-track RBPs from two datasets. In order to validate the repeatability of the RBP extraction method, the extracted across-track RBPs from both the test sites should match within their estimated errors. Figure 6.9 compares the extracted across-track RBPs. The error bars indicate the propagated SDs at 95% confidence.
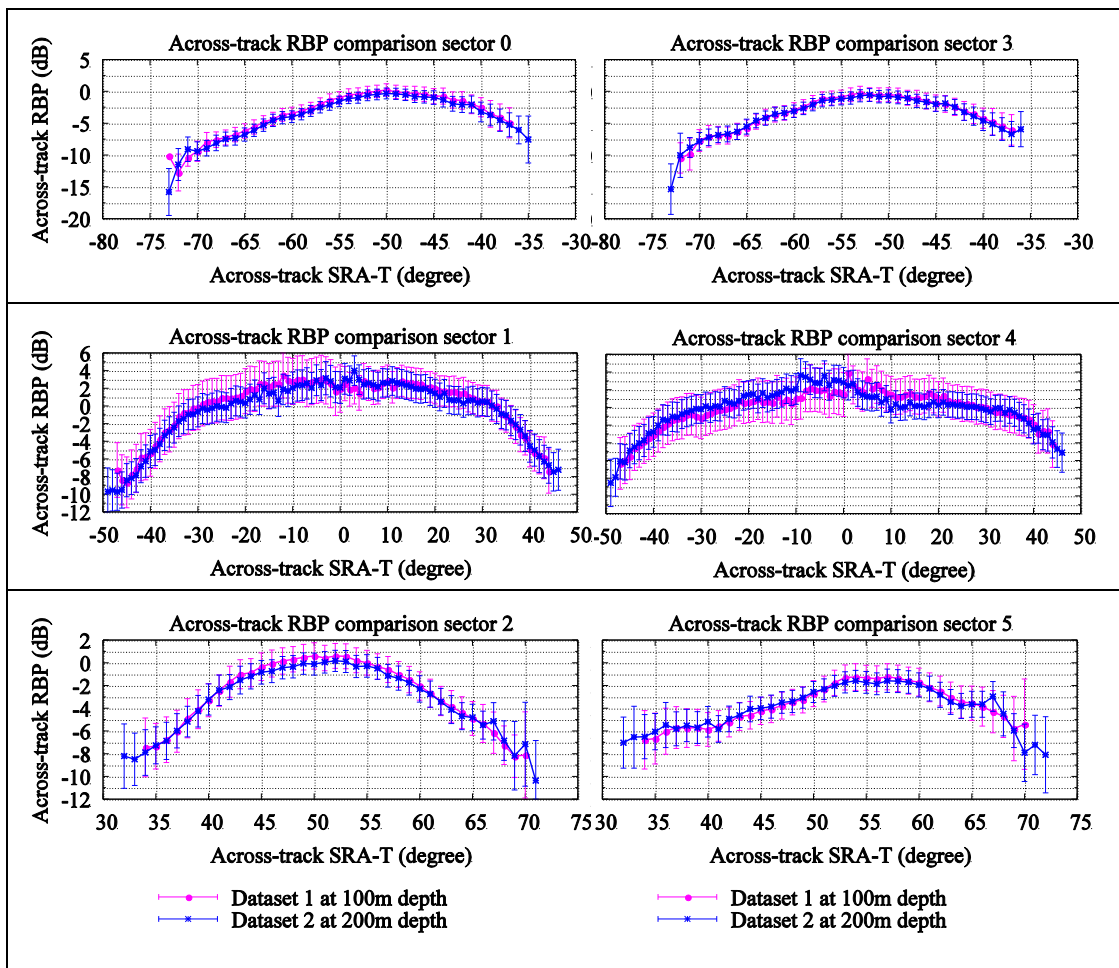
Figure 6.9: Across-track RBP comparison between dataset 1 and 2

The differences between the extracted across-track RBPs for each sector were computed and are presented in Figure 6.10 for each swath with SD at 68% confidence (1 Sigma). It can be seen from Figure 6.10 that for SRA-Ts beyond the nadir region (±20°) the differences are less than ±0.5 dB, while higher differences can be seen at nadir region. However, all the differences are within the SDs of the extracted across-track RBPs.
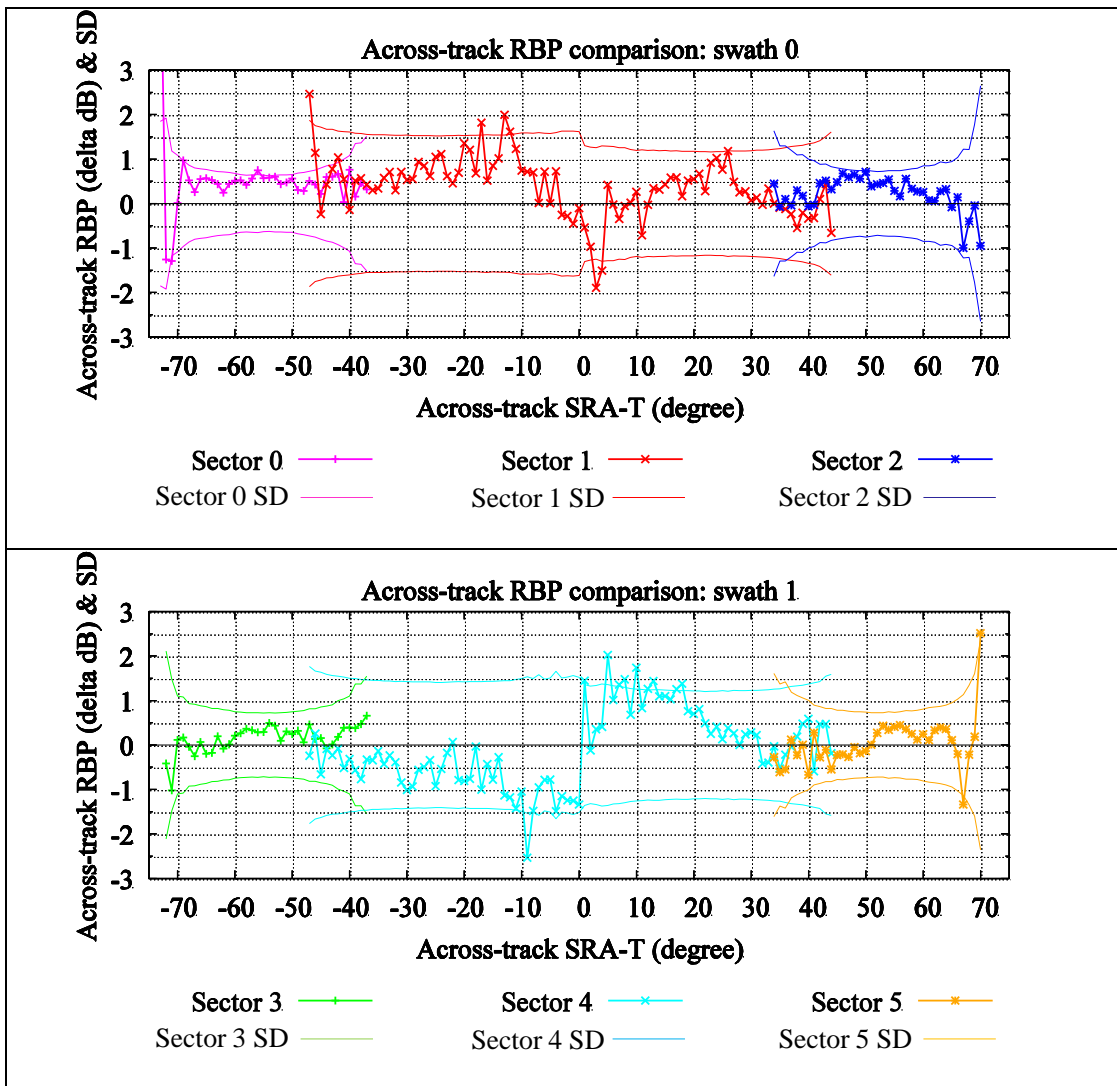
Figure 6.10: Differences in the across-track RBPs extracted from dataset 1 and 2 with SDs

The comparison indicates that the across-track RBP extracted at the 100m site is repeatable within the uncertainty to the across-track RBP extracted at the 200m site even though the sediment types were completely different. This comparison demonstrates that the developed method is reliable and capable of extracting the across-track RBP from any test site irrespective of the sediment type and geometry as long as the sediments are homogeneous, the magnitude of roll is sufficient, and seafloor/line geometry ensures enough common GRAs between the sectors.

This validation also provides more insight about the assumption made in the development of the across-track RBP extraction process. In order to compute the sector offsets between the sectors, at a given GRA, the intensities obtained from two different sectors were assumed to be the same despite different sectors being operated at different frequencies. Nothing in this analysis can indicate whether there is significant frequency dependence. However, previous work [Stanic et al., 1988; Boehme & Chotiros, 1988; Stanic et al., 1989] looking at frequency dependence at ranges from 20 to 280 kHz shows intensity changes of no more than ≈0.1 dB per 10 kHz. Thus the sector shift in the case of this research (70 to 100 kHz) would likely be no more than 0.3 dB which is within the uncertainties of the extracted RBPs.

However in the case of very high frequency and high bandwidth sonars (i.e. EM 2040) in which the frequency differences between different sectors are larger and hence frequency dependent seafloor response may be significantly different, this assumption needs to be validated before using the extracted across-track RBP. In the case of lower

frequency sonars operating below 50 kHz (i.e. EM 302, EM 112) the sector bandwidth is narrower (even as a % of center frequency) and no significant difference in the seafloor response is expected between the sectors.
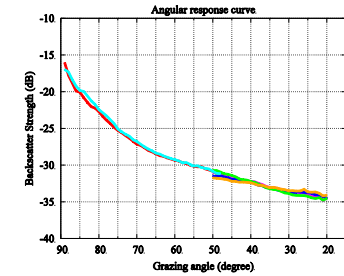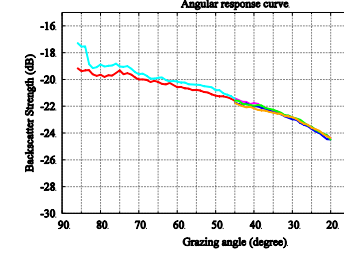
6.3 Validation 3: Repeatability of Extracted RBPs at Different Locations and Time

In Section 6.2 the repeatability of the developed RBP extraction method for the data collected on same day was successfully accessed. The next step is to assess whether we can detect the temporal variations in the extracted RBPs. In this section, RBPs extracted from datasets collected in different years and locations are examined.

For this validation, the across-track RBPs extracted for Very Shallow mode from Bute Inlet (2014) and Squamish River Delta (2015) locations were compared. The description of datasets is given in Table 6.3. The ARCs for both the sites suggests very different sediment types. For the dataset collected in Bute Inlet in year 2014, manufacturer's across-track RBP corrections (details in Section 2.4 and Appendix 9.3) were not applied (by setting them to zero). However, for the dataset collected in the following year at Squamish River Delta (Howe Sound), the manufacturer-estimated across-track RBP corrections were applied. As a result the RBP corrections extracted by the developed method for Squamish (2015) datasets were the remainder of the actual across-track RBP after the manufacturer's correction. To be able to compare these two

across-track RBPs, the manufacturer's corrections were added to the extracted RBPs from 2015 data. Any systematic mismatch between 2014 and 2015 across-track RBPs should include systematic RBP changes due to aging of sonar elements.

Table 6.3: Datasets collected in year 2014 and 2015 for validation 3

Dataset	Location	Depth	Number of profile	Mode	ARCs
1 (with manufacturer's RBP correction)	Squamish River Delta 2015	50m	697	Very Shallow	
2 (without manufacturer's RBP correction)	Bute Inlet 2014	100m	358	Very Shallow	

6.3.1 Across-Track RBP Extracted Using Dataset 1 (2015)

The dataset 1 in this validation is same as the dataset 1 used in Section 6.1. The initial backscatter data, the corrected backscatter data, and the ARCs for dataset 1 have already been presented in Section 6.1.2. The extracted across-track RBPs from dataset 1 is reproduced in Figure 6.11A.

211

A: Across-track RBP for 2015 with manufacturer's corrections

B: Manufacturer's across-track RBP for Very Shallow dual swath mode

C: Across-track RBP for 2015 without manufacturer's corrections

Sector 0   CW id:0 SL:0.30ms CFreq:70.0kHz BW:5.0kHz
Sector 1   CW id:1 SL:0.30ms CFreq:80.0kHz BW:5.0kHz
Sector 2   CW id:2 SL:0.30ms CFreq:70.0kHz BW:5.0kHz
Sector 3   CW id:0 SL:0.30ms CFreq:90.0kHz BW:5.0kHz
Sector 4   CW id:1 SL:0.30ms CFreq:100.0kHz BW:5.0kHz
Sector 5   CW id:2 SL:0.30ms CFreq:90.0kHz BW:5.0kHz

Figure 6.11: Extracted and manufacturer's across-track RBP

Kongsberg (manufacturer) has a generic estimate of the across-track RBP which is applied (by default) to the collected backscatter data; the details of this have already been discussed in Section 2.4. However as seen earlier, the data collected in Squamish (2015) with manufacturer's across-track RBP corrections still shows the presence of a residual across-track RBP. The complete manufacturer's across-track RBP is included in Appendix 9.3. For this comparison, manufacturer's RBP for Very Shallow mode in dual swath (see Figure 6.11B) is added to the extracted residual across-track RBP. In the absence of the information about how the manufacturer's across-track RBP is applied, the intermediate values at each SRA-T were estimated using a natural cubic spline fit using the values given at 10° intervals for each sector.

The estimation of the complete across-track RBP for 2015 dataset (Figure 6.11C) was done by simply adding (in dB units) manufacturer's across-track RBP from the remainder across-track RBP extracted from 2015 dataset. As the manufacturer's RBP does not have any related SDs, the estimated across-track RBP was considered to have same SDs as the computed across-track RBP from 2015 dataset.

6.3.2 Across-Track RBP Extracted Using Dataset 2 (2014)

Figure 6.12A shows the preprocessed backscatter data in which strong alternate bright and dark intensity variation patterns can be seen in outer sectors; the intensity offsets between the sectors are clearly visible at the sector boundaries. Figure 6.12B shows the

213

corrected backscatter image using extracted across-track RBP for the Very Shallow mode. This corrected image does not show any intensity variations that are related to ship motion; also no sector offsets can be seen. This indicates that extraction and removal of across-track RBP for this dataset was performed properly. Figure 6.12C shows the extracted across-track RBP for dataset 2.
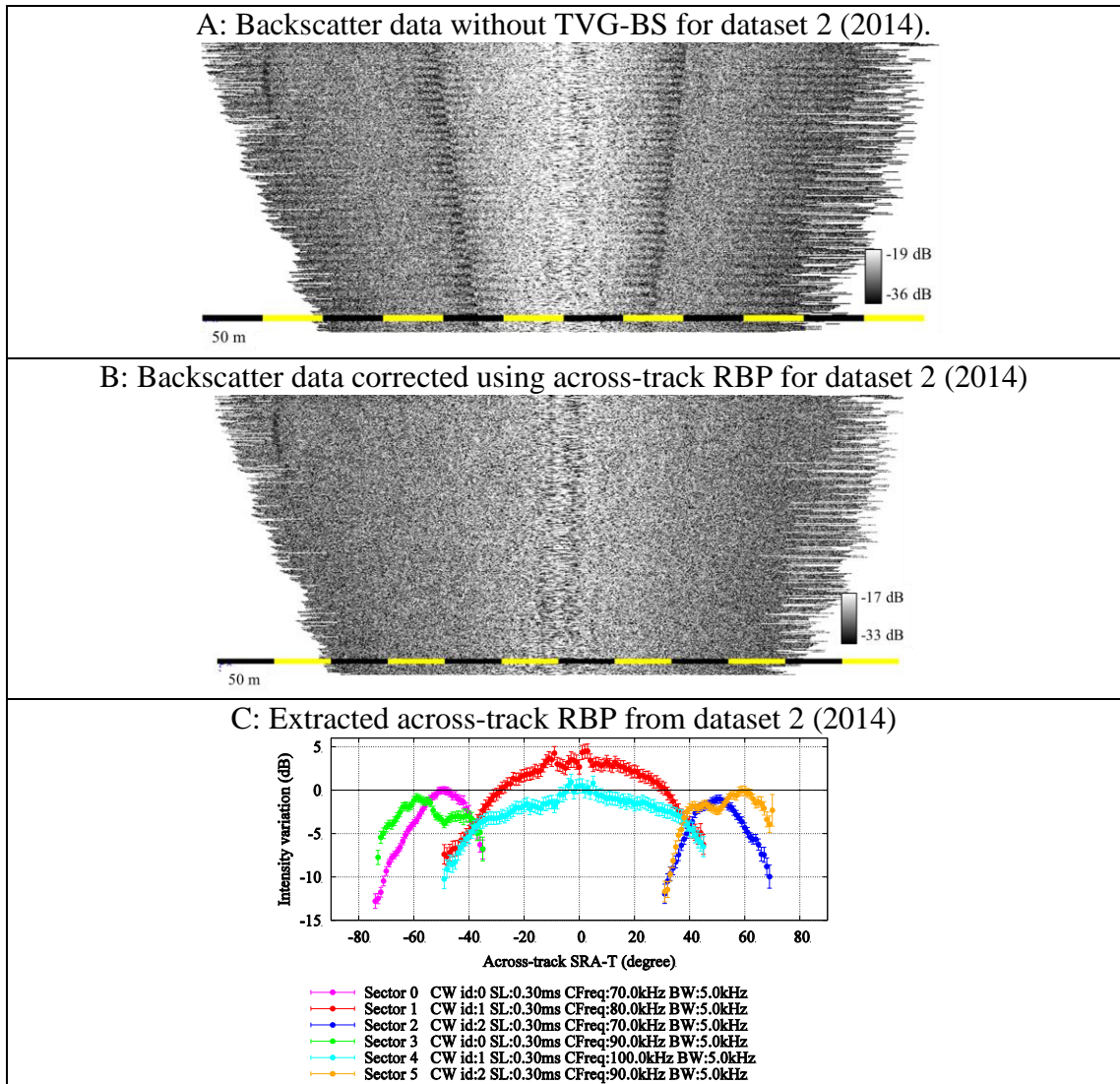
Figure 6.12: Backscatter data before and after correction and extracted across-track RBP for dataset 2 (2014)

6.3.3   Comparison of 2014 and 2015 Across-Track RBPs

Figure 6.13 compares the 2015 and 2014 across-track RBPs. The error bars shown are the propagated SDs at 95% confidence interval.
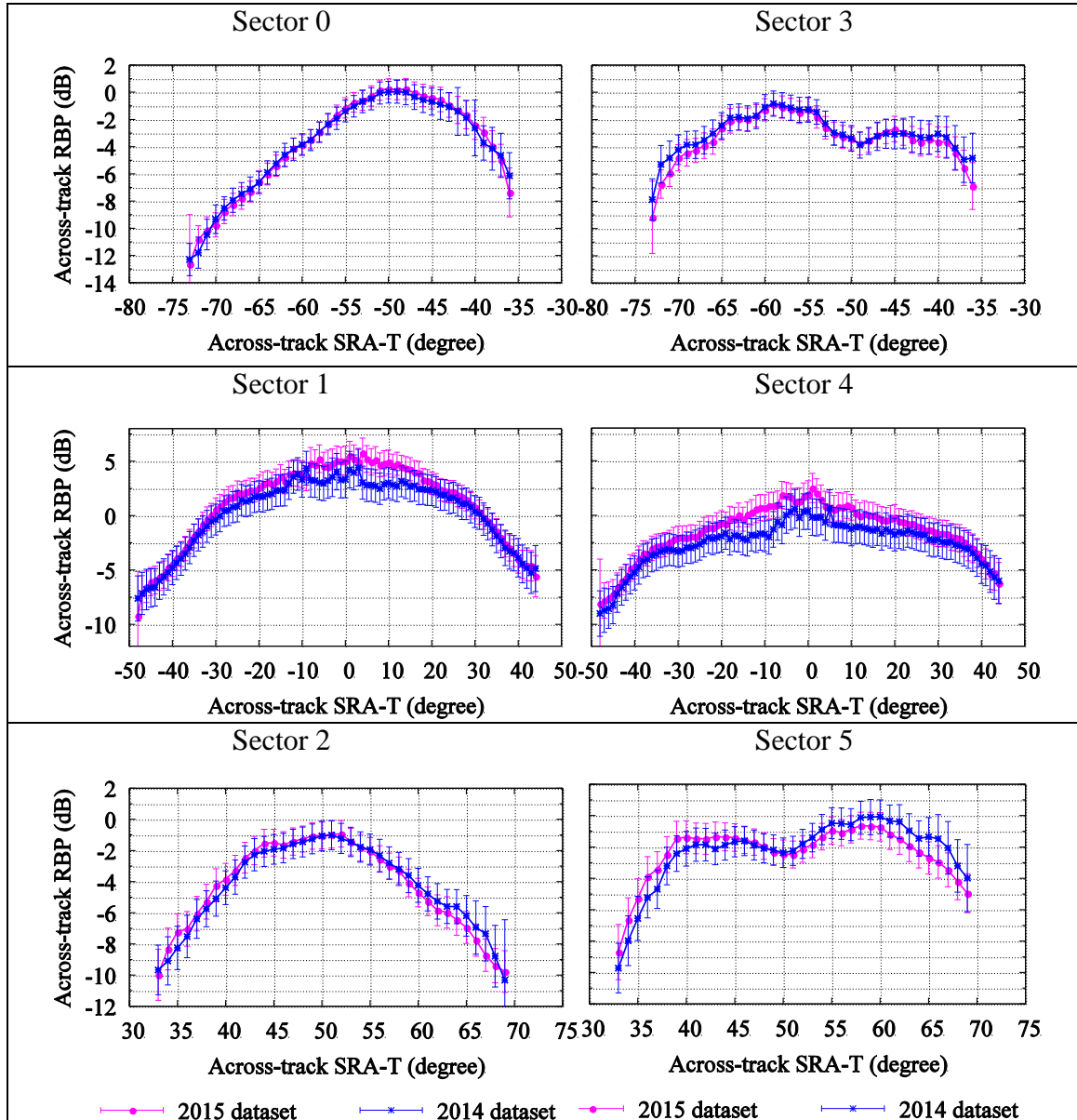
Figure 6.13: Comparison between 2014 and 2015 across-track RBP
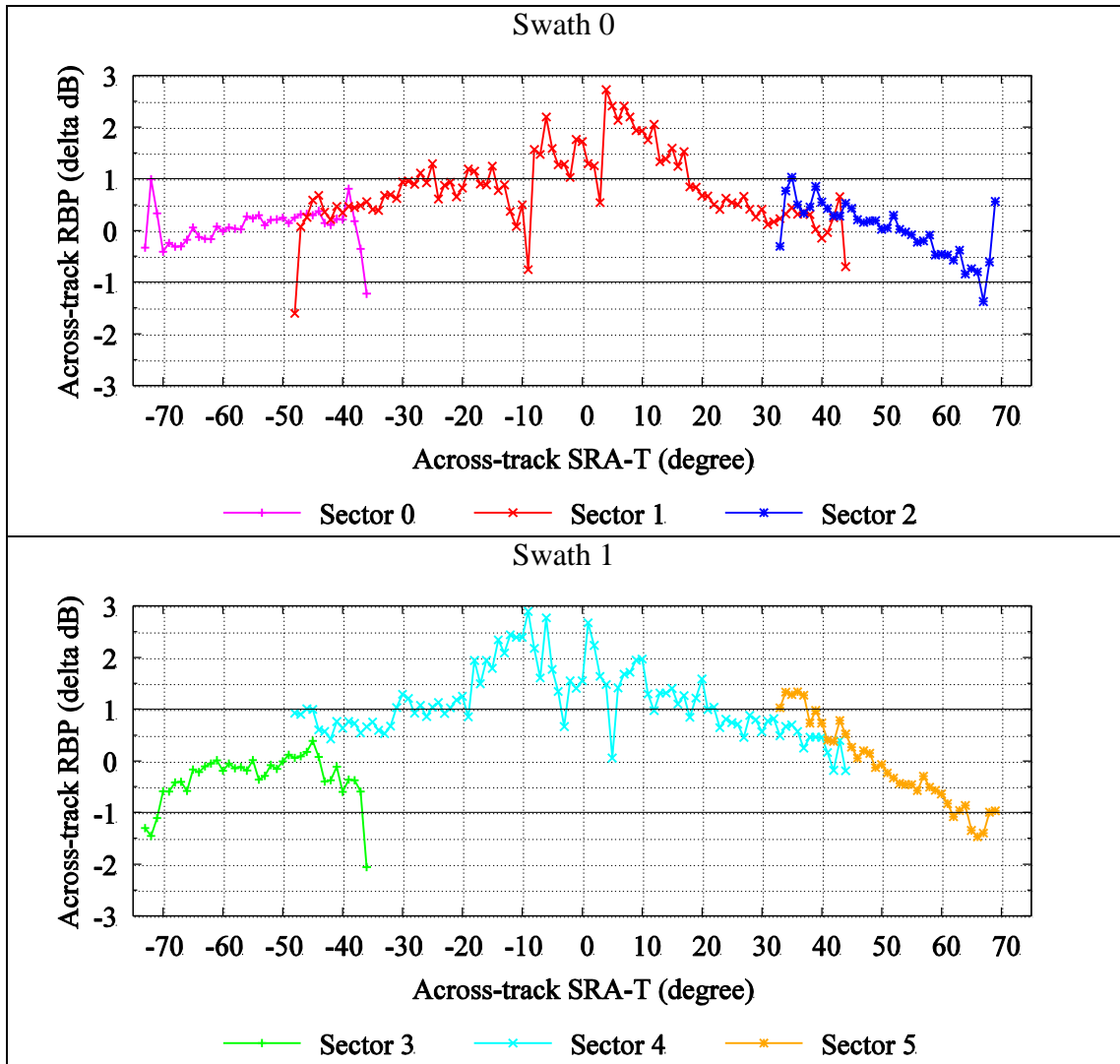
Figure 6.14: Differences between 2014 and 2015 across-track RBPs

Figures 6.13 and 6.14 illustrate the very close relation between the 2014 and 2015 across-track RBP corrections. For most of the outer sector SRA-Ts the difference is less than ±0.5dB. The maximum deviation (up to 2.5dB) can be observed for the central sectors between ± 20° from nadir. This is attributed to significantly fewer samples in that angular section as well as fewer profiles (359 compared to 695) for the 2014 dataset. There is also a significant possibility that the EM 710 hardware is slowly changing.

Bottom detection quality near nadir has notably degraded for the sonar from year 2014 to 2015 as noticed during a parallel study in the OMG.

The comparison also confirms that, unlike sector 0 and 2 (70 kHz swath 0), sector 3 and 5 (90 kHz swath 1) do not have simple parabolic shaped RBPs as indicated by arrows in Figure 6.15. This contrasts with the simple parabolic shapes that are assumed for the narrower, low frequency multi-sector sonars (EM 122, EM 302). Hence a single generic parabolic shaped RBP cannot be used for all the sonars of a particular type (for example all EM 710s) as the RBPs are exclusively related to the product of the individual radiation patterns of multiple rows and columns of the elements in the sonar. An RBP that has a significant effect from a specific malfunctioning element or group of elements can show a significantly different radiation pattern than the manufacturer's predicted RBP (Figure 6.11B).

This close comparison indicates that the extraction method can be implemented in one of two equivalent ways: A) extracting additional corrections from data with manufacturer's corrections applied (2015 RBPs) or B) extracting total corrections from data with zero corrections applied (2014 RBPs). Whether approach A or B is used, the sum of applied correction and residual can then be reentered into the transceiver as an optimal real-time RBP correction.
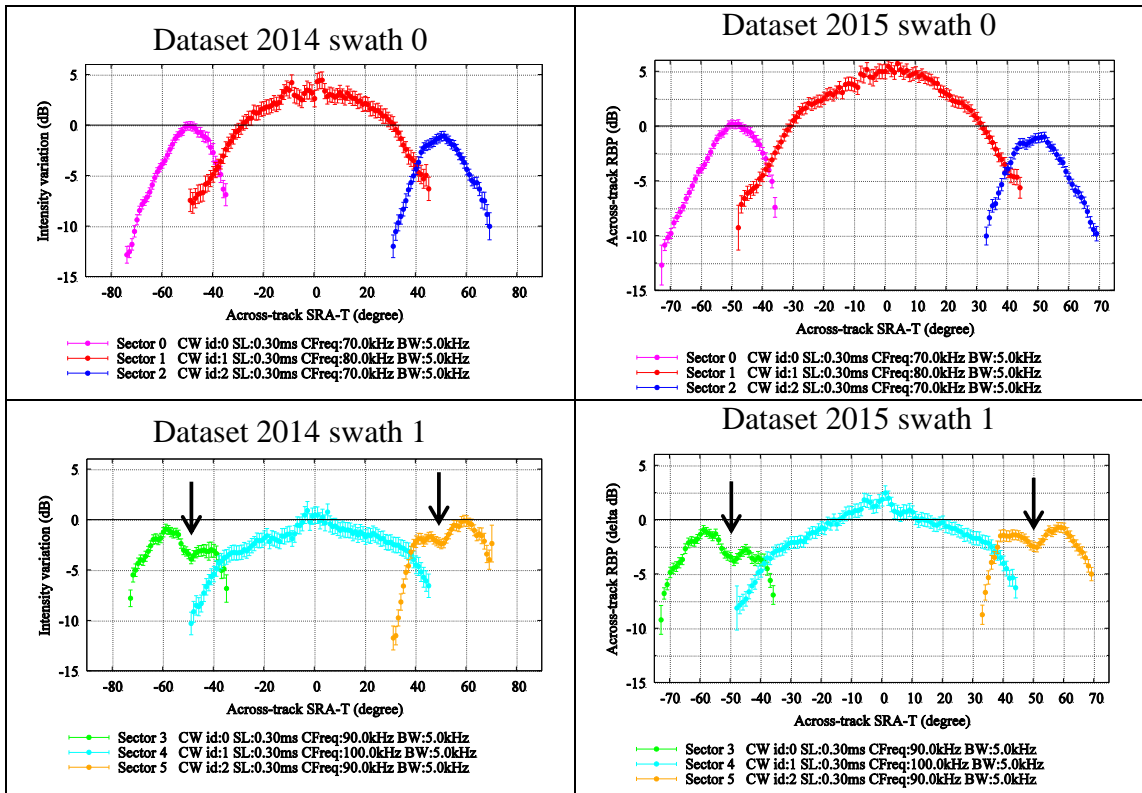
Figure 6.15: Across-track RBPs for each swath (2014 & 2015)

All the three validation approaches have demonstrated the validity and efficiency of the across- and along-track RBP extraction method developed in this research. The results also indicated that the developed method is most vulnerable near the nadir region due to fewer samples. The next chapter summarizes the findings of this research and discusses the direction of future work.

7   CONCLUSION

7.1   Summary

Prior to the approach developed in this research, RBP extraction relied upon existing knowledge of the true ARC for at least one location. Systematic biases between the actual and assumed ARC at that location, will then be overprinted on all other ARCs derived. The developed method explicitly avoids this assumption and unambiguously extracts the RBP directly from the backscatter data without the necessity of knowing the ARC characteristics of the sediment. By using unambiguous RBPs, more accurate ARCs are then obtained which can be used directly for classification. Additionally, better mosaics can be obtained by both removing the correct RBP and normalizing the data using the true local ARCs. By confidently separating RBP from the angular response and geometric effect, more reliable backscatter data for seafloor classification can now be obtained irrespective of changes in ship orientation or over rapidly varying seafloor slopes. Furthermore, this research successfully demonstrated the signature of along-track variation in the intensities due to yaw compensation. In the developed method, along-track (receiver) and across-track (transmitter) RBPs are extracted and removed separately, further increasing confidence in the backscatter data.

As demonstrated in this thesis, the developed RBP extraction method performed reliably using a smaller ship which is capable of producing controlled heavy roll and yaw. The sensitivity analysis revealed that similar results can be obtained by collecting the survey data in both directions on a sloping seafloor or on undulating seafloor without the need of heavy rolling. This should allow the method to be applied to bigger, less maneuverable vessels which are typically used for lower frequency sonars.

The basic principle used by Tamsset and Hogarth [2015] for bathymetric sidescan sonars was further expanded in this research. That principle, originally developed just for a single sector SRA-T without transmit steering, was extended so that the intensities at a given GRA should also be the same irrespective of which sector of a multi-sector multibeam was used. And the SRA-R was introduced for the first time to account for the along Tx steering employed. This further extension of the concept enabled the computation of along- and across-track RBP for multi-sector multi-swath multibeam sonar. This expansion, however, created challenges, such as referencing the RBP from each sector and swath to obtain a master function and to address the complications of roll, yaw, and pitch stabilization used in modern multibeam sonars. These challenges were successfully dealt with in this research.

For the Kongsberg systems, the manufacturer has already accepted the need for RBP removal and tried to address the across-track RBP by creating generic corrections which are only partially adequate as they do not account for SRA-R. Refinements to the default across-track generic RBP have been attended by several authors [Augustin & Lurton,

2005; Teng, 2011] but requires proper knowledge of the ARC. This research successfully created a method to compute not only across-track but also along-track RBP and provided details of its application. The computed RBPs, however, are not generic and need to be recomputed if there are any changes in the hardware or in the way the hardware operates (changes in firmware).

During this research it was also noted that the change in the frequency can alter the radiation pattern significantly between different operating modes that use the same sonar elements. This indicates that the elements can change their radiation pattern significantly with small change in the frequency. The detailed study of the change in the radiation pattern over the years and between the sectors can give insights into the performance of the sonar elements and can also be used as a tool to identify potentially malfunctioning elements along with BIST (built-in self test).

7.2   Recommended Operating Sequence

The sensitivity analysis of the developed method gave details about the data collection strategies for optimum RBP extraction. The complete operating process is recommended to be divided into 3 steps. Step 1 is to examine previously collected bathymetric and backscatter data to identify a suitable test data collection site. The ideal test site should have homogeneous material and gentle planar slope. If the vessel cannot be rolled deliberately, then the test site should be chosen with gently undulating seafloor

with homogeneous material. Enough bathymetric data should be collected at the test site to produce a DTM with highest possible resolution for the computation of GRAs.

Step 2 is the actual backscatter data collection. It is recommended that the manufacturer's across-track RBP correction be set to zero during the test data collection as no exact details of how it is applied are available from the manufacturer. The same test site can be used for test data collection for along- and across-track RBP extraction. The test data for across- and along-track RBP extraction should be collected in both directions with maximum possible swath coverage in order to obtain maximum possible range of GRAs. Specifically for across-track RBP test data, maximum possible roll should be induced with roll stabilization on (no choice), while keeping the yaw and pitch stabilization switched off; this will maximize the number of profiles with no along-track sector steering which are required for across-track RBP extraction. The developed method for across-track RBP is most vulnerable near nadir. To address this, it is recommended that the maximum possible number of profiles should be collected to increase the number of samples near nadir.

For the case of collecting along-track RBP test data, the complete range of along-track sector steering should be utilized by yawing the vessel. Care must be taken to keep the rate of change of along-track sector steering as low as possible to get equal distribution of profiles for the full available range of along-track sector steering. An extra line without yawing ensures high density of profiles with zero yaw, increasing the precision of along-track RBP.

222

Generally the maximum possible amount of data should be collected to have the best estimate of extracted RBPs. As a guide greater then 1000 pings per direction would be ideal. Note that this implies longer duration lines in deeper water.

Step 3 is the actual extraction process. Data collected should be preprocessed to remove the manufacturer-applied TVG-BS with its assumptions. All the algorithms, including the developed RBP extraction algorithms, the statistical analysis process, as well as other modified algorithms are organized in the required order in a single script for along- and across-track RBP extraction. The script first extracts across- and then along-track RBPs while continuously displaying the intermediate results and steps in variety of plots. Once the extraction is complete, the initial data are corrected for the extracted RBPs and corrected backscatter data are displayed in the form of backscatter images and ARCs. The script can be modified by the user to customize the information displayed during the extraction process.

7.3   Limitations and Future Work

The ultimate accuracy of the extracted RBP depends on the algorithms utilized in the preprocessing steps, which include the computation of GRA, SRA-T, SRA-R, geometric corrections, and removal of manufacturer-applied TVG for estimated BS. Any improvement in their accuracies will result in the increased accuracy of extracted RBPs.

The accuracy of extracted RBPs also depends on homogeneity of the seafloor material at the test site.

In this research, a new algorithm is developed to compute precise SRA-T which is independent of any bathymetric uncertainties including refraction. However, modifications need to be done in the computation of SRA-R which is computed using positional information and susceptible to uncertainties due to positional errors and strong refraction. The computation of SRA-R needs to be further developed to consider complex along-track steering geometry for transmit sectors.

The proved methodology needs to be extended for all other multi-sector multibeam sonars to provide maximum benefit of this research. The other three currently available multi-sector multibeam sonars from the same manufacturer have significant different radiation geometries. The EM 302 and EM 122 have much narrower sectors (perhaps allowing parabolic beam pattern assumptions). The EM 2040 actually has three distinct line arrays for the three sectors with notably strong RBPs. However in the case of systems with more than three sectors in single swath and for the systems with dual sonar heads, extra care (and modifications) will be required to reference all the sectors to a single sector. In the near future, it is hoped that this developed procedure will become a standard test to calibrate the sonar to obtain correct multibeam backscatter data. This would be referred alongside the patch test which is already a standard for multibeam users. The extracted across-track RBPs can be used instead of manufacturer's corrections

for real-time operations; however, additional functionality from the manufacturer will be required to correct along-track RBPs in real time.

It is important to recognize that the developed method does not address the final absolute level of backscatter. Rather it addresses the relative changes in the source level that it has computed. In order to compute absolute backscatter level, further study needs to be done to understand how much source energy was actually put in at specific SRA-T or by measuring returned intensity from a target of known reflectivity.

7.4   Recommendations

During this study the following areas for development were identified.

1) **A calibration mode:** The ideal dataset for extracting along-track RBP should have the equal distribution of swaths for the maximum possible (±10°) range of SRA-R. This dataset can be obtained with less effort if the sonar is equipped with a calibration mode in which all the sectors are steered forward and backward slowly, while the ship is stationery over homogeneous sediments. This will also allow covering an entire SRA-R range for central sectors too, which was not possible in any of the cases in this research. A swath sweep option is apparently available in real time software application (Seafloor Information System) developed by the manufacturer for EM 122s.

In order to relate sector-specific across-track RBP functions, an overlapping range of GRAs is required. This is hard to achieve on flat seafloor as the sector boundaries are roll stabilized. An option to disable sector boundary roll stabilization would significantly increase GRA overlap.

2) **Along-track RBP in the Bscorr file:** Currently some of the Kongsberg systems can correct for across-track RBPs in real time, using predetermined RBP offsets stored in the Bscorr file. This ability can be further improved to compensate for along-track RBP in real time by extending the Bscorr file and its application to include along-track RBPs computed using the developed method. Given the simple shape of the along-track RBPs extracted in this research, it seems reasonable that a basic parabolic function could be applied, just with curvature based on the center frequency.

3) **Computation of RBP as a part of sea acceptance trials and yearly system review:** Any unrealistic variations in the RBPs are a potential sign of improperly working sonar elements or faulty firmware controlling the sonar elements. The computation of RBPs at the acceptance trials will serve two purposes: 1) It will ensure proper working of transceiver hardware and software, and 2) It will prepare the sonar system for the best possible real-time backscatter data processing. The yearly computations will help to track the sonar hardware ageing or related issues.

4) **Temporal sediment changes:** The need for unambiguous RBP removal is fulfilled by the developed method. With this and previously developed tools, sediment changes over shorter periods (few days, weeks or years) can now be detected with more confidence. A specific application of this would be a detailed study to analyse

226

multibeam backscatter data collected in Squamish River Delta from year 2010 to 2015.

5) **Improved motion stabilizations:** Currently for the manufacturer's systems, motion stabilization is applied only partially, aiming just to achieve better bathymetric accuracies and coverage but in the process adding serious artefacts in backscatter data. In the roll stabilization the receiver beams are steered across-track at the reception, but transmit sectors are not steered across-track at the transmission. Similarly for pitch and yaw stabilization, the transmit sectors are steered in along-track direction but the receiver beams are not steered in along-track direction. This operating principle has hampered the backscatter data quality as shown in this research. Though this research has successfully developed the method to overcome all the radiometric effects due to the motion stabilization, those effects could be minimized by implementing more complete motion stabilization in which transmit sectors are dynamically steered across-track (with the roll) and Rx beams are steered along-track at reception watching the along-track orientation of the expected arrival. This could be done using time delay directions suggested in Figure 7.1. If any modifications are done by the manufacturer in the way the motion stabilization currently works, then those have to be accommodated in the developed method.

Length (along-track)

Width (across-track)

Recommended variable Rx time-delay for along-track steering

Used variable Rx time-delay used for across-track steering

Rx

Tx

Used Tx time-delay for along-track Tx steering

Used fixed Tx time-delay for across-track Tx sector steering

Recommended variable Tx time-delay for across-track Tx sector steering

Roll 0°

θ

Pitch 0°

Roll 10°

θ

Recommended stabilized Tx sector

Unstabilized Tx sector

Pitch 10°

Recommended stabilized Rx Beam

Unstabilized Rx Beam

Figure 7.1: Recommended time delays for complete motion stabilization

6. **Clearer description:** A technical note from the manufacturer describing how the current across-track RBPs are actually applied is required. Specifically, it should specify how the functions are interpolated (potentially extrapolated) and whether roll at transmission or reception is used.

8   REFERENCES

Augustin, J. M., Edy C., Savoye , B., & Drezen, E. Le. (1994) "Sonar mosaic computation from multibeam echo sounder," *OCEANS '94. 'Oceans Engineering for Today's Technology and Tomorrow's Preservation.' Proceedings*, Brest,. II/433-II/438 vol.2.

Augustin, J. M., Le Suave, R., Lurton, X., Voisset, M., Dugelay, S., & Satra, C. (1996). Contribution of the multibeam acoustic imagery to the exploration of the sea-bottom; examples of SOPACMAPS 3 and ZoNeCo 1 cruises. *Marine Geophysical Researches, 18*(2-4), 459-486.

Augustin, J. M., & Lurton, X. (2005). Image amplitude calibration and processing for seafloor mapping sonars. *Oceans 2005-Europe, 1*, 698-701 Vol. 1.

Beaudoin, J., Hughes Clarke, J. E., Van Den Ameele, E. J., & Gardner, J. V. (2002). Geometric and radiometric correction of multibeam backscatter derived from Reson 8101 systems. Paper presented at the *Canadian Hydrographic Conference Proceedings,* 1-22.

Beaudoin, J. (2005). *Software algorithm: deTVG* University of New Brunswick Swathed software.

Beaudoin, J., Johnson, P., Lurton, X., & Augustin, J. M. (2012). *R/V Falkor multibeam echosounder system review* Center for Coastal and Ocean Mapping / Joint Hydrographic Center \& IFREMER.

Boehme, H., Chotiros, N. P., Rolleigh, L. D., Pitt, S. P., Garcia, A. L., Goldsberry, T. G., et al. (1985). Acoustic backscattering at low grazing angles from the ocean bottom. part I. bottom backscattering strength. *The Journal of the Acoustical Society of America, 77*(3), 962-974.

Boehme, H., & Chotiros, N. P. (1988). Acoustic backscattering at low grazing angles from the ocean bottom. *The Journal of the Acoustical Society of America, 84*(3), 1018-1029.

Bragg, W. H., & Bragg, W. L. (1913). The reflection of X-rays by crystals. *Proceedings of the Royal Society of London A: Mathematical, Physical and Engineering Sciences, 88*(605), 428-438.

Brucker, S., Hughes Clarke, J. E., Beaudoin, J., Lessels, C., Czotter, K., Loschiavo, R., et al. (2007). Monitoring flood-related change in bathymetry and sediment distribution over the Squamish Delta, Howe Sound, British Columbia. Presented at US Hydro conference, Norfolk, Virginia, 15th-17th May

de Campos Carvalho, R. (2012). *Proper environmental reduction for attenuation in multi-sector sonars.* University of New Brunswick, Department of Geodesy and Geomatics Engineering, MScE thesis.

de Campos Carvalho, R., Maciel de Oliveira Junior, A., & Hughes Clarke, J. E. (2013). Proper environmental reduction for attenuation in multi-sector sonars. Paper presented at the *Acoustics in Underwater Geosciences Symposium (RIO Acoustics), 2013 IEEE/OES,* 1-6.

de Moustier, C. (1986). Beyond bathymetry: Mapping acoustic backscattering from the deep seafloor with SeaBeam. *Journal of the Acoustical Society of America, 79*(2), 316-331.

de Moustier, C., & Alexandrou, D. (1991). Angular dependence of 12 kHz seafloor acoustic backscatter. *The Journal of the Acoustical Society of America, 90*(1), 522-531.

de Moustier, C., & Matsumoto, H. (1993). Seafloor acoustic remote sensing with multibeam echo-sounders and bathymetric sidescan sonar systems. *Marine Geophysical Researches, 15*(1), 27-42.

Francois, R. E., & Garrison, G. R. (1982a). Sound absorption based on ocean measurements: Part I: Pure water and magnesium sulphate contributions. *The Journal of the Acoustical Society of America, 72*(3), 896-907.

Francois, R. E., & Garrison, G. R. (1982b). Sound absorption based on ocean measurements. Part II: Boric acid contribution and equation for total absorption. *The Journal of the Acoustical Society of America, 72*(6), 1879-1890.

Fonseca, L., & Mayer, L. (2007). Remote estimation of surficial seafloor properties through the application angular range analysis to multibeam sonar data. *Marine Geophysical Researches, 28*(2), 119-126.

Fonseca, L., Brown, C., Calder, B., Mayer, L., & Rzhanov, Y. (2009). Angular range analysis of acoustic themes from Stanton Banks Ireland: A link between visual interpretation and multibeam echosounder angular signatures. *Applied Acoustics, 70*(10), 1298-1304.

Hamilton, T., Beaudoin, J., & Hughes Clarke, J. E. (2014). An improved ray-tracing algorithm. presented at Canadian Hydrographic Conference, Saint John's, Newfoundland and Labrador, 14-17 April 2014

Hammerstad, E. (1998). Multibeam echo Sounder Accuracy: EM technical note.

Hammerstad, E. (2000). Backscattering and seabed image reflectivity: EM technical note.

Hammerstad, E. (2005). Sound levels from Kongsberg multibeams: EM technical note.

Hasan, R. C., Ierodiaconou, D., & Laurenson, L. (2012). Combining angular response classification and backscatter imagery segmentation for benthic biological habitat mapping. *Estuarine, Coastal and Shelf Science, 97*, 1-9.

Hellequin, L., Lurton, X., & Augustin, J. M. (1997). Postprocessing and signal corrections for multibeam echosounder images. *OCEANS '97. MTS/IEEE Conference Proceedings*, Halifax, NS, 1997, vol.1 23-26.

Hellequin, L., Boucher, J. -M., & Lurton, X. (2003). Processing of high-frequency multibeam echo sounder data for seafloor characterization. *IEEE Journal Of Oceanic Engineering, , 28*(1), 78-89.

Huang, Z., Nichol, S. L., Siwabessy, J. P., Daniell, J., & Brooke, B. P. (2012). Predictive modelling of seabed sediment parameters using multibeam acoustic data: A case study on the Carnarvon Shelf, Western Australia. *International Journal of Geographical Information Science, 26*(2), 283-307.

Huang, Z., Siwabessy, J., Nichol, S., Anderson, T., & Brooke, B. (2013). Predictive mapping of seabed cover types using angular response curves of multibeam backscatter data: Testing different feature analysis approaches. *Continental Shelf Research, 61*, 12-22.

Huang, Z., McArthur, M., Przeslawski, R., Siwabessy, J., Nichol, S., & Brooke, B. (2014). Predictive mapping of soft-bottom benthic biodiversity using a surrogacy approach. *Marine and Freshwater Research, 65*(5), 409-424.

Hughes Clarke, J. E. (1993). The potential for seabed classification using backscatter from shallow water multibeam sonar. *Acoustic Classification and Mapping of the Seabed International Conference,* Bath University UK. 14-16 April.

Hughes Clarke, J. E. (1994). Toward remote seafloor classification using the angular response of acoustic backscattering: A case study from multiple overlapping GLORIA data. *IEEE Journal Of Oceanic Engineering, 19*(1), 112-127.

Hughes Clarke, J. E., Mayer, L. A., & Wells, D. E. (1996). Shallow-water imaging multibeam sonars; a new tool for investigating seafloor processes in the coastal zone and on the continental shelf. *Marine Geophysical Researches, 18*(6), 607-629.

Hughes Clarke, J. E., Danforth, B. W., & Valentine, P. (1997). Areal seabed classification using backscatter angular response at 95 kHz. Paper presented at the *SACLANTCEN Conference on High Frequency Acoustics in Shallow Water,* pp. 243-250.

Hughes Clarke, J. E., Brucker, S., Muggah, J., Church, I., Cartwright, D., Kuss, P., et al. (2012). The Squamish ProDelta: Monitoring active landslides and turbidity currents. Paper presented at the *Canadian Hydrographic Conference 2012, Proceedings,* Saint John's, Newfoundland and Labrador, 14-17 April 2014

Hughes Clarke, J. E. (2012). Optimal use of multibeam technology in the study of shelf morphodynamic. *International Association of Sedimentology Special publication (2012), 44*, 1-28.

Hughes Clarke, J. E. (2015). Multispectral acoustic backscatter from multibeam, improved classification potential. *Proceedings of the US Hydrographic Conference, National Harbor, MD, 2015,* Maryland U.S.A.

Ivakin, A. N. (1998). A unified approach to volume and roughness scattering. *The Journal of the Acoustical Society of America, 103*(2), 827-837.

Jackson, D. R., Winebrenner, D. P., & Ishimaru, A. (1986). Application of the composite roughness model to high-frequency bottom backscattering. *The Journal of the Acoustical Society of America, 79*(5), 1410-1422.

Lamarche, G., Lurton, X., Verdier, A. L., & Augustin, J. M. (2011). Quantitative characterisation of seafloor substrate and bedforms using advanced processing of multibeam backscatter—Application to cook strait, new zealand. *Continental Shelf Research, 31*(2, Supplement), S93-S109.

Llewellyn, K. C. (2006). *Corrections for beam pattern residuals in backscatter imagery from the Kongsberg-Simrad EM300 multibeam echosounder.* University of New Brunswick, Department of Geodesy and Geomatics Engineering, MEng thesis..

Lurton, X. (2002). *An introduction to underwater acoustics: Principles and applications* Springer.

Lurton, X., & Lamarche, G. (2015). *Backscatter measurements by seafloor‐mapping sonar guidelines and recommendations* A collective report by members of the GeoHab Backscatter Working Group.

McKinney, C. M., & Anderson, C. D. (1964). Measurements of backscattering of sound from the ocean bottom. *The Journal of the Acoustical Society of America, 36*(1), 158-163.

Mitchell, N. C., & Somers, M. L. (1989). Quantitative backscatter measurements with a long-range side-scan sonar. *Oceanic Engineering, IEEE Journal Of, 14*(4), 368-374.

Novarini, J. C., & Caruther, J. W. (1998). A simplified approach to backscattering from a rough seafloor with sediment inhomogeneities. *Journal of Oceanic Engineering, IEEE, 23*(3), 157-166.

Pace, N. G., & Gao, H. (1988). Swath seabed classification. *IEEE Journal of Oceanic Engineering, 13*(3), 83-90.

Patterson, R. B. (1963). Backscatter of sound from a rough boundary. *The Journal of the Acoustical Society of America, 35*(12), 2010-2013.

Potter, D. P., & Shaw, J. (2010). *Backscatter strength and shaded seafloor relief, Placentia Bay North, offshore Newfoundland and Labrador* (Geoscience for Oceans Management ed.). Newfoundland and Labrador: Natural Resources Canada / Ressources naturelles Canada.

Preston, J. (2009). Automated acoustic seabed classification of multibeam images of stanton banks. *Applied Acoustics, 70*(10), 1277-1287.

Rice, S. O. (1951). Reflection of electromagnetic waves from slightly rough surfaces. *Communications on Pure and Applied Mathematics, 4*(2-3), 351-378.

Rzhanov, Y., Fonseca, L., & Mayer, L. (2012). Construction of seafloor thematic maps from multibeam acoustic backscatter angular response data. *Computers & Geosciences, 41*(0), 181-187.

Stanic, S., Briggs, K., Fleischer, P., Ray, R., & Sawyer, W. (1988). Shallow-water high-frequency bottom scattering off panama city, florida. *The Journal of the Acoustical Society of America, 83*(6), 2134-2144.

Stanic, S., Briggs, K., Fleischer, P., Sawyer, W., & Ray, R. (1989). High-frequency acoustic backscattering from a coarse shell ocean bottom. *The Journal of the Acoustical Society of America, 85*(1), 125-136.

Stockhausen, J. (1963). Scattering from the volume of an inhomogeneous Half-Space. *The Journal of the Acoustical Society of America, 35*(11), 1893-1893.

Strutt, J. W. (1945). *Lord rayleigh. the theory of sound* New York.

Tamsett, D., & Hogarth, P. (2016). Sidescan sonar beam function and seabed backscatter functions from trace amplitude and vehicle roll data. *IEEE Journal Of Oceanic Engineering, 41*(1), 155-163.

Teng, Y. (2011). *Sector-specific beam pattern compensation for multi-sector and multi-swath multibeam sonars.* Department of Geodesy and Geomatics Engineering, University of New Brunswick, MScE Thesis,

Urick, R. J. (1954). The backscattering of sound from a harbor bottom. *The Journal of the Acoustical Society of America, 26*(2), 231-235.

Urick, R. J. (1960). Side scattering of sound in shallow water. *The Journal of the Acoustical Society of America, 32*(3), 351-355.

Urick, R. J. (1983). *Principles of underwater sound*. New York: McGraw-Hill.

Weber, T. & Lurton, X. (2015). *Backscatter measurements by seafloor‐mapping sonar guidelines and recommendations* A collective report by members of the GeoHab Backscatter Working Group. Chapter 2

Zhao, J., Zhang, H., Ma, F., & Li, J. (2008). A new algorithm for clustering of seabed types. *Geo-Spatial Information Science, 11*(4), 279-282.

9   APPENDIX

9.1   Computation of GRA

The OMG software suite has a very comprehensive GRA computation algorithm, development of which started in early 2000 [Beaudoin et al., 2002]. The algorithm has two basic GRA computation methods. The first method uses the positional information (depth, across- and along-track distances) of the adjacent beams and uses a least square regression to fit a plane through these points. Once the plane is established the GRA is 90° minus the angle between the vector orthogonal to the plane and the incident angle of the ray (accounted for refraction throughout the water column). During this research two important updates are done in this method. First, an option to choose the number of adjacent profiles from which the adjacent beams will be considered for GRA calculation is added. This provided the ability to include more beams for the least square fitting to suppress noisy bottom detections. Thus, this improves the angle estimate, but potentially with the drawback of smoothing the seafloor representation. The second update is that the selection of adjacent beams from the adjacent profiles is done based on the proximity (as shown in Figure 9.1) rather than a beam number, as it was found that the beam numbering does not always ensure the closest beams.
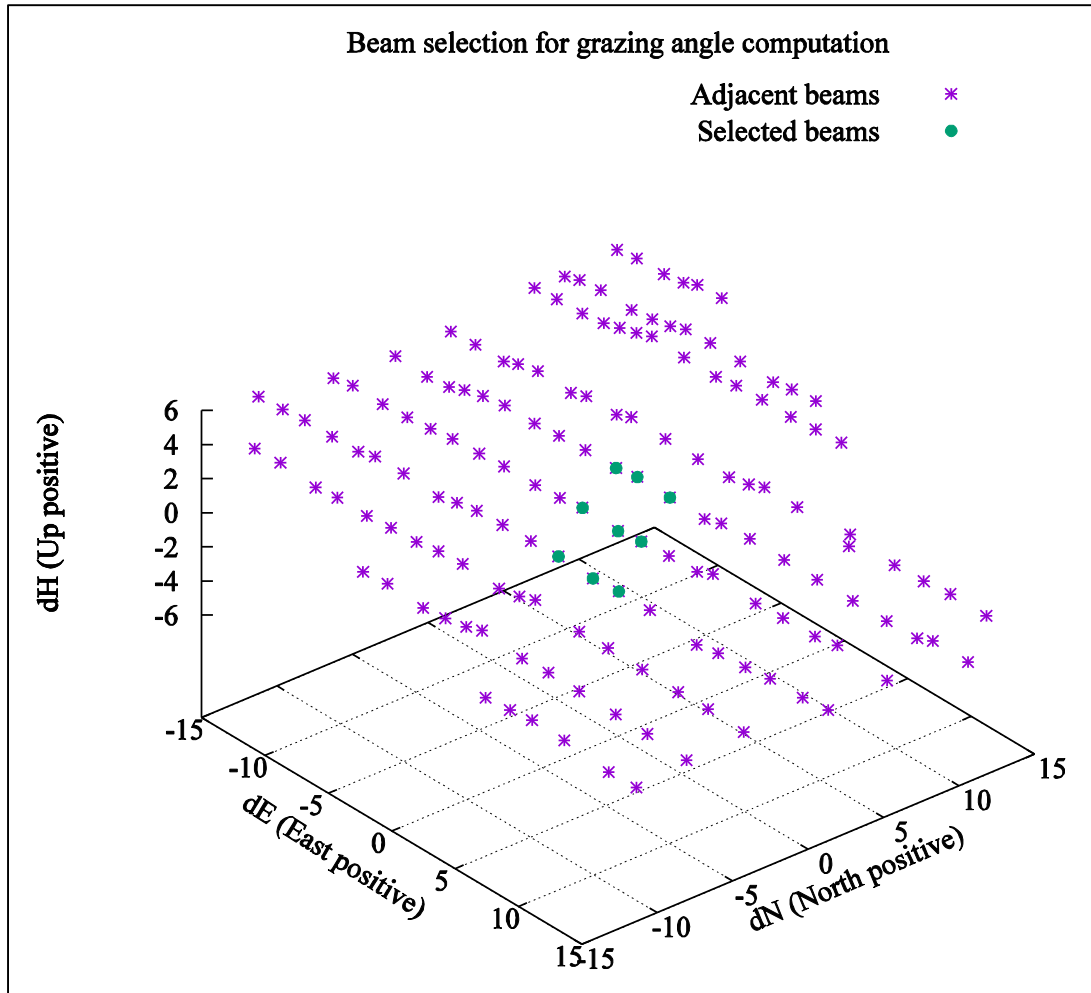
Figure 9.1: Selected 9 beams for least square plane fitting to compute GRA at the central selected beam.

Figures 9.2 and 9.3 show the GRA computed for a survey line collected over a submarine channel at a depth of about 80m in Howe Sound. Both the figures show changes in GRAs near nadir due to along-track modulations from channel bed forms (shown by Y). Also the local specular GRAs can be observed at the inward facing channel walls off nadir (shown by X). Figure 9.2 shows the GRAs computed using different numbers of beams for a section of the survey line. It can be clearly seen that Figure 9.2A is sharper than Figure 9.2B indicating smearing of computed GRAs due to

the higher number of beams used in least square fitting. The benefit of using more beams

is apparent, however, at the outer edges of the swath where sounding errors increase.
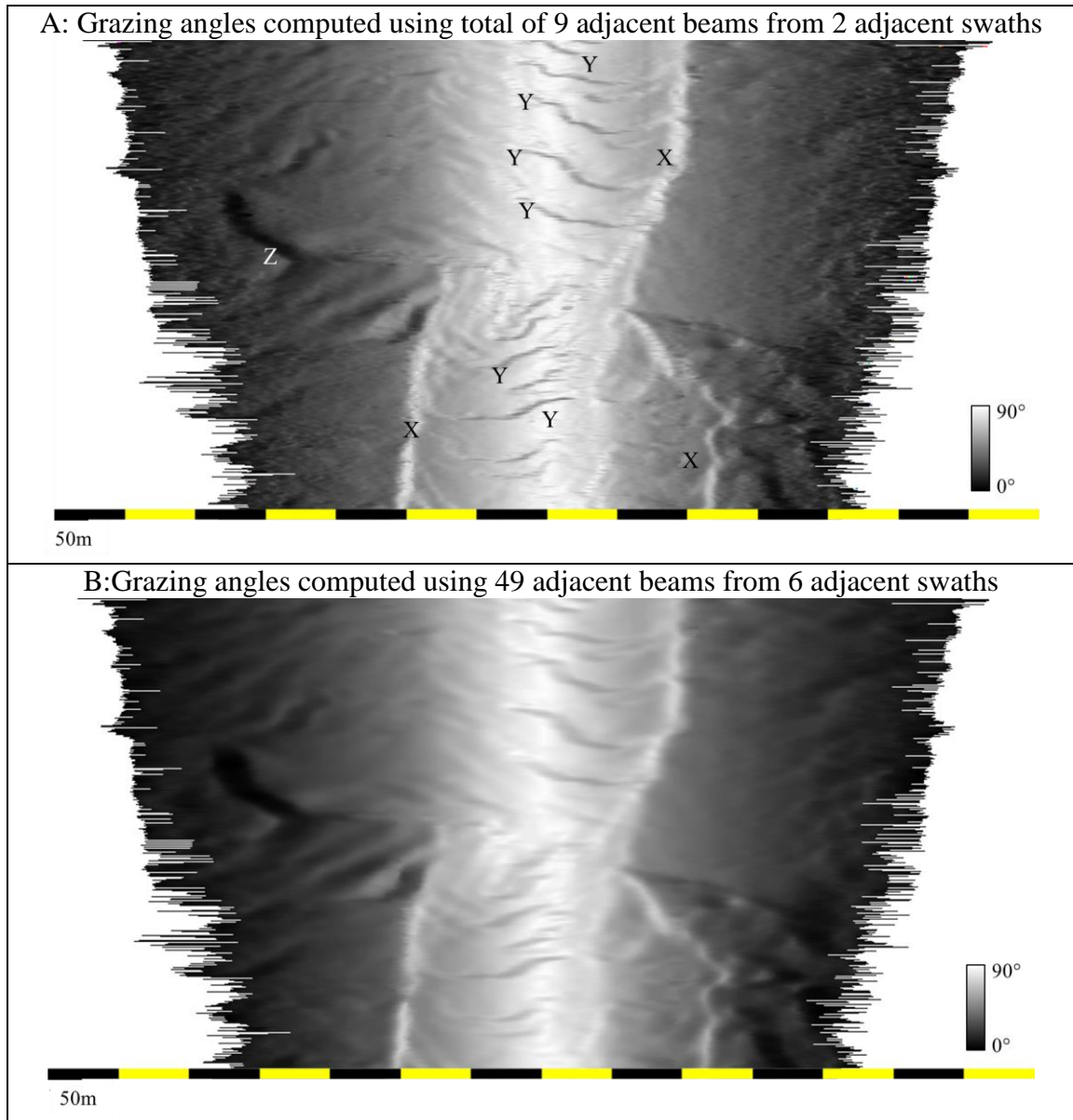
Figure 9.2: Images showing computed GRZs using different numbers of adjacent beams.
X=local high GRA due to inward facing slopes, Y= low GRA near nadir due to steep
along-track slope, Z= extremely low GRA due to outward facing slopes
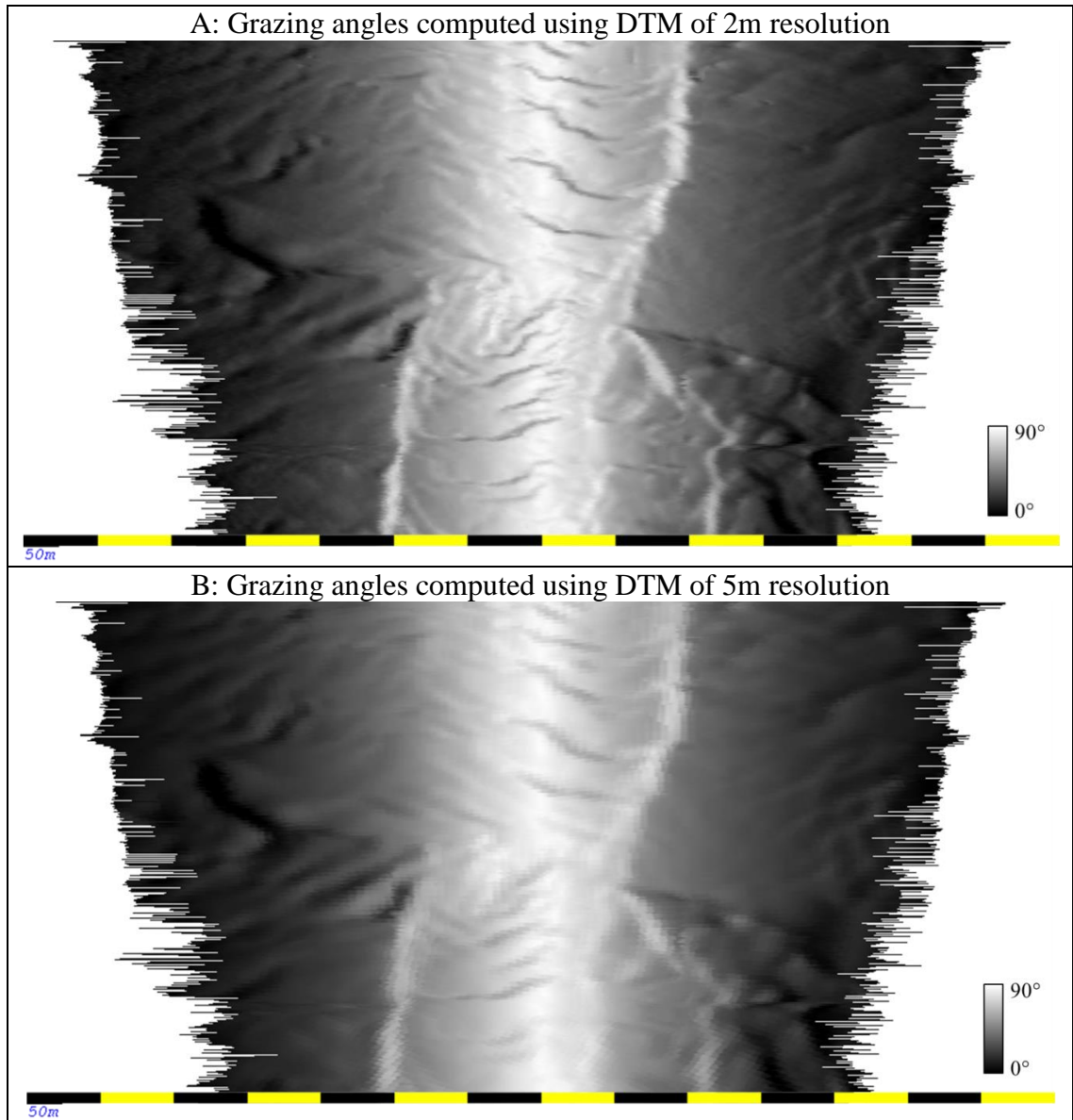
Figure 9.3: GRAs computed using different DTMs

The second method of computing GRA uses the positional information from the digital terrain model (DTM) compiled using processed (cleaned) bathymetric data. For each beam, least square regression is performed to fit a plane using the depths from 6 adjacent nodes of the DTM. Then GRA is computed as in the first method. Figure 9.3 shows GRAs computed for same section of the line shown in Figure 9.2, with two

different DTMs being used to extract positional information of adjacent beams. Figure 9.3A uses 2m resolution DTM while Figure 9.3B uses 5m resolution DTM. The sharp changes in GRAs are smeared due to poor resolution of the 5m DTM.

Both of the above methods have their advantages and disadvantages. The first method is useful to process the backscatter data along with the bathymetric data when no final DTM is available. On the other hand the GRA computations may get influenced by noisy adjacent beams. The use of DTM ensures the removal of the noisy data and the most accurate GRAs are expected from this method. However very low resolution DTM may smooth out local (within node) bathymetric changes and result in unreal values especially in very rough seafloor. Figures 9.2 and 9.3 show the map of GRAs derived from both the methods.

Figure 9.2A shows random changes in GRAs away from the nadir, reflecting the relatively high noise compared to the nadir section. On the other hand Figure 9.3A shows realistic GRAs across the swath, reflecting the contribution of adjacent survey lines into consistently more reliable positional information from the DTM. Hence the most accurate GRAs are derived by using DTMs of the highest possible resolution, and for all the further calculations high resolution DTMs are used to compute GRAs. The resolution of the DTM depends on the data density, which is generally highest for shallow water and lower for the deep water as the beam footprint grows with the depth. The range of computed GRAs is between 0° and 90° with the smallest GRAs normally occurring at extreme port or stbd beams and the largest at nadir for nearly flat seafloor.

9.2   Statistical Processes

The statistical process in this research assumes that the backscatter intensities after the initial preprocessing are free from systematic errors arising from attenuation coefficient, removal of TVG-BS, computation of different angles, and correcting insonification area. The only systematic error expected in the backscatter data is the RBP. Once the preprocessed data is sorted in different bins, however, the data in each SRA-T bin is assumed to have no systematic errors; the only variation is due to random errors.

This appendix explains the statistical process, assumptions, and formulas used in this research. In this appendix, the first section describes the statistical terms and their computations. The second section describes the error propagation strategies used in this research.

9.2.1   Statistical Terms

The sample mean: The sequence of N real numbers x_i obtained from a direct or indirect measurements are referred to as random samples. The sample mean ($\bar{x}$) is computed by Equation 12.

$$\bar{x} = \frac{1}{N} \sum_{i=1}^{N} x_i \tag{12}$$

Standard deviation (σ or SD): The SD is defined as the square root of the mean of the squares of the deviations (d_i) of all the values of a series taken from the sample mean. The SD is a measure of a precision of the random samples computed by Equation 13.

The SD of the measurement is independent of number of measurements, considering all the samples have random errors and fairly drawn from the population.

$$\sigma = \sqrt{\frac{1}{N-1}\sum_{i=1}^{N} d_i^2} \quad = \quad \sqrt{\frac{1}{N-1}\sum_{i=1}^{N}(x_i - \bar{x})^2} \tag{13}$$

In the absence of any systematic errors the standard deviation (precision) is taken as a measure of the accuracy of the measurements.

The relative standard deviation (RSD): is the ratio of SD to the mean value($\sigma/\bar{x}$). It is used to compare two SD irrespective of the magnitudes of the mean value. Hence many plots intended to compare the SD between different SRAs and sectors are plotted using the RSD. If the RSD is multiplied by 100 then it represents percent SD.

The standard error of mean (σ_m) is the precision of the mean of the random sample. In simple words it is nearness of sample mean to the population mean (or true value) and can be computed by the following equation. The standard error takes into account number of samples used to compute the mean. As number of samples increases (approaches to infinity) the mean approaches to the true mean of the population.

$$\sigma_m = \frac{\sigma}{\sqrt{N}} \qquad (14)$$

For example, previously Figure 4.12 showed the RLI distribution of backscatter intensities that falls in the bin under sector 5, SRA-R of 0°, GRA of 60°, and SRA-T of +65°. Following table shows the computed statistical terms for that bin.

Table 9.1: Example statistical values

Number of samples after outlier removal N	Sample mean RLI $\bar{x}$	Standard deviation (SD) σ	Relative Standard deviation (RSD)	Standard error of mean σ_m
3330	$3.19 \times E^{-4}$	$2.63 \times E^{-4}$	0.8256	$4.562 \times E^{-6}$

9.2.2 Averaging Process and Outlier Removal

The RBP extraction deals with thousands of samples of backscatter intensities and produces a single estimate of RBP value for each SRA. The process involves many steps that average similar quantities to obtain the best probable value from the samples. Two major approaches were followed in this research. As the initial samples (RLI) followed the Rayleigh distribution, section 9.2.2.1 describes how the samples were averaged and any outliers were rejected. During the intermediate steps the ratios of RLI were used which were assumed to have normal distribution and section 9.2.2.2 describes how the averaging was done in that case.

9.2.2.1 Case of Rayleigh Distribution

For this research the backscatter intensities that are converted into relative linear intensities are assumed to be Rayleigh distributed. The Rayleigh distribution is a skewed distribution and the most likelihood estimation of its parameter (b) using the intensity values is computed by Equation 15. Some authors, for example Lurton [2002], use symbol σ to indicate the distribution parameter but it is avoided here not to confuse with the SD symbol.

$$b = \sqrt{\frac{1}{2N}\sum_{i=1}^{N} x_i^2} \qquad (15)$$

The mean value of the random samples is computed using Equation 16.

$$\bar{x} = b\sqrt{\pi/2} \qquad (16)$$

The theoretical SD of the Rayleigh distributed samples using the parameter is computed by Equation 17.

$$\sigma = \sqrt{\frac{4-\pi}{2}b^2} \qquad (17)$$

However, it is possible that few of the samples differ from other values in same set due to unknown reasons which may include strong coherent reflections or any electronic noise. Those samples are called outliers and they can affect the mean value significantly. To remove the outliers, the values that fall outside of the average computed using all the

244

sample ± 2× theoretical SD are neglected from further computation. Once the outliers are removed the new average value was computed using Equation 12, and the SD was computed using Equation 13.

9.2.2.2 Case of Normal Distribution

During the RBP extraction process, the averaging of RLI ratios that have associated propagated SDs was required at many intermediate steps. These RLI ratios which are computed from Rayleigh distributed RLI are assumed normally distributed. A non-weighted arithmetic mean was used during the computation of the mean value of RLI ratios during various steps of RBP extraction. This was done despite having related SD for each RLI ratios that could be used as weight for the averaging process. A non-weighted arithmetic mean was adopted to avoid skewing of the mean RLI ratio as it was found that the SDs of the RLI ratios at SRA-Ts closer to nadir has higher SDs then those away from nadir. If the SDs were used as weights for the averaging process, the resulted across-track function was found to skew towards the outer SRAs.

In order to avoid this unrealistic skew of the across-track RBP functions, a simple arithmetic mean was taken applying equal weight to all RLI ratios available for the computation of mean RLI ratio. However, before the arithmetic mean was taken, the initial mean and SD was computed using Equation 12 and 13. All the values were then tested for outliers and the values that fall out of the range of the initial average ±2×initial

SD were rejected. A new mean and its SD was then computed using the filtered values and their SDs as shown in the following section.

9.2.3   Error Propagation and its Interpretation

The first part of this section primarily describes how the errors were propagated in this research. The second part explains how the propagated errors can be interpreted to give an estimate of uncertainty of the results.

9.2.3.1 Error Propagation

The average RLIs are the fundamental quantities used as the starting point of the RBP extraction. Each average value for each of the bin has a related SD which was propagated throughout the RBP extraction process until the final propagated SD of the extracted RBP was computed. The RBP extraction process includes the mathematical operations of multiplication, division, averaging, and conversion to dB of final RLI ratios. During all these processes, the related SDs were propagated to compute the SD of the end result. For the non-linear operations like multiplication, division and logarithmic functions, the function was linearized by approximation to the first-order Taylor series expansion. The generalized formula for the propagation of errors for a nonlinear function

246

$f(y, z)$ assuming that variable y and z are independent of each other (the covariance $\sigma_{yz}^2 = 0$) is shown in Equation 18, where σ_y and σ_z are SD of y and z respectively, and $\frac{\partial f}{\partial y}$ and $\frac{\partial f}{\partial z}$ are partial derivatives of function f with respect to y and z respectively.

$$\sigma_f = \sqrt{\left(\frac{\partial f}{\partial y}\right)^2 \sigma_y^2 + \left(\frac{\partial f}{\partial z}\right)^2 \sigma_z^2} \tag{18}$$

Table 9.2 shows the mathematical functions with constant a, and variable x, y, and z. The table also shows the formulas used for computing the propagated SD considering SDs of the variables. In the case of non-weighted arithmetic mean, the error propagation was done using formula shown in the last row of Table 9.2.

Table 9.2: Propagation of errors

Function	Propagated SD
$f = a \times y$	$\sigma_f = \|a\| \times \sigma_y$
$f = y \times z$	$\sigma_f = \sqrt{z^2 \times \sigma_y^2 + y^2 \times \sigma_z^2}$
$f = y/z$	$\sigma_f = \|f\| \sqrt{\left(\frac{\sigma_y}{y}\right)^2 + \left(\frac{\sigma_z}{z}\right)^2}$
$f = \log_{10}(y)$	$\sigma_f = \left\|\frac{\sigma_y}{y \times \ln 10}\right\|$
$\bar{x} = \frac{1}{N} \sum_{i=1}^{N} x_i$	$\sigma_{\bar{x}} = \sqrt{\frac{1}{N^2} \sum_{i=1}^{N} \sigma_{x_i}^2}$

9.2.3.2 Interpretation of the Propagated Errors

Statistically either SDs or standard errors can be used for error propagation as long as the final propagated errors are realistic, logical, and interpreted in correct way. In this research both the final propagated SDs and final propagated standard errors can be computed.

For the test data set used in chapter 4, the extracted across-track RBP and its final propagated SD for sector 0 SRA -50° is 0.13 dB ± 0.21 dB while the final propagated standard error is ±0.0092 dB. The final propagated SD can be interpreted as, if another dataset was collected at the same location in same conditions and with the same depth mode of the sonar and used for the across-track RBP extraction, 68.3% chance is that the second extracted across-track RBP value for sector 0 SRA -50° is within ± 0.21 dB of the first extracted value. As said earlier, the SD does not have a direct relationship with the number of samples. In other words the length of survey line or number of profiles collected should not affect the propagated SD. The SD represents the variability of the backscatter data from the test dataset for each of the bins and propagates that variability to the final extracted RBP.

On the other hand, the standard error gives an estimate of how close is the data set mean value from its actual or true population mean value which is always unknown. As the number of observations increases, the dataset mean approaches the actual population mean value and value of standard error approaches 0.0. The standard error considers the dispersion of the sample data set as well as the number of samples in it as seen from

248

Equation 14. For the case used as an example in chapter 4, the extracted across-track RBP

and its final propagated standard error for sector 0 SRA -50° is 0.1323 dB ±0.0092 dB.

This can be interpreted as, if we have infinite samples in each of the bin by collecting

infinite number of lines over the same test area and then extract the true value of the

across-track RBP at SRA -50°, then it is 68.3% likely that the true value will be within

±0.0092dB of 0.1323dB.

9.3   Manufacturer's Correction for RBP

The Kongsberg (manufacturer) Bscorr file, which details the estimate of across-track RBP for all operating modes of the sonar, is retrieved from the transceiver of EM 710 multibeam sonar which was used in this research. The entire file is presented here for the completeness.

# Very shallow - Single swath	# Very shallow - Dual swath 1	# Very shallow - Dual swath 2
1 0 3	1 1 3	1 2 3
# Port Sector	# Port Sector	# Port Sector
217.6	217.8	217.2
6	6	6
80.0 -9.8	80.0 -9.3	80.0 -7.7
70.0 -4.0	70.0 -3.7	70.0 -3.4
60.0 -0.7	60.0 -0.5	60.0 -1.1
50.0 0.0	50.0 0.0	50.0 -0.7
40.0 -1.6	40.0 -1.1	40.0 -1.2
30.0 -8.0	30.0 -7.2	30.0 -14.1
# Cent Sector	# Cent Sector	# Cent Sector
217.4	219.0	217.2
11	11	11
50.0 -9.8	50.0 -10.4	50.0 -9.6
40.0 -4.7	40.0 -6.2	40.0 -4.4
30.0 -2.0	30.0 -2.7	30.0 -1.9
20.0 -0.7	20.0 -1.0	20.0 -0.6
10.0 -0.3	10.0 -0.1	10.0 -0.4
0.0 -0.1	0.0 -0.4	0.0 -0.1
-10.0 -0.3	-10.0 -0.1	-10.0 -0.4
-20.0 -0.7	-20.0 -1.0	-20.0 -0.6
-30.0 -2.0	-30.0 -2.7	-30.0 -1.9
-40.0 -4.7	-40.0 -6.2	-40.0 -4.4
-50.0 -9.8	-50.0 -10.4	-50.0 -9.6
# Stb Sector	# Stb Sector	# Stb Sector
216.9	217.8	217.2
6	6	6
-30.0 -11.9	-30.0 -7.2	-30.0 -14.1
-40.0 -1.2	-40.0 -1.1	-40.0 -1.2
-50.0 -0.4	-50.0 0.0	-50.0 -0.7
-60.0 -0.8	-60.0 -0.5	-60.0 -1.1
-70.0 -3.5	-70.0 -3.7	-70.0 -3.4
-80.0 -8.3	-80.0 -9.3	-80.0 -7.7

# Shallow - Single swath	# Shallow - Dual swath 1	# Shallow - Dual swath 2
2 0 3	2 1 3	2 2 3
# Port Sector	# Port Sector	# Port Sector
217.7	217.7	216.2
6	6	6
80.0 -9.4	80.0 -9.4	80.0 -9.1
70.0 -3.8	70.0 -3.8	70.0 -3.7
60.0 -0.5	60.0 -0.5	60.0 -0.5
50.0 0.0	50.0 0.0	50.0 0.0
40.0 -1.3	40.0 -1.3	40.0 -1.3
30.0 -7.5	30.0 -7.5	30.0 -9.4
# Cent Sector	# Cent Sector	# Cent Sector
218.6	218.2	217.6
11	11	11
50.0 -10.7	50.0 -10.4	50.0 -9.9
40.0 -6.0	40.0 -5.6	40.0 -4.9
30.0 -2.4	30.0 -2.2	30.0 -2.0
20.0 -1.1	20.0 -1.0	20.0 -0.8
10.0 -0.1	10.0 -0.2	10.0 -0.3
0.0 -0.2	0.0 -0.2	0.0 -0.2
-10.0 -0.1	-10.0 -0.2	-10.0 -0.3
-20.0 -1.1	-20.0 -1.0	-20.0 -0.8
-30.0 -2.4	-30.0 -2.2	-30.0 -2.0
-40.0 -6.0	-40.0 -5.6	-40.0 -4.9
-50.0 -10.7	-50.0 -10.4	-50.0 -9.9
# Stb Sector	# Stb Sector	# Stb Sector
216.7	217.3	216.6
6	6	6
-30.0 -8.6	-30.0 -8.4	-30.0 -11.1
-40.0 -1.5	-40.0 -1.7	-40.0 -1.2
-50.0 0.0	-50.0 0.0	-50.0 -0.2
-60.0 -0.5	-60.0 -0.7	-60.0 -0.6
-70.0 -3.9	-70.0 -4.0	-70.0 -3.5
-80.0 -9.5	-80.0 -9.8	-80.0 -8.6

# Medium - Single swath	# Medium - Dual swath 1	# Medium - Dual swath 2
3 0 3	**3 1 3**	**3 2 3**
# Port Sector	# Port Sector	# Port Sector
217.7	217.7	217.6
6	6	6
80.0 -9.4	80.0 -9.4	80.0 -10.0
70.0 -3.8	70.0 -3.8	70.0 -4.1
60.0 -0.5	60.0 -0.5	60.0 -0.7
50.0 0.0	50.0 0.0	50.0 0.0
40.0 -1.3	40.0 -1.3	40.0 -1.8
30.0 -7.5	30.0 -7.5	30.0 -8.3
# Cent Sector	# Cent Sector	# Cent Sector
219.3	219.3	219.0
11	11	11
50.0 -10.1	50.0 -10.1	50.0 -10.4
40.0 -6.4	40.0 -6.4	40.0 -6.2
30.0 -3.0	30.0 -3.0	30.0 -2.7
20.0 -0.9	20.0 -0.9	20.0 -1.0
10.0 -0.1	10.0 -0.1	10.0 -0.1
0.0 -0.5	0.0 -0.5	0.0 -0.4
-10.0 -0.1	-10.0 -0.1	-10.0 -0.1
-20.0 -0.9	-20.0 -0.9	-20.0 -1.0
-30.0 -3.0	-30.0 -3.0	-30.0 -2.7
-40.0 -6.4	-40.0 -6.4	-40.0 -6.2
-50.0 -10.1	-50.0 -10.1	-50.0 -10.4
# Stb Sector	# Stb Sector	# Stb Sector
217.6	217.7	217.1
6	6	6
-30.0 -8.3	-30.0 -7.9	-30.0 -8.5
-40.0 -1.8	-40.0 -1.5	-40.0 -1.6
-50.0 0.0	-50.0 0.0	-50.0 0.0
-60.0 -0.7	-60.0 -0.6	-60.0 -0.6
-70.0 -4.1	-70.0 -4.0	-70.0 -4.0
-80.0 -10.0	-80.0 -9.7	-80.0 -9.8

# Deep - Single swath	# Deep - Dual swath 1	# Deep - Dual swath 2
4 0 3	4 1 3	4 2 3
# Port Sector	# Port Sector	# Port Sector
217.7	217.7	217.6
6	6	6
80.0 -9.4	80.0 -9.4	80.0 -10.0
70.0 -3.8	70.0 -3.8	70.0 -4.1
60.0 -0.5	60.0 -0.5	60.0 -0.7
50.0 0.0	50.0 0.0	50.0 0.0
40.0 -1.3	40.0 -1.3	40.0 -1.8
30.0 -7.5	30.0 -7.5	30.0 -8.3
# Cent Sector	# Cent Sector	# Cent Sector
219.3	219.3	219.0
11	11	11
50.0 -10.1	50.0 -10.1	50.0 -10.4
40.0 -6.4	40.0 -6.4	40.0 -6.2
30.0 -3.0	30.0 -3.0	30.0 -2.7
20.0 -0.9	20.0 -0.9	20.0 -1.0
10.0 -0.1	10.0 -0.1	10.0 -0.1
0.0 -0.5	0.0 -0.5	0.0 -0.4
-10.0 -0.1	-10.0 -0.1	-10.0 -0.1
-20.0 -0.9	-20.0 -0.9	-20.0 -1.0
-30.0 -3.0	-30.0 -3.0	-30.0 -2.7
-40.0 -6.4	-40.0 -6.4	-40.0 -6.2
-50.0 -10.1	-50.0 -10.1	-50.0 -10.4
# Stb Sector	# Stb Sector	# Stb Sector
217.6	217.7	217.1
6	6	6
-30.0 -8.3	-30.0 -7.9	-30.0 -8.5
-40.0 -1.8	-40.0 -1.5	-40.0 -1.6
-50.0 0.0	-50.0 0.0	-50.0 0.0
-60.0 -0.7	-60.0 -0.6	-60.0 -0.6
-70.0 -4.1	-70.0 -4.0	-70.0 -4.0
-80.0 -10.0	-80.0 -9.7	-80.0 -9.8

# Very Deep - Single swath	# Extra deep - Single swath
5 0 3	**6 0 3**
# Port Sector	# Port Sector
221.7	223.1
6	5
70.0 -9.4	60.0 -7.1
60.0 -4.7	50.0 -4.0
50.0 -2.4	40.0 -0.8
40.0 -0.3	30.0 -0.7
30.0 -1.6	20.0 -7.4
20.0 -10.9	# Cent Sector
# Cent Sector	220.1
220.1	9
9	40.0 -6.8
40.0 -6.8	30.0 -3.7
30.0 -3.7	20.0 -0.8
20.0 -0.8	10.0 -0.1
10.0 -0.1	0.0 -0.8
0.0 -0.8	-10.0 -0.1
-10.0 -0.1	-20.0 -0.8
-20.0 -0.8	-30.0 -3.7
-30.0 -3.7	-40.0 -6.8
-40.0 -6.8	# Stb Sector
# Stb Sector	222.3
221.1	5
6	-20.0 -7.3
-20.0 -10.9	-30.0 -0.7
-30.0 -1.7	-40.0 -0.7
-40.0 -0.2	-50.0 -3.5
-50.0 -2.0	-60.0 -6.8
-60.0 -4.4	
-70.0 -9.2	

9.4   Details of Test Sites

For this research data collected on two different test areas were used. This section documents the details of those test areas in detail.

9.4.1   Bute Inlet British Columbia

In 2014 OMG was involved in extensive multibeam sonar data collection in Bute Inlet, British Columbia on West coast of Canada. Kongsberg's EM 710 mounted on the CSL Heron was used for the survey from June 8th to June 12th 2014. The depths ranged from less than 10m to about 500m. After initial bathymetric and backscatter data collection, two suitable sites were identified their positions are shown in Figure 9.4. The first location at ≈100m depth is estimated to have homogeneous fine sand whereas the second test site at ≈200m depth is estimated to have homogeneous sandy gravel. No physical samplings at these sites were possible due to time and instrumentation constraints. Figures 9.5 and 9.6 shows the bathymetric maps for both test sites with navigation lines.
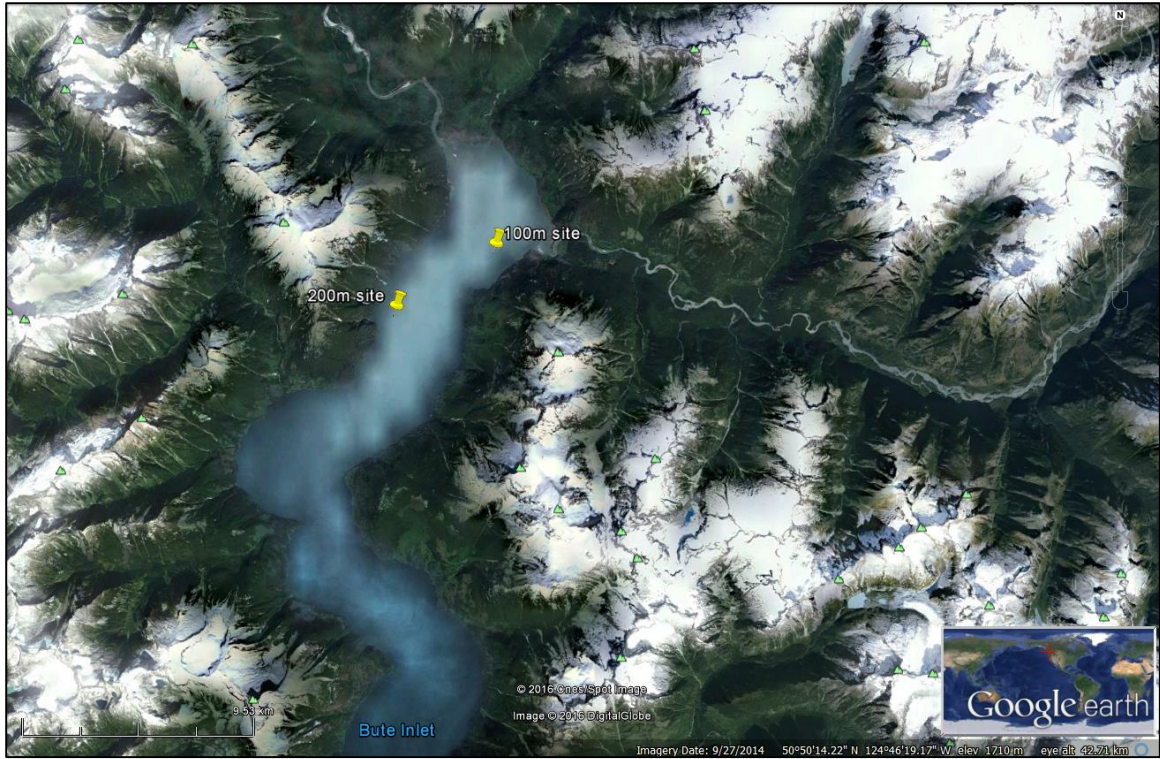
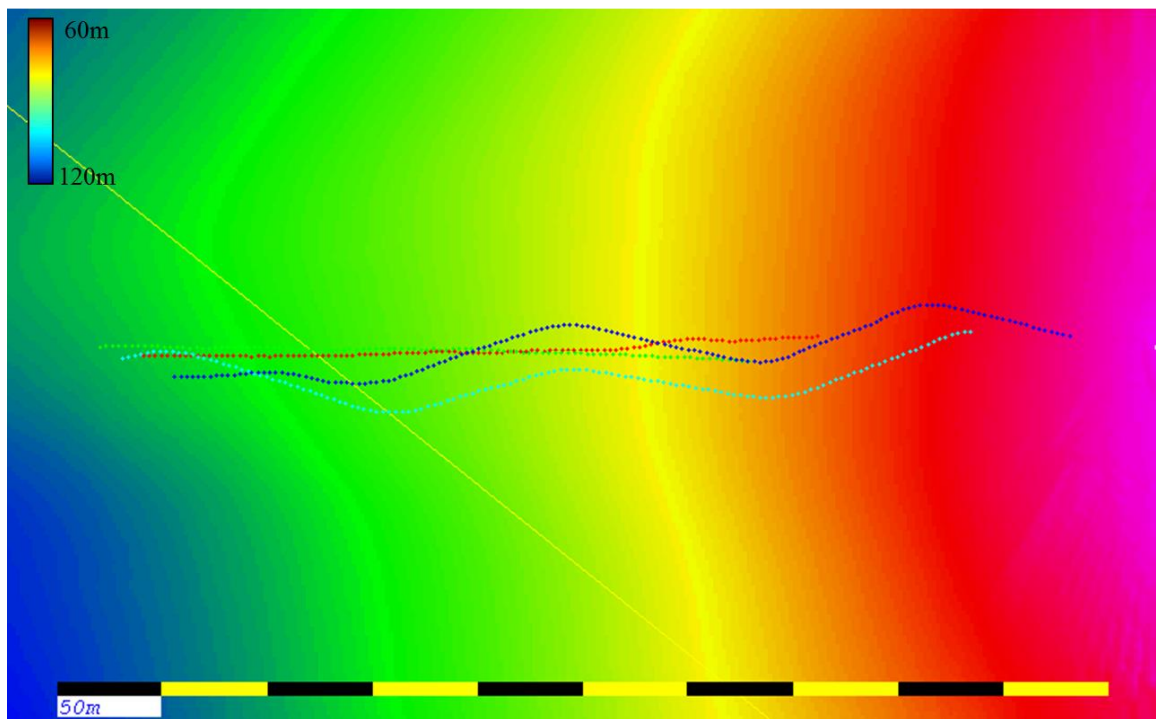Figure 9.4: General area of Bute Inlet with location of test areas

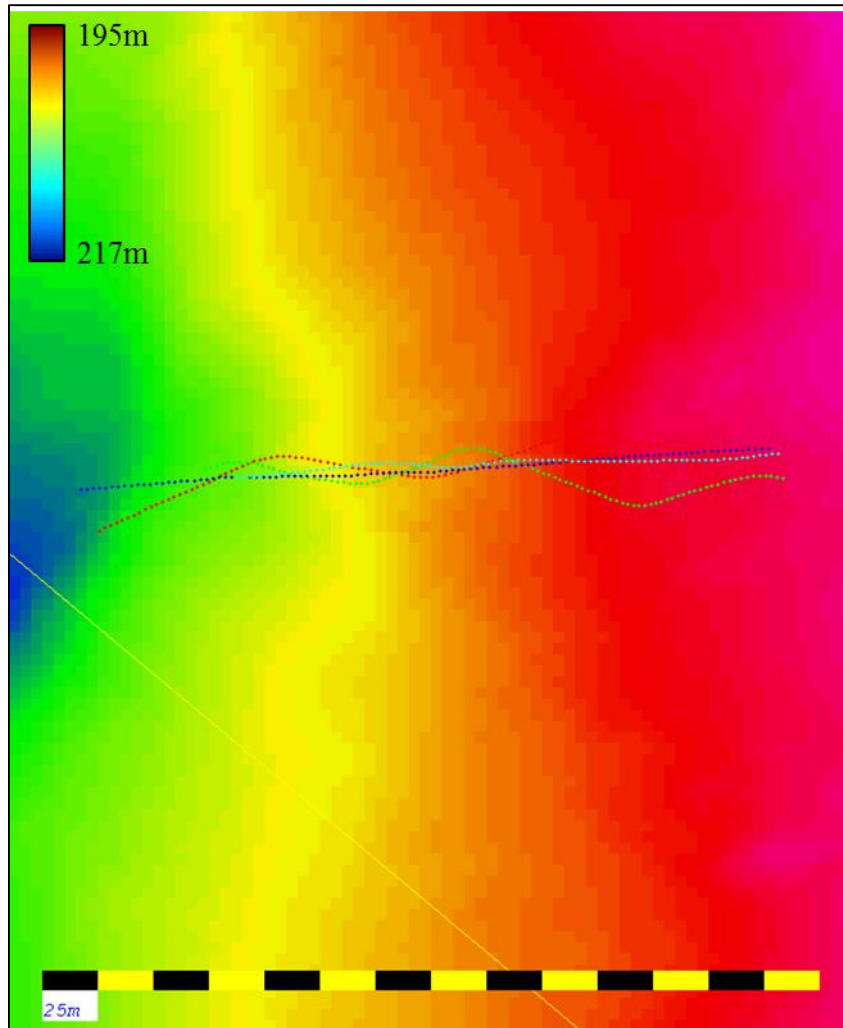Figure 9.5: DTM at 100m test site in Bute Inlet with navigation lines

257

Figure 9.6: DTM at 200m depth site with navigation lines

9.4.2 Howe Sound, Squamish River Delta

In 2015 as part of the yearly bathymetric surveys at Squamish River Delta, OMG deployed CSL Heron with the same sonar (EM 710) that was used in year 2014 in Bute Inlet. The test site at 50m depth was selected near an inactive channel on the homogeneous sediments (see Figure 9.7). Figure 9.8 shows the bathymetric map of the

test area along with navigational lines. The physical sampling of the sediments was not possible; from the ARC derived for this location the sediments are estimated to be sand or sandy gravel.
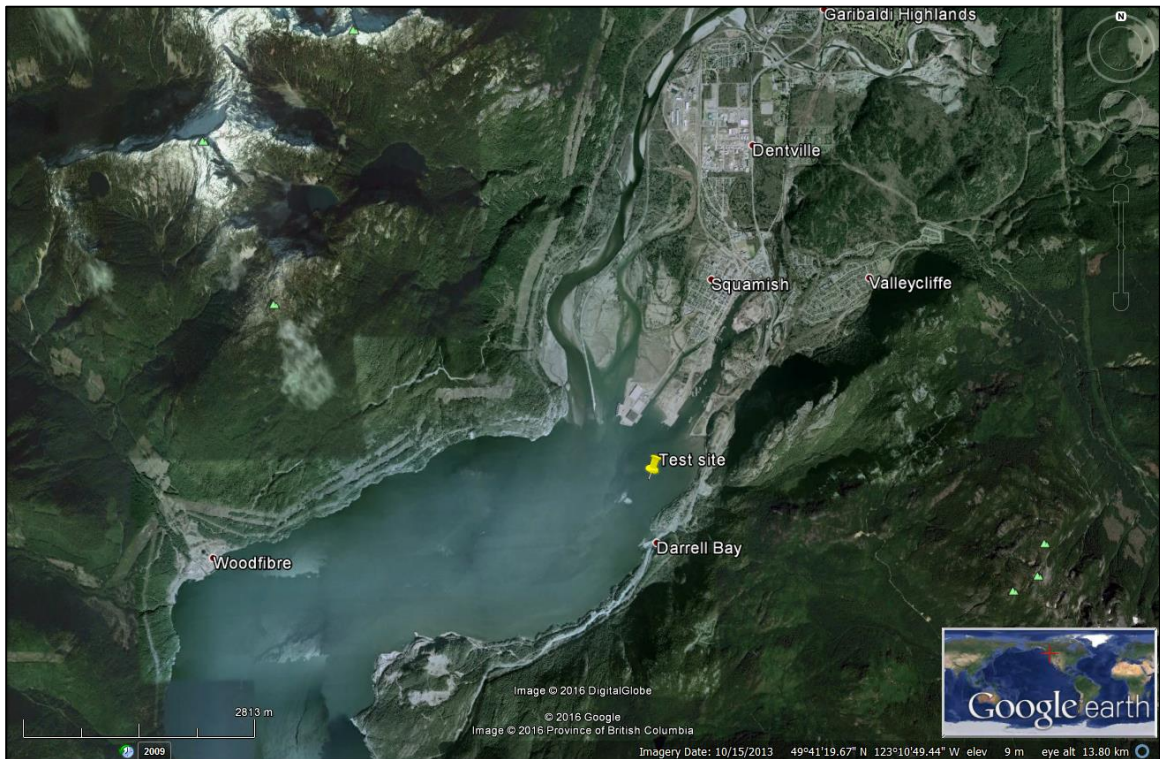

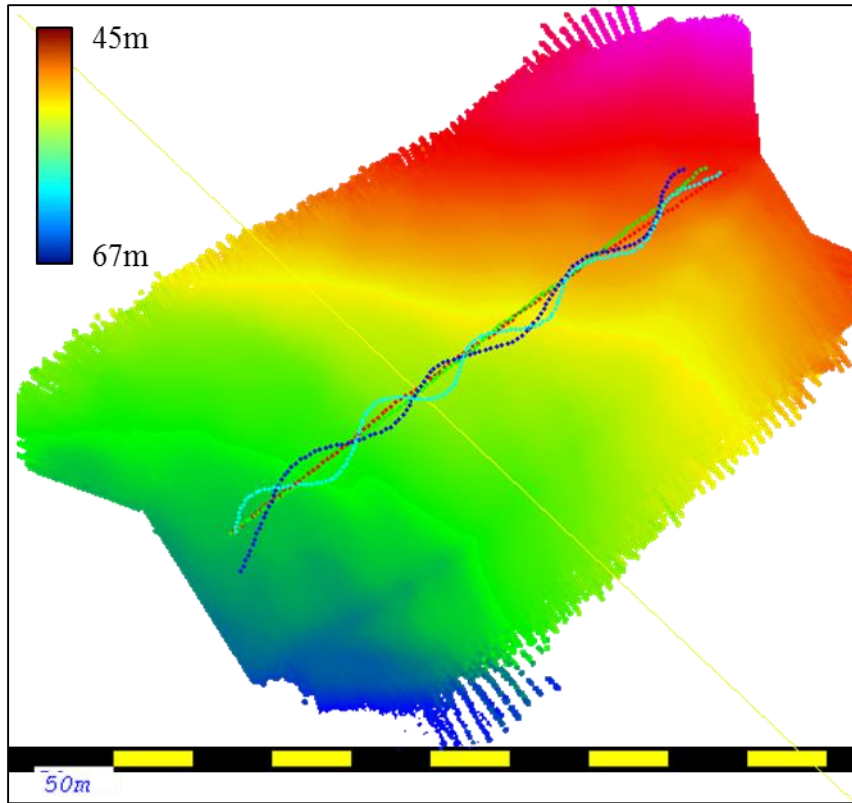Figure 9.7: General area of test site in Squamish River Delta

Figure 9.8: DTM of test site at Squamish River Delta with navigation lines.

CURRICULUM VITAE

Candidate's Name: Anand Devappa Hiroji

Universities attended:

2011-2016	Ph.D., University of New Brunswick
2009-2011	MEng (Geodesy and Geomatics Engineering), University of New Brunswick
2001-2005	BE (Civil Engineering), PVPIT Budhgaon, Shivaji University, India

Conference Paper:

Hiroji, A., D.; Hughes Clarke, J. E (2016), Multi-sector radiometric beam pattern extraction method for improved seafloor classification, presented at Canadian Hydrographic Conference, Halifax NS, 16th-19th May